DYNAMIC SOIL-STRUCTURE INTERACTION: THEORY AND VERIFICATION

by

MUTHUCUMARASAMY YOGENDRAKUMAR

B.Sc.Eng.(Hons), University of Peradeniya, Sri Lanka, 1980
M.A.Sc., The University of British Columbia, 1983

A THESIS SUBMITTED IN PARTIAL FULFILMENT OF

THE REQUIREMENTS FOR THE DEGREE OF

DOCTOR OF PHILOSOPHY

in

THE FACULTY OF GRADUATE STUDIES

(Department of Civil Engineering)

We accept this thesis as conforming

to the required standard

THE UNIVERSITY OF BRITISH COLUMBIA

January 1988

In presenting this thesis in partial fulfilment of the requirements for an advanced degree at the University of British Columbia, I agree that the Library shall make it freely available for reference and study. I further agree that permission for extensive copying of this thesis for scholarly purposes may be granted by the head of my department or by his or her representatives. It is understood that copying or publication of this thesis for financial gain shall not be allowed without my written permission.

Department of CIVIL ENGINEERING

The University of British Columbia
1956 Main Mall
Vancouver, Canada
V6T 1Y3

Date Jan. 29/88

ABSTRACT

A nonlinear effective stress method of analysis for determining the static and dynamic response of 2-D embankments and soil-structure interaction systems is presented. The method of analysis is incorporated in the computer program TARA-3. The constituitive model in TARA-3 is expressed as a sum of a shear stress model and a normal stress model. The behavior in shear is assumed to be nonlinear and hysteretic, exhibiting Masing behavior under unloading and reloading. The response of the soil to uniform all round pressure is assumed to nonlinearly elastic and dependent on the mean normal effective stresses.

The porewater pressures required in the dynamic effective stress method of analysis are obtained by the Martin-Finn-Seed porewater pressure generation model modified to include the effect of initial static shear. During dynamic analysis, the effective stress regime and consequently the soil properties are modified for the effect of seismically induced porewater pressures.

A very attractive feature of TARA-3 is that all the parameters required for an analysis may be obtained from conventional geotechnical engineering tests either in-situ or in laboratory.

A novel feature of the program is that the dynamic analysis can be conducted starting from the static stress-strain condition which leads to accumulating permanent deformations in the direction of the smallest residual resistance to deformation. The program can also start the dynamic analysis from a zero stress-zero strain condition as is done conventionally in engineering practice.

The program includes an energy transmitting base and lateral energy transmitting boundaries to simulate the radiation of energy which occurs in the field.

The program predicts accelerations, porewater pressures, instantaneous dynamic deformations, permanent deformations due to the hysteretic stress-strain response, deformations

due to gravity acting on the softening soil and deformations due to consolidation as the seismic porewater pressures dissipate.

The capability of TARA-3 to model the response of soil structures and soil-structure interaction systems during earthquakes has been validated using data from simulated earthquake tests on a variety of centrifuged models conducted on the large geotechnical centrifuge at Cambridge University in the United Kingdom. The data base includes acceleration time histories, porewater pressure time histories and deformations at many locations within the models. The program was able to successfully simulate acceleration and porewater pressure time histories and residual deformations in the models.

The validation program suggests that TARA-3 is an efficient and reliable program for the nonlinear effective stress analysis of many important problems in geotechnical engineering for which 2-D plane strain representation is adequate.

TABLE OF CONTENTS

LIST OF SYMBOLS

a	Constant
b	Constant
B	Bulk Modulus
B_t	Tangent Bulk Modulus
$[B]$	Strain Displacement Matrix
c'	Cohesion Intercept
C_1	Volume Change Constant
C_2	Volume Change Constant
C_3	Volume Change Constant
C_4	Volume Change Constant
$[C]$	Global Damping Matrix
d	Depth to the Center of Element
D_r	Relative Density
e	Void Ratio
E_r	Rebound Modulus
G	Shear Modulus
G_t	Tangent Shear Modulus
G_{max}	Shear Modulus at Small Strain
K_2	Shear Modulus Parameter
K_{2max}	Shear Modulus Parameter
K_r	Rebound Constant
K_G	Shear Modulus Constant
K_b	Bulk Modulus Number
K_{clay}	Shear Modulus Parameter for Clay
K_s	Unit Shear Stiffness
K_n	Unit Normal Stiffness
$[K]$	Global Stiffness Matrix

$[K_t]$	Global Tangent Stiffness Matrix
m	Rebound Constant
M	Mass
$[M]$	Global Mass Matrix
n	Rebound Constant
n	Bulk Modulus Exponent
N_1	Shape Function
N_2	Shape Function
N_e	Number of Elements
N_{fe}	Number of Failed Elements
P_a	Atmospheric Pressure
$\{P_{cor}\}$	Correction Force Vector
$\{P\}$	External Force Vector
$\{\Delta P\}$	Incremental External Force Vector
R	Radius of Mohr Circle
S_u	Undrained Shear Strength
t	Time
T	Time
ΔT	Time Increment
u	Porewater Pressure
$\{U\}$	Porewater Pressure Vector
$\{\Delta U\}$	Incremental Porewater Pressure Vector
V	Volume
V_s	Shear Wave Velocity
V_p	Compression Wave Velocity
x	Cartesian Coordinate
y	Cartesian Coordinate
z	Cartesian Coordinate

α	Damping Coefficient
β	Damping Coefficient
λ	Critical Damping Ratio
ω_1	Natural Frequency
γ	Shear Strain Amplitude
γ_{xy}	Shear Strain
ϵ_{vd}	Volumetric Strain
$\Delta\epsilon_{vd}$	Incremental Volumetric Strain
ρ	Mass Density
ϕ'	Internal Friction Angle
ν	Dilation Angle
τ	Shear Stress
τ_{max}	Shear Strength
σ'_1	Major Principal Effective Stress
σ'_3	Minor Principal Effective Stress
σ'_m	Mean Normal Effective Stress

LIST OF TABLES

LIST OF FIGURES

Dedicated to

Appah, Ammah, Raju, Pappy, Uma and all in my family.

ACKNOWLEDGEMENTS

I would like to thank Professor W.D. Liam Finn for his helpful guidance, constructive suggestions and encouragement which enhanced the quality of the research work. I am also indebted to all my collegues in the department of civil engineering for providing a pleasant and cordial atmosphere during the studies.

I am grateful to Mr. Ram Lingam and family for providing a home away from home and for their helps on many occasions. Special thanks are due to my wife, Uma, for her support and patience shown throughout my studies.

The U.S. Nuclear Regulatory Commission, Washington, D.C., through the U.S. Army Corps of Engineers, Waterways Experiment Station, Vicksburg, Miss., financed the series of simulated earthquake tests on centrifuged model structures at Cambridge University, U.K., which were used to validate the TARA-3 program. I am grateful to L.L. Beratan of U.S. NRC and R.H. Ledbetter of the USAE for their interests and constructive suggestions and to Professor A.N. Schofield, S.Steedman, R. Dean and F.H. Lee of Cambridge University for innovative high-quality centrifuge tests.

The financial assistance provided by the department of civil engineering in the form of graduate research assistantship and graduate teaching assistantship is greatly appreciated.

CHAPTER 1

INTRODUCTION

Since the occurrence of damaging earthquakes in Niigata and Alaska in 1964, research interests have been directed first towards understanding the phenomenon of liquefaction and then were slowly shifted towards developing methods to assess the safety of critical facilities which are located in soils susceptible to liquefaction. Typical examples of such facilities are nuclear power plants, liquefied natural gas (LNG) plants, dams, embankments and pipelines. More recently, methods have been introduced to cater to the needs of the offshore industry.

Earlier assessments of the safety of soil structures subjected to seismic loading were based primarily on factors of safety along an assumed potential failure surface. However, the trend shifted from assessment in terms of factors of safety to one in terms of deformations. The latter method of assessment is believed to be more suitable as it allows the functional aspects of the structure to be incorporated in performance criteria.

In the past, several methods were proposed to compute earthquake induced deformations in two-dimensional earth structures. The two methods of analysis which have found wide application in current engineering practice are Newmark's method of analysis (Newmark, 1965) and Seed's semi-empirical method of analysis (Seed et al, 1973; Seed, 1979).

Newmark's method of analysis is based on the concept that no movement takes place

along a potential sliding surface until the acceleration of the sliding mass exceeds the yield acceleration (Newmark, 1965). Whenever the acceleration of the sliding mass exceeds the yield acceleration, the progressive displacement is calculated using the process of double integration. While the determination of yield acceleration of the sliding mass is straightforward, difficulties may arise in determining the representative acceleration of the sliding mass, since the accelerations vary throughout the sliding mass. One of the simplest ways to find representative acceleration is to take the average of the accelerations over the sliding surface. Alternatively, procedures developed by Makdisi and Seed (1978) could be employed.

Newmark's method of analysis does not give deformation and strain fields of the earth structures. Rather, it gives an index of probable behavior which can be compared with indices of other earth structures which have behaved satisfactorily or unsatisfactorily during earthquakes (Finn, 1987). Therefore, for the assessment of the safety of new types of structures, as often found in offshore oil exploration, where experience with the application of this method is lacking, one has to be extremely careful in interpreting the index from the point of view of safety.

Furthermore, since yield acceleration is calculated using in-situ initial properties, this method of analysis is only appropriate for materials which do not suffer significant strength loss during earthquake shaking.

Another limitation in this method of analysis is that it is applicable only to cases where the movement occurs along well-defined narrow failure zones. Such a failure mechanism may not occur in many cases as the deformations are often broadly distributed within the soil structures. However, as shown by Goodman and Seed (1966), this method gives satisfactory results in situations where a well-defined failure mechanism exists.

Therefore, while this method of analysis remains a useful approach, it is not generally a satisfactory method to compute permanent deformations induced by seismic loading.

On the other hand, Seed's method of analysis is a semi-analytical method in which data from a dynamic response analysis and data from cyclic triaxial tests are used to estimate potential displacements in the soil structures. The basic steps involved in this method of analysis are summarized below:

1) Determine the pre-earthquake condition that exists in the soil structures by performing a static finite element analysis.

2) Select design earthquake motions appropriate for the site where the soil structure is situated.

3) Perform a dynamic response analysis to determine the time histories of dynamic shear stresses throughout the soil structure resulting from the design motions.

4) Apply the computed time history of stresses to representative samples and observe the effect in terms of strains and porewater pressures. Plot contours of strains and porewater pressure data. These allow interpolation of the strain and porewater pressure data for other elements so that strain and porewater pressure data are developed for all the elements.

5) Determine the minimum factor of safety against total failure by limit equilibrium methods with the assigned strengths of elements consistent with the porewater pressure data observed in the laboratory tests.

6) Assess the overall deformations from the observed strains in the laboratory samples, if the soil structure is found to be safe against a total failure.

In current practice, the dynamic response analysis in step 3 is conducted using equivalent linear elastic analyses. In these analyses, the nonlinear behavior of soil is accounted using an iterative elastic approach so that the soil properties (i.e., shear modulus and damping) are compatible with the computed strains. However, as pointed out by Desai and Christian (1979), the iterative equivalent linear elastic method, like any other iterative approaches, suffers from the fact that the solutions obtained are not unique and are dependent on the assumed properties for the first iteration.

The other limitation of equivalent linear methods is that these may overestimate the seismic response of soil structures comprising nonlinear hysteretic materials due to the phenomenon known as pseudo-resonance (Finn et al, 1978). This occurs if the fundamental period of the input motion coincides with the fundamental period of soil structures as defined by the final set of compatible properties in the iterative method.

Moreover, analyses are conducted in terms of total stresses so that the progressive effect of seismically induced porewater pressures are not reflected in stresses and accelerations. Detailed studies conducted by Finn et al (1978) on one dimensional problems indicate that total stress methods overestimate the seismic response when the seismically induced porewater pressures exceed about 30% of the effective overburden pressures. Therefore, there is reason to believe that at least similar overestimation may occur between the total stress and effective stress methods for two-dimensional problems.

There are several techniques available to compute the deformation field from the strain data obtained in step 4. The modulus reduction technique proposed by Lee (1974) and the strain harmonising technique proposed by Serff et al (1976) are common ones. In the

strain harmonising technique, the strain potentials obtained through laboratory testing are converted to shear stresses. The corresponding nodal forces are applied as loads in a static analysis to compute compatible deformations. The resulting deformations are assumed to be the seismic deformations. As pointed out by Siddharthan (1984), this approach gives rise to a set of inconsistent assumptions. First, the computed strains in the last iterations of the equivalent linear elastic analysis are ignored as being not correct but the stresses are assumed to be correct. This violates the one to one relationship of stresses and strains for a given loading. Secondly, although the final strains computed in the last iteration are assumed not to be correct the strains in the previous iteration procedure are used in the process of obtaining strain compatible soil properties as if they were correct.

Since the deformation field is obtained through a pseudo-static analysis, the time variation of the deformation field cannot be obtained. Also, the Seed approach does not take into account of the deformation that results from dissipation of the seismically induced porewater pressures.

Dynamic effective stress models are available to compute seismic deformations directly in two-dimensional problems. Many are two-dimensional elastic-plastic models based on Biot's equations (Biot, 1941) for coupled fluid-soil systems. However, few of these have been incorporated in commercially available programs. The most general program of this type is DYNAFLOW (Prevost, 1981). While the elastic-plastic models offer the most complete description of the soil response, they are difficult to use and the soil properties required in some of them are difficult to measure. They also make very heavy demands on computing time. Furthermore, there has been no extensive validation of these methods of analyses.

While Newmark and Seed methods of analyses are suitable to earth structures such as embankments and dams, they are not appropriate for analysing soil-structure interaction effects. Dynamic soil-structure interaction during earthquakes is a very complex phenomenon

because of the nonlinear response of soil to strong shaking. The interaction becomes even more complex if the soil is saturated and large seismically induced porewater pressures are generated which alter the strength and stiffness of the soil. The most commonly used program, in current engineering practice, for the analysis of soil-structure interaction systems is FLUSH (Lysmer et al, 1975). It is an equivalent linear finite element analysis in the frequency domain and as such it cannot model certain important phenomena in soil-structure interaction such as relative displacements at the soil-structure interface, uplift during rocking, transient and permanent deformations, the progressive effects of increasing porewater pressures and the hysteretic behavior. To model these phenomena and to obtain reliable estimate of seismic response, nonlinear dynamic effective stress analysis in the time domain is necessary.

Therefore, it is indeed necessary to develop an efficient, practical and reliable method of analysis to compute seismic response of soil structures and soil-structure interaction systems. This need has been already recognised by the National Research Council of the United States. The state-of-the-art for analysing permanent deformations was assessed in a report on eathquake engineering research by the National Research Council of the United States (NRC 1982) as follows:

"Many problems in soil mechanics, such as safety studies of earth dams, require that the possible permanent deformations that could be produced by earthquake shaking of prescribed intensity and duration be evaluated. Where failure develops along well-defined failure planes, relatively simple elasto-plastic models may suffice to calculate displacements. However, if permanent deformations are distributed throughout the soil, the problem is much more complex and practical, reliable methods of analysis are not available."

Consequently, NRC recommended that active research should be directed toward de-

veloping practical and reliable methods to compute seismic deformations (NRC 1982 and 1985).

1.1 Scope

As a first step towards achieving the NRC goal, Siddharthan and Finn developed a dynamic nonlinear effective stress method of analysis and incorporated it into the computer program TARA-2 (Siddharthan and Finn, 1982). A very limited verification of this method of analysis has been reported (Siddharthan, 1984). This thesis undertakes to enhance TARA-2 and to provide an extensive verification of the method of analysis. The enhanced version of the method of analysis has been incorporated in TARA-3 (Finn et al, 1986).

One of the major problems in validating dynamic response analysis is the lack of data from suitably instrumented structures in the field. Some limited validations have been reported for the limited but practical case of the level ground conditions (Finn et al, 1982; Iai et al, 1985). Most of the methods are often validated using data from element tests such as cyclic triaxial or simple shear tests. Although this type of validation is an important first step, it is inadequate because in these tests either the stress or strain is prescribed and both are considered homogeneous. Therefore, the tests do not provide the rigorous test of either the constitutive relations or the robustness of the computational procedure that would be made possible by data from an instrumented structure in the field with inhomogeneous stress and strain fields.

Having this in mind, the United States Nuclear Regulatory Commission (USNRC), through the United States Army Corps of Engineers (USAE), sponsored a series of centrifuge model tests to provide data for the verification of the method of analysis incorporated in TARA-3. The tests were conducted on the large geotechnical centrifuge at Cambridge University in the United Kingdom by Dean and Lee (1984) and Steedman (1985 and 1986).

The centrifuge models were of a variety of structures with foundations of both dry and saturated sands.

The comprehensive data base generated through the simulated earthquake tests on the centrifuged models included acceleration time history at selected locations within the sand foundation and on the structure, porewater pressure time history at selected locations within the saturated sand foundation and deformations along the surface of structure and sand foundation.

1.2 Thesis Outline

Chapter 2 deals exclusively with the method of static analysis. The formulations, basic assumptions and the stress strain model are discussed. Approximate ways of handling some of the limitations are also presented.

Chapter 3 discusses extensively the important aspects of the dynamic nonlinear effective stress method of analysis. The finite element formulation, the numerical treatment and the porewater pressure generation model are presented in detail.

Chapter 4 is entirely devoted to the introduction and implementation of energy transmitting boundaries into the method of analysis. The effectiveness of different boundaries are discussed and examples of the performance of the more useful types are presented.

The principles of centrifuge testing and its applicability for validation of numerical analysis are briefly discussed in Chapter 5. In particular, aspects related to Cambridge geotechnical centrifuge and associated procedures are briefly mentioned. Model construction, data acquisition, instrumentation and related accuracy and model tests selected for the TARA-3 verification study are also discussed.

The selection of soil parameters and other relevant data required for the analyses are

summarised in Chapter 6.

The verification of the predictive capability of TARA-3 using data from the model tests on dry and saturated sand foundations is presented in Chapter 7 and Chapter 8 respectively.

The summary and the conclusions drawn from this research are given in Chapter 9.

CHAPTER 2

METHOD OF STATIC ANALYSIS IN TARA-3

2.1 Introduction

For a complete analysis of the response of a soil-structure system subject to earthquake loading, it may often be necessary to first conduct a static analysis to determine the stress-strain state of the system prior to the earthquake. The knowledge of the in-situ stress-strain state is essential since soil properties such as stiffness and strength which govern the response of the system to earthquake loading depend on these in-situ stress-strain states.

In general, in order to determine in a realistic manner the behavior of the soil structure system to any load, it is necessary to make simplifying assumptions, particularly, regarding the modelling of soil behavior, structural behavior and the site. The significant assumption regarding the geometric modelling of the soil structure system is that the three dimensional nature of the system can be adequately represented by a transverse cross section in which a state of plane strain exists. This assumption is often useful since many geotechnical engineering structures such as earth embankments and dams approximate conditions of plane strain.

The method of static analysis incorporated in TARA-3 takes into account the nonlinear stress dependent behavior of the soil to loads. Furthermore, the soil behavior depends on

the loading path. Therefore, a method of analysis that simulates the construction sequence where an additional layer of elements is added at each step is incorporated. In this way, it may be possible to follow the actual sequence of construction loading in a simplified manner. Provision is also included to analyse an earth structure using only one layer, the so-called gravity switch on analysis. Comparison of this analysis with that based on the construction sequence can be found in Serff et al (1976), Desai and Christian (1979) and Naylor and Pande (1981).

This chapter deals with aspects related to modelling of soil behavior, the simplified assumptions and the basic framework for conducting static analysis.

2.2 Finite Element Representation

The region of interest is approximated by an assembly of a finite number of elements that are connected through nodal points. The type of element used in TARA-3 is the 4 node iso-parametric quadrilateral element with 8 degrees of freedom. Triangular elements are also permissible. The unknowns are the horizontal and vertical displacements at each node of the element. The interpolation function that describes the variation of the unknown displacement within the element in terms of nodal displacements is such that it produces a linear variation in strain within the element. Such an element is found to predict strains and stresses accurately in typical problems. Also, this type of element is useful as it can model the geometry of soil structures quite accurately.

The incremental matrix equation, including the effect of porewater pressures, governing the static response of the system (see Appendix I) is:

$$[K_t]\ \{\Delta\} = \{\Delta P\} - [K^*]\ \{\Delta U\} \tag{2.1}$$

where,

$[K_t]$ = the global tangent stiffness matrix,

$\{\Delta\}$ = the incremental nodal displacement vector,

$\{\Delta P\}$ = the incremental nodal force vector,

$[K^*]$ = the matrix associated with porewater pressures.

$\{\Delta U\}$ = the incremental porewater pressure vector.

The stiffness matrix $[K_t]$ in equation (2.1) depends on the tangent moduli. The stress-strain and the volume change behavior assumed in the analysis to obtain tangent moduli are described in the following section.

2.3 Stress-Strain-Volume Change Behavior

The stress strain relationship of structural elements is assumed to be linearly elastic. This assumption follows from the fact that the structural elements remain elastic for the range of stresses encountered during the loading. However, to model the nonlinear behavior of soils, an incrementally elastic approach has been adopted. The soil is assumed to be isotropic and elastic during the load increment and therefore the stress-strain relationship can be described in terms of any pair of elastic constants. Tangent shear modulus, G_t, and tangent bulk modulus, B_t, have been selected. These moduli are particularly appropriate for soils because special test procedures are available to evaluate one independent of the other. The selection of these moduli also facilitates the imposition of good controls on stresses and strains. For example, at failure, the shear modulus could be reduced to a small value (almost to zero) and the bulk modulus could be maintained at a higher value (Serff et al 1976; Wedge 1977; Vaziri-Zanjani 1986).

Apart from this, the selection of G_t and B_t has another distinct advantage for plane strain problems in dynamic analysis as described in Chapter 3.

2.3.1 Shear Stress-Strain Relationship

The shear stress-strain relationship of many soils under drained and undrained conditions is found to resemble a hyperbola. Many researchers have used hyperbolic stress strain relationships (Kulhawy et al 1969; Duncan and Chang 1970; Serff et al 1976). Part of the reason for its popularity is that it is a simple model and its parameters can be obtained using conventional laboratory testing.

In TARA-3, the relationship between shear stress, τ, and shear strain, γ, in terms of the hyperbolic model parameters, G_{max} and τ_{max}, is given by

$$\tau = \frac{G_{max}\,\gamma}{(1 + \frac{G_{max}\,|\gamma|}{\tau_{max}})} \tag{2.2}$$

where,

G_{max} = maximum shear modulus as $\gamma \rightarrow 0$,

τ_{max} = appropriate ultimate shear strength.

Fig. 2.1 shows the shear stress-strain curves applicable during the loading, unloading and reloading phases.

2.3.1.1 Estimation of Hyperbolic Model Parameters

The hyperbolic parameters in equation (2.2) depend on many factors so that computation should at least reflect the influence of the most important factors. For sandy soils and silts, the maximum shear modulus, G_{max}, depends primarily on the mean normal effective stress, σ'_m, relative density, D_r, and previous stress history. This is estimated using either of the following expressions depending on the option invoked:

$$G_{max} = K_G\,P_a\,(OCR)^k\,\left(\frac{\sigma'_m}{P_a}\right)^{1/2} \tag{2.3}$$

in which

K_G = shear modulus constant for a given soil,

OCR = overconsolidation ratio,

k = a constant dependent on the plasticity of the soil,

P_a = atmospheric pressure,

or,

$$G_{max} = 1000\ K_2\ (\sigma'_m)^{1/2}\ \ (OCR)^k \qquad (in\ psf) \tag{2.4}$$

in which,

K_2 = a constant which depends on the type of soil and relative density.

Equation (2.3) is similar to the equation proposed by Hardin and Drnevich (1972) and equation (2.4) is similar to the expression proposed by Seed and Idriss (1970) for computation of G_{max} for the dynamic analysis.

For clayey soils, G_{max} is computed using the expression:

$$G_{max} = K_{clay}\ S_u \tag{2.5}$$

in which,

K_{clay} = a constant for a given clay,

S_u = undrained shear strength of the clay.

For sandy soils, the value of τ_{max} depends on the current stress state, the criterion governing failure and the path by which failure is brought about in the soil mass. It is usually assumed that the failure is governed by the Mohr-Coulomb criterion which is defined by the parameters, effective cohesion, c', and angle of internal friction, ϕ'.

In practice, it is widely assumed that failure in a soil element with current stress state, as shown in Fig. 2.2, is brought about by increasing the major principal effective stress, σ'_1,

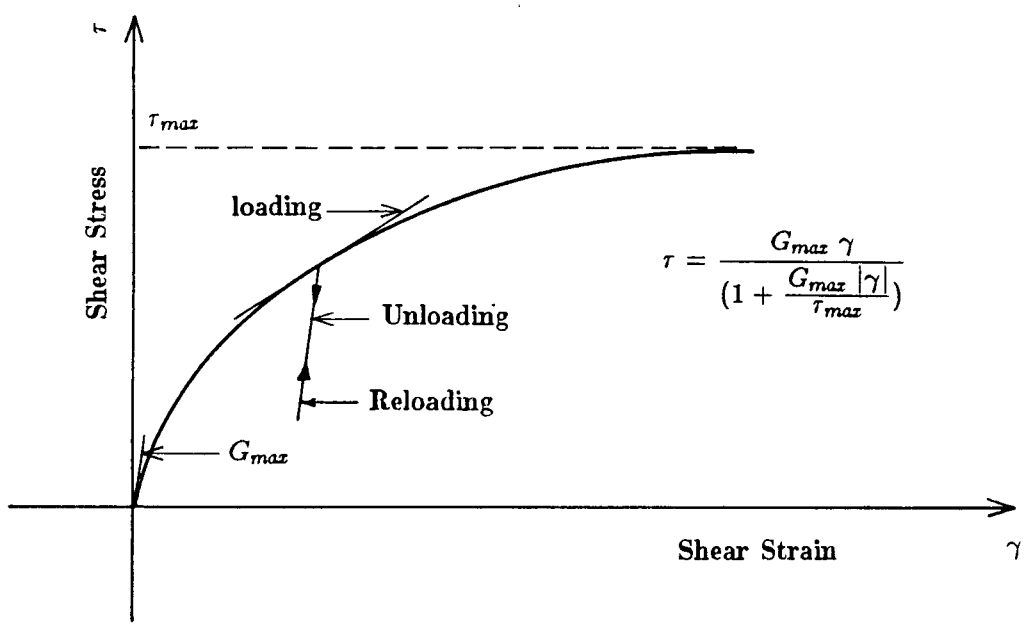

Fig. 2.1 Stress Strain Curve For Loading and Unloading

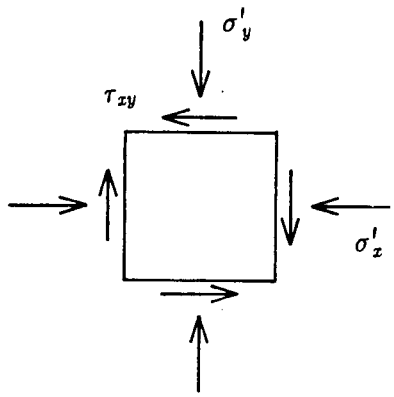

Fig. 2.2 Stress State of an Element

while holding the minor principal effective stress, σ_3', constant. This follows from conventional triaxial testing conditions. Under this assumption, the value of τ_{max} for an element under the current stress state shown in Fig. 2.2, can be computed using Fig. 2.3. The smaller Mohr circle represents the initial stress state of the element and the larger circle represents the failure state.

The radius, R, of the larger Mohr circle which touches the failure envelope can be computed as:

$$R = \frac{c' \cos\phi' + \sigma_3' \sin\phi'}{(1 - \sin\phi')} \tag{2.6}$$

Therefore, in this case,

$$\tau_{max} = R \tag{2.7}$$

However, if it is assumed that τ_{max} is the value of shear stress at failure on the failure plane, then

$$\tau_{max} = R \cos\phi' \tag{2.8}$$

In field conditions, the soil mass may not follow a path similar to the triaxial conditions as assumed in the above derivations. It is sometimes assumed that the soil mass fails in a manner in which the mean normal stress remains constant (Hardin and Drnevich 1972). Under this condition, for a plane strain problem, the centre of the Mohr circle remains fixed. Therefore, the circle that represents the failure can be drawn by simply enlarging the initial Mohr circle until it touches the failure envelope (see Fig. 2.4). In this case, the radius, R, of the Mohr circle representing failure can be obtained as,

$$R = c' \cos\phi' + (\frac{\sigma_x' + \sigma_y'}{2}) \sin\phi' \tag{2.9}$$

therefore,

$$\tau_{max} = R \tag{2.10}$$

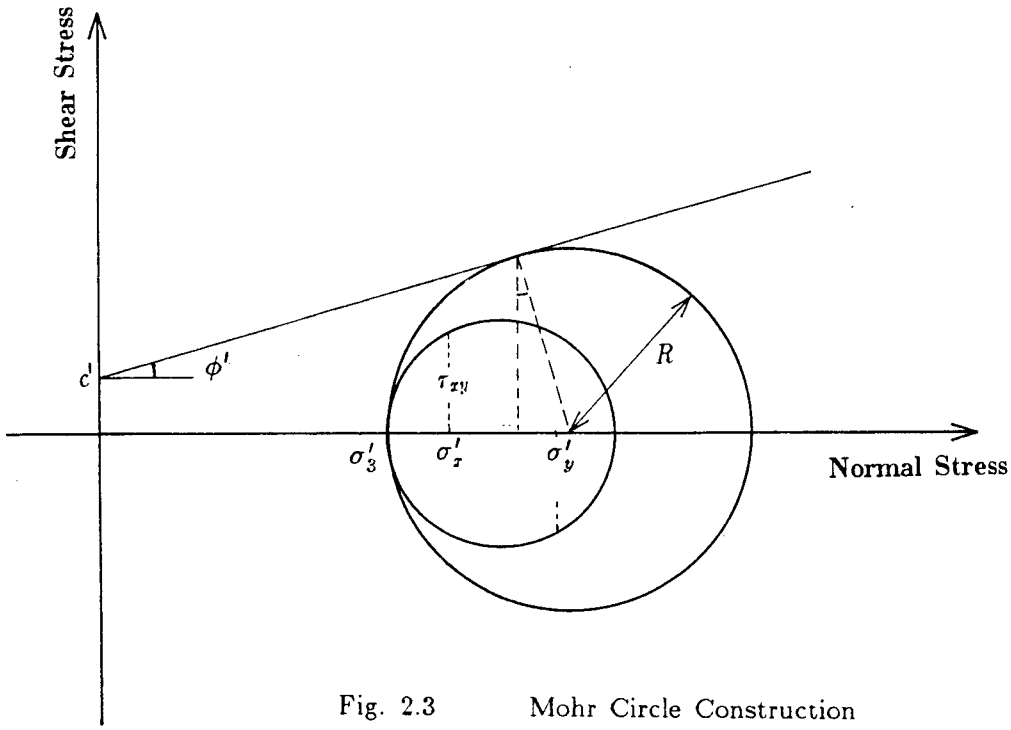

Fig. 2.3 Mohr Circle Construction

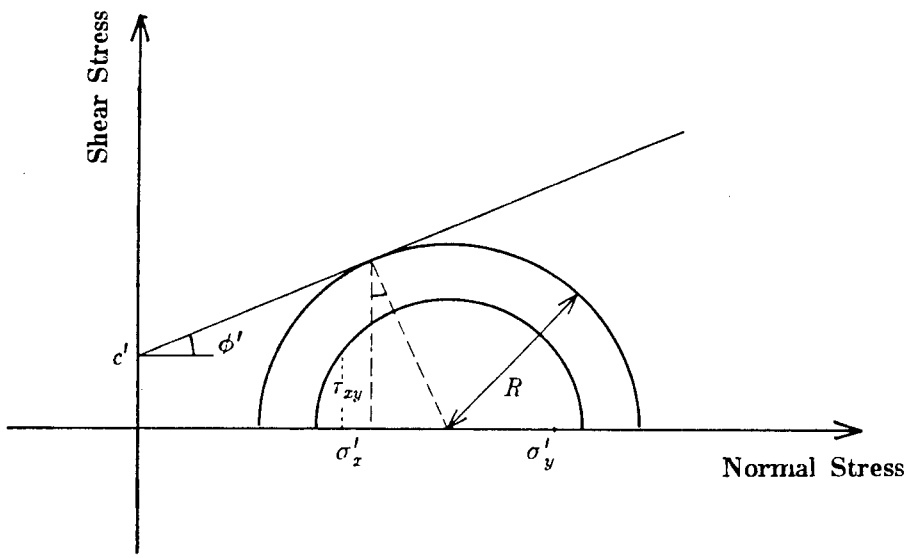

Fig. 2.4 Mohr Circle Construction

As described earlier, if it is assumed that τ_{max} is the shear stress at failure on the failure plane, then

$$\tau_{max} = R \cos\phi' \tag{2.11}$$

The two failure options are included in TARA-3 and one should invoke the option appropriate to the problem that is being analysed.

2.3.2 Volume Change Behavior

The tangent bulk modulus, B_t, is assumed to be a function of mean normal effective stress only. The value of B_t at any stress level is given by,

$$B_t = K_b \, P_a \, (\frac{\sigma'_m}{P_a})^n \tag{2.12}$$

in which,

K_b = bulk modulus number,

n = bulk modulus exponent,

P_a = atmospheric pressure.

The parameters K_b and n in equation (2.12) can be determined using conventional triaxial test data following procedures proposed by Duncan et al (1978, 1980). They can also be obtained from isotropic consolidation tests as described by Byrne (1981).

Typical values of K_b vary between 300 and 1000 depending on the relative density of the soil and soil type. Tables of K_b and n applicable to normal sands are presented by Byrne (1981) and Byrne and Cheung (1984).

2.4 Load Shedding Technique

The stresses computed by incremental elastic analysis at any stage of loading or unloading must be checked continuously to ensure that they do not violate the failure criterion. A technique known as load shedding (Desai and Christian 1979; Byrne and Janzen 1984) is employed to redistribute excess stresses in an element to other elements in a sub-failure state whenever the failure criterion is violated. This technique has been already applied sucessfully in the past for analysis of underground openings (Desai and Christian 1979) and of tunnels and shafts (Byrne and Janzen 1984). The deformations computed by the load shedding technique has been found to be in good agreement with closed form solutions (Byrne and Janzen 1984).

The first step involved in this technique is to determine the correcting stresses in each of the elements that have stress states violating the failure criterion. In TARA-3, the correcting stresses are computed assuming a constant mean normal stress condition which is similar to the approach suggested by Byrne and Janzen (1984). Fig. 2.5 shows the offensive stress state in terms of the Mohr circle for an element. The stress state $\{\sigma\}$ of an element which violates the Mohr-Coulomb failure criterion is given by,

$$\{\sigma\} = \begin{Bmatrix} \sigma_x \\ \sigma_y \\ \tau_{xy} \end{Bmatrix} \tag{2.13}$$

The assumption of constant mean normal stress condition for a plane strain problem implies that the centre of the Mohr circle remains fixed. Therefore, the centre of the corrected Mohr circle should be coincident with the centre of the uncorrected Mohr circle as shown in Fig. 2.5. The corrected Mohr circle should also touch the failure surface defined by c' and ϕ'.

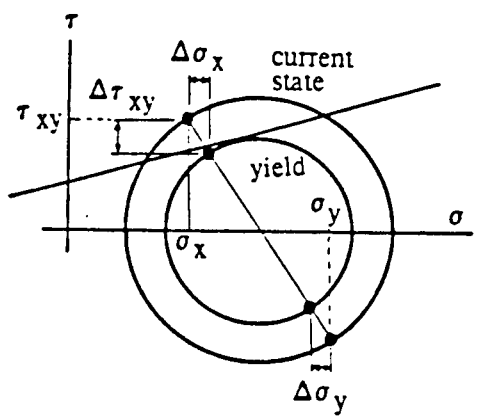

Fig. 2.5 Corrected and Uncorrected Mohr Circles

The overstresses $\{\Delta\sigma\}$ is given by,

$$\{\Delta\sigma\} = \begin{Bmatrix} \Delta\sigma_x \\ \Delta\sigma_y \\ \Delta\tau_{xy} \end{Bmatrix} \tag{2.14}$$

Using geometric principles, it can be shown that,

$$\Delta\sigma_x = (\frac{\sigma_x - \sigma_y}{2}) \frac{R_y}{R_{unc}} \tag{2.15}$$

$$\Delta\sigma_y = (\frac{\sigma_y - \sigma_x}{2}) \frac{R_y}{R_{unc}} \tag{2.16}$$

$$\Delta\tau_{xy} = \tau_{xy} \frac{R_y}{R_{unc}} \tag{2.17}$$

in which,

R_y = radius of the corrected Mohr circle (yield circle),

R_{unc} = radius of the uncorrected Mohr circle.

R_y and R_{unc} can be computed as,

$$R_y = c' \cos\phi' + (\frac{\sigma_x + \sigma_y}{2}) \sin\phi' \tag{2.18}$$

and

$$R_{unc} = \sqrt{(\frac{\sigma_x - \sigma_y}{2})^2 + \tau_{xy}^2} \tag{2.19}$$

The second step is to redistribute these overstresses to adjacent stable elements that are capable of accepting additional loads. This is achieved following procedures proposed by Byrne and Janzen (1984). In this procedure, the overstresses are converted to equivalent nodal forces, $\{\Delta f_{cor}\}$, acting on the corresponding nodes of the elements using the expression (see Appendix I),

$$\{\Delta f_{cor}\} = \int\int\int_V [B]^t \{\Delta\sigma\} \, dV \tag{2.20}$$

The global nodal force vector, $\{\Delta F_{cor}\}$, is calculated taking the contribution from all the failed elements as shown below:

$$\{\Delta F_{cor}\} = \sum_{i=1}^{N_{fe}} \int\int\int_{V} [B]^t \{\Delta\sigma\} \, dV \tag{2.21}$$

where,

N_{fe} is the total number of failed elements.

The stresses, strains and deformations resulting from the nodal force application is added to the existing values.

2.5 Shear Induced Volume Change

The volume change behavior described in section 2.3.2 is only due to change in the mean normal effective stress. That is, only the increment in volumetric strain, $\Delta\epsilon_{vm}$, resulting from a change in the mean normal effective stress, $\Delta\sigma'_m$, is included. But in soils volumetric strains can also occur due to changes in shear stresses. Experimental evidence for such behavior has been reported in detail in several studies using different test equipment. Examples are studies by Lee (1965) based on the drained triaxial tests and Vaid et al (1981) based on the drained simple shear tests.

Fig. 2.6 shows the characteristic drained behavior of initially loose and dense samples in a simple shear device. The samples exhibit volume reduction for small strains followed by volume expansion with an approximate constant rate for a considerable range of strain. Finally, at very large strains, they both exhibit a constant volume condition. In order to fit this behavior into an analytical formulation, the behavior is idealised as shown in Fig. 2.7. In this, it is assumed that there is no shear induced volume change until a shear strain level given by γ_o. After the exceedence of γ_o, the dilation is assumed to be governed by the

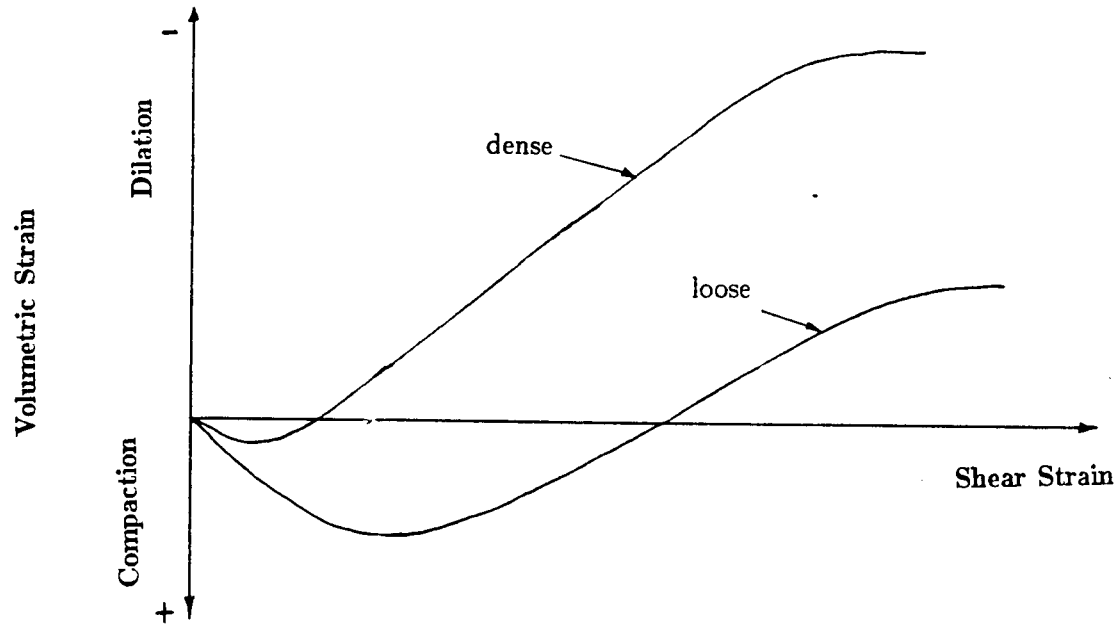

Fig. 2.6 Characteristic Drained Behaviour of Dense and Loose Sands

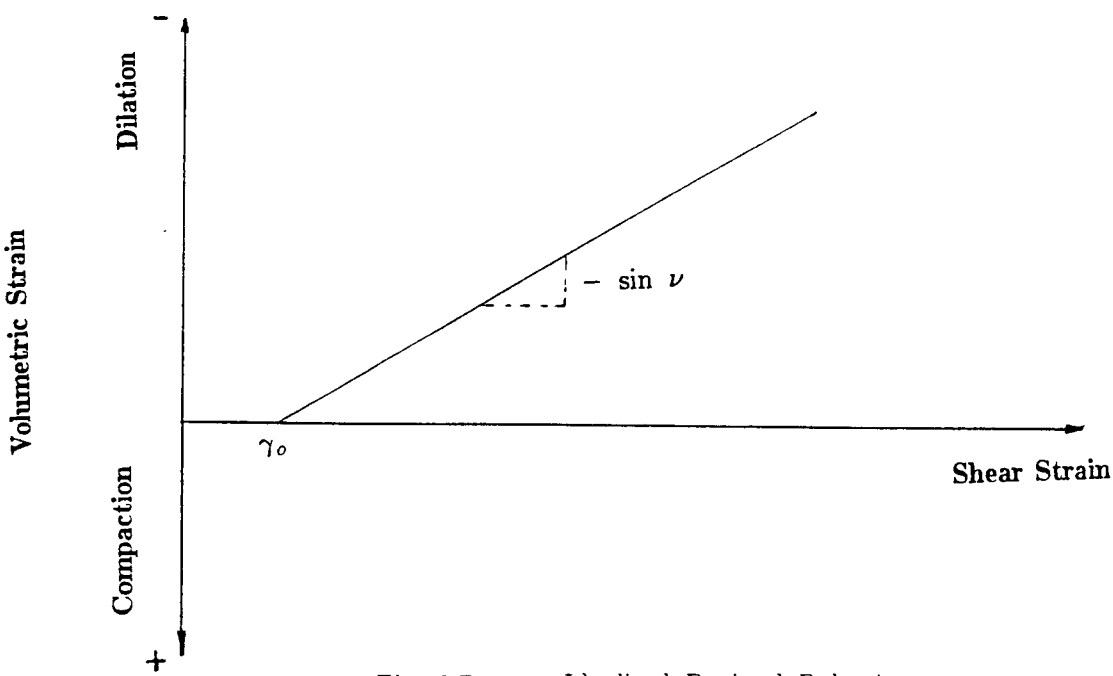

Fig. 2.7 Idealised Drained Behaviour

constant rate (Hansen 1958). That is,

$$\frac{\Delta\epsilon_v^d}{\Delta\gamma} = -\ \sin\ \nu \tag{2.22}$$

in which,

$\Delta\epsilon_v^d$ = increment of the shear induced volume change,

$\Delta\gamma$ = increment of shear strain,

ν = dilation angle defining the dilation rate (Hansen 1958).

The final phase where the constant volume condition is reached is not modelled. This may not be an important concern since the strains at which this condition occurs are usually very large.

The dilation angle is dependent on the density and increases with increasing relative density. Also, it is dependent on the level of mean normal effective stress. It is observed from the study carried out by Robertson (1982) that the variation of dilation angle, ν, with mean normal effective stress for a number of different sands at a given relative density lies on a narrow band when plotted in a semi-logarithm plot as shown in Fig. 2.8. Note that the data in Fig. 2.8 is for a relative density, $D_r = 80\%$ only. For analytical purposes, the variation of dilation angle, ν, versus the logarithm of mean normal effective stress can be assumed to be linear for a given relative density. This, along with the idealisation shown in Fig. 2.7, forms the framework for inclusion of shear induced volume change in TARA-3.

There are several methods one could adopt to include shear induced volume changes. The most straightforward method would be to introduce appropriate terms in the elasticity matrix $[D]$ that would reflect the coupling between shear stress and the volume change. This approach will result in an unsymmetrical stiffness matrix and hence additional computational effort. The method adopted in TARA-3 is to treat the problem in the same

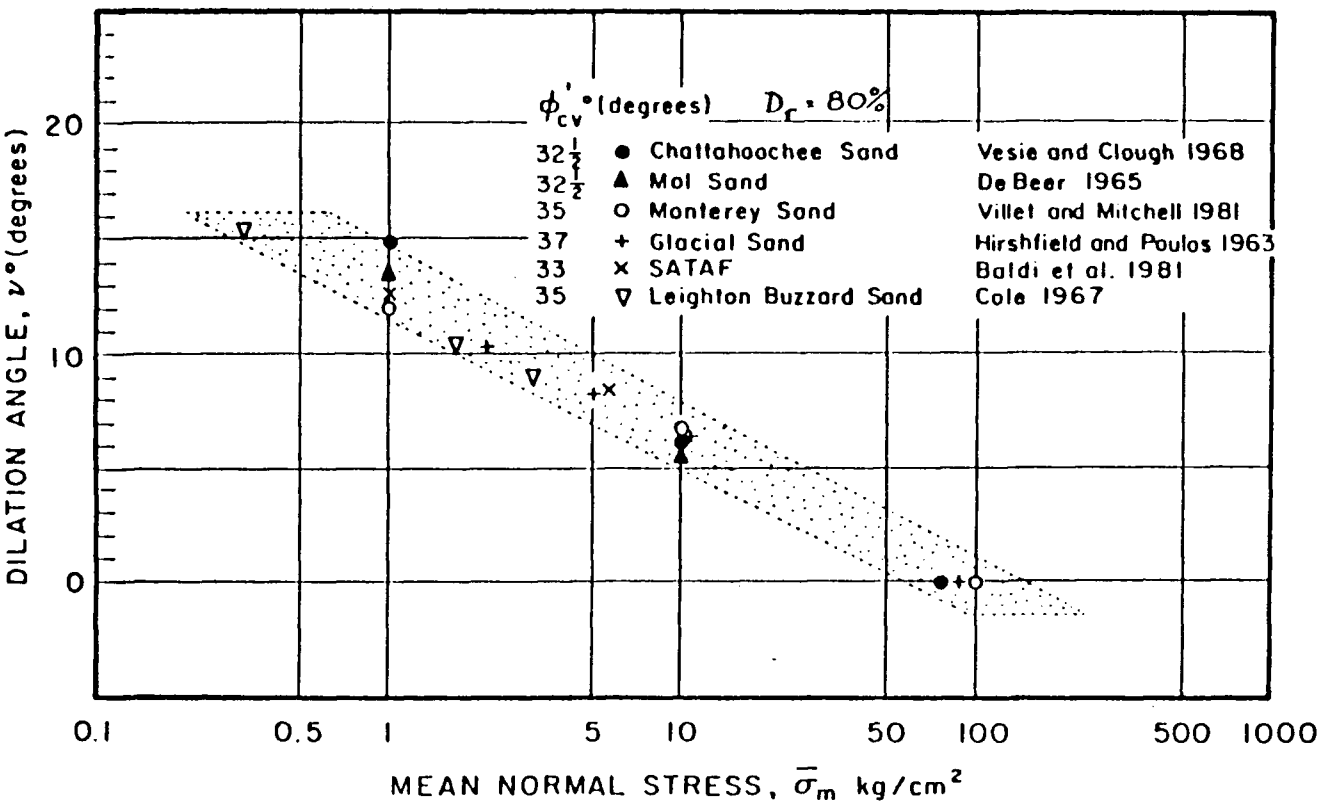

Fig. 2.8 Variation Of Dilation Angle with Mean Normal Stress (Adapted From Robertson 1982)

way as temperature variations are handled in structural mechanics (Zienkiewicz et al 1967; Byrne 1981). In this method, since the elasticity matrix $[D]$ is unchanged, the stiffness matrix remains symmetrical. The basic steps involved in the approach are summarised below:

Step 1

The incremental stresses and strains in all elements resulting for the load increment are calculated, ignoring the effect of shear induced volume change.

Step 2

The dilation angle is computed based on the new mean normal effective stress. The variation of dilation angle with mean normal effective stress supplied as the input is used for this purpose. With the calculated dilation angle, $\Delta\epsilon_v^d$ is calculated from equation (2.22).

Step 3

$\Delta\epsilon_v^d$ is split into $\Delta\epsilon_x^d$ and $\Delta\epsilon_y^d$ to form the dilational strain vector as,

$$\{\Delta\epsilon_o^d\} = \begin{Bmatrix} \alpha\ \Delta\epsilon_v^d \\ \beta\ \Delta\epsilon_v^d \\ 0 \end{Bmatrix} \tag{2.23}$$

where α and β are constants which may be varied to cover the likely range of strain response.

Step 4

The incremental nodal forces corresponding to $\{\Delta\epsilon_o^d\}$ are computed using the expression, (Appendix I),

$$\{\Delta f\} = \int\int\int_V [B]^t\,[D]\,\{\Delta\epsilon_o^d\}\ dV \tag{2.24}$$

Step 5

The global nodal force vector in step 4 is added to the incremental load in step 1 to give the new applied load. For this new load, the strain and stress increments, $\Delta\epsilon$ and $\Delta\sigma$, are

calculated. For the stress increment, the following equation is used.

$$\{\Delta\sigma\} = [D]\ [\{\Delta\epsilon\} - \{\Delta\epsilon_o^d\}] \tag{2.25}$$

Step 6

Step 2 to 5 are carried out until the convergence occurs in stress and strain increments under the applied incremental loads or until a specified number of iterations.

2.6 Simulation of Construction Sequence

2.6.1 Introduction

Many geotechnical engineering structures are constructed sequentially. Typical examples are earth embankments and dams. For a realistic solution to these problems, the construction sequences should be simulated as carefully as possible. In the cases involving large volumes of earthworks, it is often impractical to simulate the actual construction sequences partly because of the complexity involved and partly because of the computer storage and cost requirements. Therefore, in practice, the problems are analysed using a limited number of construction steps. For the cases involving materials that exhibit non-linear stress strain behavior, the computed stresses are relatively insensitive to the number of layers employed, but the computed displacements are quite sensitive to the number of layers (Kulhawy et al 1969; Desai and Christian 1979). Typically 10 to 15 layers have been used in the analysis of major dams (Naylor and Pande 1981).

A layer by layer construction procedure is incorporated in TARA-3 for the purpose of simulating the sequence of construction loading. The method of analysis is detailed in the following sections.

2.6.2 Method of Analysis

The construction sequence is modelled by computing the incremental stresses, strains and deformations due to the placement of each new layer. There are several methods by which the layer by layer construction can be handled. They all differ in the approach by which the stress dependent moduli are evaluated (Kulhawy et al 1969; Desai and Christian 1979). There are three cases possible:

(1) The initial stress approach

(2) The final stress approach

(3) The average stress approach

For both the final stress and the average stress approach, one cycle of interation is necessary for each layer placement, so that the final stresses will be known for the evaluation of moduli directly or to find the average stresses and for subsequent evaluation of moduli. Studies carried out by Kulhawy et al (1969) showed that the average stress approach is much more accurate and efficient than the other two approaches.

In TARA-3, the average stress approach is adopted and therefore, placement of a layer is analysed twice. The first time analysis is carried out using the moduli based on the stresses at the beginning of the increment and the second time using the moduli based on the average stresses during the increment. The changes in stresses, strains and displacements are added to the values at the beginning of the increment.

Apart from this option, there is also a provision to evaluate moduli based on average strains, as in TARA-2, rather than on average stresses.

Since only one iteration is carried out for a layer placement, equilibrium may not

necessarily be satisfied (Desai and Abel 1972). Therefore, correction forces are employed to satisfy the equilibrium condition. The correction forces corresponding to changes in shear stresses are computed and applied as nodal forces at the next load increment. The procedure for obtaining nodal forces is outlined in Appendix I.

The placement of a fresh layer is simulated by applying forces to represent the weight of the fresh layer. For freshly placed elements, moduli are based on the estimated stresses. The vertical effective stress, σ'_y, the horizontal effective stress, σ'_x, and the shear stress, τ_{xy}, of a freshly placed element are estimated following the suggestion by Ozawa et al (1973), as

$$\sigma'_y = \gamma_s \, d \tag{2.26}$$

$$\sigma'_x = K_o \, \sigma'_y \tag{2.27}$$

$$\tau_{xy} = 0.5 \, \sigma'_y \, \sin \alpha_o \tag{2.28}$$

where,

d = the depth of the centre of the element from the top surface,

K_o = coefficient of earth pressure at rest,

γ_s = appropriate unit weight of the soil depending on the submerged condition,

α_o = slope of the overlying surface.

In the method adopted here, it is assumed that the position of newly placed elements immediately after placement is the reference state for movements resulting from subsequent loadings. Therefore, the displacements at the top of a newly placed elements are set equal to zero. Also, the strains in the newly placed elements are set equal to zero.

Earth structures are often built by placing layers on existing foundation. In these cases, the foundation should be treated as consisting of pre-existing elements. Provision is

included in TARA-3 to account for pre-existing elements, in which case the initial stress state of the elements is required to compute the moduli for the subsequent analysis.

CHAPTER 3

METHOD OF DYNAMIC ANALYSIS IN TARA-3

3.1 Introduction

The greatest challenge in developing a method of dynamic analysis of a soil structure system during earthquakes is the inclusion, in a realistic manner, of all the factors that have a strong influence on soil behavior. The major factors that must be included are:

(1) in-situ stress states and corresponding moduli,

(2) stress strain variation during phases of initial loading, unloading and reloading,

(3) seismically induced porewater pressures,

(4) effective stress changes due to porewater pressure changes,

(5) viscous and hysteretic damping,

(6) volume changes induced by shear.

In order to incorporate these factors into any mathematical modelling process, the real behavior of a soil structure system has to be idealised. The dynamic method of analysis incorporated in TARA-3 includes all these factors. It is an extensively revised and greatly expanded version of an earlier program TARA-2 (Siddharthan and Finn 1982). The the-

oretical foundations of this method of analysis and the assumptons implied in relation to the dynamic analysis are presented in this chapter.

3.2 Equations of Motion

The dynamic equilibrium equations for a linear finite element system subjected to earthquake ground motions can be expressed in the form

$$[M]\ \{\ddot{X}\} + [C]\ \{\dot{X}\} + [K]\ \{X\} = \{P\} \tag{3.1}$$

in which $\{\ddot{X}\}$, $\{\dot{X}\}$ and $\{X\}$ are the vectors of relative nodal acceleration, velocity and displacement respectively and $[M]$, $[C]$ and $[K]$ are the mass, damping and stiffness matrices respectively. $\{P\}$ is the inertia force vector. This is defined as,

$$\{P\} = -\ [M]\ \{I\}\ \ddot{X}_b \tag{3.2}$$

in which $\{I\}$ is a column vector of 1 and $\ddot{X}_b$ is the base acceleration. The base acceleration is assumed to be identical at every nodal point along the base and therefore $\{P\}$ is strictly a function of time.

Dynamic analysis of a linear system may be solved either by the mode superposition method or by direct step-by-step integration method (Clough and Penzien 1975). Each of these methods has its own advantages and disadvantages. The mode superposition method requires the evaluation of the vibration modes and frequencies. It essentially uncouples the response of the system and evaluates the response of each mode independently of others. The main advantage of this approach is that an adequate estimate of the dynamic response can often be obtained by considering only a few modes of vibration, even in systems that may have many degrees of freedom; thus the computational efforts may be reduced significantly. The main disadvantage is that it is not applicable to nonlinear systems.

On the other hand, the direct step-by-step integration method which involves the direct numerical integration of the dynamic equilibrium equations has the advantage that it can be applied to both linear and nonlinear systems. The nonlinear analysis is approximated as a sequence of analyses of successively changing linear systems. In other words, the response is calculated for a short time increment assuming a linear system having the properties determined at the start of the interval. Before proceeding with the next increment, properties are determined which are consistent with the state of deformation and stress at that time.

In TARA-3, the step-by-step method is used so as to account for the nonlinear behavior of the soil structure system. The basic formulation for the step-by-step integration method employed in TARA-3 is given in the next section.

3.3 Incremental Equations of Motion

As described earlier, in order to account for the nonlinear behavior, it is neccessary to work with the incremental equations rather with the original equations in equation (3.1).

Let t anf T be the times corresponding to the beginning and end of a short time interval Δt. That is, $T = t + \Delta t$. Equation (3.1) should hold at these two instants of time and therefore,

$$[M]_t \{\ddot{X}\}_t + [C]_t \{\dot{X}\}_t + [K]_t \{X\}_t = \{P\}_t \tag{3.3}$$

and

$$[M]_T \{\ddot{X}\}_T + [C]_T \{\dot{X}\}_T + [K]_T \{X\}_T = \{P\}_T \tag{3.4}$$

where subscripts refer to the instant of time.

The mass matrix is constant throughout the analysis. A lumped mass matrix is used in TARA-3 instead of the more accurate consistent mass matrix. The procedure for obtaining the lumped mass matrix along with the reasons for adopting the lumped mass approach are

discussed in section 3.5. The damping and stiffness matrices in equations (3.3) and (3.4) are, however, dependent on the current responses owing to the nonlinear behavior of the soil. Therefore, approximations are required to solve these equations. One way would be to represent the damping and stiffness matrices by an average damping and stiffness matrices applicable to the time interval Δt. This would yield the incremental equation shown below.

$$[M]\ \{\Delta\ddot{X}\} + [C]_{av}\ \{\Delta\dot{X}\} + [K]_{av}\ \{\Delta X\} = \{\Delta P\} \tag{3.5}$$

where the subscript av refers to the average damping and stiffness matrices and $\Delta\ddot{X}$, $\Delta\dot{X}$, ΔX and ΔP refer to the incremental values during the time interval Δt, defined as,

$$\{\Delta\ddot{X}\} = \{\ddot{X}\}_T\ -\ \{\ddot{X}\}_t \tag{3.6}$$

$$\{\Delta\dot{X}\} = \{\dot{X}\}_T\ -\ \{\dot{X}\}_t \tag{3.7}$$

$$\{\Delta X\} = \{X\}_T\ -\ \{X\}_t \tag{3.8}$$

and

$$\{\Delta P\} = \{P\}_T\ -\ \{P\}_t \tag{3.9}$$

However, this approach will involve an iterative solution scheme and may become very expensive as iterations are required at every time increment. Therefore, in practice, tangent damping and tangent stiffness matrices which correspond to time t (at the beginning of the interval) are used. This would produce a tendency for the computed stress-strain response to deviate from the stress-strain relationship of the soil since the nonlinear behavior is approximated by a series of linear steps. Appropriate corrections are made so that the stress-strain state at the end of the increment is on the stress-strain curve of the soil. The stress-strain relationship is described in section 3.4 and the formulation of the tangent stiffness matrix at time t, $[K_t]_t$, is given in section 3.6. In TARA-3, damping other than hysteretic is accounted through the use of Rayleigh damping in which case the element

damping matrix is expressed as a linear combination of element mass and stiffness matrices. The procedure is described in section 3.7.

The dynamic incremental equilibrium equations can now be rewritten as,

$$[M]\ \{\Delta\ddot{X}\} + [C]_t\ \{\Delta\dot{X}\} + [K_t]_t\ \{\Delta X\} = \{\Delta P\} \tag{3.10}$$

where,

$[C]_t$ = the global damping matrix at time t.

Equations (3.10) represent a set of second order differential equations and can be solved using numerical procedures developed by Newmark (1959) or Wilson et al (1973).

3.4 Dynamic Stress-Strain Behavior

As noted earlier, an incrementally elastic approach has been adopted to model nonlinear behavior of soils. In this approach, the soil behavior is assumed to be linear within each increment of the load.

The soil is assumed to behave isotropically. Therefore only two elastic constants are required to represent its behavior. As in the case of static analyses, the tangent shear and bulk modulus, G_t and B_t were selected as the required constants. The stress strain relationship in shear and the volume change behavior assumed in TARA-3 for the dymanic analysis is described in detail in the next section.

3.4.1 Dynamic Shear Stress-Shear Strain Behavior

The seismic loading imposes irregular loading pulses which consist of loading, unloading and reloading. The soil exhibits different behavior in each of these above phases. Adequate

modelling of each of these phases is essential in order to obtain the true dynamic response of the soil system. In TARA-3, the behavior of soil in shear is assumed to be nonlinear and hysteretic, exhibiting Masing (1926) behavior during unloading and reloading.

The relationship between shear stress, τ, and shear strain, γ, for the initial loading phase under either drained or undrained loading conditions is assumed to be hyperbolic and is given by

$$\tau = \frac{G_{max}\,\gamma}{(1 + \frac{G_{max}\,|\gamma|}{\tau_{max}})} \tag{3.11}$$

or,

$$\tau = f(\gamma) \tag{3.12}$$

in which,

G_{max} = the maximum shear modulus,

τ_{max} = the appropriate shear strength.

This initial loading or skeleton curve is shown in Fig. 3.1(a). The unloading-reloading has been modelled using the Masing criterion. This implies that the equation for the unloading curve from a point (γ_r, τ_r) at which the loading reverses direction is given by

$$\frac{\tau - \tau_r}{2} = \frac{G_{max}\,(\gamma - \gamma_r)/2}{(1 + \frac{G_{max}\,|(\gamma - \gamma_r)|}{2\tau_{max}})} \tag{3.13}$$

or

$$\frac{\tau - \tau_r}{2} = f(\frac{\gamma - \gamma_r}{2}) \tag{3.14}$$

The shape of the unloading-reloading curve is shown in Fig. 3.1(b). The Masing criterion implied in equations (3.13) and (3.14) means that the unloading and reloading branches of a hysteretic loop are the same skeleton curve with the origin translated to the reversal point and the scales for the stress and strain increased by a factor of two.

Lee (1975) and Finn et al (1976) proposed rules for extending the Masing concept for irregular loading. They suggested that the unloading and reloading curves should follow the previous skeleton loading curves when the magnitude of the previous maximum shear strain is exceeded. In Fig. 3.2(a), the unloading curve beyond B becomes the extension of the initial loading in the negative direction, i.e., BC. In the case of a general loading history, they assumed that when the current loading curve intersects a previous loading curve, the stress strain curve follows the previous loading curve. Two typical examples are provided in Fig. 3.2(b) to illustrate these rules (Finn et al 1976).

(1) If loading along path BC is continued, the loading path is assumed to be BCAM, where AM is the extension of OA;

(2) If unloading along path CPB is continued, then the unloading path will be ABP'.

The tangent shear modulus, G_t, needed in the formulation is the value of the tangent to the stress strain curve at the stress strain point. For instance, if the point is on the skeleton curve given by equation (3.11), then the tangent shear modulus in terms of strain, γ, is given by

$$G_t = \frac{G_{max}}{(1 + \frac{G_{max}\,|\gamma|}{\tau_{max}})^2} \tag{3.15}$$

Alternatively, G_t can be expressed in terms of shear stress, τ, as

$$G_t = G_{max}\,(1 - \frac{|\tau|}{\tau_{max}})^2 \tag{3.16}$$

Methods of dynamic analysis commonly used in practice start the analysis from the origin of the stress strain curve for all the elements. These methods ignore the static strains in the soil structure system even in those elements which carry high shear stresses. However, in TARA-3, an option is provided so that the dynamic analysis can start from the static stress-strain condition. It is believed that this option permits a more realistic estimation of dynamic response and of residual or permanent deformations.

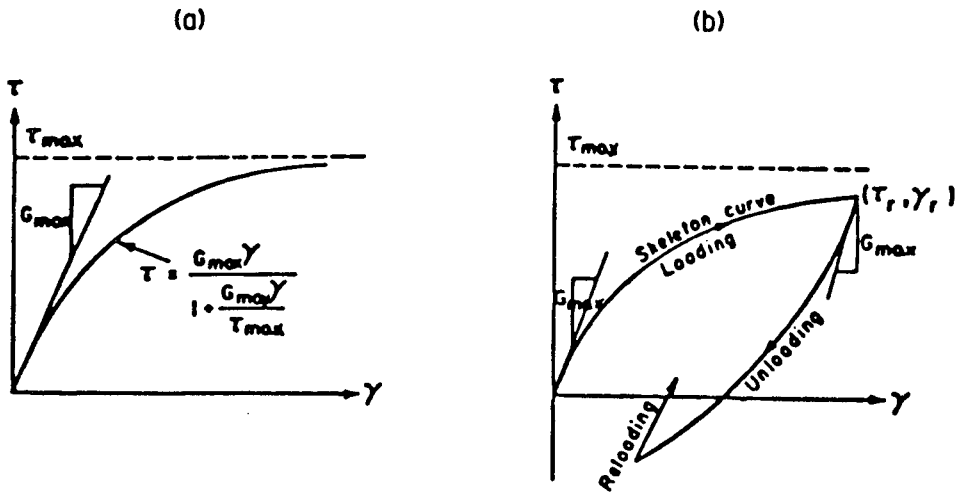

Fig. 3.1(a) Initial Loading Curve

Fig. 3.1(b) Masing Stress Strain Curves for Loading and Unloading

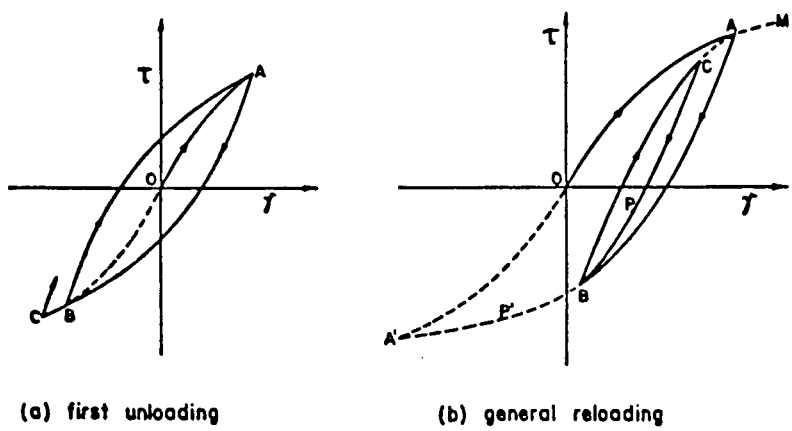

Fig. 3.2 Hysteretic Characteristics

3.4.1.1 Computation of Hyperbolic Model Parameters

The maximum shear modulus, G_{max} for sands is calculated using the equations proposed either by Hardin and Drnevich (1972) based on resonant column tests or by Seed and Idriss (1970). The Hardin and Drnevich (1972) equation is of the form

$$G_{max} = 320.8\ P_a\ \frac{(3.973 - e)^2}{(1+e)}\ (OCR)^k\ (\frac{\sigma'_m}{P_a})^{1/2} \tag{3.17}$$

in which

e = void ratio,

OCR = overconsolidation ratio,

k = a constant dependent on the plasticity of the soil,

P_a = atmospheric pressure,

σ'_m = current mean normal effective stress.

The equation suggested by Seed and Idriss (1970) takes the form

$$G_{max} = 1000\ K_{2max}\ (\sigma'_m)^{1/2} \qquad (in\ psf) \tag{3.18}$$

in which

K_{2max} = a constant dependent on the type of soil and relative density D_r.

Equation (3.18) has been modified to reflect previous stress history by including a term with the overconsolidation ratio and also to allow its usage in any system of units by expressing it in a similar form as in the Hardin and Drnevich equation.

$$G_{max} = 21.7\ K_{2max}\ P_a\ (\frac{\sigma'_m}{P_a})^{1/2}\ (OCR)^k \tag{3.19}$$

The variation of K_2 with shear strain and relative density for sands (Seed and Idriss

1970) is shown in Fig. 3.3. The constant K_{2max} (the value of K_2 at small strains) may be estimated using the approximation suggested by Byrne (1981),

$$K_{2max} = 15 + 0.61\ D_r \tag{3.20}$$

where D_r is expressed in percentage.

For clays, the maximum shear modulus is calculated based on the undrained shear strength, S_u, using the equation,

$$G_{max} = K_{clay}\ S_u \tag{3.21}$$

in which,

K_{clay} = a constant for a given clay.

The variation of G/S_u with shear strain for saturated clays is shown in Fig. 3.4 (Seed and Idriss 1970). Typical values of K_{clay} vary between 1000 and 3000.

The maximum shear strength, τ_{max}, for soils is dependent on the current stress system, the way by which the soil element is brought to failure and the failure criterion. Hardin and Drnevich (1972) suggested that the value of τ_{max} calculated using the Mohr-Coulomb failure envelope defined by the static strength parameters such as c' (effective cohesion) and ϕ' (internal angle of friction) is adequate for dynamic loadings. Therefore, the options for selecting the value of τ_{max} reported in section 2.3.1.1 are all retained in the case of dynamic analyses.

It should be noted that there is also a provision in TARA-3 for both G_{max} and τ_{max} to be specified directly by the user. This facilitates the input of values obtained from either field or laboratory tests directly.

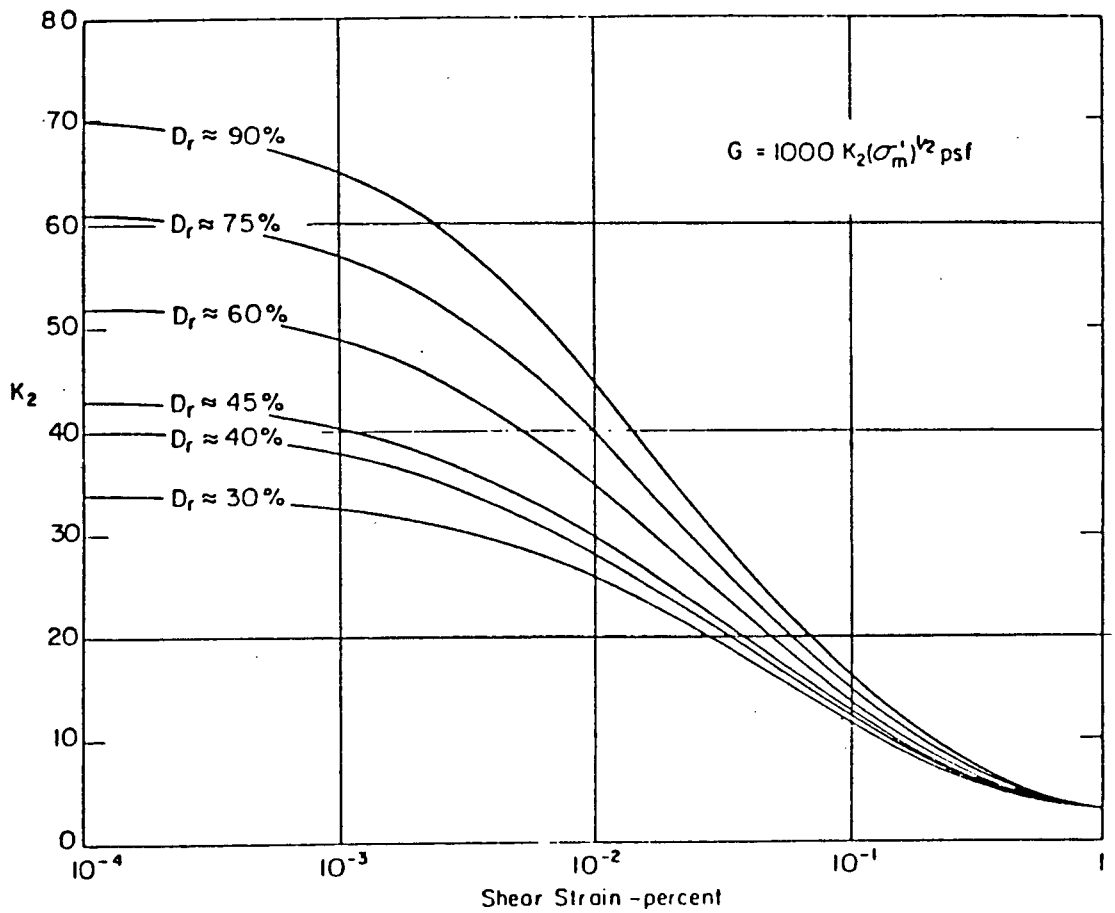

Fig. 3.3 Shear Moduli of Sands at Different Relative Densities (Adapted From Seed and Idriss 1970)

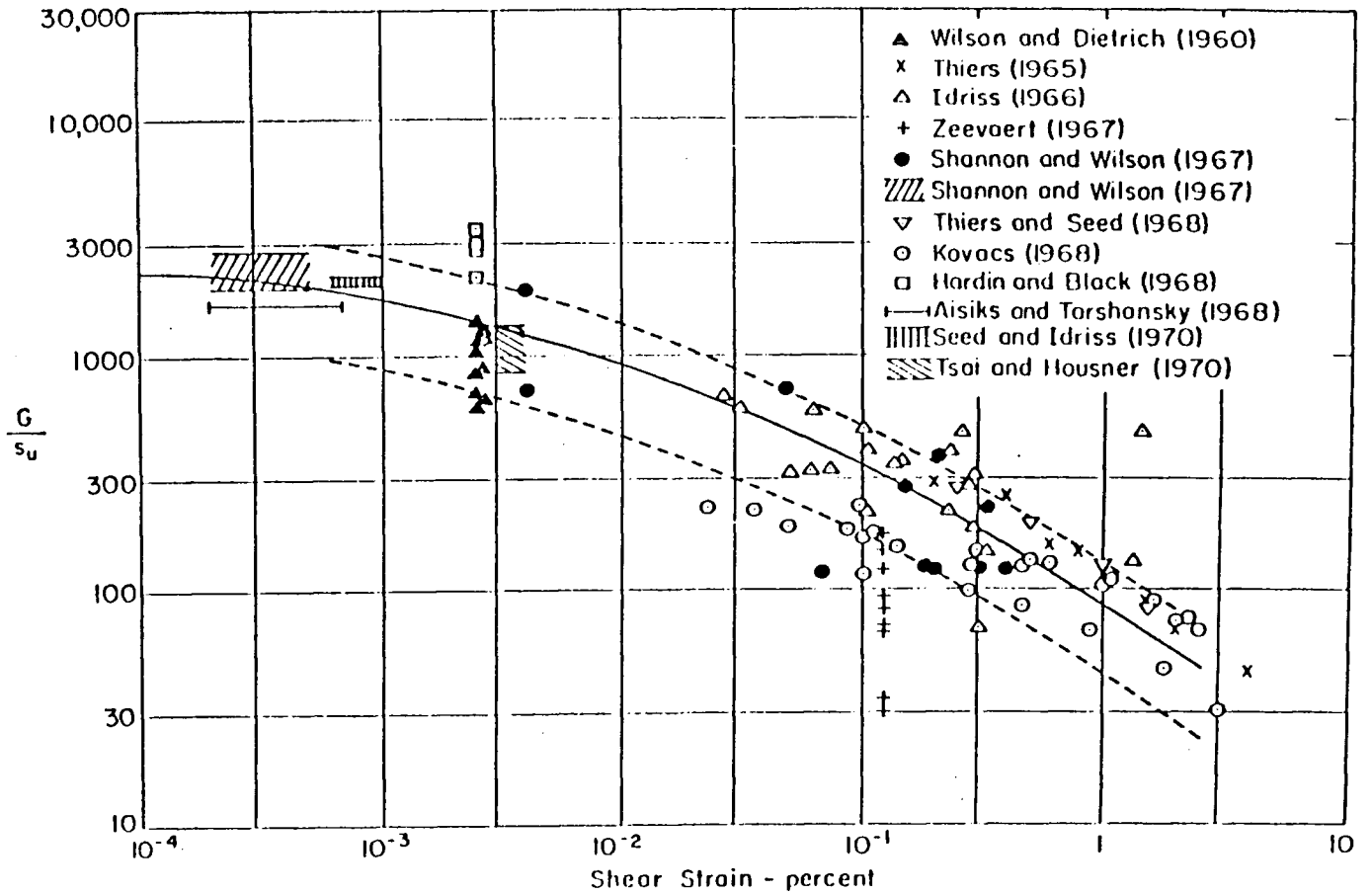

Fig. 3.4 Shear Moduli for Saturated Clays
(Adapted From Seed and Idriss 1970)

3.4.2 Volume Change Behavior

The response of the soil to uniform all round pressure is assumed to be nonlinearly elastic and dependent on the mean normal effective stress. Hysteretic behavior, if any, is neglected in this mode. The relationship between tangent bulk modulus, B_t, and mean normal effective stress, σ'_m, is assumed to be in the form

$$B_t = K_b \; P_a \; (\frac{\sigma'_m}{P_a})^n \tag{3.22}$$

in which,

K_b = the bulk modulus constant,

P_a = the atmospheric pressure in units consistent with σ'_m,

n = the bulk modulus exponent.

For fully saturated deposits, B_t has to be of high value to simulate undrained conditions in the case of dynamic analysis.

3.5 Formulation of Mass Matrix

The mass matrix in equation (3.10) can be obtained by two different methods. In the first method, the mass matrix is formulated so as to be consistent with the assumed displacement interpolation function. The resulting matrix is known as the consistent mass matrix. In the second method, the mass matrix is obtained through a lumped mass approximation, giving what is called a lumped mass matrix.

The presence of the off diagonal terms in the consistent mass matrix greatly increases the computational time required to solve the dynamic equilibrium equations. On the other hand, the lumped mass matrix is simple to obtain and has only diagonal terms. The degree

of accuracy obtained through the use of lumped mass approximation is considered to be good enough for typical geotechnical problems (Desai and Christian 1979).

In TARA-3, the lumped mass approximation is used, in which one-fourth of the mass of each quadrilateral element and one-third of the mass of each triangular element are lumped at respective nodes. The total mass at any one node is the summation of the contributions from all the elements common to that particular node.

3.6 Formulation of Stiffness Matrix

As mentioned earlier, the analysis incorporated in TARA-3 assumes isotropic behavior of soil and further it is applicable to the restricted but practical case of plane strain. Under these conditions, the relationship between the incremental stresses $\{\Delta\sigma\}$ and incremental strains $\{\Delta\epsilon\}$ in an element of soil, can be written as,

$$\{\Delta\sigma\} = [D]\ \{\Delta\epsilon\} \tag{3.23}$$

where $[D]$ is the elasticity matrix which, in this case, is a function of any two elastic constants. In the present analysis, tangent shear and bulk moduli are selected to form the $[D]$ matrix.

As shown in Appendix I, $[D]$ in terms of G_t and B_t, is given as

$$[D] = \begin{bmatrix} B_t + 4/3\ G_t & B_t - 2/3\ G_t & 0 \\ B_t - 2/3\ G_t & B_t + 4/3\ G_t & 0 \\ 0 & 0 & G_t \end{bmatrix} \tag{3.24}$$

This could be rewritten as,

$$[D] = B_t \begin{bmatrix} 1 & 1 & 0 \\ 1 & 1 & 0 \\ 0 & 0 & 0 \end{bmatrix} + G_t \begin{bmatrix} 4/3 & -2/3 & 0 \\ -2/3 & 4/3 & 0 \\ 0 & 0 & 1 \end{bmatrix} \tag{3.25}$$

or

$$[D] = B_t\,[Q_1] \;+\; G_t\,[Q_2] \tag{3.26}$$

where $[Q_1]$ and $[Q_2]$ are the constant matrices. Now the expression for the element tangent stiffness matrix $[k_t]$, as obtained in Appendix I, can be written as

$$[k_t] = \iiint_V [B]^t\,[D]\,[B]\;dV \tag{3.27}$$

When the expression for $[D]$ in equation (3.26) is incorporated into equation (3.27), the resulting expression for $[k_t]$ can be written as,

$$[k_t] = B_t \iiint_V [B]^t\,[Q_1]\,[B]\;dV \;+\; G_t \iiint_V [B]^t\,[Q_2]\,[B]\;dV \tag{3.28}$$

It should be noted that equation (3.28) is valid only if B_t and G_t are assumed constants for an element. However, in the isoparametric formulation adopted in TARA-3, the stresses and strains vary and consquently moduli are not constant within the element. It is therefore assumed that the values of moduli computed using the stresses obtained at the centre of the element are the representative values for the element. Under this assumption, equation (3.28) can be used. Therefore, $[k_t]$ can be written in the form,

$$[k_t] = B_t\,[R_1] \;+\; G_t\,[R_2] \tag{3.29}$$

where,

$$[R_1] = \iiint_V [B]^t\,[Q_1]\,[B]\;dV \tag{3.30}$$

and

$$[R_2] = \iiint_V [B]^t\,[Q_2]\,[B]\;dV \tag{3.31}$$

$[R_1]$ and $[R_2]$ will be constant matrices provided changes in the geometry of the elements are not considered. In TARA-3, changes in the geometry of the elements are not taken into account. Therefore $[R_1]$ and $[R_2]$ are evaluated only once during the dynamic analysis.

The element tangent stiffness matrix $[k_t]$ can be updated merely by multiplying matrices $[R_1]$ and $[R_2]$ by the current B_t and G_t values respectively and adding them together. This procedure can save computing time as $[k_t]$ need not be re-formulated at every load step. The global tangent stiffness matrix $[K_t]$ can be assembled using element tangent stiffness matrices $[k_t]$ following conventional procedures.

3.7 Formulation of Damping Matrix

The types of damping that occur when the vibrational energy is transmitted through a medium can be broadly divided into two categories: viscous and hysteretic damping.

Viscous damping depends on the velocity and is frequency dependent. On the other hand, hysteretic damping depends largely on the magnitude of the strain and is frequency independent.

For linear analysis, the damping must be introduced in the form of viscous damping. However, in the true non-linear analysis, where the hysteretic stress strain law is used, the damping is already introduced in the form of hysteretic damping and therefore viscous damping may not be needed. However, to take into account of the effect of flow of water inside the soil structure, some viscous damping is required. Moreover, small amounts of viscous damping may be needed to control any pseudo high frequency responses that are introduced by the numerical integration procedures.

While the hysteretic damping is inherent, the viscous damping in TARA-3 is of the Rayleigh type. In this context, the element damping matrix is expressed as a linear combination of mass matrix $[m]$ and tangent stiffness matrix $[k_t]$ as shown below,

$$[c] = a\,[m] + b\,[k_t] \tag{3.32}$$

in which a and b are constants.

The element tangent stiffness matrix $[k_t]$ varies with time during the dynamic analysis. Therefore whenever $[k_t]$ is changed, $[c]$ matrix is also changed. However, TARA-3 has also an option whereby the $[c]$ matrix is not varied according to the current stiffness matrix but kept constant based on $[k_t]_{t=0}$. Accordingly, $[c]$ is expressed as

$$[c] = a\,[m] \;+\; b\,[k_t]_{t=0} \tag{3.33}$$

The above formulation will give a damping ratio λ_n for the n^{th} mode as,

$$\lambda_n = \frac{a}{2\,\omega_n} + \frac{b\,\omega_n}{2} \tag{3.34}$$

where ω_n is the n^{th} mode frequency.

Equation (3.34) implies that if $a = 0$ the damping is proportional to the frequency and when $b = 0$, the damping is inversely proportional to the frequency. Also from equations (3.32) and (3.33), if $a = 0$, the damping matrix contains only the mass proportional components and if $b = 0$, it contains the stiffness proportional component.

In a typical soil strucure system only the first few modes of vibration govern the dynamic response and therefore it is unnecessary to include the higher mode components. It is customary to compute b and, if necessary, a using only the natural frequency of the system (Lee 1975). For instance, if it is desired to have stiffness proportional damping ($a = 0$), b could be computed as,

$$b = \frac{2\,\lambda}{\omega_1} \tag{3.35}$$

where λ is the critical damping ratio and ω_1 is the fundamental natural frequency of the system.

3.8 Computation of Correction Force Vector

As mentioned earlier, in TARA-3 the nonlinear behavior of soil is approximated by a series of linear steps. Therefore, at the end of a load increment, the computed strains and stresses for an element may not be compatible with the stress-strain relation of the soil. In order to make them compatible, correction forces are used. The correction forces are calculated assuming that the computed strains are the true strains. However, the correction forces do not necessarily satisfy the equilibrium equations. Therefore, a condition of global equilibrium at each step of the analysis is imposed. In order to do this, it is necessary to compute all components representing both the right and left hand sides of the equilibrium equation. Any differences constitute the correction force vector, $\{P_{cor}\}$.

Among the components of the left hand side of the equilibrium equation, the inertia and damping terms at time t, $\{F_I\}_t$ and $\{F_D\}_t$ respectively, can be calculated in a straightforward manner as,

$$\{F_I\}_t = [M]\ \{\ddot{X}\}_t \tag{3.36}$$

and

$$\{F_D\}_t = [C]_t\ \{\dot{X}\}_t \tag{3.37}$$

The spring force term, $\{F_S\}_t$, is obtained by representing the element dynamic stresses, $\{\sigma_d\}$, as nodal forces acting on the nodes and summing the contributions from all the elements as shown below,

$$\{F_S\}_t = \sum_{i=1}^{N_e} \iiint_V [B]^t\ \{\sigma_d\}\ dV \tag{3.38}$$

where, N_e is the total number of elements and $[B]^t$ is the transpose of the displacement matrix $[B]$ defined in Appendix I.

If the right hand side of the equation representing the external load, at time t, is $\{P\}_t$,

then $\{P_{cor}\}$ can be calculated as,

$$\{P_{cor}\} = \{P\}_t - \{F_I\}_t - \{F_D\}_t - \{F_S\}_t \tag{3.39}$$

Combining equations (3.36) through (3.38) into equation (3.39) will yield,

$$\{P_{cor}\} = \{P\}_t - [M]\{\ddot{X}\}_t - [C]_t\{\dot{X}\}_t - \sum_{i=1}^{N_e}\int\int\int_V [B]^t\{\sigma_d\}\, dV \tag{3.40}$$

The correction force vector calculated above can be added to the right hand side of the incremental equation formulated at time t for solving the responses at time T, as

$$[M]\{\Delta\ddot{X}\} + [C]_t\{\Delta\dot{X}\} + [K_t]_t\{\Delta X\} = \{\Delta P\} + \{P_{cor}\} \tag{3.41}$$

3.9 Residual Porewater Pressure Model

During seismic shaking two kinds of porewater pressures are generated in staurated sands. They are the transient and residual porewater pressures. The transient pressures are due to changes in the applied mean normal stresses during seismic excitation. For saturated sands, the transient changes in porewater pressures are equal to changes in the mean normal stresses. Since they balance each other, the effective stress regime in the sand remains largely unchanged. Hence the stability and deformability of the sand are not seriously affected due to the transient pressures. On the other hand, the residual pressures are due to plastic deformation in the sand skeleton. These persist until dissipated by drainage or internal diffusion and therefore they exert a major influence on the strength and stiffness of the sand skeleton. Changes in the total mean normal stresses also affect the post earthquake value of the residual pressures. These pressures can be calculated using Skempton's B value. In all studies in this thesis, these changes are small and hence are ignored.

In TARA-3, the residual porewater pressures are generated using the Martin-Finn-Seed model (Martin et al 1975). The transient pressures are not modelled. Therefore, computed porewater pressure time histories will show the steady accumulation of pressure with time but will not show the fluctuations in pressure caused by the transient changes in mean normal stresses.

3.9.1 Martin-Finn-Seed Model

The original M-F-S model applies only to level ground, so that there are no static shear stresses acting on horizontal planes prior to the seismic loading. The model was subsequently modified to include the effects of initial static shear stresses present in two dimensional analyses. The original model is briefly described in this section and the modifications in the subsequent section.

In the model, the increments in porewater pressure ΔU that develop in a saturated sand under cyclic shear strains are related to the volumetric strain increments $\Delta\epsilon_{vd}$ that occur in the same sand under drained conditions with the same shear strain history.

Consider a sample of saturated sand under a vertical effective stress, σ'_v. Let the increment in volumetric compaction strain due to grain slip caused by a cycle of shear strain, γ, during a drained cyclic simple shear test be $\Delta\epsilon_{vd}$. Let the increment in porewater pressure caused by a cycle of shear strain, γ, during an undrained cyclic simple shear test starting with the same effective stress system be ΔU. It was shown by Martin et al (1975) that for fully saturated sands and assuming that water to be incompressible, that ΔU and $\Delta\epsilon_{vd}$ are related by

$$\Delta U = E_r \, \Delta\epsilon_{vd} \tag{3.42}$$

in which E_r is the one-dimensional rebound modulus of sand at a vertical effective stress σ'_v.

They also showed that under simple shear conditions the volumetric strain increment,

$\Delta\epsilon_{vd}$, is a function of the total accumulated volumetric strain, ϵ_{vd}, and the amplitude of the shear strain cycle, γ, and is given by

$$\Delta\epsilon_{vd} = C_1\ (\gamma - C_2\ \epsilon_{vd})\ + \frac{C_3\ \epsilon_{vd}^2}{(\gamma + C_4\ \epsilon_{vd})} \tag{3.43}$$

in which C_1, C_2, C_3 and C_4 are volume change constants. These constants depend on the sand type and relative density.

An analytical expression for the rebound modulus, E_r, at any vertical effective stress level σ'_v is given by Martin et al (1975) as,

$$E_r = \frac{(\sigma'_v)^{1-m}}{m\ K_r\ (\sigma'_{vo})^{n-m}} \tag{3.44}$$

in which σ'_{vo} is the initial vertical effective stress and K_r, m and n are rebound constants. These are derived from rebound tests in a consolidation ring.

The increment in porewater pressure, ΔU, during a given loading cycle with a maximum shear strain amplitude, γ, can now be computed using equations (3.42), (3.43) and (3.44) given the volume change and rebound constants.

The important assumption in the formulation of the M-F-S model is that there is a unique relationship between the volumetric strains in drained tests and porewater pressures in undrained tests for a given sand at the same effective stress system and subjected to the same strain histories. This assumption has been verified to be valid through an extensive laboratory program involving drained and undrained tests on normally and overconsolidated sands (Bhatia 1982 and Finn 1981). Bhatia (1982) found out that when the M-F-S model is coupled with the stress strain model reported in section 3.4, it can satisfactorily predict both the rate of porewater pressure generation and liquefaction strength curve in undrained tests for cyclic stress histories representative of earthquake loading.

3.9.2 Extension Of M-F-S Model to 2-D Conditions

In the 2-D analysis of isotropic soil, the permanent volume changes due to shearing action are related to the cyclic shear stresses on horizontal planes because the seismic input motions are usually assumed to be shear waves propagating vertically. Therefore, in TARA-3, for computation of $\Delta\epsilon_{vd}$ in equation (3.43), the shear strain on the horizontal plane, γ_{xy}, is substituted in place of γ. Also, σ'_v and σ'_{vo} in equation (3.44) are replaced by σ'_y and σ'_{yo} respectively, where σ'_y and σ'_{yo} are the current and initial vertical effective stresses.

Static shear stresses are present on horizontal planes in 2-D problems. The presence of initial static shear stresses may significantly affect the cyclic behavior of sands depending on the relative density of the sand and the level of the initial static shear stress (Vaid and Finn 1978; Vaid and Chern 1983). In saturated sands, the rate of development of porewater pressures, the level to which they may rise and the liquefaction potential curve are all dependent on the static shear stress level. These effects are taken into account in the porewater pressure model by specifying model constants such that they produce a reasonable match for the liquefcation potential curves and the rates of porewater pressure generation observed in laboratory samples with different initial static shear stress ratios.

3.10 Evaluation of Current Effective Stress System

The global system of equations that relate the incremental nodal forces $\{\Delta P\}$ and incremental displacements $\{\Delta\}$ is given by (see Appendix I)

$$\{\Delta P\} = [K_t]\ \{\Delta\} + [K^*]\ \{\Delta U\} \tag{3.45}$$

in which,

$[K_t]$ = the global tangent stiffness matrix,

$[K^*]$ = the matrix associated with porewater pressures,

$\{\Delta U\}$ = the incremental porewater pressures.

This equation is used to evaluate the changes in effective stresses resulting from the changes in residual porewater pressures by setting $\{\Delta P\} = 0$. The incremental displacements, strains and stresses given by this procedure constitute the response of the deposit to softening of the elements. The incremental stresses give rise to the new effective stress system which can now be used to modify soil properties as described in the next section. The incremental strains are components of the permanent strains.

3.10.1 Modification of Soil Properties

The maximum shear modulus, G_{max}, and the shear strength, τ_{max}, in the hyperbolic stress strain relationship are dependent on effective stresses. As the seismically induced porewater pressure increases, and reduces the effective stress, the modulus and strength must be adjusted to be compatible with the current effective stress system.

In TARA-3, the maximum shear modulus is assumed to be proportional to $(\sigma'_m)^{1/2}$. Therefore, the maximum shear modulus, G_{max} for the current cycle of loading is obtained by

$$\frac{G_{max}}{(G_{max})_o} = (\frac{\sigma'_m}{\sigma'_{mo}})^{1/2} \tag{3.46}$$

in which $(G_{max})_o$ is the maximum shear modulus corresponding to the initial effective stress system defined by σ'_{mo}.

The computation of τ_{max} compatible with the current effective stress system is already outlined in section 3.4.1.1.

3.10.2 Estimation of Maximum Residual Porewater Pressure

Laboratory investigations of samples with initial static shear stress on potential failure planes (Chern 1981) reveal that there is a limit to which the residual porewater pressures can rise. For triaxial conditions, the limiting residual porewater pressure, U_{max}, has been found to be given by (Chern 1981; Chang 1982)

$$U_{max} = \sigma'_{3c} \left[1 - \left(\frac{\sigma'_{1c}}{\sigma'_{3c}} - 1\right) \frac{1 - \sin\phi'}{2 \sin\phi'}\right] \tag{3.47}$$

in which σ'_{1c} and σ'_{3c} are the major and minor principal consolidation stresses respectively and ϕ' is the angle of internal friction.

Equation (3.47) implies that the limiting value of the residual porewater pressure depends on the static shear stress level that existed after the end of consolidation.

The direct application of equation (3.47) to estimate U_{max} based on the field stress conditions will not be correct since loading from earthquakes resembles simple shear rather than triaxial conditions. Therefore, equation (3.47) should be modified to reflect simple shear conditions. The modification takes the form,

$$U_{max} = \sigma'_{3*} \left[1 - \left(\frac{\sigma'_{1*}}{\sigma'_{3*}} - 1\right) \frac{1 - \sin\phi'}{2 \sin\phi'}\right] \tag{3.48}$$

in which σ'_{1*} and σ'_{3*} are the applied major and minor principal stresses in a triaxial sample that would produce a stress condition on a plane inclined at an angle $(45 + \phi'/2)$ to the horizontal, the same as on the horizontal plane in the field with initial stresses $(\sigma_y\ ,\ \tau_{xy})$. The condition is clearly illustrated in Fig. 3.5. From the Mohr circle in Fig. 3.6, σ'_{1*} and σ'_{3*} can be calculated as,

$$\sigma'_{1*} = \sigma'_y + \tau_{xy} \frac{(1 + \sin\phi')}{\cos\phi'} \tag{3.49}$$

$$\sigma'_{3*} = \sigma'_y - \tau_{xy} \frac{(1 - \sin\phi')}{\cos\phi'} \tag{3.50}$$

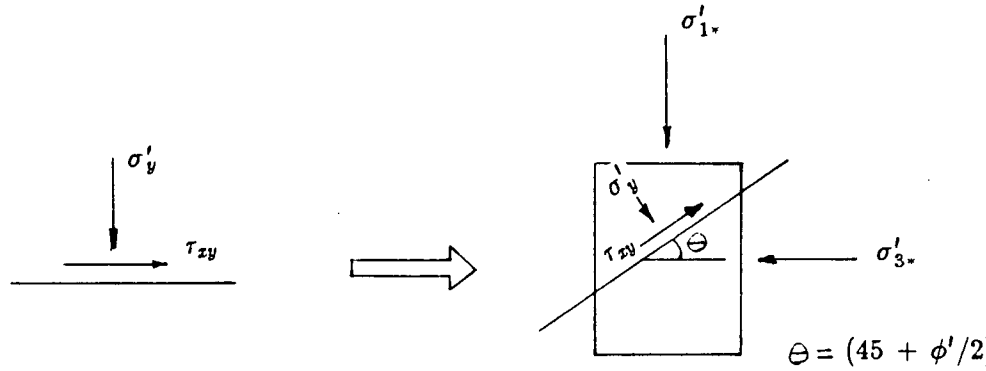

Fig. 3.5 Simple Shear and Triaxial Stress Conditions

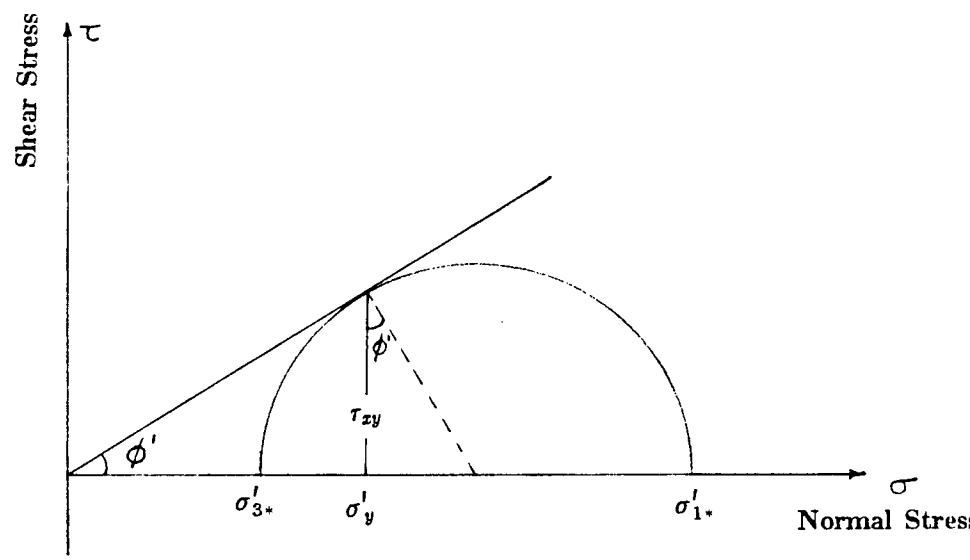

Fig. 3.6 Mohr Circle Construction

It should be noted that the above computation can be equally applied in the case of the level ground conditions, where the limit on residual porewater pressure will be equal to the initial vertical effective stress.

One of the options included in TARA-3 regarding the porewater pressure limit is the one described above. However, there are other options available including the option that would terminate porewater pressure generation in an element which has reached failure according to Mohr-Coulomb failure criterion.

3.11 Interface Representation

In the conventional finite element approach, the relative displacement at the interface between two finite elements is not modelled. But, in practice, particularly at the soil-structure interface, realtive movements do occur. Therefore, in situations where relative motions are anticipated, a model that incorporates the relative movement at the interface is indeed necessary for a realistic solution of the problem.

In TARA-3, the relative movement at the interface between two finite elements is modelled using the two-dimensional slip elements presented by Goodman et al (1968). The element is of zero thickness and capable of allowing relative movement in both sliding and rocking modes during the earthquake excitation. The slip element formulation is presented in the subsequent section.

3.11.1 Slip Element Formulation

The slip element incorporated in the method of analysis is a two-dimensional element with four nodes and eight degrees of freedom. The horizontal and vertical displacements at each node are the degrees of freedom. Fig. 3.7 shows a slip element with the global (x, y) and local element (s, n) axes. Since the element thickness is zero, nodes P and Q will have

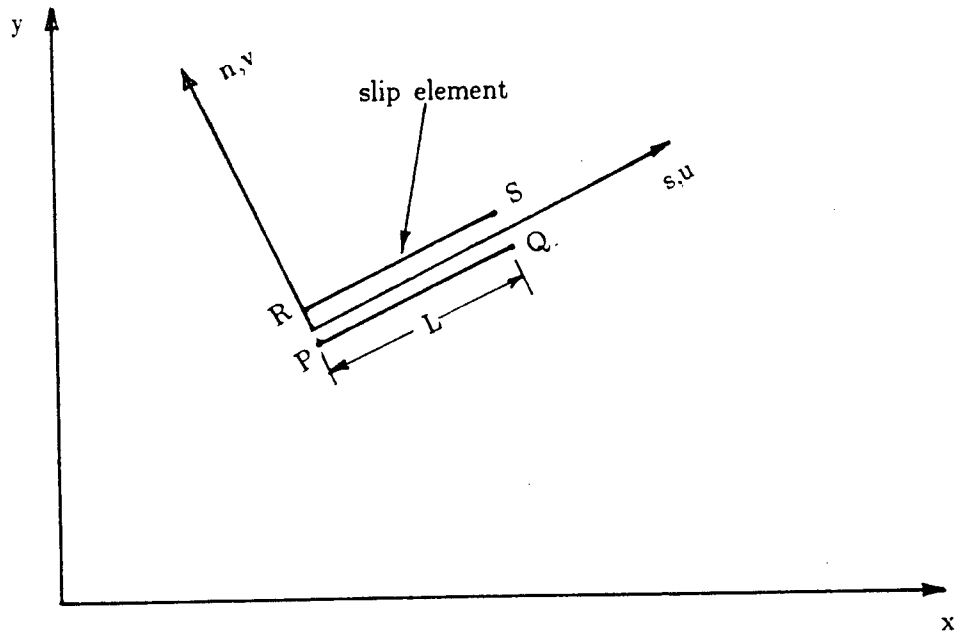

Fig. 3.7 Definition of Slip Element

the same (x, y) coordinates as that of R and S respectively.

The force displacement relationship at any point within the slip element is assumed to be of the form,

$$\begin{Bmatrix} f_s \\ f_n \end{Bmatrix} = \begin{bmatrix} K_s & 0 \\ 0 & K_n \end{bmatrix} \begin{Bmatrix} w_s \\ w_n \end{Bmatrix} \tag{3.51}$$

in which,

f_s = shear force per unit area of the element,

f_n = normal force per unit area of the element,

K_s = unit shear stiffness in the direction of the element,

K_n = unit normal stiffness in the direction normal to the element,

w_s = shear displacement at the point of interest and,

w_n = normal displacement at the point of interest.

A linear variation of displacement in the slip element is assumed. Then the stiffness matrix K_{sn} in terms of local co-ordinates as derived in Appendix II, is

$$K_{sn} = \frac{L}{6} \begin{bmatrix} 2K_s & 0 & K_s & 0 & -K_s & 0 & -2K_s & 0 \\ 0 & 2K_n & 0 & K_n & 0 & -K_n & 0 & -2K_n \\ K_s & 0 & 2K_s & 0 & -2K_s & 0 & -K_s & 0 \\ 0 & K_n & 0 & 2K_n & 0 & -2K_n & 0 & -K_n \\ -K_s & 0 & -2K_s & 0 & 2K_s & 0 & K_s & 0 \\ 0 & -K_n & 0 & -2K_n & 0 & 2K_n & 0 & K_n \\ -2K_s & 0 & -K_s & 0 & K_s & 0 & 2K_s & 0 \\ 0 & -2K_n & 0 & -K_n & 0 & K_n & 0 & 2K_n \end{bmatrix} \tag{3.52}$$

in which

L= the length of the slip element.

The assumed linear displacement variation is consistent with the variation in the isoparametric quadrilateral finite element along a side. The stiffness matrix in terms of the global co-ordinates can be obtained using the transformation matrix consisting of the di-

rection cosines.

3.11.2 Analysis Procedure

In the incremental analysis, the values of K_s ans K_n are kept constant until yield is indicated. Therefore, the incremental stresses Δf_s and Δf_n are obtained using the incremental force displacement relationship,

$$\begin{Bmatrix} \Delta f_s \\ \Delta f_n \end{Bmatrix} = \begin{bmatrix} K_s & 0 \\ 0 & K_n \end{bmatrix} \begin{Bmatrix} \Delta w_s \\ \Delta w_n \end{Bmatrix} \tag{3.53}$$

in which,

Δw_s = incremental shear displacement,

Δw_n = incremental normal displacement.

Because of the linear displacement field, the stresses vary from point to point within the slip element. The average stresses are assumed to be representative stresses of the element. The average incremental stresses Δf_{sav} and Δf_{nav} are calculated using the relationship,

$$\begin{Bmatrix} \Delta f_{sav} \\ \Delta f_{nav} \end{Bmatrix} = \begin{bmatrix} K_s & 0 \\ 0 & K_n \end{bmatrix} \begin{Bmatrix} \Delta w_{sav} \\ \Delta w_{nav} \end{Bmatrix} \tag{3.54}$$

in which,

$$\Delta w_{sav} = (\Delta u_R + \Delta u_S)/2 - (\Delta u_P + \Delta u_Q)/2 \tag{3.55}$$

and

$$\Delta w_{nav} = (\Delta v_R + \Delta v_S)/2 - (\Delta v_P + \Delta v_Q)/2 \tag{3.56}$$

Here R and S are the top nodes and P and Q are the bottom nodes defining the slip element (Fig. 3.7).

The total stresses f_s and f_n are computed by adding the incremental values from all load steps.

The stress displacement relationship along the direction of the slip element is assumed to be elastic-perfectly plastic, while along the normal direction it is assumed to be elastic. The plastic region is defined by the Mohr-Coulomb yield criterion. Slip is assumed to occur when the shear stress exceeds the shear strength, f_{max}, given by

$$f_{max} = c_s + f_n \tan \phi'_s \tag{3.57}$$

in which,

c_s = cohesion,

ϕ'_s = friction angle.

When slip is indicated, the shear stiffness K_s is set equal to zero, but the normal stiffness K_n is kept at its current value. The separation is also indicated when the normal stress f_n reaches a negative value. Under this circumstance, both K_s and K_n are set to a small value.

The parameters K_s, K_n, c_s and ϕ'_s adequately define the behavior of the slip element. These parameters depend on many factors such as surface roughness and shape and characteristics of the asperities. Estimates of the parameters can be obtained from direct shear tests (Goodman et al 1968; Tatsuoka et al 1985), simple shear tests (Uesugi et al 1986), ring torsion tests (Yoshimi et al 1981) and rod shear tests (Felio et al 1987).

3.12 Computation of Deformation Pattern

There are basically three components of deformation that occur in a soil structure system as a result of earthquake loading. The first component is the dynamic residual deformation that occurs at the end of the earthquake as a result of the hysteretic stress strain response. In order to compute this, an earthquake record with enough trailing zeros

should be used so that the free damped vibration response of the system can be included in the analysis.

The second component is the deformation of the system that occurs as a result of increasing porewater pressures during the dynamic analysis. This occurs because of the gravity acting on the softening soil. This is mostly of the constant volume type of deformation in the saturated regions of the soil structure.

The third component is the deformation of the system that occurs after the earthquake due to consolidation as the seismically induced residual porewater pressures dissipate.

All three components are computed in TARA-3 analysis. The first two components are computed directly in a straightforward manner. The deformation due to dissipation of residual porewater pressures can be obtained by treating the problem as a two-dimensional consolidation problem in which the deformations are obtained at discrete time intervals as porewater pressures dissipate. The post consolidation deformations can also be obtained using the volumetric strains computed by the porewater pressure model. The computed volumetric strains are distributed to form a strain field depending on the degree of freedom of the nodes forming the element. The obtained strain field is used to compute nodal forces, which are then applied to the nodes to obtain the deformation field. This procedure is carried out at several equal steps, each time only a portion of the total accumulated volumetric strains is used. Both of these options are available in TARA-3.

The final post earthquake deformation computed by TARA-3 is the sum of all three components described in this section.

CHAPTER 4

ENERGY TRANSMITTING BOUNDARY

4.1 Introduction

Numerical techniques for dynamic analysis of a continuum require a finite domain with well defined boundaries. These boundaries often do not exist naturally and therefore must be artificially imposed on the computational model.

In dynamic analysis involving earthquake excitations, two different types of artificial boundaries are imposed when a semi-infinite medium is modeled by a finite domain, namely, the bottom boundary (base) and lateral boundaries. In a typical soil-structure interaction problem involving earthquake excitations, it is common practice to apply the input excitation along the base of the finite element mesh and to assume vertical propagation of waves through the soil. The incident waves that are produced by the earthquake excitation and any waves reflected downward from the surface or any structures in the region pass through the bottom boundary. The lateral boundary divides the core region from the free field. Any waves other than those that pass through the bottom boundary pass through the lateral boundary. For a realistic computation of dynamic responses, the conditions imposed on these boundaries must be such that they reproduce the physical behavior of the actual problem being analyzed.

Often boundaries are represented by elementary boundaries on which either forces (free boundary) or displacements (fixed boundary) or combination of forces and displacements (roller boundary) are specified depending on the problem. The major problem with elementary boundaries is that the energy that is transmitted out of the finite domain does not correspond to what is transmitted in the field. For example, either acceleration or velocity or displacement is often specified as the condition on the bottom boundary. Such an assignment implies that the underlying medium is rigid. Therefore, no energy is allowed to radiate out of the system into the underlying medium.

The use of elementary boundaries for the lateral boundaries in dynamic analysis is appropriate only in cases where the boundaries are located far enough from the zone of interest so that either the reflected waves will not reach the zone of interest within the time period under consideration or they will be removed before they reach the zone of interest by internal damping. If the boundaries are located far away from the zone of interest, the finite element mesh will become large and therefore the computing time and cost will increase. Hence, elementary boundaries may not be practical in some cases.

Boundaries that account for the radiation of energy out of the finite domain are desirable for the proper evaluation of the dynamic response. Such boundaries are termed as energy transmitting or energy absorbing boundaries. These boundaries are achieved by precribing a set of normal and tangential stresses in such a way that the continued effect of these stresses and the stresses due to any incident waves will reflect the proper amount of energy back into the finite domain.

Over the span of the last 20 years, many types of transmitting boundaries have been proposed for use in dynamic analyses involving wave propagation. However, many of them are not applicable to true nonlinear systems and most importantly they cannot be accommodated within the framework of time domain analysis. The next section describes briefly

the review of the possible transmitting boundaries that can be adopted for implementation in computer program TARA-3.

4.2 Review of Possible Transmitting Boundaries

One of the simplest and most effective energy transmitting boundary that could be accommodated in time domain analyses is the viscous boundary. In concept, this boundary is achieved by connecting viscous dashpots with appropriate constant properties along the nodes of the boundary. The properties of the viscous dashpots are based on the specific type of wave.

The earliest solution for the viscous boundary was proposed by Lysmer and Kuhlemeyer (1969) for two-dimensional plane strain problems. In their formulation the properties of the nodal dashpots were assumed to be $a\rho V_s$ and $b\rho V_p$, where ρ is the mass density of the medium and V_s and V_p are the shear (S) and compression (P) wave velocities and a and b are constants. In their evaluation of this boundary, they showed that for any choice of a and b, the effectiveness of the boundary in absorbing energy depends on the Poisson's ratio. The case with $a = 1$ and $b = 1$ was found to be most efficient in absorbing plane body waves and was termed the standard viscous boundary. Their study and subsequent studies by White et al (1977) indicated that the standard viscous boundary is efficient in absorbing plane body waves for Poisson's ratio ranging from 0.0 to 0.40.

Another possibilty is the transmitting boundary known as the superposition boundary. The technique for the superposition boundary was first introduced by Smith (1974). It is a method where the complete solutions of two independent boundary value problems using Neumann (free) and Dirichlet (fixed) boundary conditions are superimposed so as to cancel out single boundary reflections. The formulation is independent of frequency and incident angles and very effective for both body and surface waves. It requires 2^n complete dynamic

solutions if n reflections occur during the time span of interest. However, the method fails when a given wave is reflected at the same boundary more than once.

There have been refinements proposed to the original superposition boundary. The notable refinement is the one proposed by Kunar and Marti (1981), in which the boundary conditions are changed from fixed and free to constant velocity and constant stress. The reflected waves are eliminated as they occur in the boundaries. According to Kunar and Marti (1981), this refinement has the advantage that it avoids multiple reflections and the need for 2^n complete solutions as required in the original superposition boundary formulation.

Between both of these boundaries, the viscous boundary was selected to be incorporated in TARA-3 for the simple reason that it is easy to implement. In fact, Simons and Randolph (1986), who conducted a comparative study of the standard viscous boundary and the superposition boundary of Kunar and Marti, concluded that while the superposition boundary is found to be an effective absorber, the improvement in results obtained by the more rigorous superposition boundary formulation in preference to a simple viscous boundary formulation does not appear to warrant the increased computational effort required for the superposition formulation.

Roesset et al (1977) have conducted parametric studies to compare the effect of different boundaries using single frequency oscillation input. They have shown for the examples considered, that the responses (transfer functions) depend strongly on the distance from the boundary to the structure and that satisfactory results can be obtained if elementary and viscous boundaries are located at an appropriate distance from the structure. They recommended a distance of 10B to 20B for the cases with moderate values of internal damping and a distance of 5B for cases with high values of internal damping, where B is the width of the structure. They have also shown that both roller and viscous boundaries are effective and the differences resulting from the use of these boundaries are not significant provided

boundaries are located at an appropriate distance away from the edge of the structure. These studies were restricted to linear systems. Consequently, it is not known whether an improvement could be achieved by incorporating the viscous boundary for nonlinear problems with earthquake type of excitations. In order to investigate this, the viscous boundary formulation is incorporated in TARA-3 and the effectiveness of the boundary is evaluated through simple examples.

4.3 Energy Transmitting Boundaries in TARA-3

The transmittimg base in TARA-3 is modeled by viscous dashpots with constant properties as used in the 1-D nonlinear program DESRA-2 (Lee and Finn, 1978). The dashpots are similar to the ones proposed by Joyner and Chen (1975) which are extensions of the viscous dashpots proposed by Lysmer and Kuhlemeyer (1969) to allow for incident waves from excitations outside the model to come into the model. The viscous dashpots placed along the lateral boundary are very similar to the ones proposed by Lysmer and Kuhlemeyer (1969). However, the formulation is such that the properties of the dashpots placed along the lateral boundary can be either constant or varying. In the case of constant properties, the boundary is identical to the standard viscous boundary. The formulation is such that the lateral boundaries have to be vertical. This places a limitation on the capability of the program. However, this does not seem to be a serious limitation in the case of the soil-structure interaction problem involving earthquake excitations.

4.4 Finite Element Formulation For Transmitting Base

Consider a system of horizontal soil deposit bounded above by free surface and below by a semi-infinite medium. In the method proposed by Joyner and Chen (1975), the finite rigidity of the underlying medium is taken into account by including the stresses transmitted

across the boundary between the soil deposit and the underlying medium into the lumped mass system. In order to evaluate the stresses at the boundary, the following assumptions are implied. The underlying medium is elastic and the propagating shear and compression waves are plane waves travelling vertically.

If U is the horizontal displacement of a particle in the underlying medium located at a depth z, then the shear stress τ is given by,

$$\tau = G \frac{\partial U}{\partial z} \tag{4.1}$$

where,

G = shear modulus of the underlying medium.

If U_I and V_I are the displacement and velocity components due to the incident wave and U_R and V_R are the displacement and velocity components due to the reflected waves, then

$$U_I = U_I(z + V_s t) \tag{4.2}$$

$$U_R = U_R(z - V_s t) \tag{4.3}$$

where,

V_s = shear wave velocity in the underlying medium,

t = time.

Now from equation (4.1), the shear stress at any point in the medium is given by,

$$\tau = G \left(\frac{\partial U_I}{\partial z} + \frac{\partial U_R}{\partial z}\right) \tag{4.4}$$

From equations (4.2) and (4.3),

$$\frac{\partial U_I}{\partial z} = \frac{V_I}{V_s} \tag{4.5}$$

and

$$\frac{\partial U_R}{\partial z} = -\frac{V_R}{V_s} \tag{4.6}$$

therefore,

$$\tau = G \frac{(V_I - V_R)}{V_s} \tag{4.7}$$

Supposing V_{IB} and V_{RB} are the velocity components of the incident and reflected waves at the boundary, then the shear stress at the boundary, τ_B, is given by,

$$\tau_B = G \frac{(V_{IB} - V_{RB})}{V_s} \tag{4.8}$$

The particle velocity at the boundary, V_B, is given by,

$$V_B = V_{IB} + V_{RB} \tag{4.9}$$

From equations (4.8) and (4.9), τ_B can be rewritten as,

$$\tau_B = G \frac{(2V_{IB} - V_B)}{V_s} \tag{4.10}$$

now, G and V_s are related by,

$$G = \rho V_s^2 \tag{4.11}$$

where,

ρ = mass density of the underlying medium.

Combining equations (4.10) and (4.11) will yield,

$$\tau_B = \rho V_s (2V_{IB} - V_B) \tag{4.12}$$

This is the expression for the shear stress transmitted across the boundary between the soil deposit and the underlying medium. This shear stress can be included in the lumped mass system by considering the equilibrium of the mass on the boundary.

Consider a discrete mass q at node Q on the bottom boundary shown in Fig. 4.1. Let x and y be the horizontal and vertical directions respectively, and the boundary stresses on segment ST in the x and y direction be τ and σ, respectively.

In the case of transmitting boundaries, the input base motion is interpreted as the "control outcrop motion". This is simply the surface motion expected at the outcrop of the base material. Supposing the velocity of the motion in the horizontal direction expected at the outcrop of the base material is $\dot{x}_b$, then equation (4.12) can be rewritten as

$$\tau = \rho \; V_s \; (\dot{x}_b - \dot{x}_q) \tag{4.13}$$

where,

$\dot{x}_q$ = velocity of the mass q in the horizontal direction.

Similar arguments give the expression for normal stress as

$$\sigma = \rho \; V_p \; (\dot{y}_b - \dot{y}_q) \tag{4.14}$$

where,

$\dot{y}_b$ = velocity of the motion in the vertical direction expected at the outcrop of the base material,

$\dot{y}_q$ = velocity of the mass q in the vertical direction,

V_p = compression wave velocity in the underlying medium.

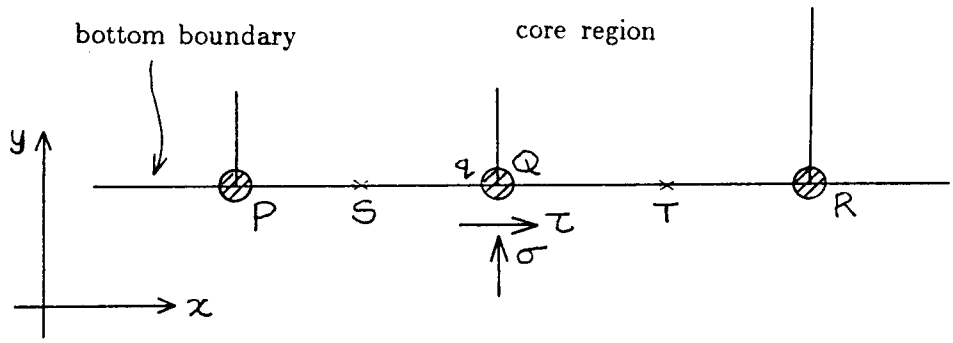

Fig. 4.1 Boundary Stresses on a Discrete Mass on Horizontal Bottom Boundary

The corresponding boundary forces S_x and S_y are then given by

$$S_x = \rho \; V_s \; \Delta l \; (\dot{x}_b - \dot{x}_q) \tag{4.15}$$

$$S_y = \rho \; V_p \; \Delta l \; (\dot{y}_b - \dot{y}_q) \tag{4.16}$$

where,

Δl = length of segment ST, which is the sum of 1/2 of the distance between nodes P and Q and 1/2 of the distance between nodes Q and R (Fig. 4.1).

Now the dynamic equilibrium of the discrete mass q in the horizontal direction gives the equation in the form,

$$m_q \; \ddot{x}_q + c_q \; (\dot{x}_q - \dot{x}_{q-1}) + k_q \; (x_q - x_{q-1}) \; = \; S_x \tag{4.17}$$

where m_q, c_q, and k_q are the mass, damping and stiffness terms associated with mass q. Subscript "$q-1$" refers to responses of the mass connected to mass q.

Substituting for S_x from equation (4.15) into equation (4.17) and rearranging will yield

$$m_q \; \ddot{x}_q + (c_q + \rho \; V_s \; \Delta l) \; \dot{x}_q - c_q \; \dot{x}_{q-1} + k_q \; (x_q - x_{q-1}) = \rho \; V_s \; \Delta l \; \dot{x}_b \tag{4.18}$$

Equation (4.18) indicates that in order to account for the bottom transmitting base, it is necessary to increase the diagonal components of the $[c]$ matrix associated with the nodes on the bottom boundary by $\rho \; V_s \; \Delta l$ and introduce a term $\rho \; V_s \; \Delta l \; \dot{x}_b$ on the right hand side of the equilibrium equation.

Similar arguments would lead to the conclusion that for the vertical degree of freedom, the diagonal components of the $[c]$ matrix associated with nodes on the bottom boundary should be increased by $\rho \; V_p \; \Delta l$ and a term $\rho \; V_p \; \Delta l \; \dot{y}_b$ be introduced to the right hand side

of the equilibrium equation. Therefore, the increase in the damping matrix coefficents $[c]_{inc}$, and the term on the right hand side of the equation $\{F\}_{add}$, associated with a node on the bottom transmitting boundary are given by

$$[c]_{inc} = \begin{bmatrix} \rho\ V_s\ \Delta l & 0 \\ 0 & \rho\ V_p\ \Delta l \end{bmatrix} \tag{4.19}$$

and

$$\{F\}_{add} = \begin{Bmatrix} \rho\ V_s\ \Delta l\ \dot{x}_b \\ \rho\ V_p\ \Delta l\ \dot{y}_b \end{Bmatrix} \tag{4.20}$$

4.5 Finite Element Formulation For Lateral Viscous Boundary

In the standard viscous boundary proposed by Lysmer and Kuhlemeyer (1969), the boundary stresses on a vertical boundary are expressed as,

$$\sigma = \rho\ V_p\ \dot{u} \tag{4.21}$$

$$\tau = \rho\ V_s\ \dot{w} \tag{4.22}$$

where σ and τ are the normal and shear stresses, respectively, and $\dot{u}$ and $\dot{w}$ are the normal and tangential velocities, respectively.

However, in seismic soil-structure interaction problems where the input is applied along the base of finite element mesh, it is important to formulate the lateral energy transmitting boundary in such a way that it reacts only to waves radiating away from the structure rather than to motion resulting from the propagation of the seismic input. This can be achieved by having a formulation that permits the lateral viscous boundary to react only to any response different from the free field response, i.e., the differential velocity field.

In order to impose this condition, let consider a discrete mass n at node B on the vertical lateral boundary. Let x and y be the horizontal and vertical directions as shown in

Fig. 4.2. Let the boundary stresses on the segment DE in the x and y directions be σ and τ respectively. These are now defined as,

$$\sigma = \rho \; V_p \; (\dot{x}_{an} - \dot{x}_{af}) \tag{4.23}$$

$$\tau = \rho \; V_s \; (\dot{y}_{an} - \dot{y}_{af}) \tag{4.24}$$

where ρ is the mass density of the soil, V_p and V_s are the compression and shear wave velocities in the free field and subscript "*an*" refers to absolute velocities of discrete mass n and subscript "*af*" refers to absolute velocities of the free field at the location of node B.

The boundary forces F_x and F_y corresponding to the boundary stresses expressed in equations (4.22) and (4.23) are given by

$$F_x = \rho \; V_p \; \Delta l \; (\dot{x}_{an} - \dot{x}_{af}) \tag{4.24}$$

$$F_y = \rho \; V_s \; \Delta l \; (\dot{y}_{an} - \dot{y}_{af}) \tag{4.25}$$

where,

Δl is the length of segment DE, which is the sum of 1/2 of the distance between nodes A and B and 1/2 of the distance between nodes B and C (Fig. 4.2).

Equations (4.24) and (4.25) can be rewritten in terms of quantities relative to the base as

$$F_x = \rho \; V_p \; \Delta l \; (\dot{x}_{rn} - \dot{x}_{rf}) \tag{4.26}$$

$$F_y = \rho \; V_s \; \Delta l \; (\dot{y}_{rn} - \dot{y}_{rf}) \tag{4.27}$$

where,

subscript "*r*" refers to the velocities relative to the base.

The dynamic equilibrium in the horizontal direction of the discrete mass n on the lateral

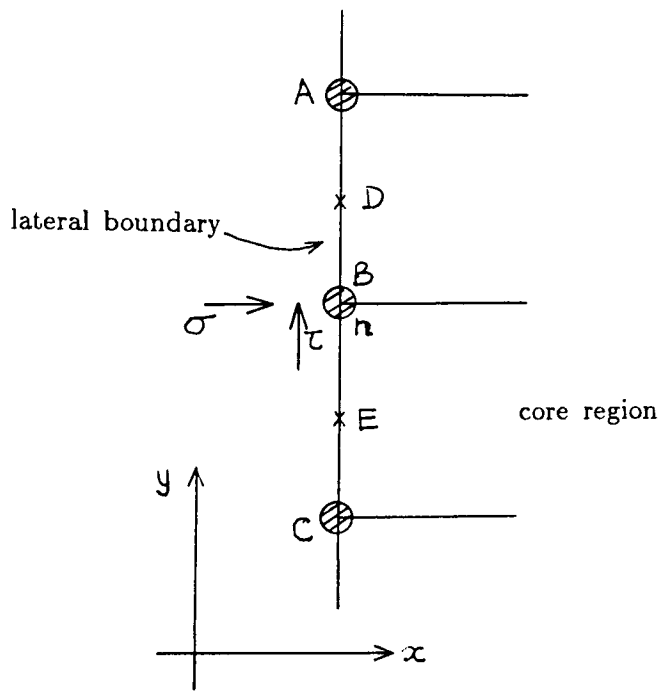

Fig. 4.2 Boundary Stresses on a Discrete Mass on Vertical Lateral Viscous Boundary

boundary without consideration of the boundary forces yields a typical equation of the form

$$m_n \ddot{x}_{rn} + c_n (\dot{x}_{rn} - \dot{x}_{rn-1}) + k_n (x_{rn} - x_{rn-1}) = - m_n \ddot{x}_b \qquad (4.28)$$

where,

m_n, c_n, and k_n are the mass, damping and stiffness terms associated with mass n and $\ddot{x}_b$ is the base input acceleration. Subscript "$n-1$" refers to responses of the mass connected to mass n.

If the boundary force given by equation (4.26) is introduced, then equation (4.21) should be rewritten as,

$$m_n \ddot{x}_{rn} + c_n (\dot{x}_{rn} - \dot{x}_{rn-1}) + k_n (x_{rn} - x_{rn-1}) = - m_n \ddot{x}_b - \rho V_p \Delta l (\dot{x}_{rn} - \dot{x}_{rf}) \qquad (4.29)$$

Here, the force on the segment DE is assumed to be applied at the node B. Rearrangement of equation (4.29) yields

$$m_n \ddot{x}_{rn} + (c_n + \rho V_p \Delta l) \dot{x}_{rn} - c_n \dot{x}_{rn-1} + k_n (x_{rn} - x_{rn-1}) = - m_n \ddot{x}_b - \rho V_p \Delta l \dot{x}_{rf} \qquad (4.30)$$

Comparison of equations (4.28) and (4.30) indicates that in order to account for lateral viscous boundary, it is necessary to increase the diagonal components of the damping matrix associated with the nodes on the boundary by $\rho V_p \Delta l$ and introduce an additional term $- \rho V_p \Delta l \dot{x}_{rf}$ on the right hand side of the equilibrium equation. The relative velocity of the free field at location of the node B , $\dot{x}_{rf}$, has to be determined by a separate site amplification study. It should be noted here that the finite element discretization for the separate free field response study should be consistent with the discretization of the lateral boundary. The free field response study may be conducted using TARA-3 in the one-dimensional mode.

Similar arguments will indicate that for the vertical degree of freedom, the increase in the diagonal components of the damping matrix associated with nodes on the lateral

boundary is $\rho\ V_s\ \Delta l$ and the additional term on the right hand side of the equilibrium equation is $-\ \rho\ V_s\ \Delta l\ \dot{y}_{rf}$. However, in the cases where the earthquake input at the base is assumed to be of horizontal shear waves propagating in the vertical direction, this additional term will be zero because $\dot{y}_{rf}$ is zero.

Therefore, for general cases the increase in the damping matrix, $[c]_{inc}$ and the additional term on the right hand side of the equation, $\{F\}_{add}$, associated with a node on the lateral boundary, such as node B, is given by

$$[c]_{inc} = \begin{bmatrix} \rho\ V_p\ \Delta l & 0 \\ 0 & \rho\ V_s\ \Delta l \end{bmatrix} \tag{4.31}$$

and

$$\{F\}_{add} = \begin{Bmatrix} -\rho\ V_p\ \Delta l\ \dot{x}_{rf} \\ -\rho\ V_s\ \Delta l\ \dot{y}_{rf} \end{Bmatrix} \tag{4.32}$$

4.6 Effectiveness of the Transmitting Base

The effectiveness of the transmitting base is evaluated by analysing a horizontally layered soil column, 58m deep, using both a rigid and energy transmitting base. In the latter case, the underlying medium is assumed to have the same maximum shear modulus as that of the soil layer above the boundary.

The soil column is similar to that at Station 7 of the El Centro Strong Motion Array in Imperial Valley, California. The soil is assumed to behave nonlinearly and the variation of shear modulus and shear strength are as shown in Fig. 4.3. Further details regarding the site can be found in Chen (1985). The selection of a one-dimensional deposit eliminates any influences that might arise from the inclusion of lateral boundaries.

The horizontal input motion for the TARA-3 analysis is the reversed spike with a duration of 3.0 seconds (Fig. 4.4). The input motion consists of two parts; the first part is

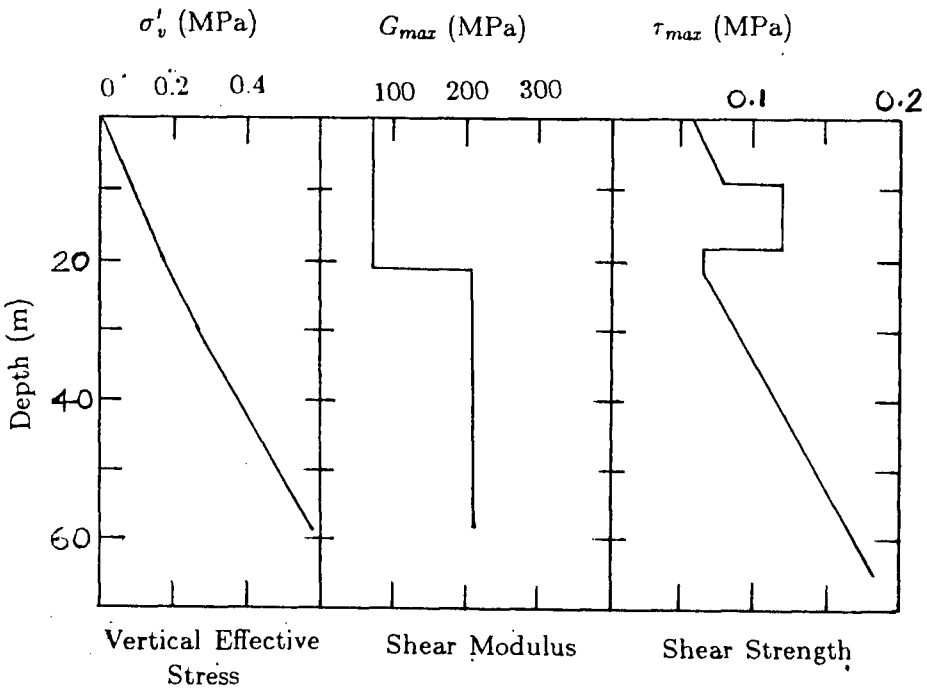

Fig. 4.3 Soil Property Profile

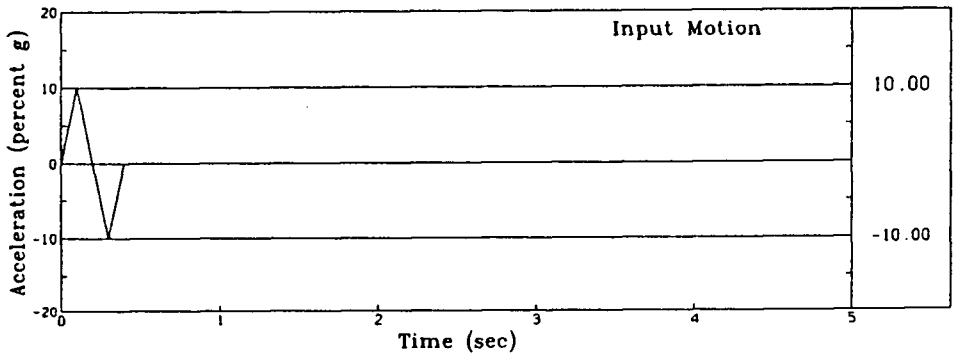

Fig. 4.4 Reversed Spike Input Motion

the reversed spike scaled to a peak acceleration value of 10.0%g with duration of 0.4 seconds and the peaks of the spike occurring at times 0.1 and 0.3 seconds; the second part consists of zero input from time 0.4 seconds up to 3.0 seconds.

The soil column was analysed using TARA-3 with the nonlinear analysis option in the total stress mode. The results for the case of the rigid base are shown in Fig. 4.5, which shows the computed surface acceleration response and the input motion. The input acceleration is amplified on passage to the surface by a factor of 1.37. The effects of wave reflection from the rigid base are clearly evident in Fig. 4.5. Three distinctly different parts can be identified in the surface acceleration response. First, there is a time lag of about 0.18 seconds. Second, the big cyclic pulse starting at about time 0.18 seconds and extending to 0.78 seconds which corresponds to the reversed spike of the input motion. Finally, there is the considerable surface response in the time range from about 0.78 seconds to 3.0 seconds during which the input motion is zero. This response can be attributed to the effect of multiple reflections from the rigid boundary of incident waves reflected from the free surface. At successive reflections, the wave amplitudes are being attenuated slowly by viscous and hysteretic damping in the soil and, as a result, the surface response decays with time.

The soil column was also analysed using an energy transmitting base. The results are shown in Fig. 4.6. Results for the rigid base are shown for the purpose of comparison. In constrast to the rigid base response, the surface motions in this case diminish rapidly with time after the input motions ceases. This clearly indicates that very little wave reflection from the base occurs in the case of the transmitting base. The little reflections found in the case of transmitting base are due to the fact that there is constrast in rigidity between the soil layers within the deposit.

This example shows that the energy transmitting base incorporated in TARA-3 is very

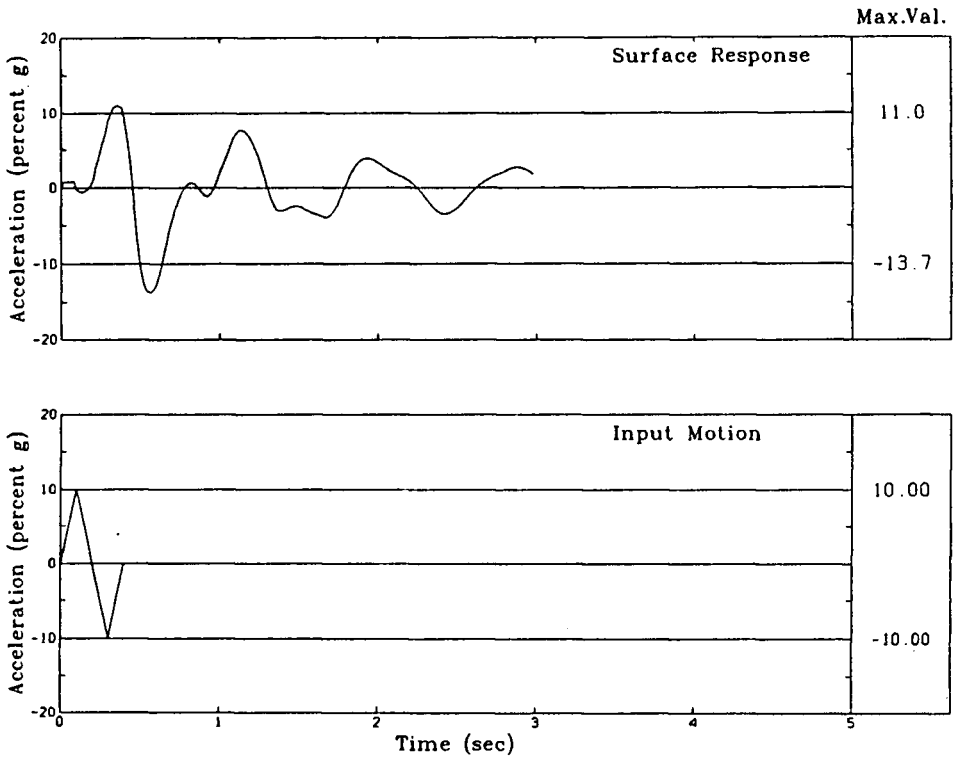

Fig. 4.5 Surface Acceleration Response With Rigid Base

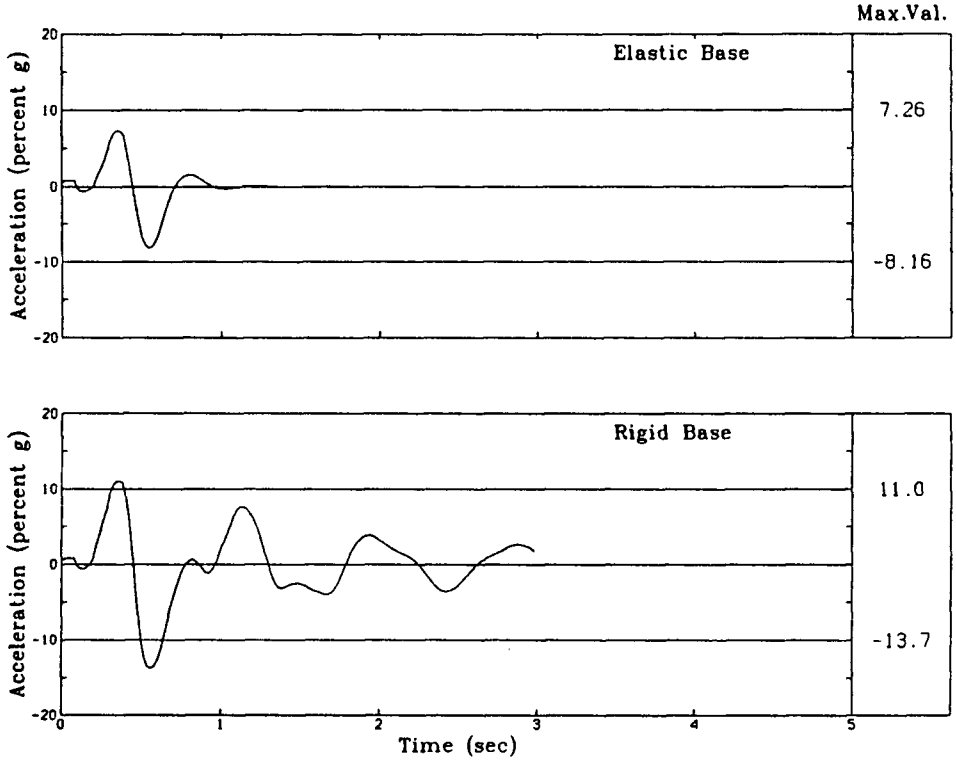

Fig. 4.6 Surface Acceleration Responses With Rigid and Elastic Bases

effective in simulating the energy radiation into the underlying medium.

4.7 Effectiveness of the Lateral Viscous Boundary

The soil-structure interaction problem shown in Fig. 4.7, involving a stiff elastic structure on a dry sand foundation, was selected to demonstrate the effectiveness of the lateral viscous boundary. The material properties of the structure and the sand foundation are given in Table 4.1.

Table 4.1 Properties Selected for the Example Problem

Property	Structure	Foundation Soil
Unit Weight (pcf)	400.0	120.0
Shear Modulus (psf)	1.6×10^9	$K_{2max} = 51.0$
Bulk Modulus (psf)	3.5×10^9	$K_b = 800.0$
Bulk Modulus Exponent	-	0.40
Poisson Ratio	0.30	-
Angle of Internal Friction	-	35.0
Cohesion	-	0.0
Damping Coefficient, α	0.0	0.0
Damping Coefficient, β	0.005	0.005

For TARA-3 analysis, a horizontal computational boundary is imposed at a depth 5B below the base of the structure, where B is the width of the structure. The base was assumed to be rigid. Lateral boundaries are placed at various distances from the structure.

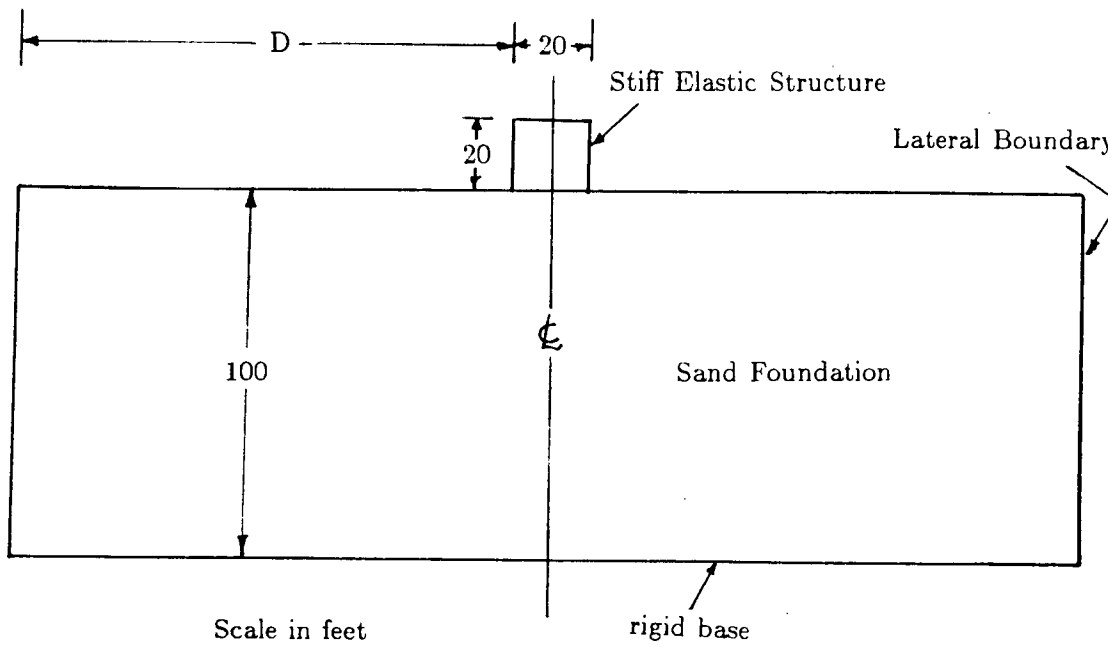

Fig. 4.7 Soil-Structure Interaction Problem

The TARA-3 analyses were conducted assuming both linear and nonlinear soil response.

The horizontal input motions applied at the base correspond to the first 3 seconds of the 1940 El Centro, S00E horizontal acceleration record, scaled to 10.0%g peak acceleration. The free field relative velocities required for the lateral viscous boundary were computed using TARA-3 with a finite element discretization in the vertical direction consistent with that of the soil-structure problem.

4.7.1 Linear Analysis

The peak free field accelerations computed by TARA-3 for the case of linear analysis is shown in Table 4.2.

Table 4.2 Linear Analysis: Free Field Peak Accelerations

Depth (ft)	Acceleration (%g)
0.00	26
20.0	22
40.0	16
60.0	13
80.0	11
100.0	10

The distribution of peak accelerations when horizontal roller boundaries are placed at distance D=20B, where D is the distance between the boundary and the edge of structure, is shown in Fig. 4.8. The values at the grid intersection are the peak horizontal accelerations

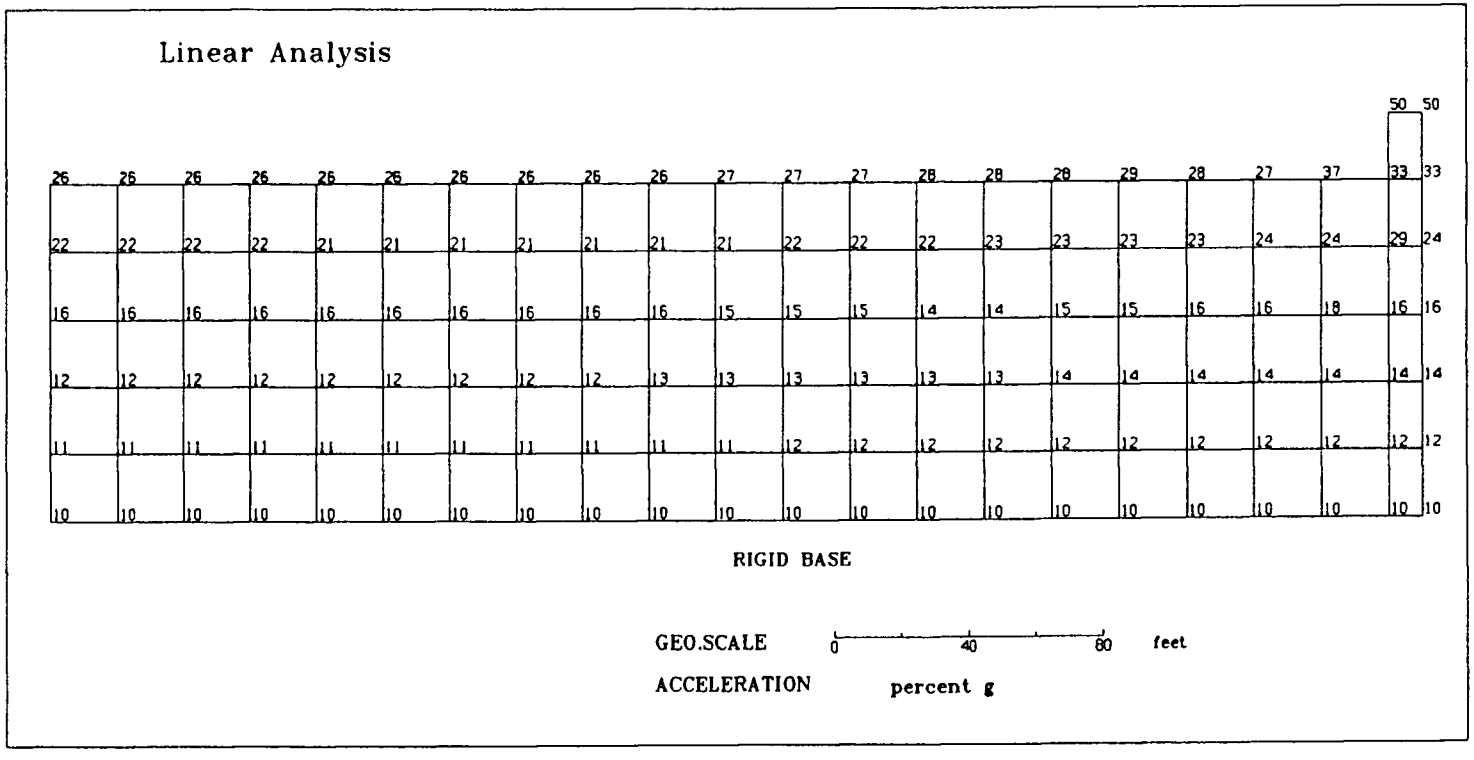

Fig. 4.8 Linear Analysis - Distribution of Accelerations When Roller Boundaries are at D=20B

in %g. It should be noted that the results are quoted only for the region on the left hand side of the centerline of the model. The accelerations at locations far away from the edge of the structure are close to those of free field and do not vary much with distances from the structure. This indicates that true free field conditions are achieved in the wider region bounded by the boundary and the vertical grid at a distance around 10B. Therefore, these results can be assumed to be "correct" responses and consequently be used to assess the effectiveness of other boundary conditions.

Fig. 4.9 shows the acceleration distribution for the case when horizontal roller boundaries are placed at distance D=10B. Accelerations at the boundary and at locations near to the boundary are close to those of free field given in Table 4.2. Further, the accelerations at locations on and closer to the structure are still similar to the corresponding accelerations when the boundaries were at distance D=20B. The differences are within a few percent. For instance, at top center point of the structure, the acceleration is only 2% different when the boundary is at D=10B.

The results for the case when horizontal roller boundaries are situated at distance D=4B are shown in Fig. 4.10. These results are significantly different from the "correct" response. The deviations in acceleration, particularly at locations on and closer to the structure, are higher than the corresponding deviations when the boundaries were located at D=10B. For instance, the difference in acceleration at top center point of the structure is now around 10%.

The results clearly indicate that the responses are strongly dependent on distance D. As D is changed, the natural periods that contribute strongly to the resposne are changed resulting in quite different responses. For a given problem, the choice of D depends on the degree of accuracy desired. In this case, for practical purposes, the boundary could be placed at distances not less than 4B.

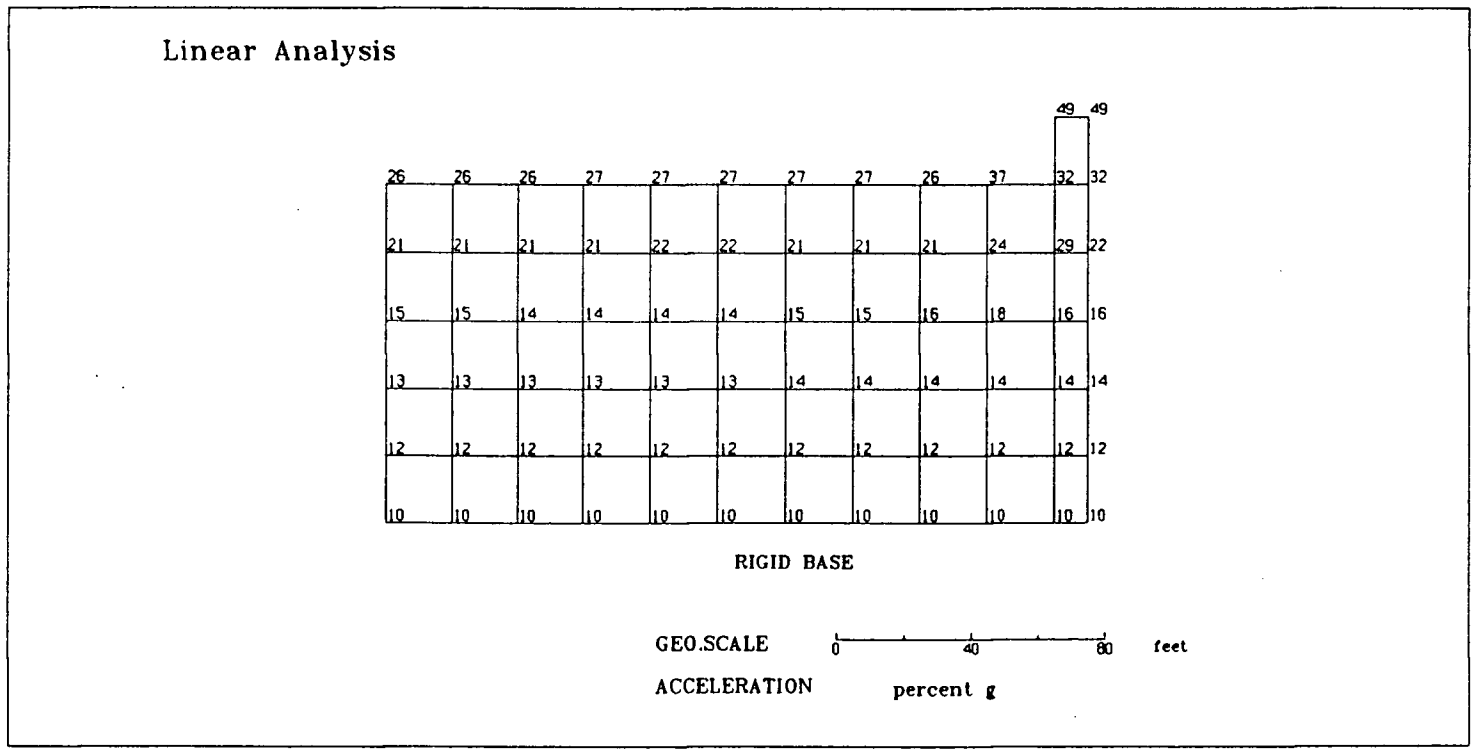

Fig. 4.9 Linear Analysis - Distribution of Accelerations When Roller Boundaries are at D=10B

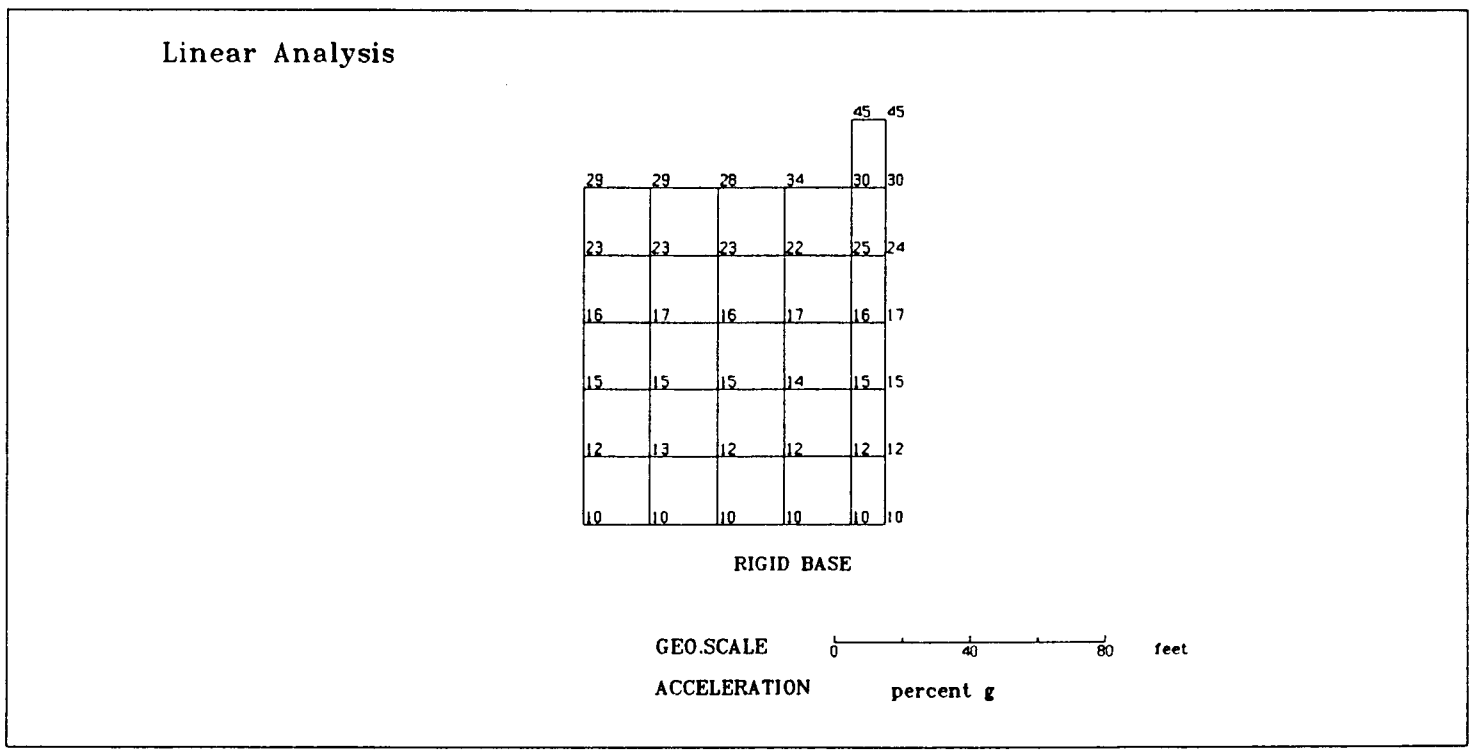

Fig. 4.10 Linear Analysis - Distribution of Accelerations When Roller Boundaries are at D=4B

Fig. 4.11 shows horizontal acceleration distribution when viscous boundaries with constant dashpot properties are placed at distance D=20B. The accelerations at locations far away from the edge of the structure are close to those of the free field. The computed accelerations at locations on and closer to the structure are similar to the corresponding responses when horizontal roller boundaries are in place.

However, as shown in Fig. 4.12, when the viscous boundaries are at D=10B, the acceleration response particularly at locations on and closer to the structure are quite different than the corresponding response when D=20B. At top center point of the structure, the acceleration is underestimated as much as 14%.

Marked differences are noticeable when the viscous boundaries are located at distance D=4B as shown in Fig. 4.13. Structural responses are underestimated. For instance, at top center point on the structure, the horizontal acceleration is underestimated as much as 16%. Similar differences are also noticeable in the case of responses at locations closer to the structure.

Therefore, for elastic analysis the roller boundary seems preferable than the viscous boundary.

4.7.2 Nonlinear Analysis

The peak free field acceleration responses assuming the nonlinear soil behaviour are presented in Table 4.3. They are slightly less than the values in Table 4.2. This is due to the fact that additional inherent hysteretic damping is present in the nonlinear case.

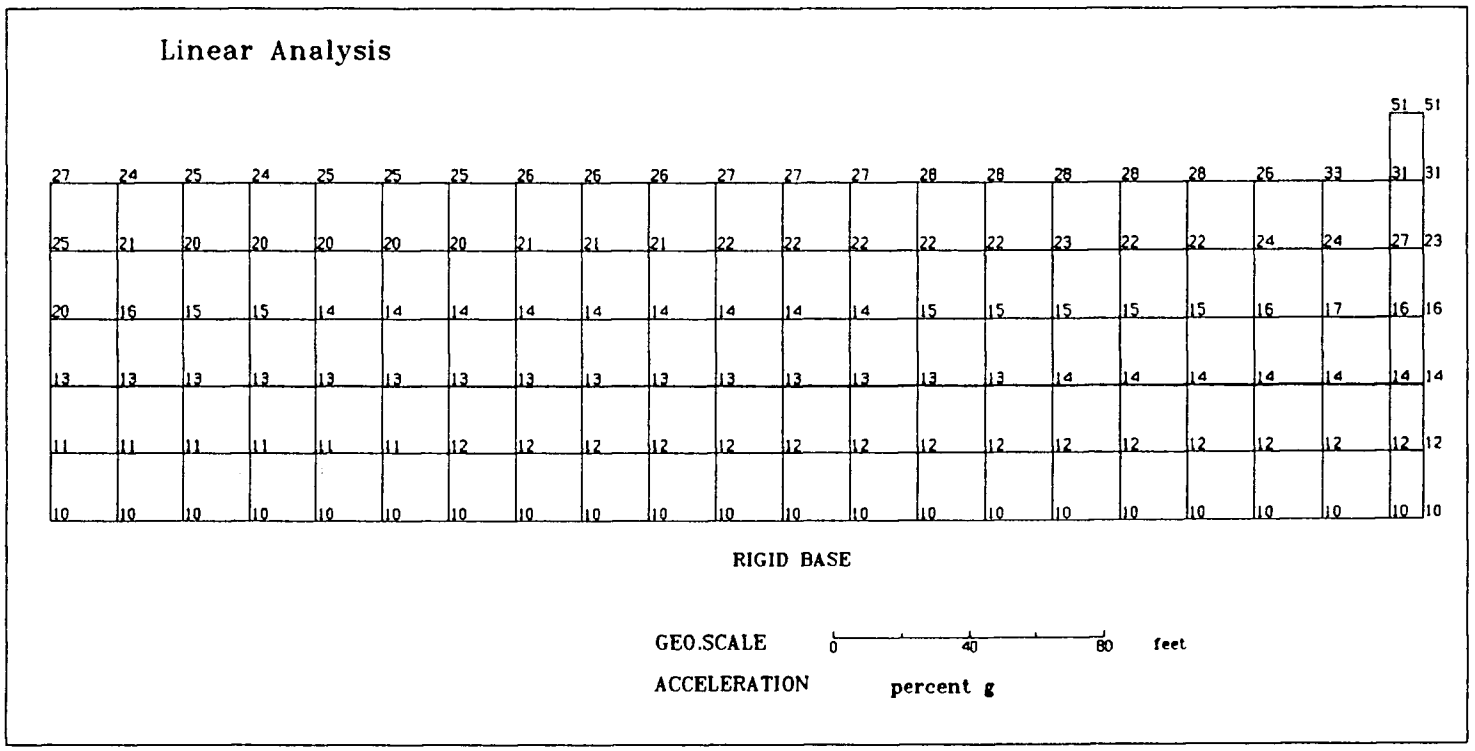

Fig. 4.11 Linear Analysis - Distribution of Accelerations When Viscous Boundaries are at D=20B

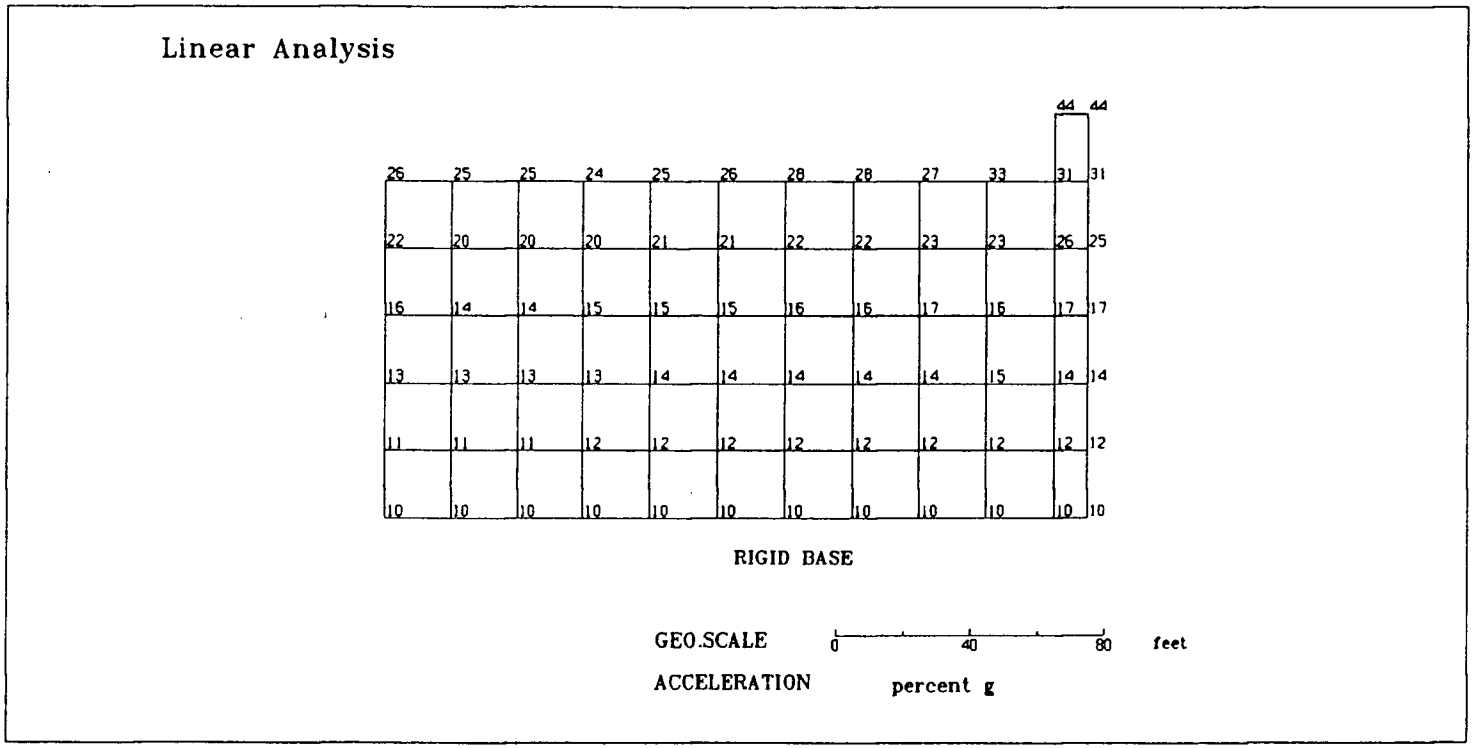

Fig. 4.12 Linear Analysis - Distribution of Accelerations When Viscous Boundaries are at D=10B

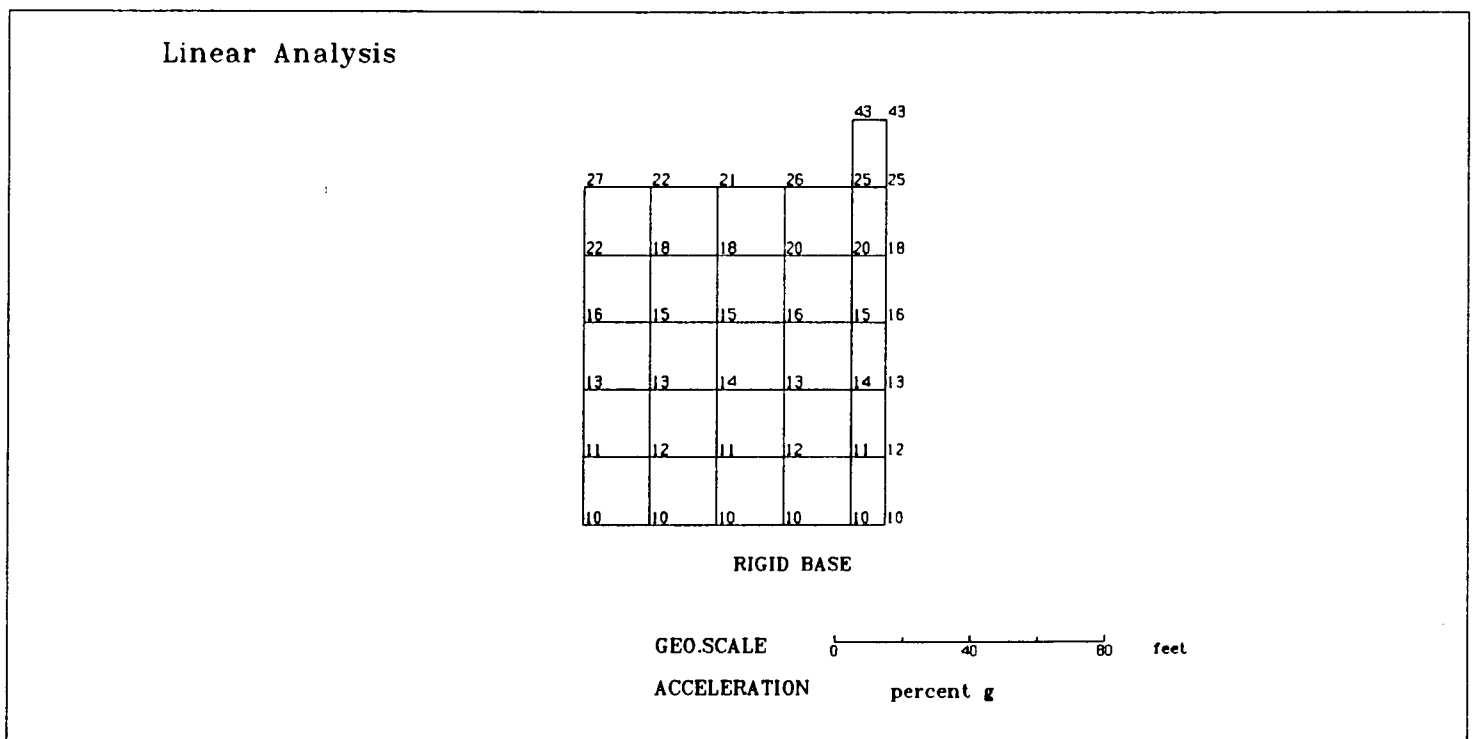

Fig. 4.13 Linear Analysis - Distribution of Accelerations When Viscous Boundaries are at D=4B

Table 4.3 Nonlinear Analysis: Free Field Peak Accelerations

Depth (ft)	Acceleration (%g)
0.00	22
20.0	19
40.0	15
60.0	14
80.0	12
100.0	10

Fig. 4.14 shows the horizontal acceleration responses when horizontal roller boundaries are placed at distance D=20B. As in the case of linear analysis, the response computed at locations far away from the structure are close to those of the free field. Fig. 4.15 shows the acceleration response when the horizontal roller boundaries are located at distance D=10B. It is clearly seen that at locations close to the boundary free field conditions are achieved. Also, the structural response is similar to those when D=20B.

However, as may be seen form Fig. 4.16, the structural responses for the case D=4B are somewhat underestimated. For instance, at top center point on the structure, the acceleration is 10% smaller than the corresponding value when D=20B.

Fig. 4.17 shows results obtained when viscous boundaries with constant dashpot properties are placed at distance D=20B instead of roller boundaries. The structural responses in both cases are within very few percent.

As seen from Fig. 4.18, when the viscous boundaries are at D=10B, structural response is close to that when D=20B. However, the acceleration values computed at locations on

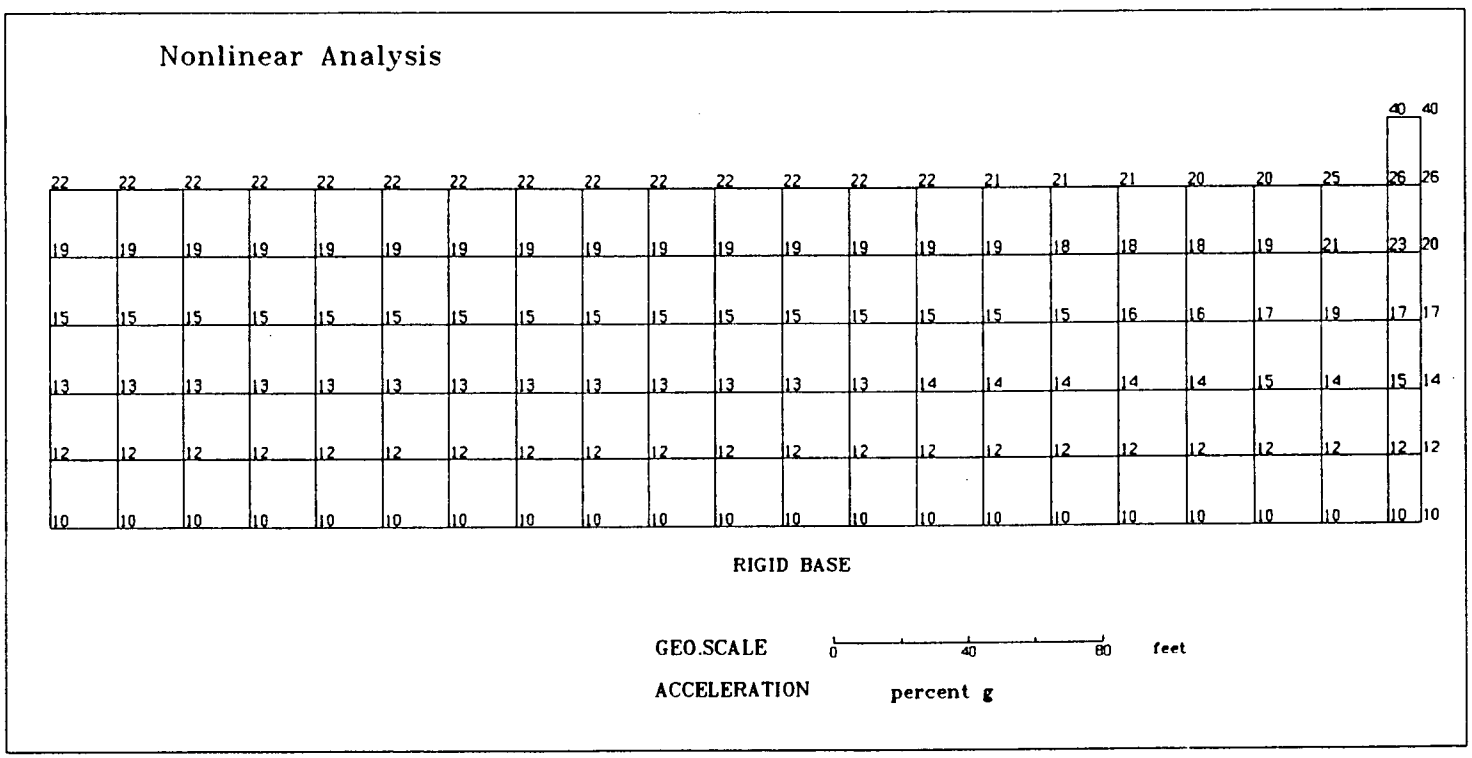

Fig. 4.14 Nonlinear Analysis - Distribution of Accelerations When Roller Boundaries are at D=20B

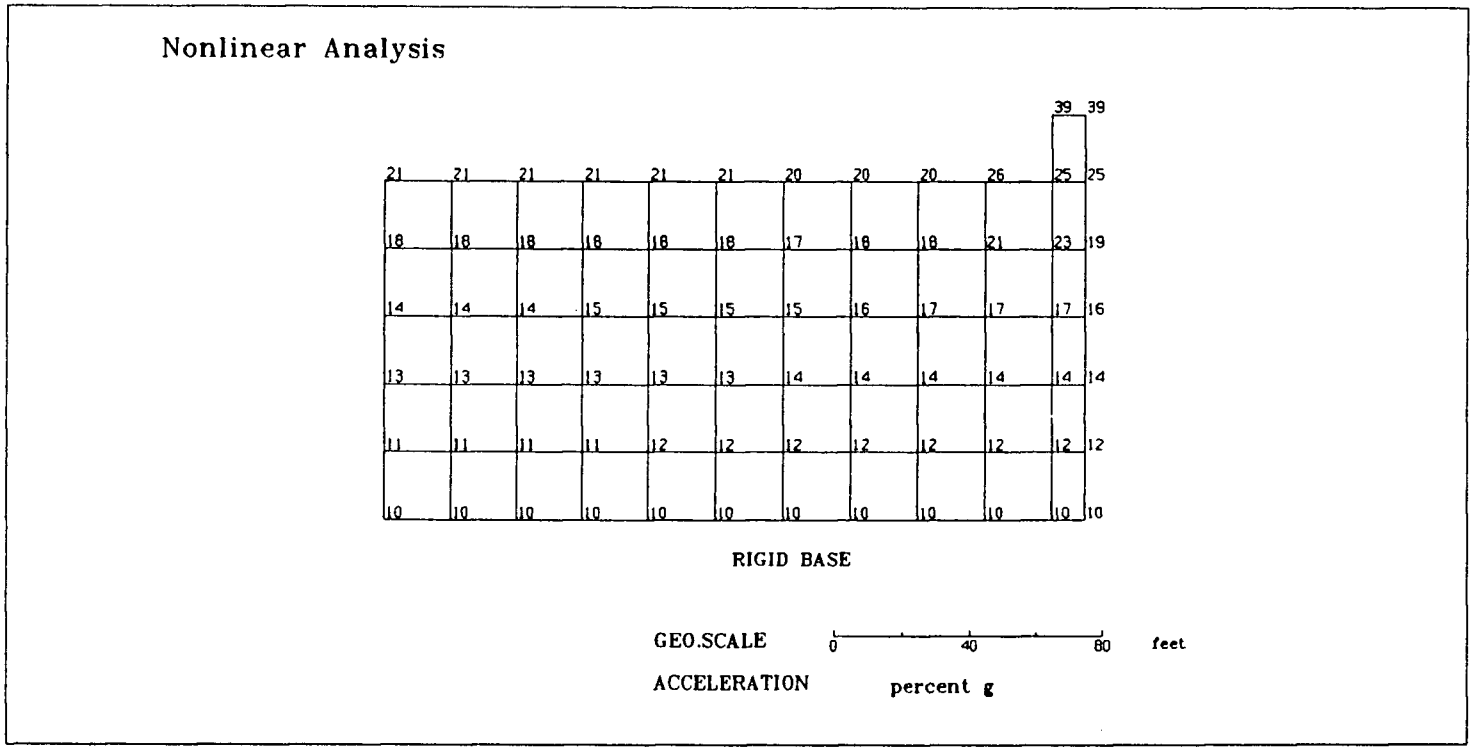

Fig. 4.15 Nonlinear Analysis - Distribution of Accelerations When Roller Boundaries are at D=10B

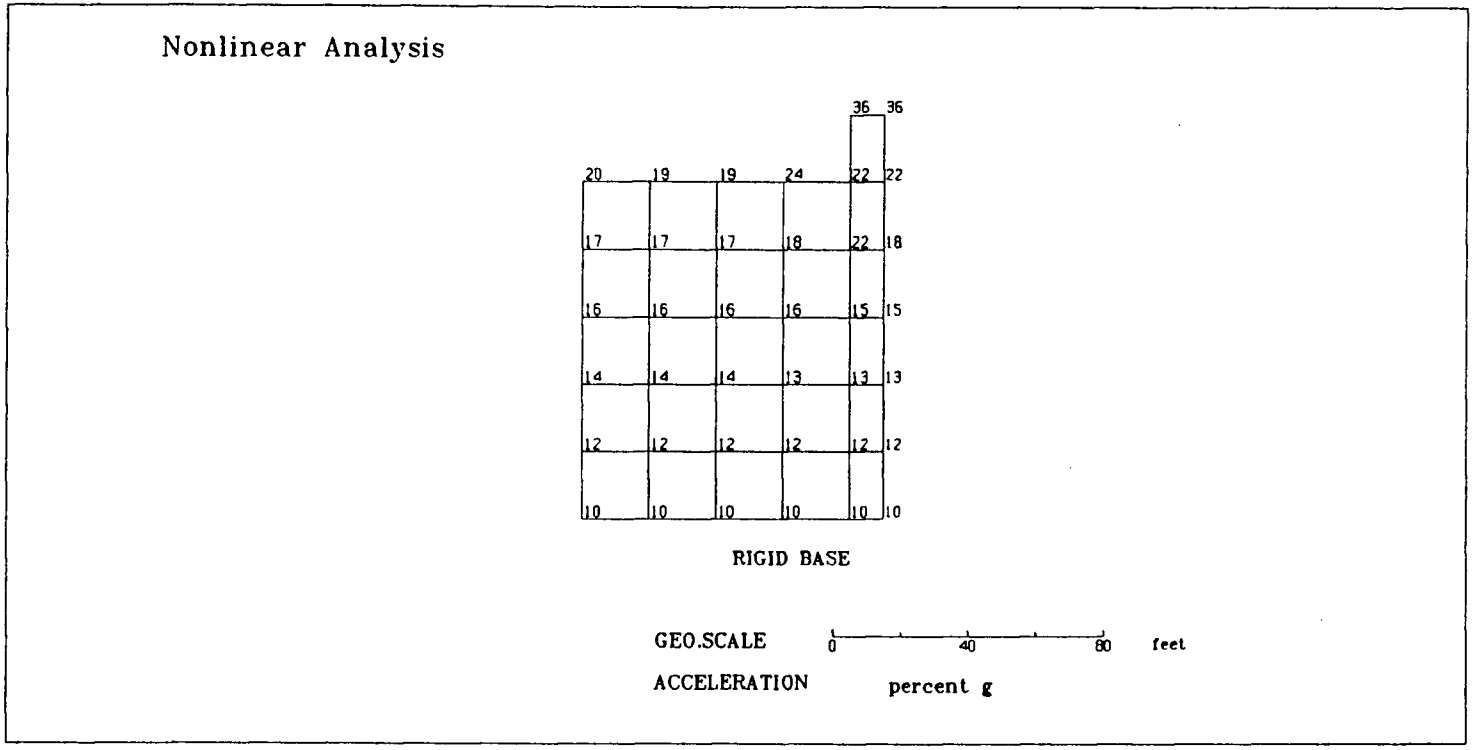

Fig. 4.16 Nonlinear Analysis - Distribution of Accelerations When Roller Boundaries are at D=4B

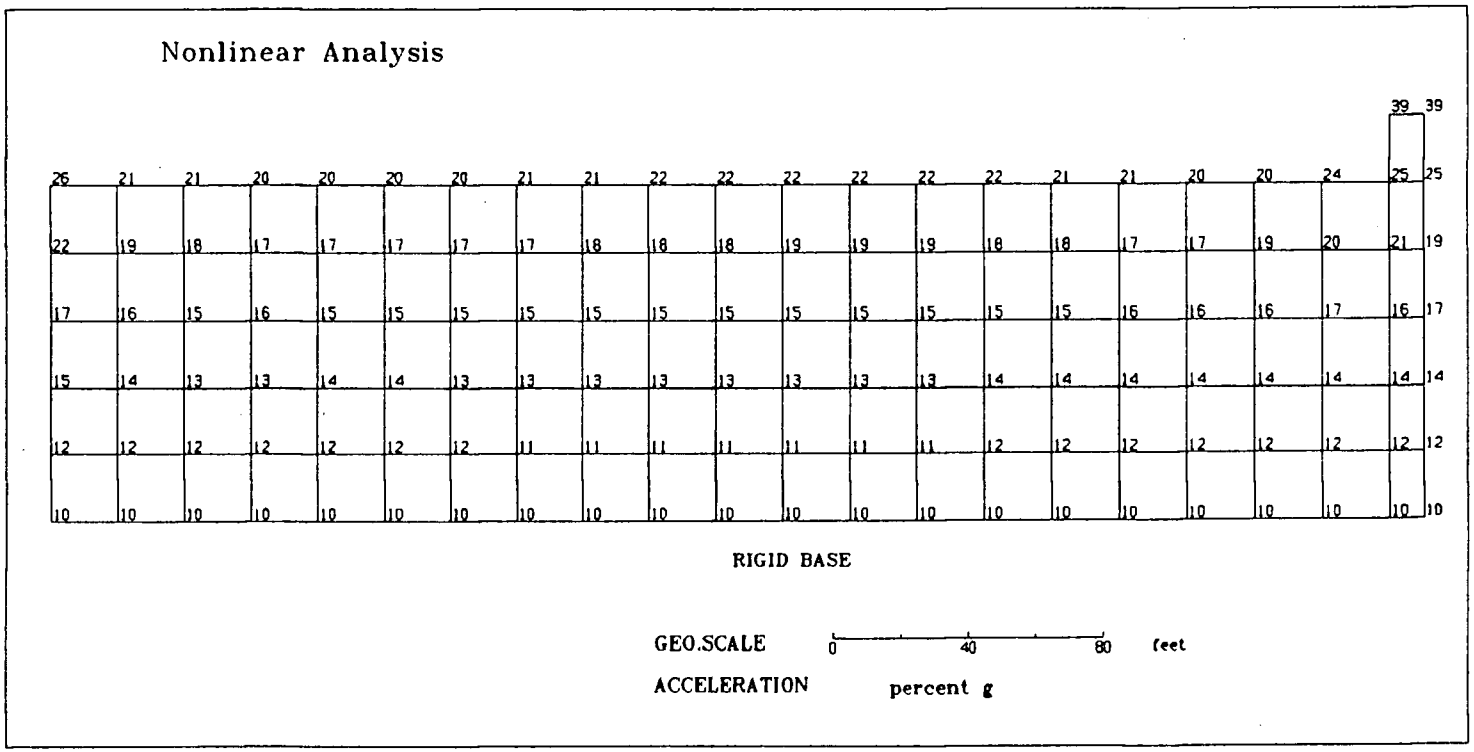

Fig. 4.17 Nonlinear Analysis - Distribution of Accelerations When Viscous Boundaries are at D=20B

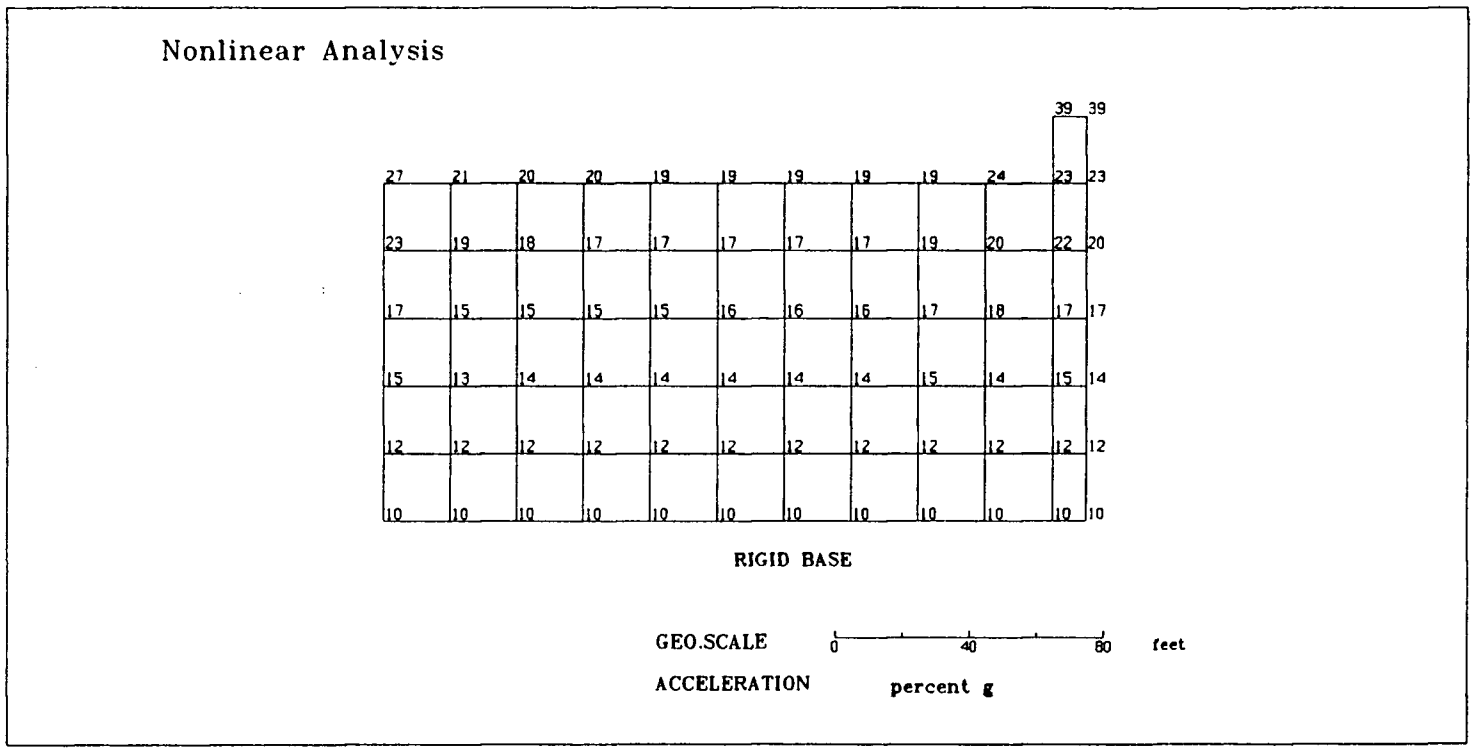

Fig. 4.18 Nonlinear Analysis - Distribution of Accelerations When Viscous Boundaries are at D=10B

the boundary are greater than that of the corresponding free field response values. This may be due to disturbances caused by incomplete absorption of the surface waves and to some extent the body waves. As the depth increases, the acceleration values become closer to the corresponding free field values.

The distribution of accelerations when viscous boundaries are placed at distance D=4B is shown in Fig. 4.19. The structural response in this case shows that the difference in acceleration at top center point on the structure is now only 5.1%.

4.7.3 Discussion

The results in both linear and nonlinear analysis clearly reveal that the responses of the soil-structure system depend on the distance D and the type of boundary conditions. However, the effect of boundary distance is much more significant in the linear than in the nonlinear case because of the greater damping in the latter case. In both cases, the results show that satisfactory results can be obtained using viscous or roller boundaries provided that they are located at an appropriate distance from the edge of the structure. The minimum distance for the nonlinear case seem to be 4B and for the linear case a minimum distance somewhat greater than 4B seems to be appropriate.

In the linear case, the results reveal that the roller boundaries perform better than the viscous boundaries with respect to structural response. Also, in the nonlinear case, except for the case when D=4B, the roller boundary performs better than the viscous boundary. Therefore, the use of roller boundary is preferable. The roller boundary not only performs more efficiently but also requires less effort in data preparation and computer cost.

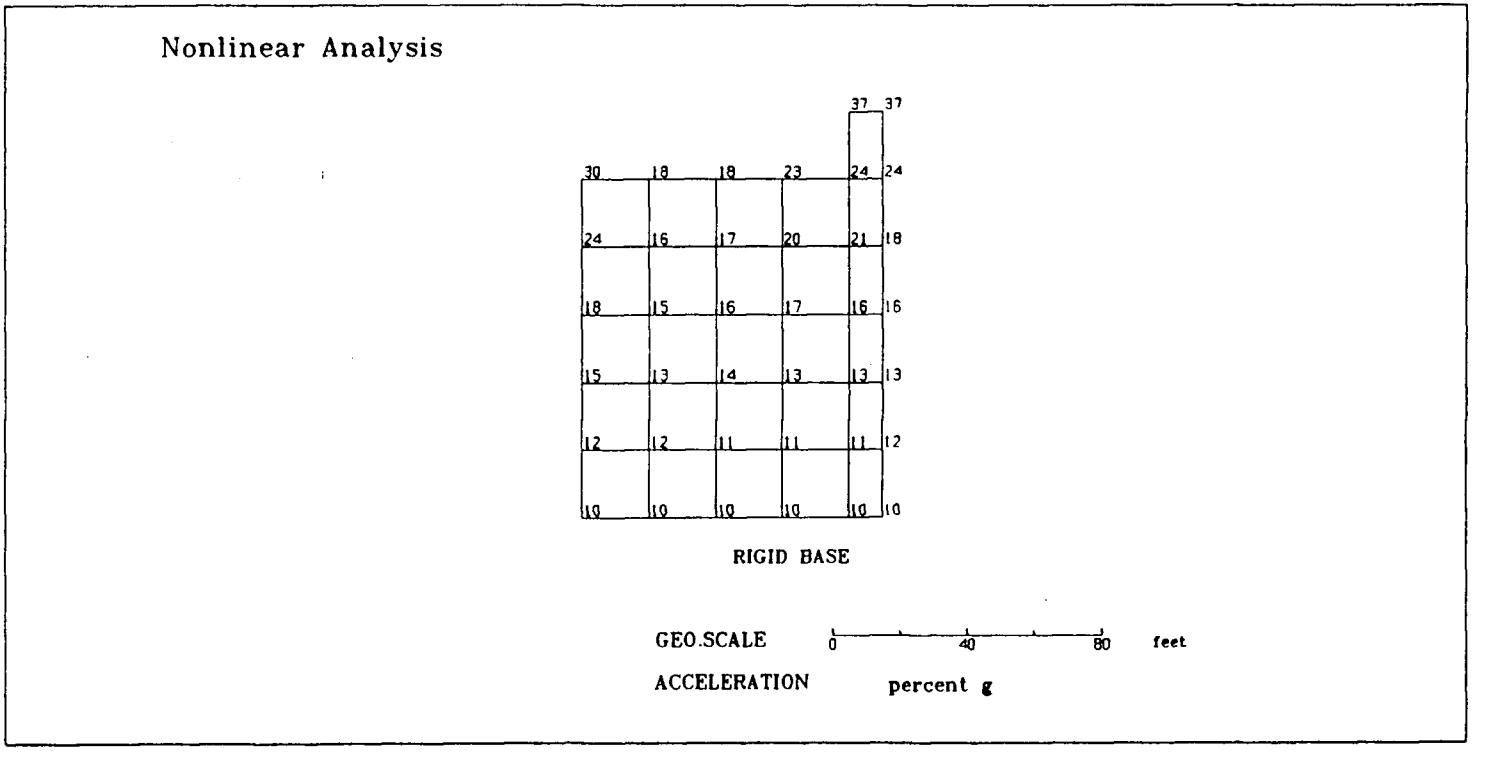

Fig. 4.19 Nonlinear Analysis - Distribution of Accelerations When Viscous Boundaries are at D=4B

CHAPTER 5

SIMULATED SEISMIC TESTS ON CENTRIFUGE

5.1 Introduction

At present, only simulated seismic tests on centrifuge models can provide the flexibility and cost effectiveness necessary to provide a data base against which concepts of response to loading and methods of seismic analyses can be checked. Data from simulated seismic tests on centrifuge models of simple 1-D system (Abghari 1983; Lambe and Whitman 1985) and pile foundations (Finn and Gohl 1987) have been used successfully to verify methods of numerical analyses. This chapter deals with the important aspects of the simulated seismic tests that were conducted on various centrifuged models to generate data to explore the capacity of TARA-3 to model soil structure and soil-structure interaction problems. These models include both dry and saturated embankments, and surface and embedded gravity structures on both dry and saturated sand foundations. All tests were conducted on the Cambridge University Geotechnical Centrifuge in the United Kingdom by Dean and Lee (1984) and Steedman (1985 and 1986) under the general direction of Professor A.N. Schofield. The tests were sponsored by the United States Nuclear Regulatory Commission through the United States Army Corps of Engineers (USAE) and were monitored by Professor W.D. Liam Finn on behalf of the U.S Army Corps of Engineers. The tests were

designed jointly with the collabaration of the University of British Columbia, the Cambridge University and the USAE to ensure the rigorous evolutionary testing of the capability of TARA-3.

The subsequent sections describe briefly a review of centrifuge testing and test procedures in Cambridge Geotechnical Centrifuge. Detailed descriptions can be found elsewhere (Schofield, 1981).

5.2 Centrifuge Testing

In a centrifuge, the same unit stresses that exist in a full-scale structure can be reproduced at corresponding points in a small scale model by rotating the model around the axis of the centrifuge to create an artificial gravity field, Ng, where g is the acceleration due to the earth's gravity and $1/N$ is the linear scale of the model. The ability to create prototype stresses in the model is important in studies of soil-structure interaction since many soil properties are dependent on effective stresses. For this reason, seismic tests on a centrifuge are superior to those conducted on a shaking table in 1g environments. Since all stresses at each point in a centrifuged model can, in theory, be made the same at the corresponding point in the prototype, each element of soil can be expected to undergo the same response to loading as corresponding elements in the prototype (Barton, 1982). Since each model is of finite size, different parts of the model are at different radii from the rotational axis of the centrifuge. Therefore, at any given speed of the centrifuge arm, different parts of the model will be subjected to different gravitational intensities. This results in a stress difference at corresponding points in the model and the prototype. The stress difference will be small if the space that the model occupies in the direction of the centrifuge arm is small compared to the radius of the centrifuge arm. For example (as illustrated by Schofield 1981) for a model that extends for a radial distance of one tenth of the centrifuge radius,

the error in vertical pressure within the model in the Cambridge Geotechnical Centrifuge is typically around $\pm$ 2%. Errors of this magnitude are certainly within the acceptable range of accuracy in the engineering profession.

5.3 Scaling Laws

Scaling laws for the centrifuged models have been reported for granular media by many researchers (Roscoe, 1968 and Scott, 1978). A summary (Scott 1978) is given in Table 5.1.

Table 5.1 Scaling Relations

Quantity	Full Scale	Model at N g's
Linear Dimension	1	$1/N$
Area	1	$1/N^2$
Volume	1	$1/N^3$
Stress	1	1
Strain	1	1
Force	1	$1/N^2$
Acceleration	1	N
Velocity	1	1
Time - In Dynamic Terms	1	$1/N$
Time - In Diffusion Cases	1	$1/N^2$
Frequency in Dynamic Problems	1	N

In a $1/N$ linear scale model, excess porewater pressures dissipate N^2 times faster in the

model than in the prototype if the same fluid is used in both. The rate of loading by seismic excitation will be only N times faster. Therefore, to model prototype drainage conditions during the earthquake, a pore fluid with a viscosity N times the prototype viscosity must be used. Commercial silicon oil blended to the appropriate viscosity is often used as pore fluid in centrifuge model tests.

Saturated tests of centrifuged models for the verification study of TARA-3 were carried out using silicon oil as pore fluid (Dean and Lee, 1984 and Steedman, 1985 and 1986). Triaxial tests by Eyton (1982) showed that the stress-strain behavior of fine sand was not changed when the silicon oil was substituted for water as pore fluid. Centrifuge model tests conducted at different linear scale ratios (40 and 80) also indicated that the responses were not changed when silicon oil was used as pore fluid.

5.4 Earthquake Simulation in Cambridge Geotechnical Centrifuge

The Cambridge centrifuge has a 10m long rotor arm driven by a 225kW motor. The effective radius of the centrifuge is around 4m. The centrifuge is housed in a reinforced concrete chamber of diameter slightly larger than 10m.

In general, earthquake simulation in a centrifuged model is accomplished through the use of some form of a shaking system. There are many designs of shaking systems available, each of which has its own advantages and disadvantages (Arulanandan et al, 1984). The system that is currently adopted in the Cambridge centrifuge is a mechanical type. Seismic excitations are generated by a wheel linked to the model container travelling on a track with precisely machined sinusoidal undulations attached to the wall of the centrifuge chamber. The track extends over one third of the circumference of the centrifuge chamber. The system is known as the bumpy road. A model earthquake involves a single pass of the actuating wheel along the bumpy road track. The intensity of model shaking is controlled

by adjusting the linkage between the wheel and model container. For a given bumpy road configuration, the frequency of oscillation is governed by the angular velocity of the rotor arm.

Ideally, the bumpy road should generate a model earthquake that is sinusoidal in nature with a constant period. However, the actual motion is much more complicated mainly due to resonances, mechanical linkage clearances and other factors, and as a result it has a broader frequency range. A typical model earthquake consists of three important components (Dean and Lee, 1984):

(1) Small "wheel-on" accelerations associated with initial contact of the wheel with the track;

(2) the model earthquake proper consisting of roughly sinusoidal pulses;

(3) small "wheel-off" accelerations associated with the wheel leaving the track.

In the bumpy road system, it is difficult to obtain precisely the earthquake motions one wants. Often the linkage adjustments between the wheel and the model container produce earthquakes of very small amplitudes. Therefore, in order to obtain earthquake motions of significant amplitudes, a series of earthquakes is initiated and each time the linkage is adjusted so as to produce earthquakes of greater amplitudes.

5.5 Model Construction

The models were constructed in a container whose exterior dimensions are 902mm long, 481mm wide and 225mm deep. Overflow troughs are provided to take excess soil should a failure occur.

Leighton Buzzard sand was used in the construction of all centrifuged models. For most tests, sand passing through British Standard Sieve No. 120 and retained by B.S.S No. 200

(B.S.S 120/200) was used. The aperture sizes of these two sieves are 0.125mm and 0.075mm respectively. For the remaining tests, Leighton Buzzard B.S.S 52/100 sand was used. The properties of each of these sands are given in Table 5.2.

The standard sand was chosen to minimize the potential variability of model properties and it is not intended to model any real in-situ conditions. The model tests are not being used to simulate specific real type prototypes but to provide data for the direct verification of the program TARA-3.

Table 5.2 Properties of Model Sand

Sand Type	G_s	e_{min}	e_{max}	Mean Grain Size (mm)
B.S.S 52/100	2.65	0.585	0.928	0.225
B.S.S 120/200	2.65	0.650	1.025	0.100

5.5.1 Dry Model Construction

The dry models were constructed to a uniform density by allowing sand to fall through a fixed height. Aluminum formworks were first fitted inside the model container to guide construction. A hopper, fitted with a nozzle, containing a known weight of dry sand was suspended at an appropriate height above the base of the container. The nozzle and the height of drop required to give a specified relative density was determined by calibration tests in advance of the construction. The hopper valve was opened and the nozzle was moved slowly over the area of construction so that the sand surface rose roughly at the same rate over the entire area. As the surface level rose, the hopper was raised so as

to keep its height above the sand surface approximately constant. Pouring of the sand was temporarily stopped whenever transducers were installed. Leads were carefully laid and attached to the side of the container in such a manner to avoid tensioning or jerking of leads during the flight. Before placement of the structure, the top sand surface was levelled by vacuuming. For embedded structures, pouring of the sand continued around the structure to the required design profile. The transducers were then mounted at appropriate places on the structure. Once pouring was complete, the top sand surface was levelled and measurements were taken to define the actual surface. The formworks were removed and the roof of the container was then bolted on.

5.5.2 Saturated Model Construction

Two different techniques of saturated model construction were employed. The first method (Method 1) involves pluviating de-aired sand/oil mixture through de-aired silicon oil. Under these conditions, it was difficult, to maintain uniform density, to determine relative density and to specify accurately the transducer locations. Therefore, a new construction technique (Method 2) was adopted in the later tests. This involves placing the sand dry as described above and then saturating it slowly under a high vacuum. Each of the methods is discussed briefly in the subsequent sections.

5.5.2.1 Method 1

A sufficient quantity of silicon oil at appropriate viscosity was de-aired under a vacuum of 27-30 inches of mercury for a period of 24 hours. The model container with the aluminum formworks in place was then filled with the de-aired silicon oil.

Sufficient mass of dry sand was weighed and placed in a small dessicator. Silicon oil was then added to cover the sand surface and was thoroughly mixed with the sand. The

mixture was placed under vacuum for 1/2 hour. The sand/oil mixture was tranferred to the model container using a small beaker. The beaker was inverted beneath the surface of the oil in the container to prevent the entrapment of air and the sand was allowed to pluviate through the oil. On removal from the model container, a beaker full of silicon oil was transferred back to the dessicator. During the pouring process, the beaker was moved slowly over the area of construction in order to achieve equal rate of rise of surface at all points. At appropriate levels, transducers were placed. The porewater pressure transducers were also placed under the vacuum. The accelerometers were coated with a thin layer of silicon rubber as a seal. Once pouring was complete, the formworks were removed. The soil profile was surveyed and the roof of the container was bolted on.

During the deposition process, the silicon oil in the container became very murky as some sand remained in suspension. This made it difficult to see how the model was progressing. Also the sand surface was very soft which posed problems for the installing transducers.

5.5.2.2 Method 2

In this technique, the model is constructed first using dry sand as described in section 5.5.1. Once the dry model construction was completed, the model container was sealed. The container was then evacuated to a vacuum of 28-30 inches of mercury. Silicon oil, de-aired under a similar vacuum, was slowly introduced at both ends of the model. The vacuum was maintained until the oil was up to the desired level. Then, the vacuum was slowly released and the model container was unsealed.

5.6 Relative Density Estimation

Estimates of average relative density of each model were made from estimates of the volume and mass of sand in the model. The void ratio e and relative density D_r (in percentage)

of the models were then calculated from :

$$e = G_s\,(V/M) \;-\; 1 \tag{5.1}$$

$$D_r = 100.0\;[(e_{max} - e)\;/\;(e_{max} - e_{min}] \tag{5.2}$$

where G_s is the specific gravity of the sand, V is the model volume, M is the mass of the sand, e_{max} is maximum void ratio and e_{min} is minimum void ratio.

Errors in the calculation of void ratio arise from inaccuracies of the balance used to weigh the model container and errors in volume measurement. The compounded error from these two sources is of the order of ± 2%. This leads to a possible error of up to ± 10% in relative density (Dean and Lee, 1984). However, for saturated models constructed using Method 1, the error can be much greater especially because of migration of sand into the overflow troughs during construction. An unknown amount of fines also remained in suspension in the oil.

5.7 Instrumentation and Accuracy

The models were instrumented with accelerometers, porewater pressure transducers and linearly variable displacement transducers designated ACC, PPT and LVDT respectively. The number of transducers used in a test was limited by the number of channels available in the data acquisition system and the size of the model.

5.7.1 Accelerometers

Miniature piezo-electric DJB A23 type accelerometers supplied by D.J. Birchall Ltd., Cheltenham, England, were used in the model tests. The frequency response is flat to above 10 kHz. The accuracy of calibration is about ± 4% of the measured values (Dean and Lee,

1984). Besides calibration accuracy, a number of operating factors also affects the accuracy of measured response.

The piezo-electric accelerometers respond sharply to sudden increases in tension in leads giving the appearance of spiky high frequency response. In order to minimize the effect of lead tension, leads were laid perpendicular to the direction of shaking as shown in Fig. 5.1.

Since accelerometers are capacitive devices, any lead bending may affect the capacitance of the leads and consequently alter the measurement.

A poor earth connection can cause the signals to "float" about its base line. Often, it is possible to correct data using simple digital techniques. However, even if corrected, some error is likely to remain.

Taking all these factors into account, Dean and Lee (1984) concluded that the overall accuracy of the accelerometer is believed to be in the order of $\pm$ 5% of the measured values.

5.7.2 Porewater Pressure Transducers

Porewater pressures were measured using PDCK 81 type porewater pressure transducers, supplied by Druck Ltd., Leicester, England. A silicon integrated pressure sensor forms the diaphragm of the device. The calibration accuracy for these transducers is about $\pm$ 5% of the measured values (Dean and Lee, 1984).

In order to register pressure, the transducer requires a small but finite volume of fluid to flow into and out of it. This volume has to be provided by the surrounding soil. Kutter (1983) has found that in saturated clays the required flow causes negligible measurement inaccuracies and has a negligible effect on model behavior. Dean and Lee (1984) concluded that in fine sands the effects were also negligible.

Occasionally drainage channels may be introduced along the path of the leads. Such

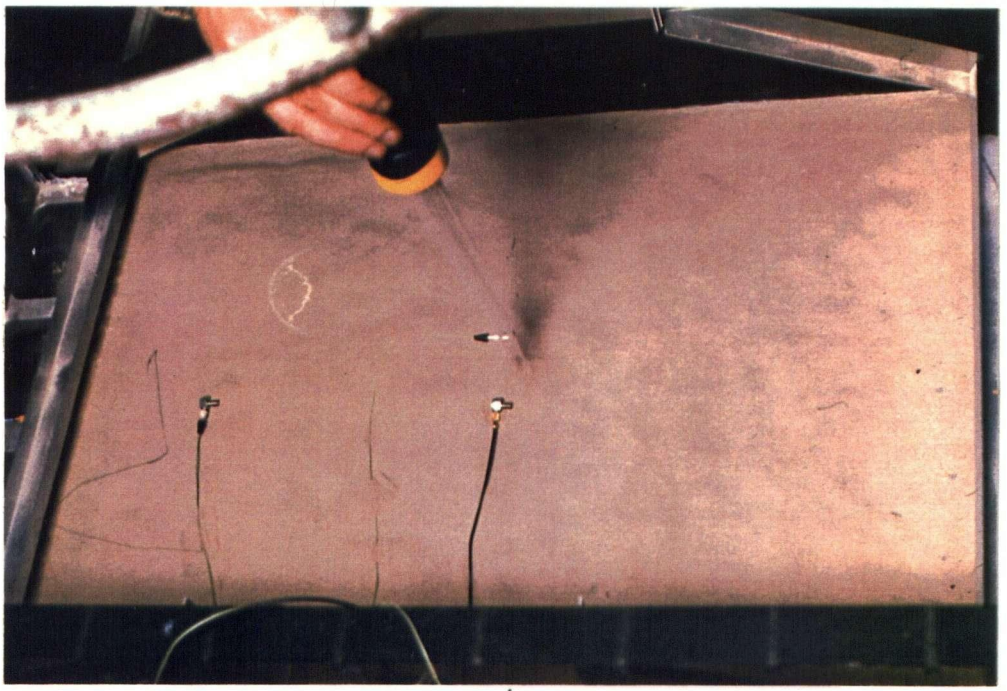

Fig. 5.1 Layout of the Accelerometer Leads

an event can be detected by the fall off in measured porewater pressures with respect to measured pressures by adjacent transducers.

If tension is suddenly applied to the lead, the transducer may move relative to the surrounding soil and a sudden decrease in the porewater pressure will be measured. Therefore, careful study is necessary to determine whether sharp drops in porewater pressures are due to this effect or dilations due to shearing.

The overall accuracy of the porewater pressure transducers is estimated to be of the order $\pm$ 10% of the measured values (Dean and Lee, 1984).

5.7.3 Linearly Variable Displacement Transducers (LVDT's)

The LVDT's were used mostly to measure vertical settlements and were attached to the gantry spanning the box. Because of the poor dynamic response of these devices and limitations of available channels the LVDT's were read only at discrete times- for instance, during swing up and at the beginning and end of earthquakes to give complete settlement increments during the tests. The accuracy of these devices is about $\pm$ 2% for static readings (Steedman, 1985).

5.8 Data Acquisition and Digitisation

Signals from the model were recorded on a 14 track RACAL tape recorder. These analogue signals were processed and digitised at a suitable time increment using the software package, FLY-14, developed by Dean (1984). The raw digitised data was smoothed once using a three point smoothing scheme as suggested by Dean (1984). According to this scheme, the current value at any time is replaced by the sum of 1/2 of the current value plus 1/4 of the previous value and 1/4 of the next value. The smoothing function is symmetric and therefore does not introduce phase shift. The smoothing was necessary to filter out

very high frequency electrical noise which contained negligible energy. This type of noise is unavoidable in dynamic centrifuge tests as it originates as a result of ambient sources such as container vibrations etc.

The accuracy of digitisation from analogue magnetic tape is dependent on the magnitude of the signal. In general, a strong signal is digitised with an accuracy of better than $\pm$ 0.1%. For a weak signal, the error in digitisation may exceed $\pm$ 2% (Steedman, 1985). These cases are identified with a code PAP standing for "Possible Accuracy Problem" in the time history plot.

5.9 Centrifuge Flight

The container is first secured on the centrifuge. As the centrifuge speed is increased, the box swings up and encounters end stops which prevent the box from swinging further. At this point, the base of the container is vertical. Further increase in centrifuge speed will make the radial acceleration field more dominant. The centrifuge acceleration is increased in steps of 20g until the desired g level is reached. At every 20g steps, readings from porewater pressure transducers (PPT) and displacement transducers are recorded. After the centrifuge has reached the desired g level, sufficient time is allowed for porewater pressures to come into equilibrium before the model is subjected to earthquake loading.

During each earthquake, the transducer data are recorded by the high speed RACAL analogue tape recorder. About 15 minutues is allowed between earthquakes in a sequence to allow the model to drain and porewater pressure and LVDT transducers to stabilize. LVDT measurements are taken at the beginning and the end of each earthquake. After the test series, the centrifuge is brought to a stop and the model container is removed from the centrifuge. The post-test site profile is measured and the final locations of the transducers are determined during careful excavation of the model.

5.10 Typical Test Data

A centrifuge model of a gravity structure and foundation is illustrated in Fig. 5.2. The foundation layer is 110mm thick and the width perpendicular to the plane of the figure is 480mm. The gravity structure is modelled by an aluminum cylinder 150mm in diameter and 100mm high, embedded 30mm in the foundation soil. The centrifugal acceleration was nominally 80g. The model, therefore, simulated a structure approximately 8m high and 12m in diameter embedded to a depth of 2.4m in the foundation soil. The average contact pressure of the structure on the soil was 200kPa.

The model was instrumented by accelerometers, porewater pressure transducers and displacement transducers. The locations of these instruments are shown in Fig. 5.2. The typical output of smoothed data from FLY-14 is shown Fig. 5.3. It should be noted that there are wide variations in the scales of the various records and the apparently quite different forms of some of the records are due primarily to differences in the scale. All scales are model scales. The accelerations are expressed as percentages of the centrifuge acceleration. Porewater pressures are those actually measured. Equivalent prototype times are given by multiplying measured times by the linear scale factor. The accelerations expressed as percentage of model gravity and porewater pressures are the same in model and prototype.

The peak acceleration of the input motion as measured by ACC 2036 is 0.16g. The peak acceleration transmitted to the soil near the base (ACC 1487) is almost the same. The peak horizontal acceleration recorded on the structure by ACC 2033 is 0.26g.

The porewater pressures increase steadily during the shaking. The porewater presure transducers far away from the structure on the right hand side of the model (PPT 2338, 2335, 2251 and 2511) show a relatively smooth development of porewater pressure with none of the large oscillations usually associated with dilatant behavior or rocking of the

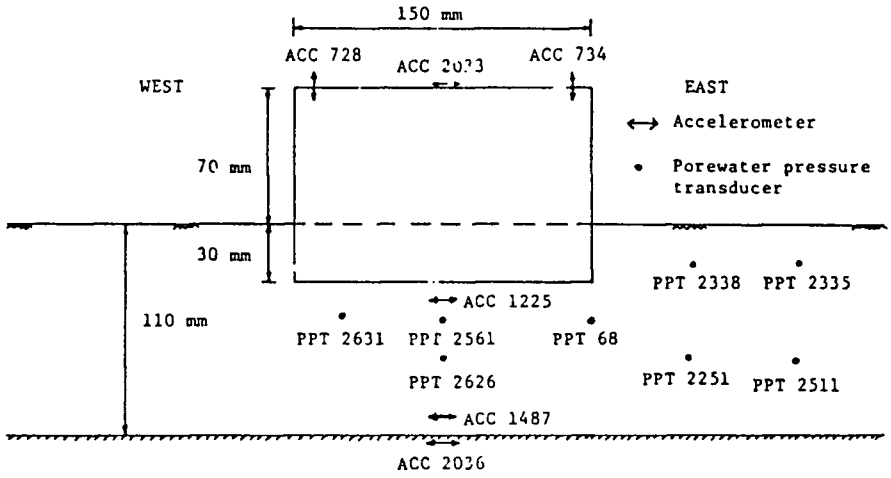

Fig. 5.2 Instrumentation of a Centrifuged Model

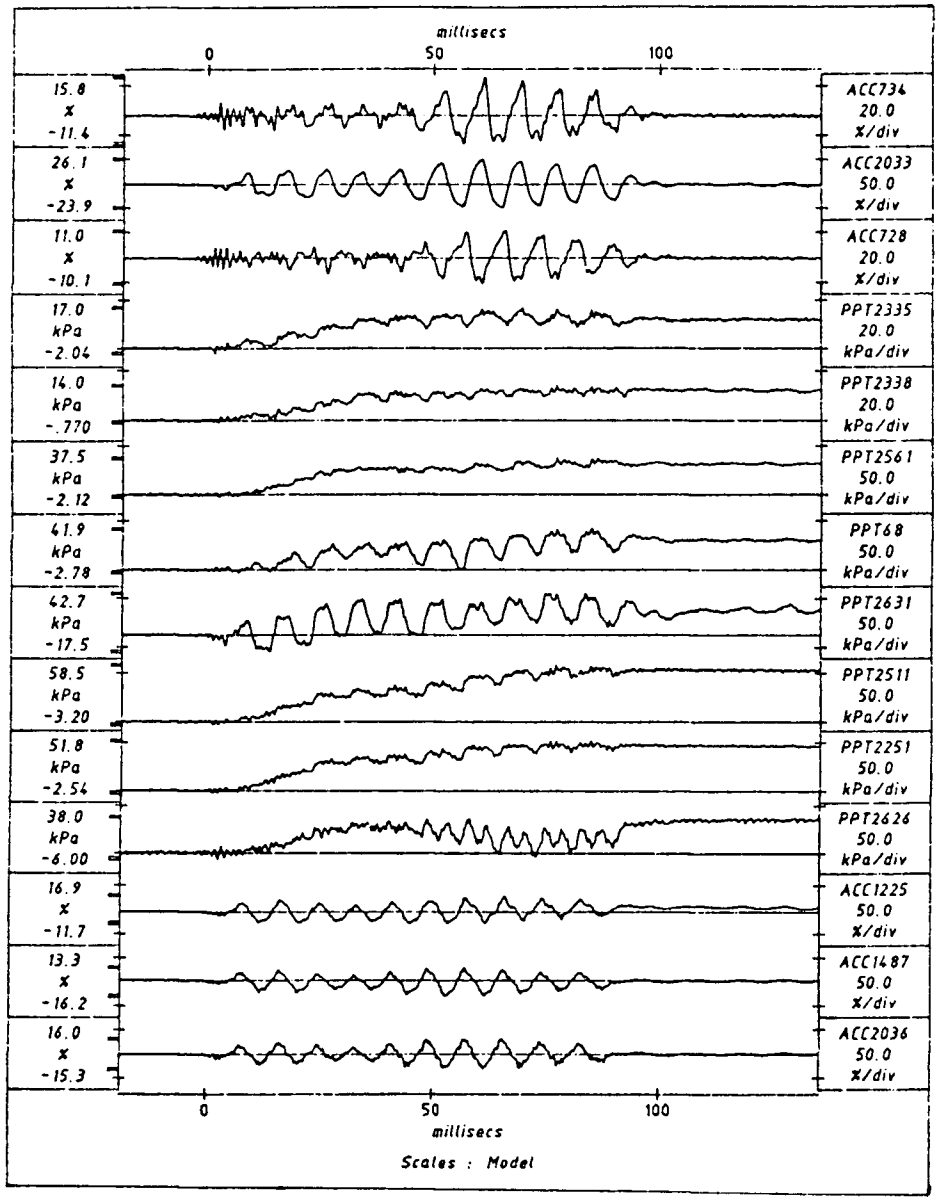

Fig. 5.3 Typical Test Data on Seismic Response of the Model

structure. It seems that cyclic shear strains in the free field area are not sufficient to cause significant dilation. On the contrary, the porewater pressure transducers beneath the structure (PPT 2631, 2626 and 68) show large swings in the recorded porewater pressure with cycles of loading indicating that the effects of rocking and the cyclic shear strains under the structure are sufficiently large to induce significant dilation. However, despite the oscillations, there is a steady increase in residual porewater pressure under the structure.

The effects of increasing porewater pressure on the rocking mode are clearly evident. The rocking is portrayed by the vertical acceleration records ACC 728 and ACC 734 at opposite ends of the diameter of the structure in the plane of excitation. These records are 180 degrees out of phase. When ACC 728 indicates an upward acceleration, ACC 734 indicates a downward acceleration. The input motion, except for random effects, is primarily a horizontal acceleration, and in the initial stages of shaking the recorded vertical accelerations are very small, showing insignificant rocking, which is not surprising in such a squat structure. However, as porewater pressure increases, the vertical accelerations become quite large, upto 0.16g at ACC 734 and 0.11g at ACC 728.

The amplitude of the input motion to the base of the structure (ACC 1225) increases slightly with duration and it may be thought that the sharp increase in rocking may be due to this. However, it should be noted that despite significant horizontal acceleration (at ACC 2033) at the level of ACC 734 and ACC 728, in the early stages of shaking there is very little rocking evident from the records despite the fact the scale of the vertical accelerations is 2.5 times that of the horizontal accelerations.

The data presented in this section are a typical sample of the kind of information obtained during a centrifuge model test. The description of the data is intended to be a guide to the reader in interpreting similar data for the tests to be discussed later. This will help to avoid tiresome repetition in the presentation of the data.

5.11 Centrifuge Tests Used in the Verification Study

Six different centrifuge tests, one from each series, were used in the TARA-3 verification study. They involve two-dimensional (2-D) plane strain and three-dimensional (3-D) models simulating a variety of structures and soil-structure interaction systems. These range from the simple embankments to surface and embedded structures on both dry and saturated sand foundations. The surface structures are modeled by mild steel plates and the embedded structures are modeled by a solid piece of aluminum alloy. A summary of the test series is given in Table 5.3. Detail descriptions of each of the models are presented in chapter 7 and chapter 8 along with the TARA-3 analyses.

Table 5.3 Centrifuge Test Summary

Series	Model	Description	Foundation
LDO1	2-D	Embankment	Dry
LDO2	2-D	Surface Structure	Dry
LDO4	2-D	Surface Structure	Saturated
RSS 110	2-D	Embedded Structure	Dry
RSS 111	2-D	Embedded Structure	Saturated
RSS 90	3-D	Embedded Structure	Dry

CHAPTER 6

SOIL PROPERTIES FOR TARA-3 ANALYSES

6.1 Introduction

The centrifuge model tests used in the verification of TARA-3 were conducted over a three year period from 1983 to 1986. In 1983 the technology for conducting seismic tests on large scale models was in its infancy and techniques were not available for measuring the in-situ properties of the sand models in flight. Not until 1987 (Finn and Gohl, 1987) was a technique developed for measuring reliably the in-situ shear modulus. This technique involves measuring shear wave velocities using piezoceramic bender elements in the sand model while the model is in flight.

Therefore, the soil properties required for the TARA-3 analyses have to be derived using other procedures. It is fortunate that the constitutive model in TARA-3 is based on three robust parameters, shear modulus, bulk modulus and shear strength which can be related to the relative density and effective stresses in the model. Hence the required soil properties were estimated on the basis of the relative density of the model.

As outlined in section 5.6, the gross density of a model was determined from its geometry and weight and the relative density was then calculated from a knowledge of the density at minimum and maximum void ratios of the sand. This procedure worked well for dry models which could be constructed to defined geometry. All sand placed in the model stayed within

the boundaries of the model thus ensuring that an accurate model weight could be obtained.

However, in the case of saturated models where the sand-oil mixture was pluviated through silicon oil this procedure was less accurate. Some fines remained in suspension in the oil resulting in an overestimation of model weight. During construction the sand-oil mixture sometimes migrated outside the boundary of the model proper and ended up in the overflow trough and other areas of the container. In these circumstances it was difficult to calculate accurate densities.

As the test series progressed, model construction improved with experience. A new technique for the construction of saturated models, referred to as Method 2 in this thesis, was developed in 1985 and in later tests such as the RSS 111 series the relative density can be determined as accurately as in dry tests.

The technology of model construction had important implications also for the homogeneity of the model. Test data show that the models constructed using Method 2 were very homogeneous. The earlier models show evidence of non-homogeneity. This does not appear to affect very much parameters such as acceleration which depend strongly on average global properties but can have a marked effect on porewater pressures which are very strongly affected by purely local conditions. These effects are discussed fully later when reviewing the test data.

6.2 Shear and Bulk Moduli Parameters

As mentioned previously, the initial in-situ shear modulus is related directly to the relative density and effective stresses. This was calculated using the expression proposed by Seed and Idriss (1970) as given in equation (2.4). The value of shear modulus parameter, K_{2max}, was obtained using the expression proposed by Byrne (1981) as shown in equation (2.5). Finn and Gohl (1987) showed that the correlations proposed by Seed and

Idriss (1970) and Hardin and Drnevich (1972) give very good estimates of shear moduli for centrifuge modeling in flight by comparing estimates by these procedures with moduli measured directly in-situ using their new technique.

The bulk modulus parameter, K_b, for the static analysis was obtained using the expression reported by Byrne and Cheung (1984). This takes the form

$$K_b = \frac{19}{0.0655 - 0.0535\ log\ \frac{D_r}{10}} \tag{6.1}$$

where,

D_r = relative density expressed in percentage.

For dynamic analysis, a value of K_b five times the value given by equation (6.1) was used for saturated portions. The higher value is necessary to simulate the undrained conditions during the earthquake loadings. Parametric studies with different higher values of K_b, some as high as twenty times of that given by equation (6.1), indicate that the responses were not affected significantly. The bulk modulus exponent, m, was selected to be equal to 0.40.

The effective angle of internal friction of the Leighton Buzzard sand was determined by both triaxial tests (Eyton 1982) and simple shear tests and over the range of density used in the model tests was taken to be around 35 degrees.

6.3 Liquefaction Resistance Curve

The liquefaction resistance of the Leighton Buzzard sand was determined using the University of British Columbia simple shear device. The liquefaction resistance curve determined for a relative density of $D_r = 65\%$ is shown in Fig. 6.1. Resistance at other

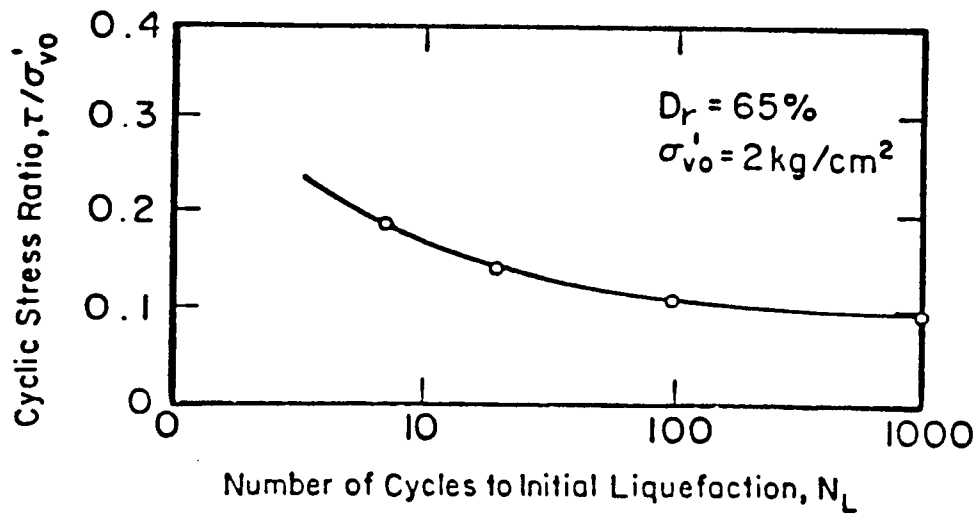

Fig. 6.1 Liquefaction Resistance Curve

relative densities were estimated on the assumption of a linear dependence on relative density as shown by Seed and Lee (1966).

The volume change constants C_1 to C_4 and the rebound constants in the Martin-Finn-Seed porewater pressure model were determined by regression analysis using SIMCYC-2 (Yogendrakumar and Finn 1984) to result in a close fit between the measured and predicted liquefaction resistance curves. Table 6.1 gives the set of volume change and rebound constants for different relative densities used in the tests.

Table 6.1 Porewater Pressure Model Constants

Constants	$D_r = 75\%$	$D_r = 64\%$	$D_r = 52\%$
C_1	0.820	0.960	1.00
C_2	0.790	0.430	0.40
C_3	0.450	0.161	0.161
C_4	0.730	0.376	0.376
m	0.430	0.430	0.430
n	0.620	0.620	0.620
K_r	0.006	0.007	0.007

6.4 Structural Properties

The structural response is assumed to be linearly elastic in the analyses and therefore the structure was modeled using linear elastic elements. The assumption of linear elastic behavior is justifiable, because of the very small strains that develop in the structure during the earthquake.

The properties selected for aluminum alloy (Dural) and mild steel are shown in Table 6.2.

Table 6.2 Structural Properties.

Property	Aluminum	Mild Steel
Specific Gravity	2.83	7.80
Unit Weight (kN/m^3)	27.8	76.5
Shear Modulus (kPa)	2.4×10^7	7.6×10^7
Bulk Modulus (kPa)	6.7×10^7	1.7×10^8
Poisson Ratio	0.34	0.30
Damping Coefficient, α	0.0	0.0
Damping Coefficient, β	0.005	0.005

6.5 Slip Element Properties

Experimental studies by many researchers (Tatsuoka el al 1985; Uesugi et al 1986; Uesugi et al 1987) on the behavior of sand-structure interface under cyclic loading reveal that the interface behavior is essentially of the rigid-perfectly plastic type. Therefore, the

high unit stiffnesses deduced from the test results involving sand and steel surfaces (Tatsuoka et al 1985) were used in the TARA-3 analyses. These values are considered appropriate for the steel structures used in the centrifuge studies. The properties for the slip element are tabulated in Table 6.3.

Table 6.3 Slip Element Properties.

Property	Slip Element
Unit Normal Stiffness (kPa/m)	6.3×10^5
Unit Shear Stiffness (kPa/m)	6.3×10^5
Friction Angle, ϕ_s'	10.0
Cohesion, c_s	0.0

CHAPTER 7

VERIFICATION BASED ON DRY MODEL TESTS

7.1 Verification Study Based on Test Series LDO1

7.1.1 Centrifuge Model in Test Series LDO1

A schematic view of a 2-D plane strain model embankment is shown in Fig. 7.1. The embankment is 116mm high and has a flat crest 239mm wide and a base 732mm wide. The length of the model in the direction perpendicular to the plane of shaking is 481 mm.

The model was constructed using Leighton Buzzard B.S.S 120/200 sand by the dry construction method outlined in section 5.5.1. The estimated relative density of the sand is about 50 $\pm$ 10%.

The model was shaken by an earthquake, EQ1, while under a nominal centrifugal acceleration of 80g. The model, therefore, corresponds to a prototype embankment 9.2m high with a crest and base width of 18.9m and 58.5m respectively.

The responses of the model embankment to the simulated earthquake were measured by the instruments located in the model as shown in Fig. 7.2. All accelerometers measured horizontal acceleration responses. Accelerometers ACC 1544 and ACC 1486 were not

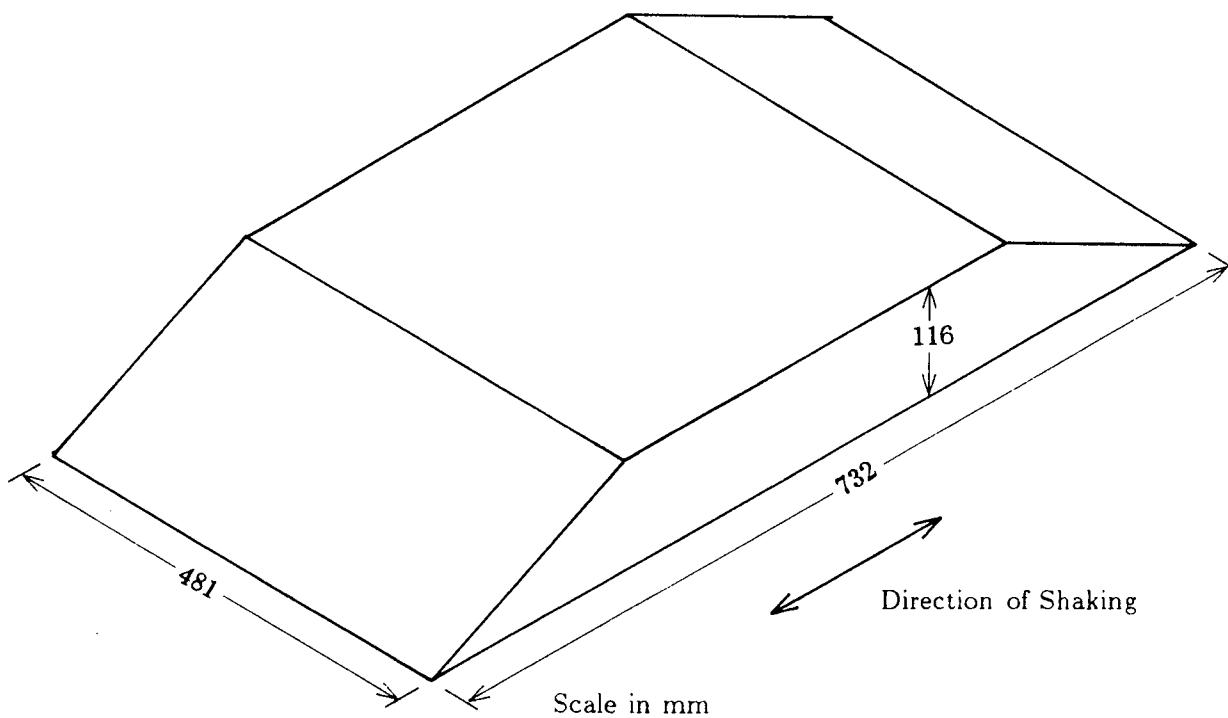

Fig. 7.1 Schematic of a Model Embankment

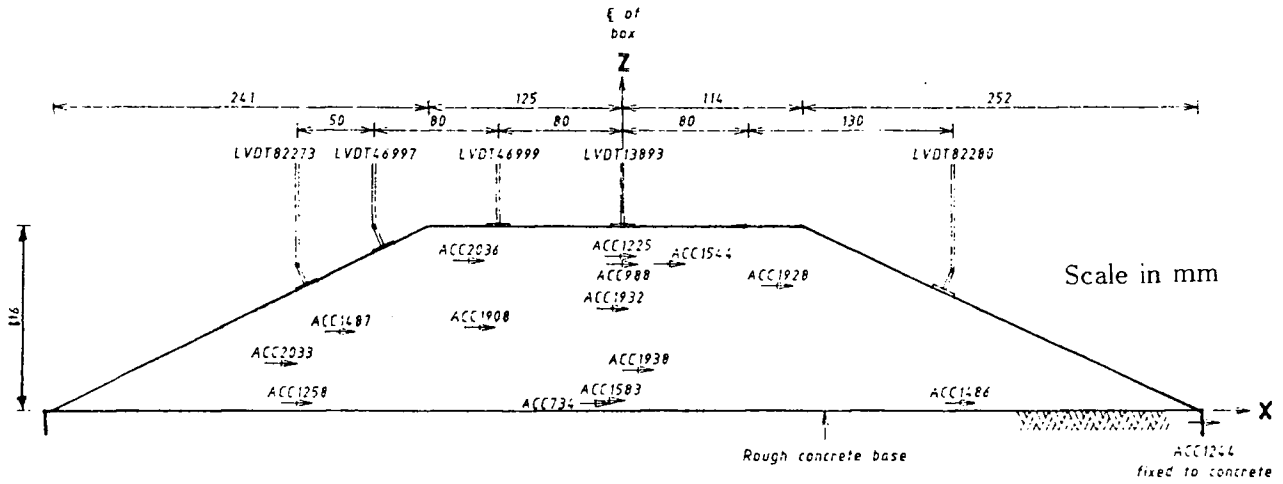

Fig. 7.2 Instrumented Model Embankment in Test Series LDO1

activated for this particular test.

7.1.2 Model Response in Test LDO1

The model responses recorded during the test are shown in Fig. 7.3 at model scale. ACC 1244 fixed to the concrete base measured the acceleration input to the model. The peak amplitude of the input is 10.1% of the centrifuge acceleration and it occurs at approximately 50.0 milliseconds. ACC 1932 was reported to have been functioning incorrectly during the test (Dean and Lee, 1984) and will therefore be ignored. ACC 734 malfunctioned during this and subsequent test series and data from it are not used (Dean and Lee 1984). Accelerometers ACC 988, ACC 1225, ACC 1908, ACC 1928 and ACC 2036 show responses that are distinctly different in frequency content from the other accelerometer responses and the input motion. These transducers were located in the upper part of the embankment and therefore they responded differently from those located in the lower part. ACC 1225 and ACC 988 were located at the same elevation (Z=90 mm) but at different positions in the direction perpendicular to the plane of shaking. ACC 1225 was near the centre section (Y=10 mm) and ACC 988 was near the rear window (Y= -200 mm). They both show responses that are somewhat different in peak amplitudes and in frequency content. ACC 988 was close to the window and end effects might have distorted the response and hence the record has to be interpreted with caution.

The input motion as measured by ACC 1244 is shown in Fig. 7.4 along with the baseline corrected motion at prototype scale. The baseline corrected ACC 1244 record was used as the input motion for the TARA-3 analysis. It has about 10 roughly sinusoidal pulses of horizonal base shaking with a predominant frequency of about 1.50 Hz. It consists of 5 cycles of more-or-less constant amplitude shaking followed by 2 big cycles of shaking. The amplitude gradually decreases in the last three 3 cycles and significant shaking ceases at

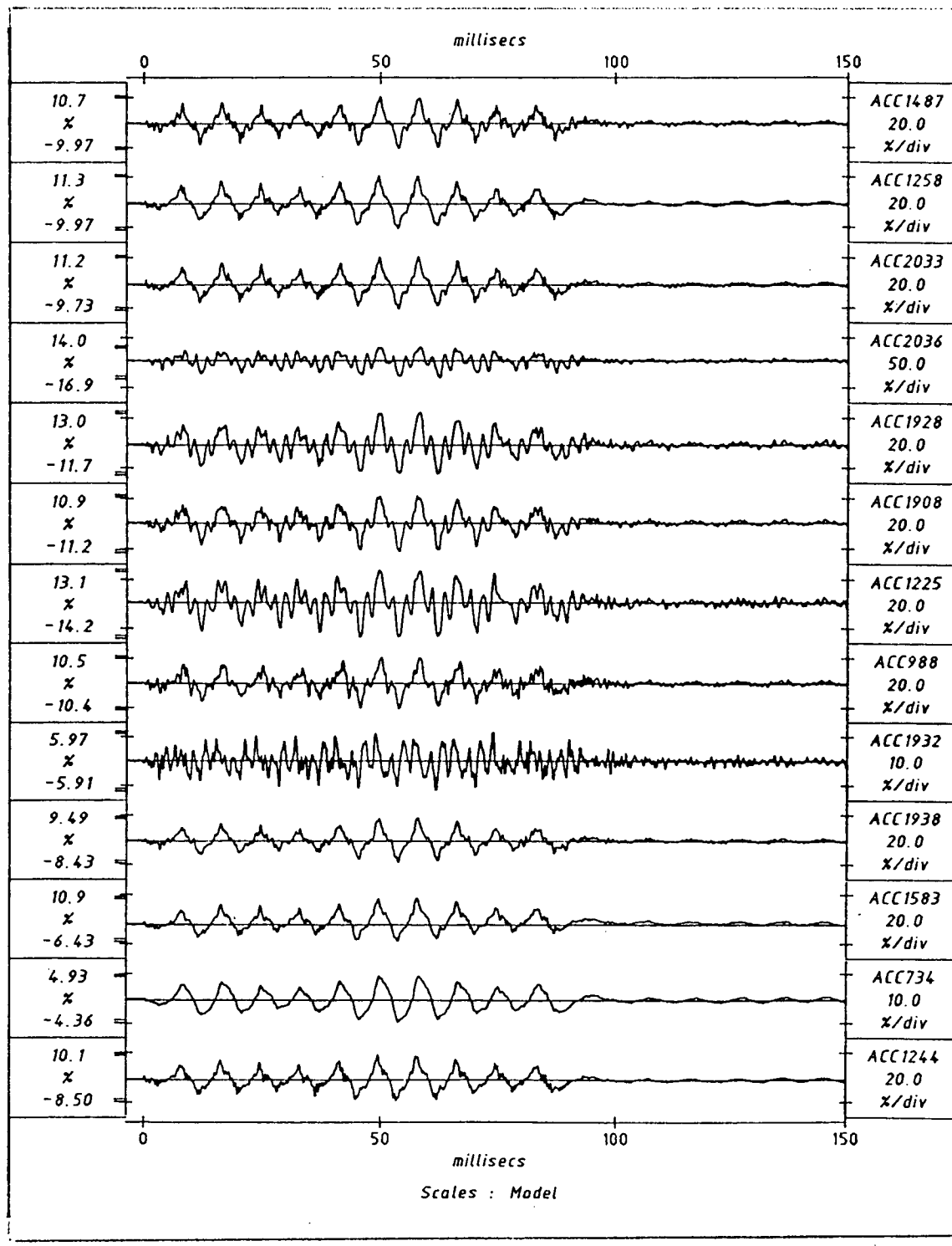

Fig. 7.3 Model Response in Test LDO1/EQ1

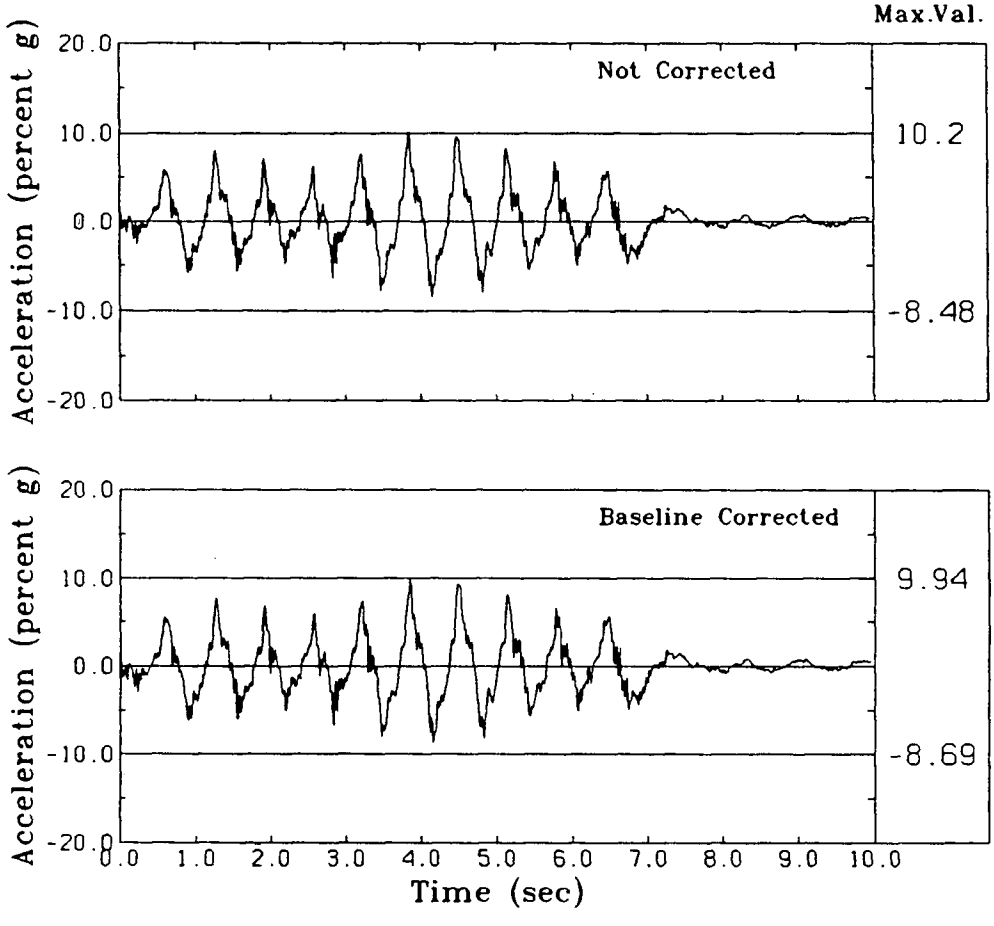

Fig. 7.4 Input Motion for Test LDO1/EQ1

around 7.50 seconds. The relative density of the sand was taken as 50% for the TARA-3 analysis.

7.1.3 Comparison of Acceleration Responses of Test LDO1/EQ1

The computed and measured accelerations near the base at the locations of ACC 1583, ACC 1258, ACC 1938 and ACC 2033 are shown in Figs. 7.5 to 7.8 respectively. In each of these locations, the responses are very similar in frequency content, each corresponding to the frequency of the input motion. The peak amplitudes and the variation of amplitudes with time agree very closely. The computed and measured peak amplitudes at these locations are tabulated in Table 7.1 and they differ only by a few percent.

ACC 1487 and ACC 1908 were located at half way between the crest and base with ACC 1487 closer to the left hand side slope. The comparison of accelerations at these locations is shown in Figs. 7.9 and 7.10. The agreement between the measured and computed accelerations in terms of frequency content and amplitude variation with time is good at both locations.

Figs. 7.11 to 7.14 show comparison of acceleration responses in the upper part of the embankment at the locations of ACC 1928, ACC 2036, ACC 988 and ACC 1225 respectively. The overall agreement is good except at the locations of ACC 988 and ACC 2036. As pointed out earlier, ACC 988 may have been affected by end-effects because of its proximity to the end and therefore it is not surprising to see differences between the measured and computed responses.

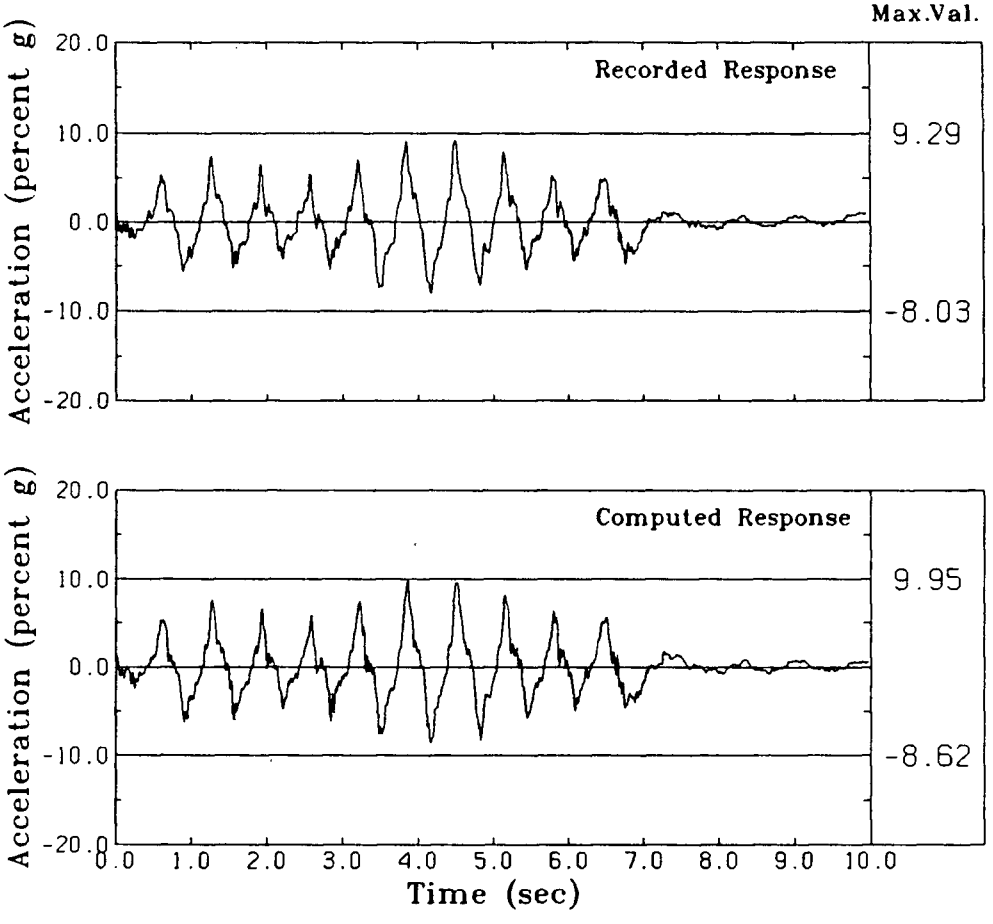

Fig. 7.5 Computed and Measured Accelerations at the Location of ACC 1583 in Test LDO1/EQ1

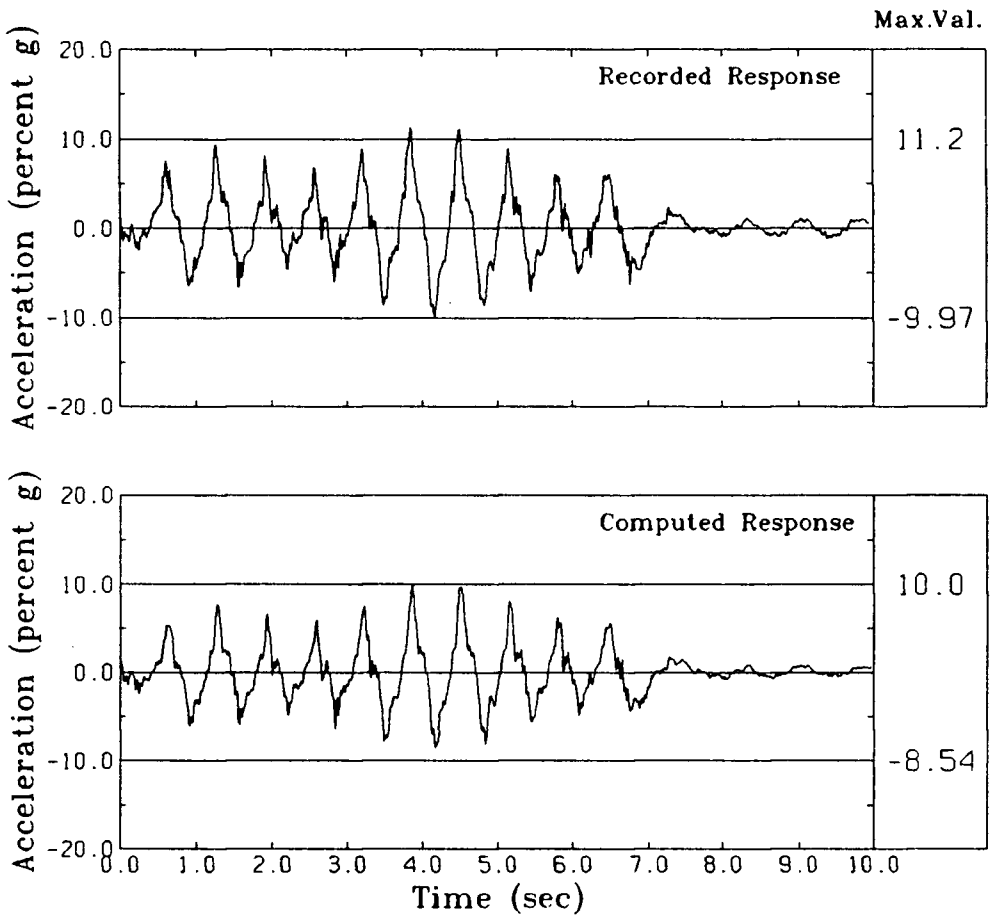

Fig. 7.6 Computed and Measured Accelerations at the Location of ACC 1258 in Test LDO1/EQ1

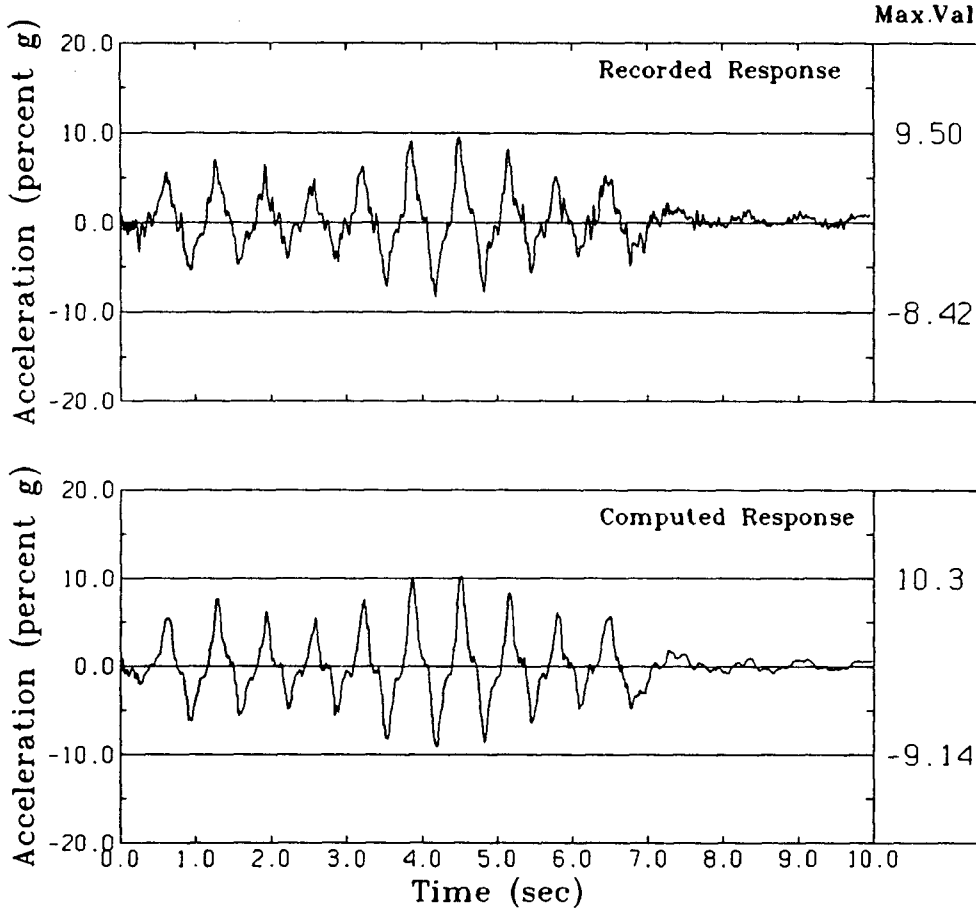

Fig. 7.7 Computed and Measured Accelerations at the Location of ACC 1938 in Test LDO1/EQ1

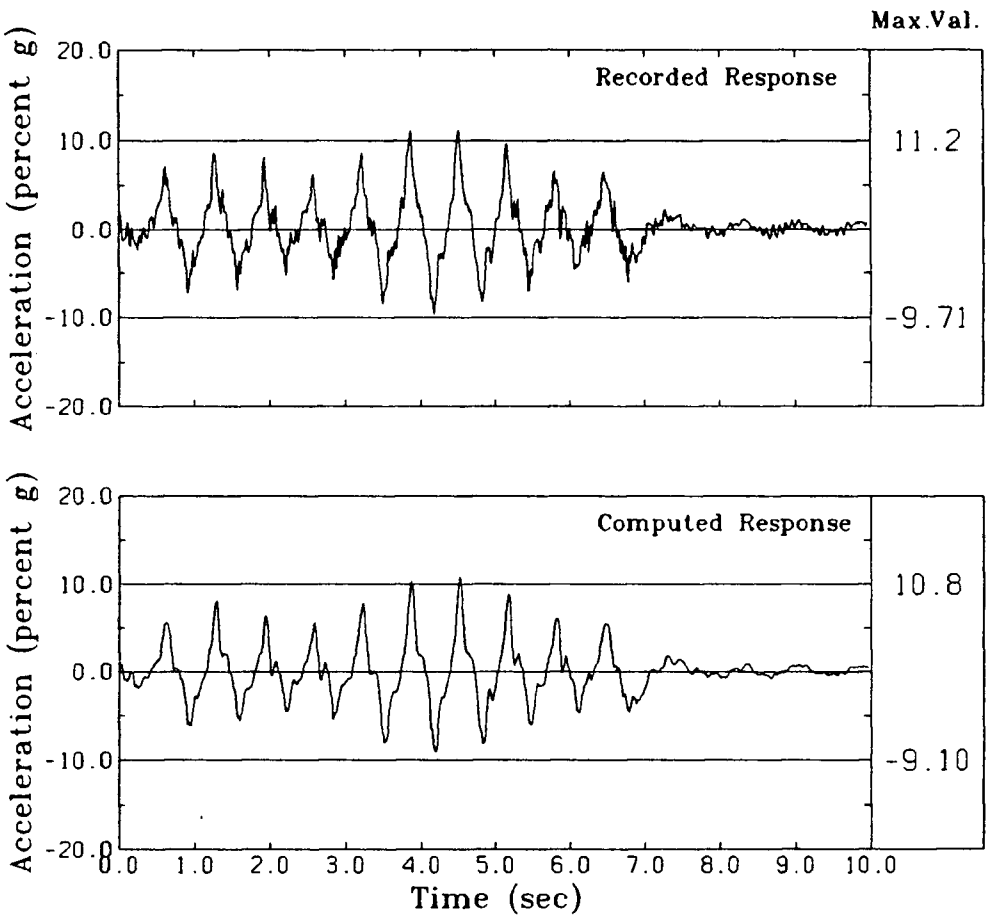

Fig. 7.8 Computed and Measured Accelerations at the Location of ACC 2033 in Test LDO1/EQ1

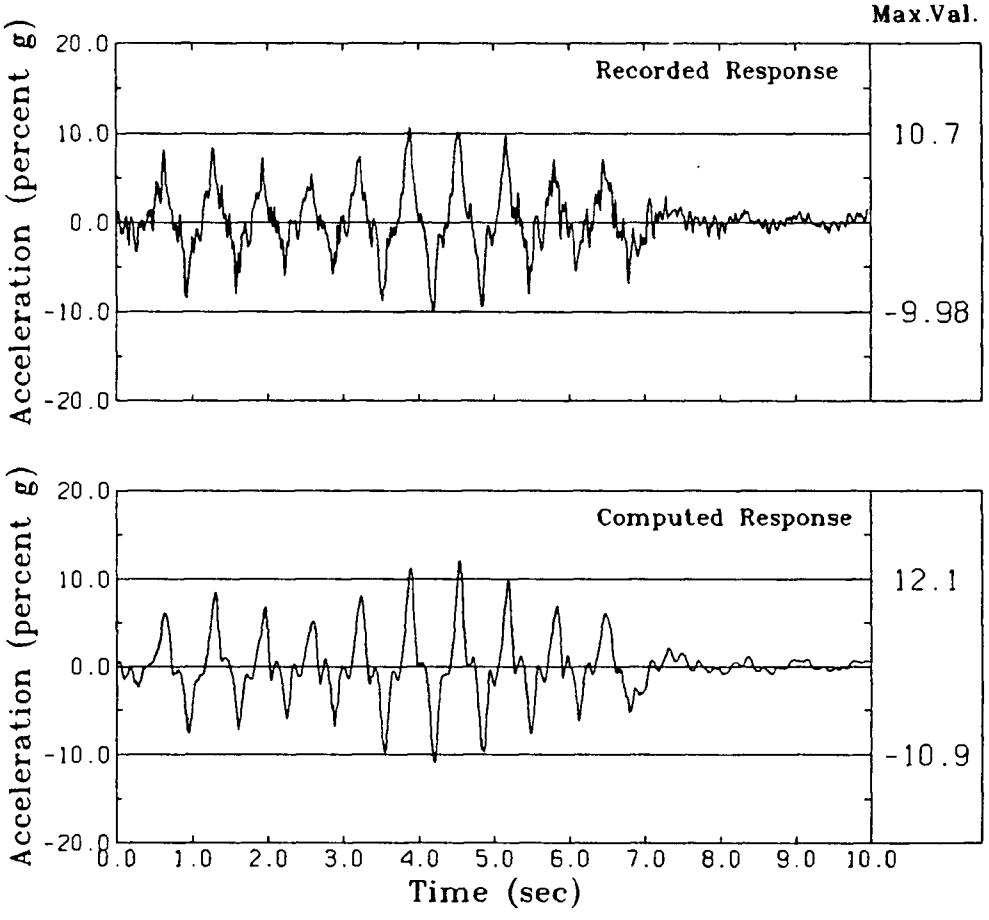

Fig. 7.9 Computed and Measured Accelerations at the Location of ACC 1487 in Test LDO1/EQ1

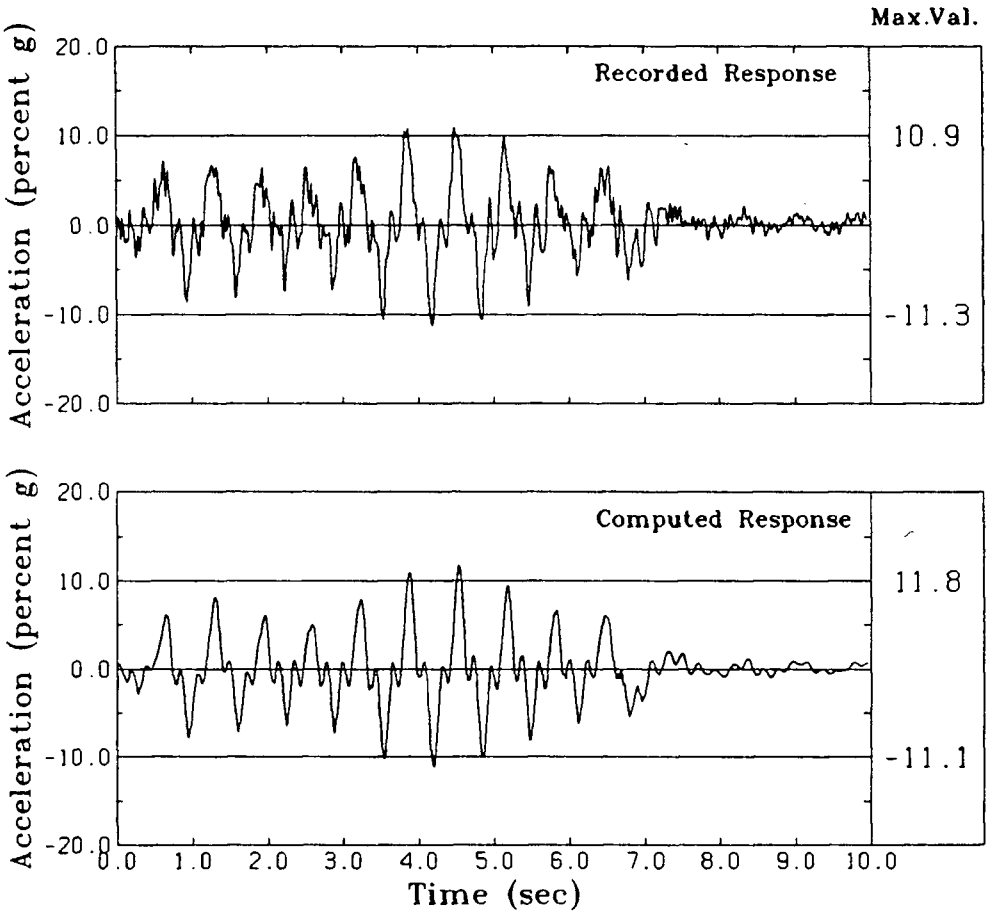

Fig. 7.10 Computed and Measured Accelerations at the Location of ACC 1908 in Test LDO1/EQ1

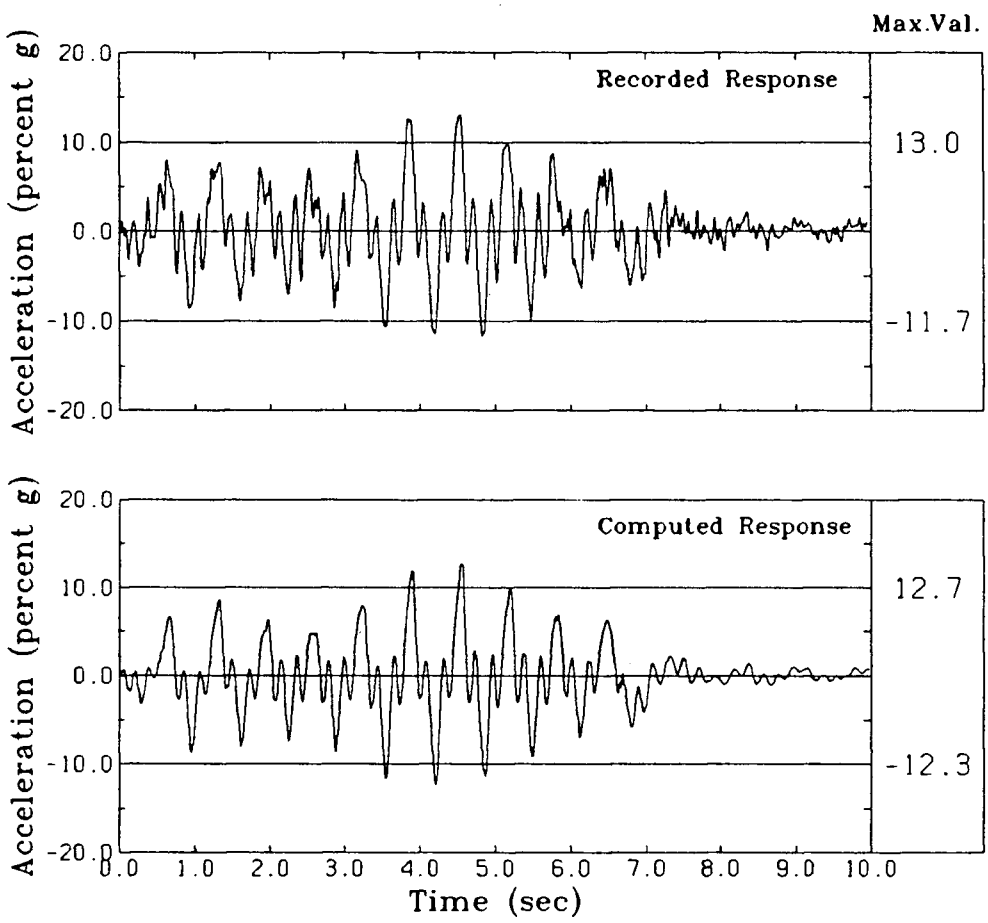

Fig. 7.11 Computed and Measured Accelerations at the Location of ACC 1928 in Test LDO1/EQ1

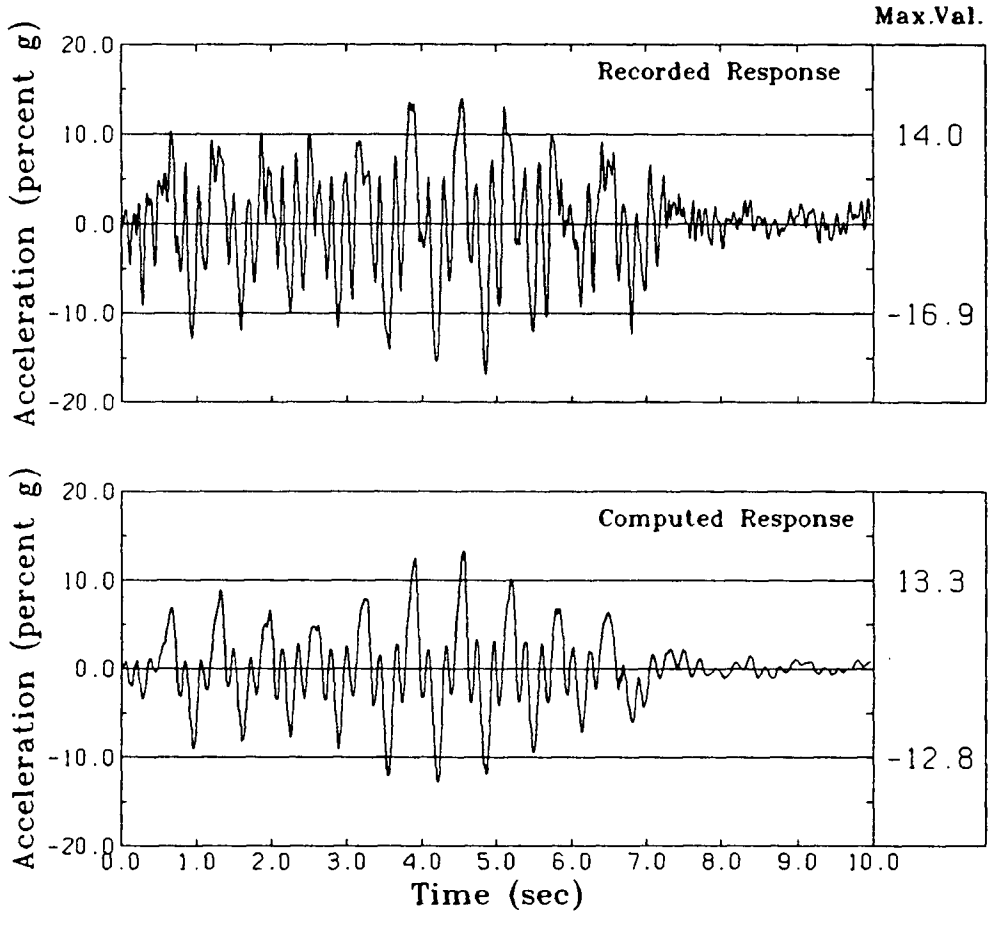

Fig. 7.12 Computed and Measured Accelerations at the Location of ACC 2036 in Test LDO1/EQ1

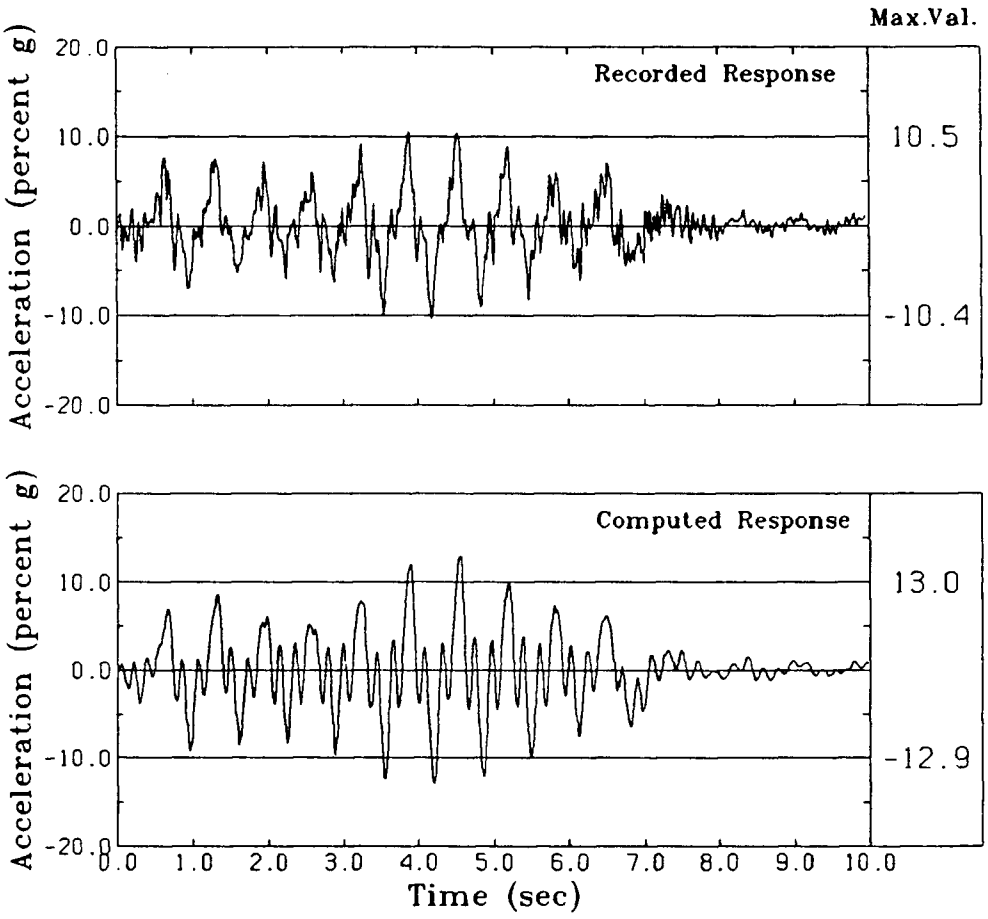

Fig. 7.13 Computed and Measured Accelerations at the Location of ACC 988 in Test LDO1/EQ1

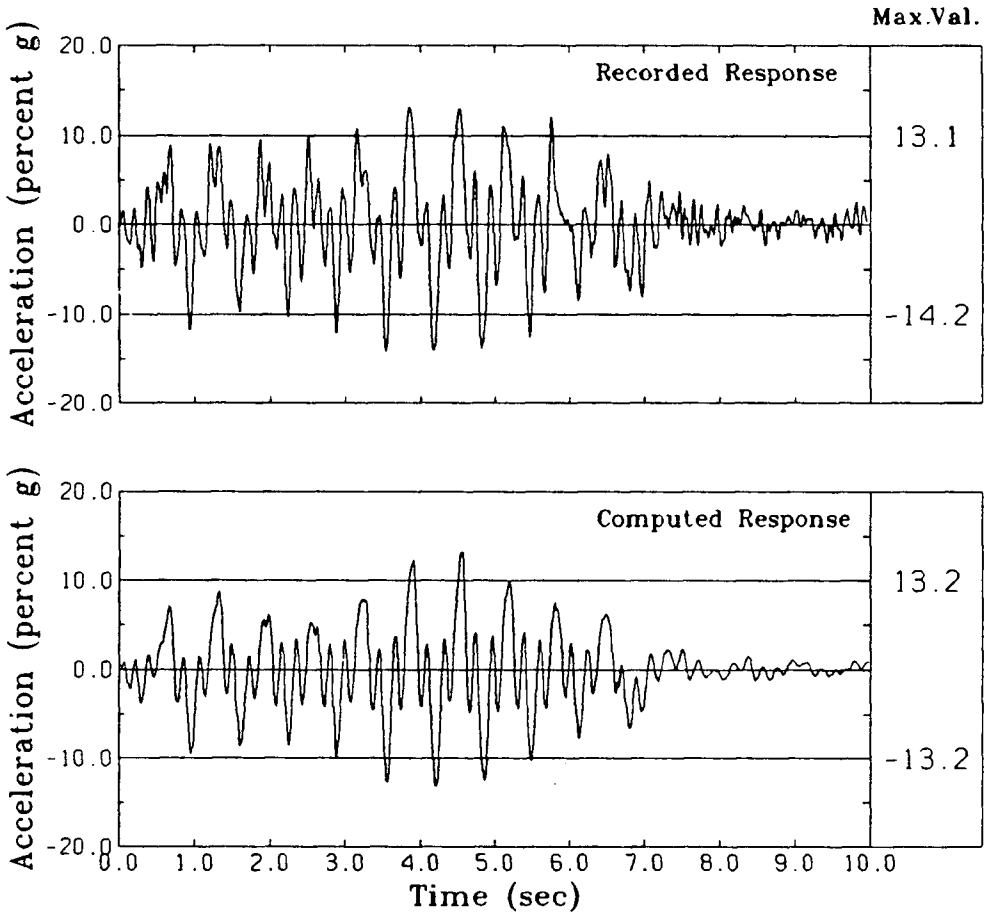

Fig. 7.14 Computed and Measured Accelerations at the Location of ACC 1225 in Test LDO1/EQ1

Table 7.1 Comparison of Peak Acceleration in Test LDO1/EQ1

Transducer No.	Measured (%g)	Computed (%g)
ACC 1583	9.3	9.9
ACC 1258	11.2	10.0
ACC 1938	9.5	10.3
ACC 2033	11.2	10.8
ACC 1487	10.7	12.1
ACC 1908	11.3	11.1
ACC 1928	13.0	12.7
ACC 2036	16.9	12.8
ACC 988	10.5	13.0
ACC 1225	14.2	13.2

The stress strain response at two locations near ACC 1583 and near ACC 1932 are shown in Fig. 7.15 and Fig. 7.16 respectively. They are drawn to the same scale and hence they offer direct comparison of stress strain response at representative locations in the lower and upper part of the embankment. The responses are not strongly nonlinear. However, the hysteretic behavior at location near ACC 1583 is somewhat more pronounced than at location ACC 1932.

7.1.4 Comparison of Settlements in Test LDO1/EQ1

The measured and computed settlements at the locations of LVDT 46999 and LVDT 13893 are tabulated in Table 7.2. The values quoted in the table are at prototype scale. At

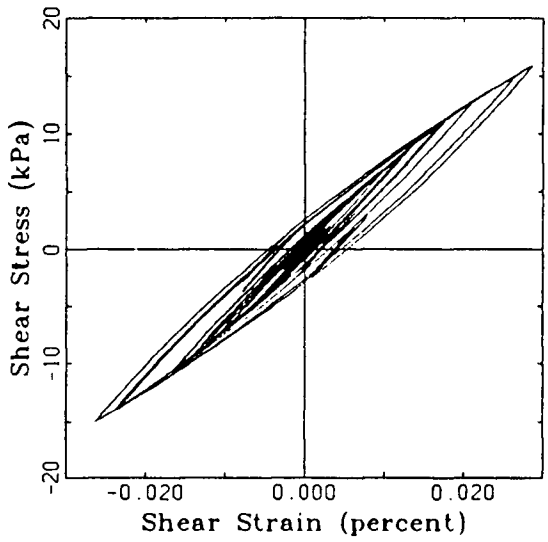

Fig. 7.15 Computed Shear Stress-Strain Response Near the Location of ACC 1583 in Test LDO1/EQ1

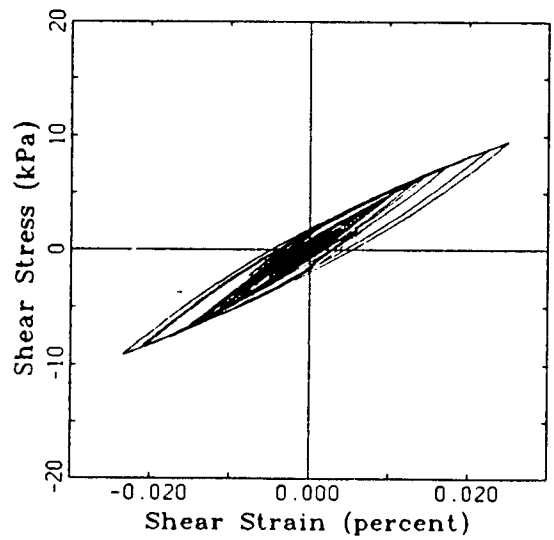

Fig. 7.16 Computed Shear Stress-Strain Response Near the Location of ACC 1932 in Test LDO1/EQ1

both locations, the settlements are predicted satisfactorily.

Table 7.2 Comparison of Settlements in Test LDO1/EQ1

LVDT No.	Measured (mm)	Computed (mm)
46999	10.2	9.0
13893	10.8	9.4

The vertical settlements of the embankment are also shown in Fig. 7.17. The dotted lines show the initial shape and the solid lines show the computed post-earthquake shape taking only the vertical settlements into account. The circular points indicate the locations of the tips of LVDTs and the triangular points show the final positions. It is clear that the agreement between the measured and computed vertical settlements is very good.

Vertical settlements could not be measured satisfactorily on the slopes of the embankment due to the sliding of material during shaking, the effects of wind erosion and the difficulties in setting up the LVDT properly on the slope.

7.2 Verification Study Based on Test Series LDO2

7.2.1 Centrifuge Model in Test Series LDO2

A schematic view of a 2-D plane strain soil-structure model is shown in Fig. 7.18. The embankment was constructed by dry method described in section 5.5.1 using Leighton Buzzard B.S.S 120/200 sand. The estimated relative density of the sand is 71 $\pm$ 8%. The embankment is 105mm high and has a flat crest 230mm wide and a base 720mm wide. The

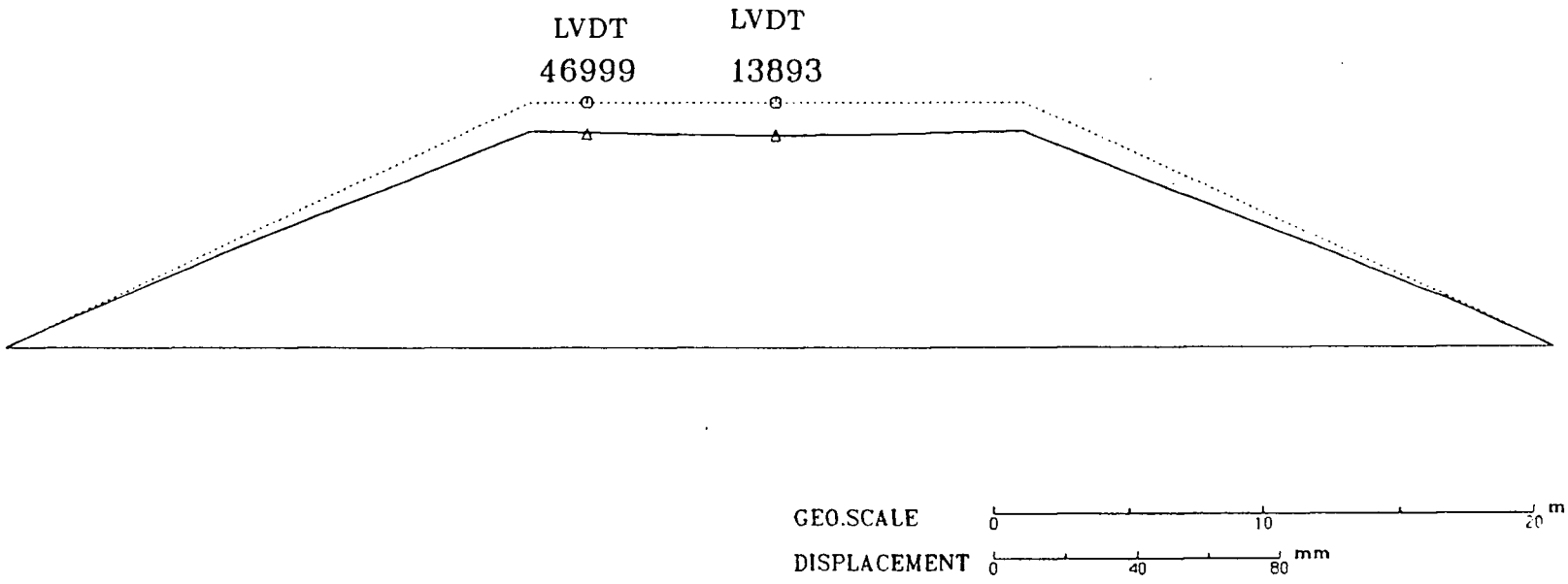

Fig. 7.17 Settlement Pattern in Test LDO1/EQ1

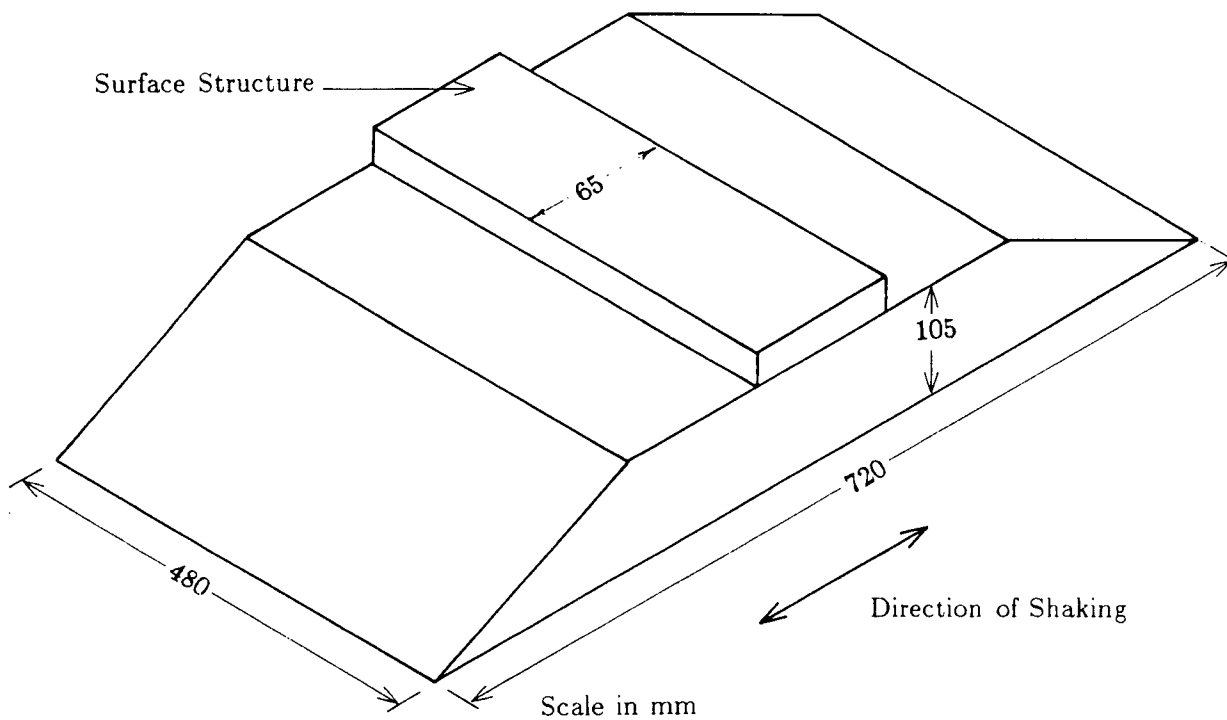

Fig. 7.18 Schematic of a Model Embankment With Surface Structure

length of the embankment perpendicular to the direction of shaking is 480 mm.

The surface structure consisted of three mild steel plates, each of which is 15mm thick and 65mm wide. The steel plates were placed end to end along the centerline of the crest. The two end pieces were each 40mm long and the central piece was 385mm long.

The model experienced a nominal centrifugal acceleration of 80g. The model, therefore, simulated a prototype embankment approximately 8.8m high with crest width and base width of 18.4m and 57.6m respectively and a structure approximately 1.2m high and 5.2m wide.

The complete instrumentation of the model is shown in Fig. 7.19. The transducers are distributed in the model in order to obtain a comprehensive picture of the model responses. ACC 1932 and ACC 1938 measured vertical accelerations while other accelerometers measured horizontal accelerations. ACC 1544 mounted on the concrete base recorded the acceleration input to the model.

7.2.2 Model Response in Test LDO2

For the first three earthquakes (EQ1 to EQ3), ACC 1544 was not working. These earthquake motions are of small amplitudes with peak values less than 5%g. The response to these earthquakes was not analysed. Only the response to the fourth earthquake (EQ4) which has a peak amplitude of 12.4%g was analysed using TARA-3.

The output of smoothed data for test LDO2/EQ4 is shown in Fig. 7.20. The number of channels in the data acquistion system was limited and less than the number of transducers. Therefore, not all transducers could be recorded in each test in the sequence. For this particular test, only the accelerometers whose responses were given in Fig. 7.20 were activated.

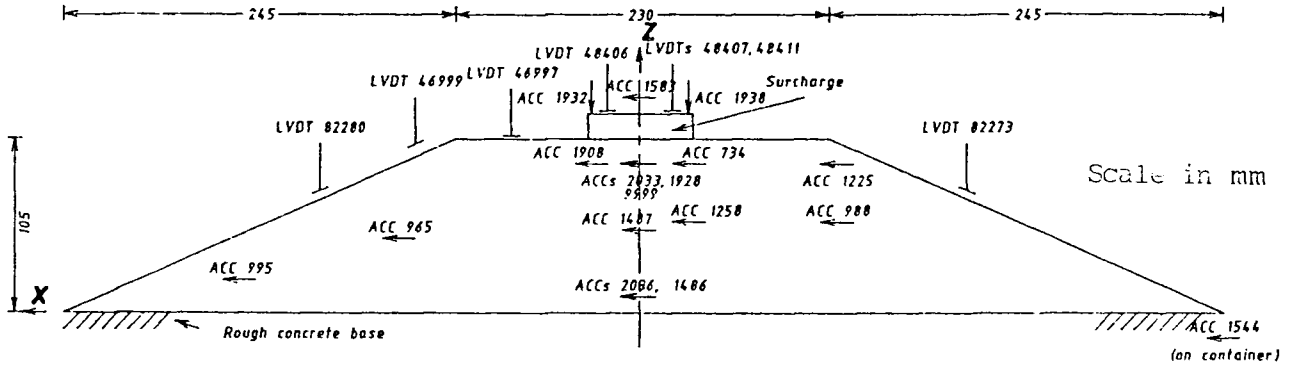

Fig. 7.19 Instrumented Model in Test Series LDO2

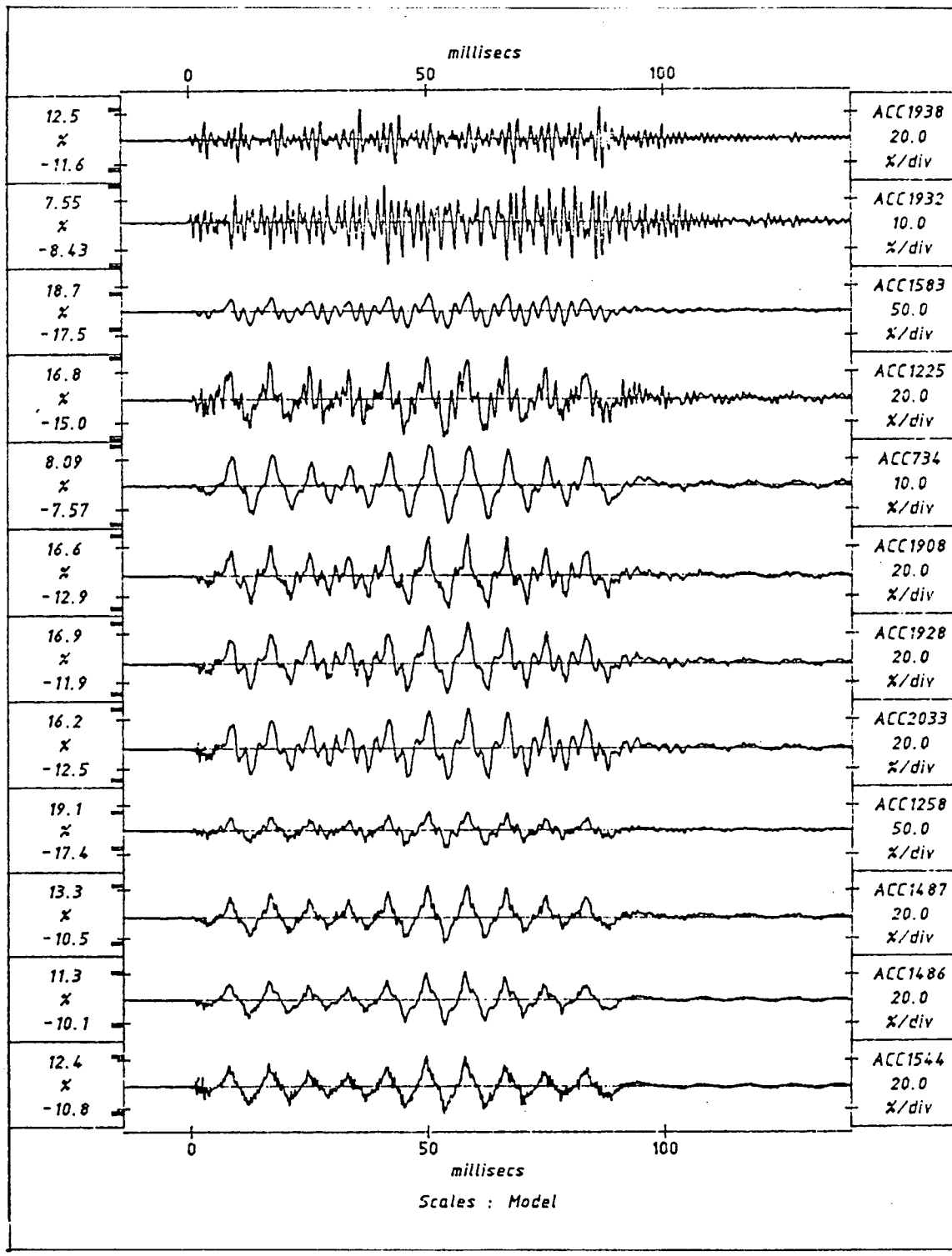

Fig. 7.20 Model Response in Test LDO2/EQ4

As noted earlier in section 7.1.2, ACC 734 malfunctioned during this test series and data from it is ignored. The records ACC 1225, ACC 1258, ACC 1932 and ACC 1938 should also be viewed with caution as they show considerable high frequency response during shaking and even after 90 milliseconds when the earthquake motion had already ceased. A possible explanation for this noisy response is given in the next section.

The peak horizontal acceleration of the input motion as recorded by ACC 1544 is 12.4%g. Fig. 7.21 shows the input motion along with the base corrected motion. Both of these records are smoothed once and are shown at prototype scale. They show no apparent differences. The Fourier spectrum of the base corrected ACC 1544 record is shown in Fig. 7.22. It has a predominant frequency of 1.5 Hz. It also contains relatively small energy at higher frequencies, for instance, at 4.5 Hz and 7.5 Hz.

Except for a small drop in peak values, the acceleration transmitted to the soil near the base as given by ACC 1486 is similar to that of the input motion. There is an increase in peak acceleration values as the structure is approached. Close to the base of the surface structure, the peak acceleration recorded by ACC 2033 is 16.9%g. The peak acceleration measured at the top of the structure (ACC 1583) is 18.7%g. These indicate that there is a steady amplification of the response as the motion is transmitted from the base of the model to the top of the surface structure.

ACC 1932 and ACC 1938 were placed to measure vertical accelerations at opposite edges of the steel plate. They show quite a different type of response with frequency content higher than that of the other records. The reason for this is explained later.

ACC 2033 and ACC 1928 were located at same elevation (Z = 90mm) but in different vertical planes, 60mm (model scale) apart. These records are almost identical. This observation suggests that the model behaved in a plane strain mode.

The prototype of the model was analysed using TARA-3 with base corrected ACC 1544

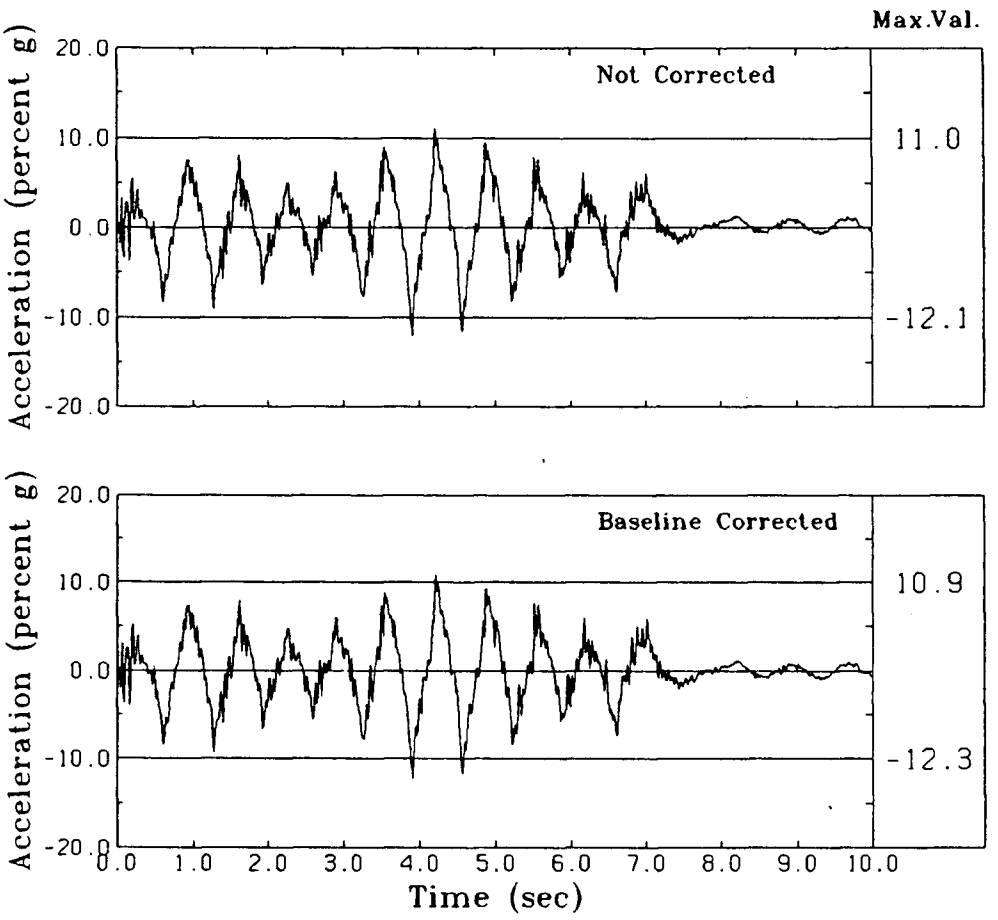

Fig. 7.21 Input Motion for Test LDO2/EQ4

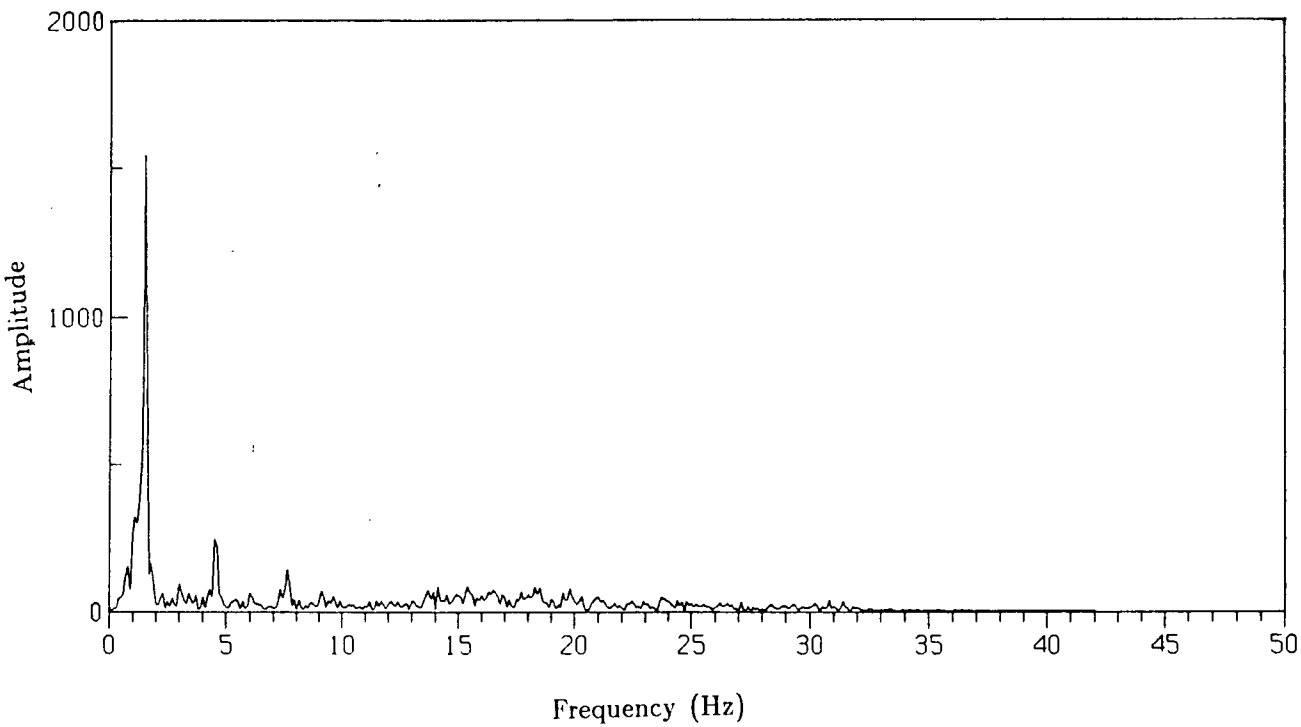

Fig. 7.22 Fourier Spectrum of ACC 1544 Record in Test LDO2/EQ4

record as the input. The relative density of the sand was taken at 71%. Two analyses were conducted: one with slip elements between the soil and structure and the other without slip elements. Computed responses were compared with the corresponding measured responses at prototype scale in the following section.

7.2.3 Comparison of Acceleration Responses of Test LDO2/EQ4

Comparison between the measured and computed horizontal acceleration responses at locations of ACC 1486, ACC 1487, ACC 2033 and ACC 1928 is shown in Fig. 7.23 through Fig. 7.26 respectively. These accelerometers are located in the foundation soil along the centerline of the model, with ACC 1486 near the concrete base, and ACC 1487 midway between the base of the surface structure and the concrete base, and ACC 2033 and ACC 1928 near the base of the surface structure. The magnitude and the frequency content of the computed responses are similar to the corresponding measured responses. The comparisons in terms of peak acceleration values shown in Table 7.3 are quite good.

Table 7.3 indicates that the computed responses with and without slip elements show little differences. However, predictions are generally better when the slip elements are used. It appears, however, that very little slip occurs during shaking.

Figs. 7.27 to 7.29 show the comparison of measured acceleration responses with the computed responses at the locations ACC 1908, ACC 1258 and ACC 1225 respectively. At location ACC 1908, agreement between the measured and computed responses in terms of magnitude and frequency content, as shown in Fig. 7.27, is good. The difference in peak acceleration values with and without slip elements is not very significant although again prediction with slip elements is better.

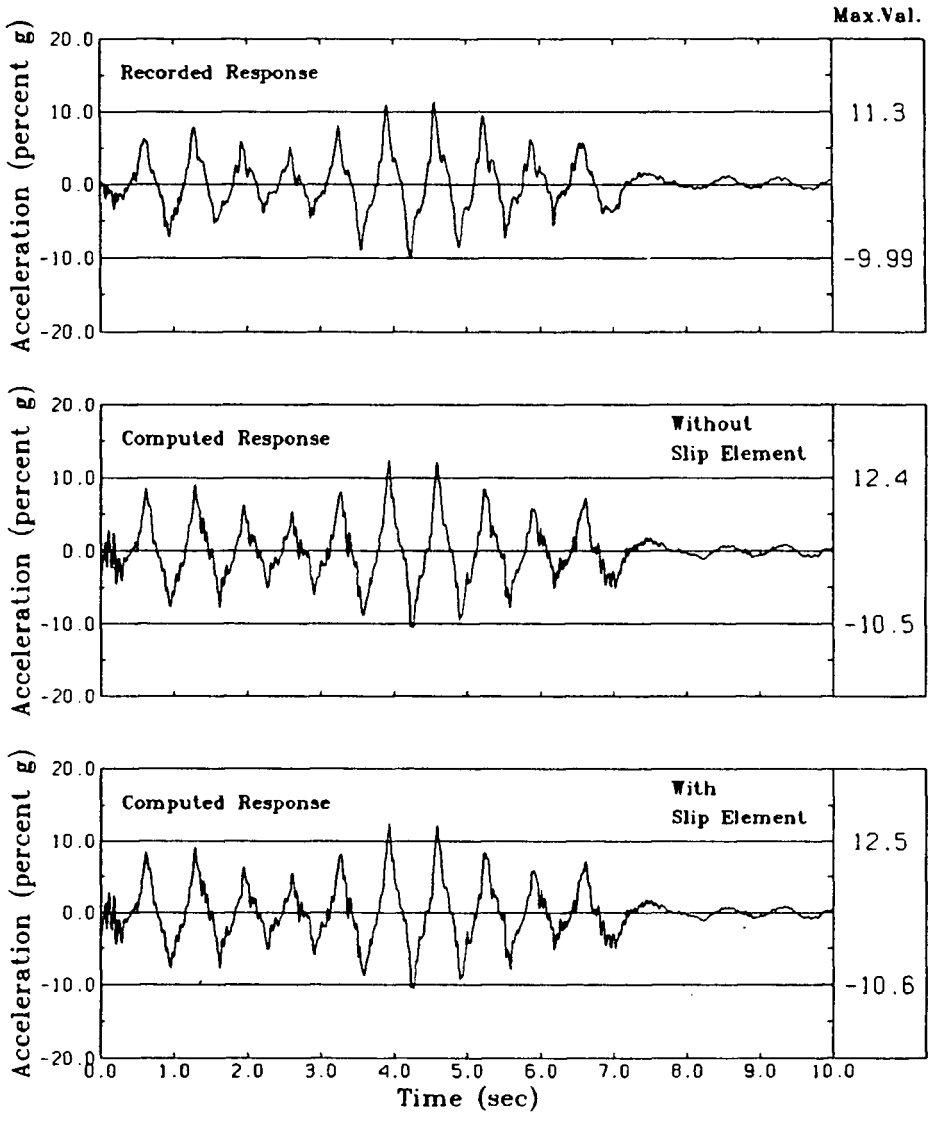

Fig. 7.23 Computed and Measured Accelerations at the Location of ACC 1486 in Test LDO2/EQ4

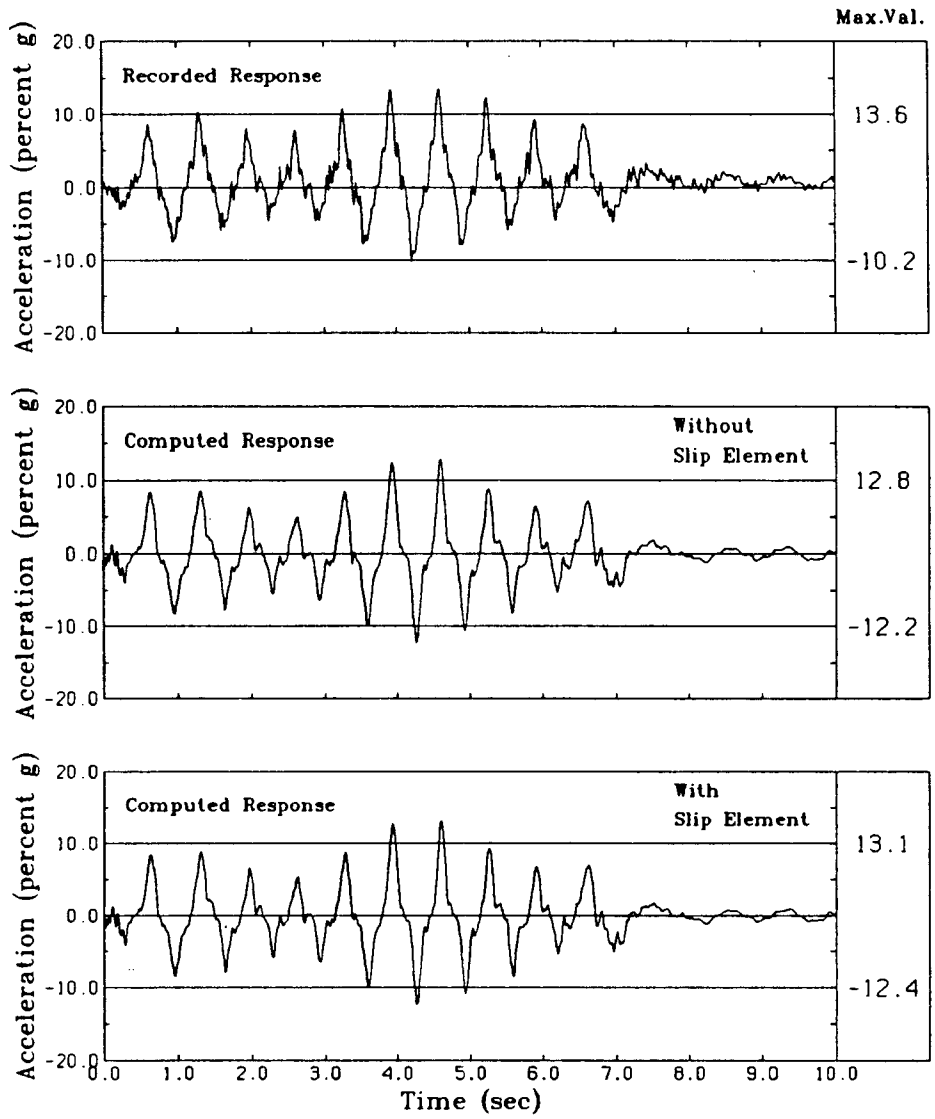

Fig. 7.24 Computed and Measured Accelerations at the Location of ACC 1487 in Test LDO2/EQ4

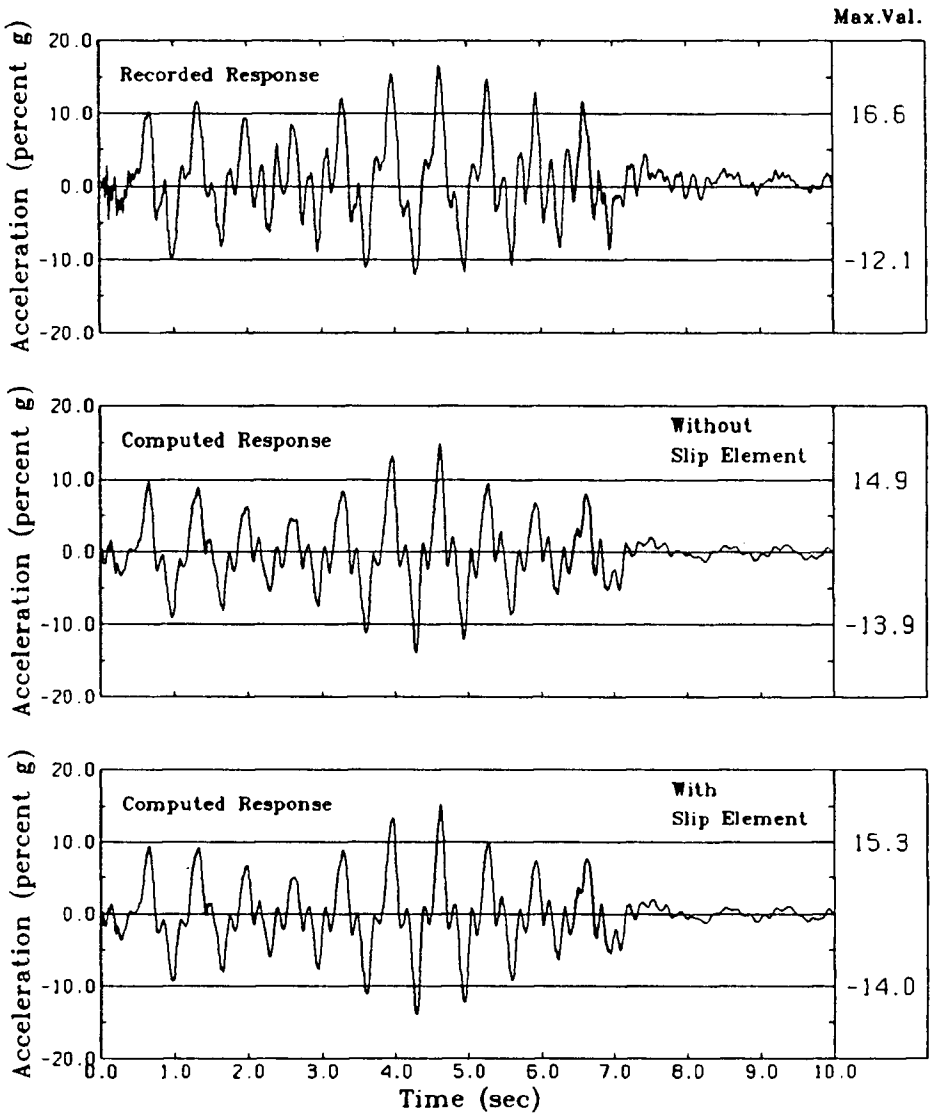

Fig. 7.25 Computed and Measured Accelerations at the Location of ACC 2033 in Test LDO2/EQ4

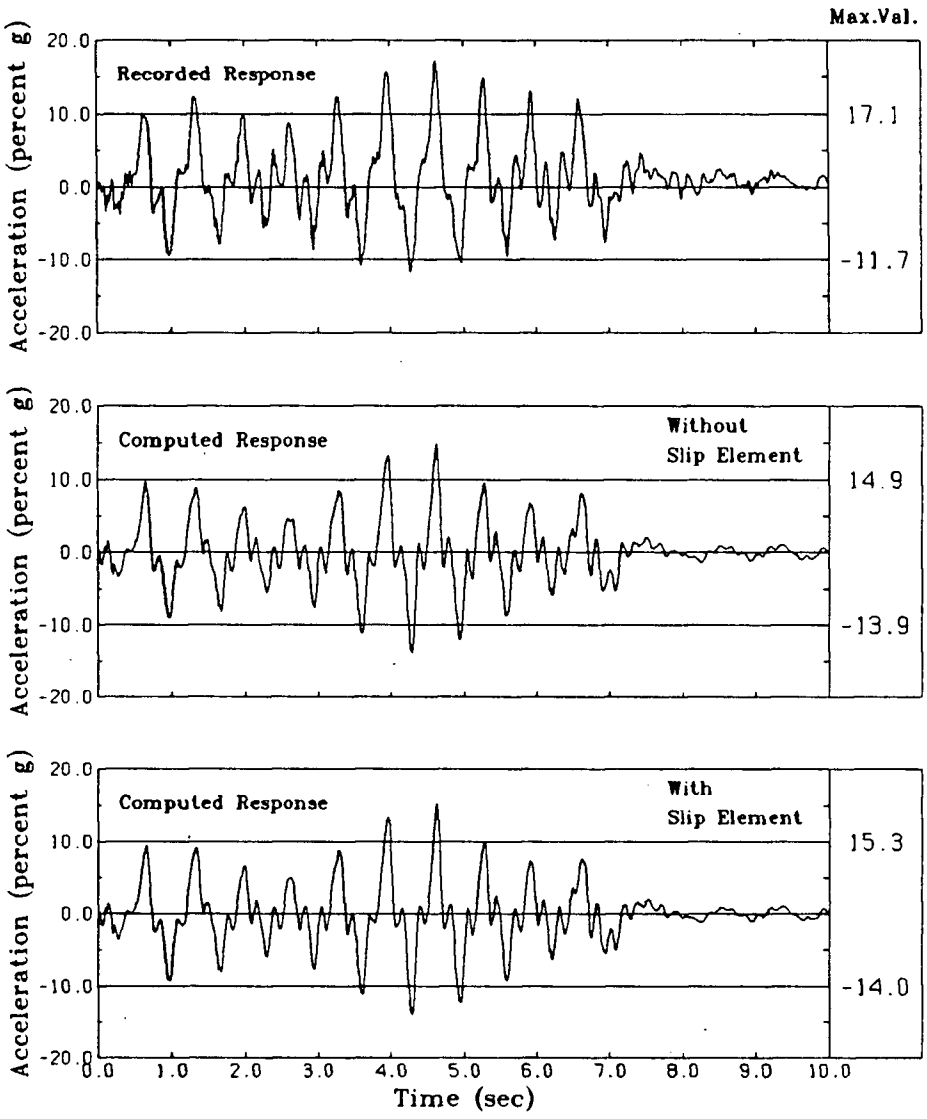

Fig. 7.26 Computed and Measured Accelerations at the Location of ACC 1928 in Test LDO2/EQ4

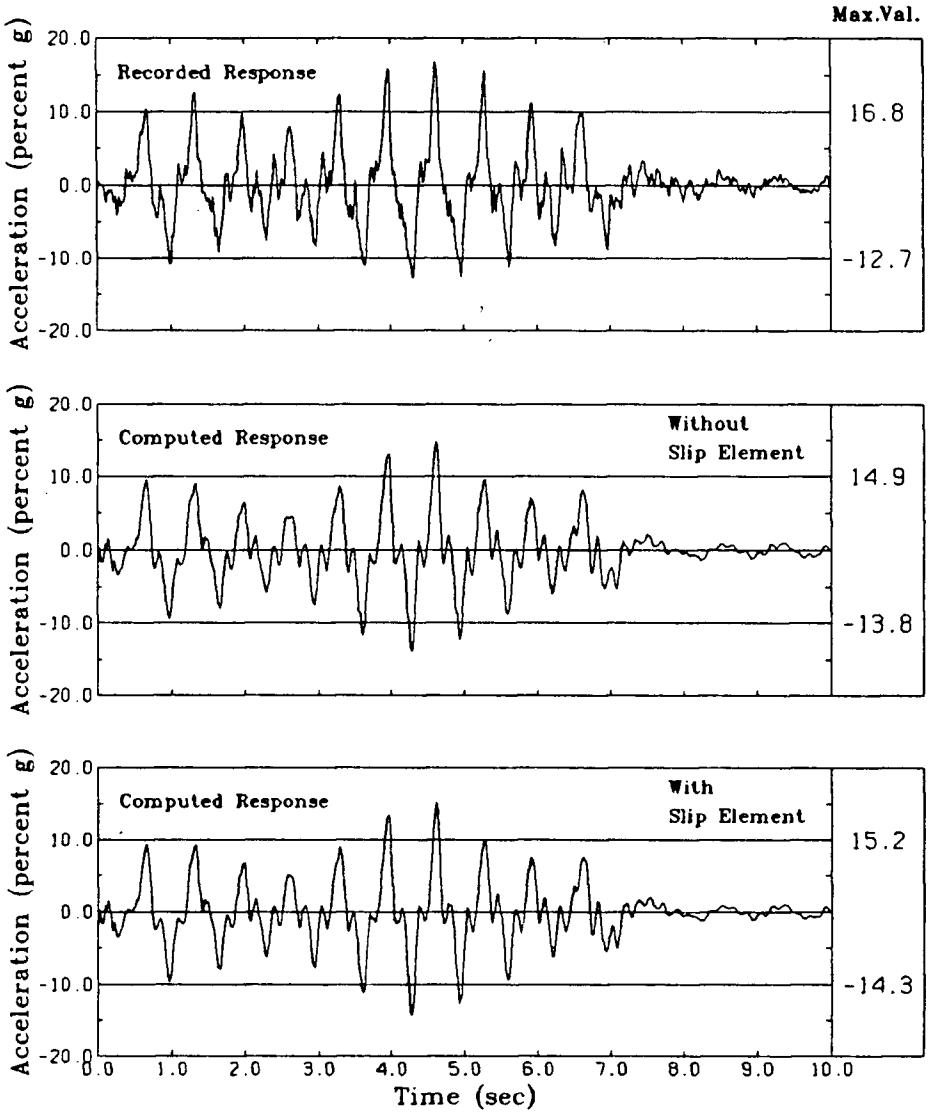

Fig. 7.27 Computed and Measured Accelerations at the Location of ACC 1908 in Test LDO2/EQ4

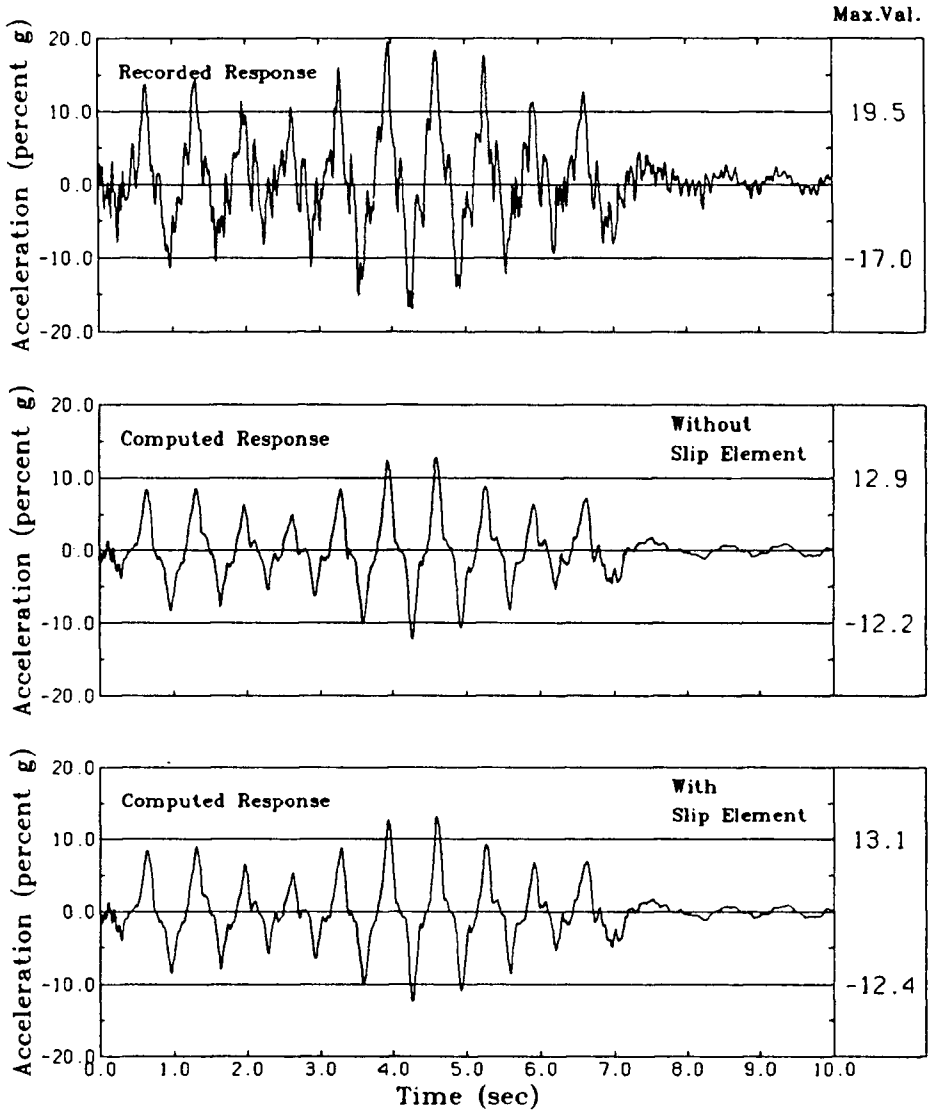

Fig. 7.28 Computed and Measured Accelerations at the Location of ACC 1258 in Test LDO2/EQ4

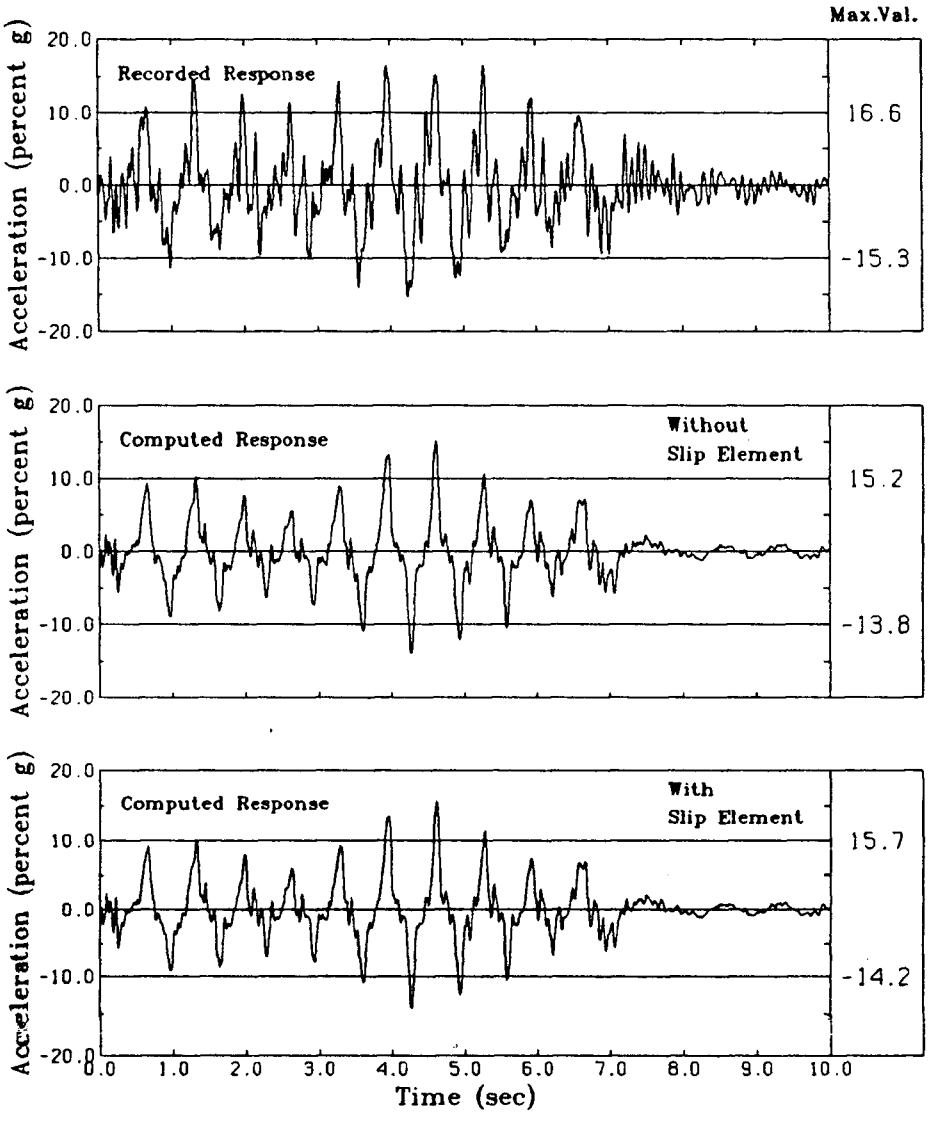

Fig. 7.29 Computed and Measured Accelerations at the Location of ACC 1225 in Test LDO2/EQ4

Table 7.3 Comparison of Peak Acceleration in Test LDO2/EQ4

Transducer No.	Measured (%g)	Computed (%g)	Computed (%g)
		Without slip elements	With slip elements
ACC 1486	11.3	12.4	12.5
ACC 1487	13.6	12.8	13.1
ACC 2033	16.6	14.9	15.3
ACC 1928	17.1	14.9	15.3
ACC 1908	16.8	14.9	15.2
ACC 1583	18.4	16.3	17.0

Measured acceleration histories at ACC 1258 and ACC 1225 show higher peak values and more high frequency noise than the computed responses. ACC 1487 together with ACC 1908 may provide some indication as to whether ACC 1258 record is anomalous or not. ACC 1487 is at the same elevation as ACC 1258 and ACC 1908 is at the same distance away from the centerline as ACC 1258. Clearly both of them do not show the high frequency characteristics as seen in the ACC 1258 record. Also the peak values in the ACC 1258 record are in excess of those in ACC 1487. Therefore it is apparent that the ACC 1258 record contains responses other than the motions resulting from shear wave transmission from the base. The fact that ACC 1258 has recorded significant responses after the earthquake supports the aforementioned notion. The same conclusion may be extended to the ACC 1225 record. In centrifuge tests, the measured acceleration responses may usually have components other than those resulting from shear wave transmission from the base. These are motions due to container vibrations and are transmitted to soil

through the side walls and the top of the container. These motions are usually of the high frequency type and contain negligible energy. One of the other possible sources for the spiky high frequecy response is the tension in the transducer leads as discussed in section 5.7.1. However, TARA-3 analysis takes into account only the motions resulting from the base input. Hence, it is not surprising to see differences between the computed and measured responses. Despite this, the comparison at location ACC 1225 is good.

Figs 7.30 to 7.32 show the comparison of measured acceleration responses to that of the computed responses at locations ACC 1583, ACC 1932 and ACC 1938 respectively. These accelerometers are mounted on the structure in such a way that ACC 1583 measures the horizontal acceleration at the middle of the structure and ACC 1932 and ACC 1938 measure the vertical (rocking) accelerations at opposite edges of the structure. It is apparent from the measured acceleration responses that the frequency content of the vertical accelerations is very different from that of the horizontal acceleration at the same level in the structure. The frequency content of the horizontal acceleration (ACC 1583) is similar to that of the input motion while the frequency content of vertical accelerations (ACC 1932 and ACC 1938) is much higher than that of the input motion (ACC 1544). This phenomenon is reproduced in the corresponding computed acceleration responses. The high frequency content in vertical accelerations is due to the fact that the foundation soils are much stiffer under the normal compressive stresses due to rocking than under the shear stresses induced by the horizontal accelerations. As shown in Fig. 7.30 and Table 7.3, the acceleration response at the location ACC 1583 is predicted satisfactorily.

As noted earlier, both ACC 1932 and ACC 1938 have recorded significant responses even after the earthquake motion ceased. As in the case of ACC 1258 and ACC 1225, this casts doubts as to whether or not both ACC 1932 and ACC 1938 were measuring only the motions resulting from the base input. The vertical accelerations appear to be relatively

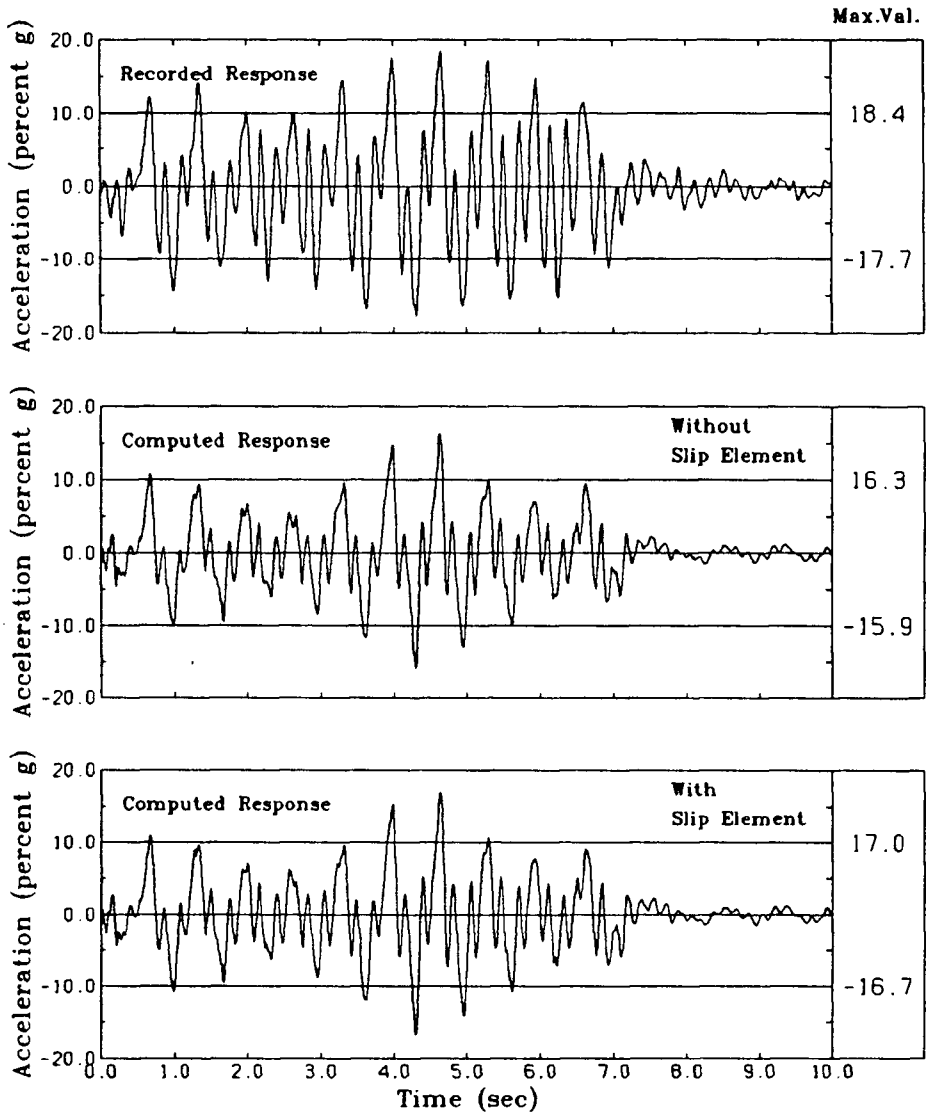

Fig. 7.30 Computed and Measured Accelerations at the Location of ACC 1583 in Test LDO2/EQ4

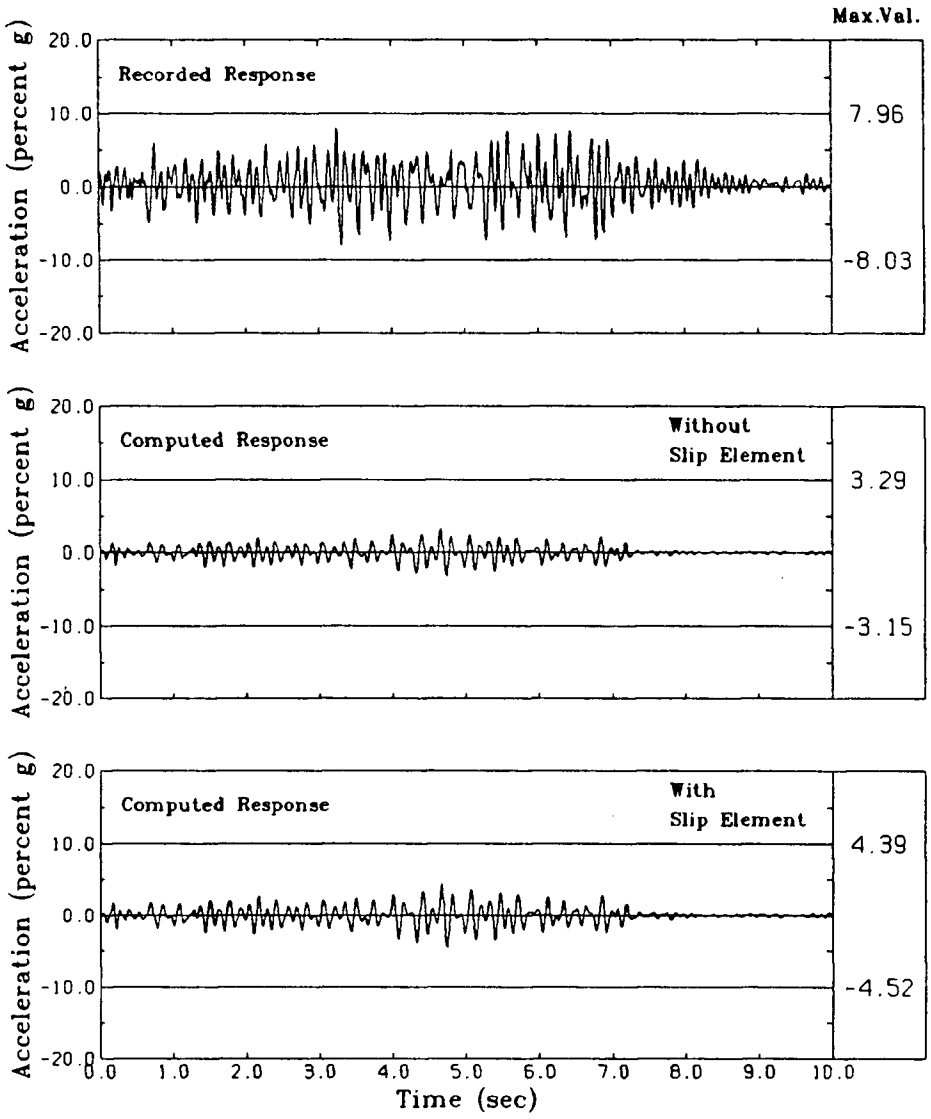

Fig. 7.31 Computed and Measured Accelerations at the Location of ACC 1932 in Test LDO2/EQ4

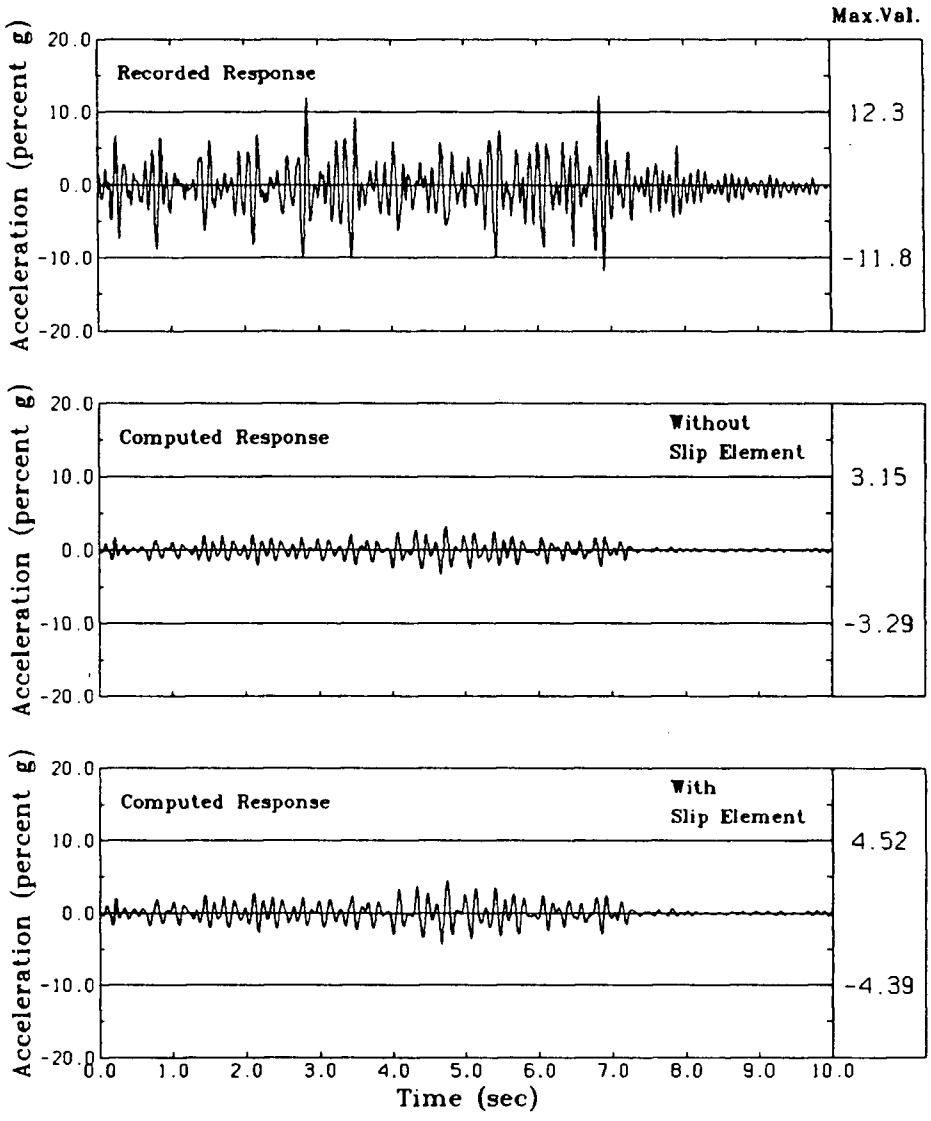

Fig. 7.32 Computed and Measured Accelerations at the Location of ACC 1938 in Test LDO2/EQ4

more sensitive to the presence of high frequency noise than the horizontal accelerations. ACC 1932 and ACC 1938, which are located symmetrically about the centerline, are supposed to record almost similar histories showing a phase lag of 180 degrees. It is clear that both accelerometers are measuring very different peak values. As seen in Fig. 7.31 and Fig. 7.32, the peak values measured by ACC 1932 and ACC 1938 are 7.55%g and 12.5%g respectively. Recall that the input motion has high energy at 1.5 Hz and relatively low energy at 4.5 and 7.5 Hz. Fig. 7.33 and Fig. 7.34 show the Fourier spectrum of ACC 1932 and ACC 1938 records. It is seen that both have significant energy at frequencies higher than 7.5 Hz, which may be primarily due to noise. Therefore, in an attempt to isolate the noise, these records were passed through a low pass 8.0 Hz filter whereby responses at frequencies higher than 8.0 Hz were removed. Fig. 7.35 and Fig. 7.36 compare the filtered responses with computed responses at the locations of ACC 1932 and ACC 1938 respectively. The comparison in terms of frequecy contents is fairly good at both locations but the peak values are somewhat different to each other.

7.2.4 Comparison of Settlements in Test LDO2/EQ4

The computed and measured vertical settlements at the locations of LVDT 48406, LVDT 48407 and LVDT 46997 are tabulated at prototype scale in Table 7.4. The computed values are for the analysis with slip elements. LVDT 48406 and LVDT 48407 were mounted on opposite edges of the structure, and LVDT 46997 was located on the flat crest of the sand berm. At all three locations the comparison is good between computed and measured settlements.

The complete settlement pattern as computed by TARA-3 is shown in Fig. 7.37. The dotted lines show the initial shape and the solid lines show the computed post-earthquake shape taking only vertical settlements into account. The circular points indicate the initial

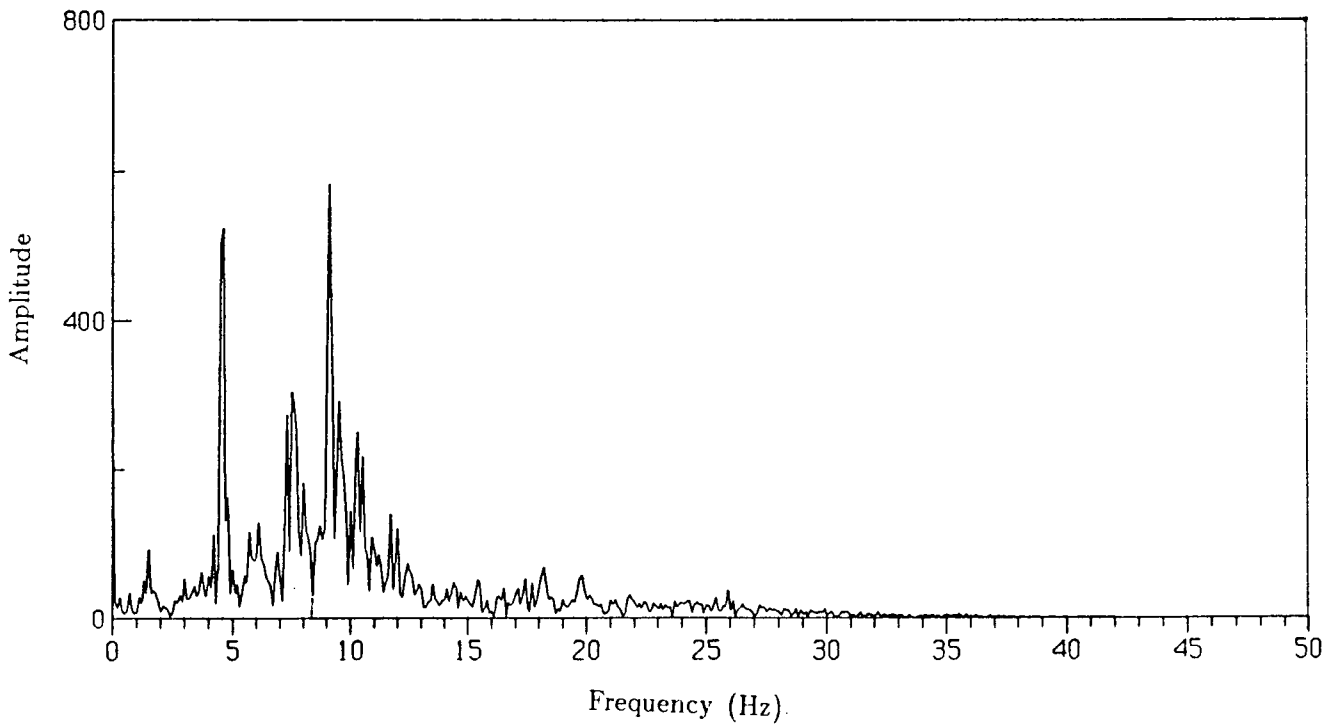

Fig. 7.33 Fourier Spectrum of ACC 1932 Record in Test LDO2/EQ4

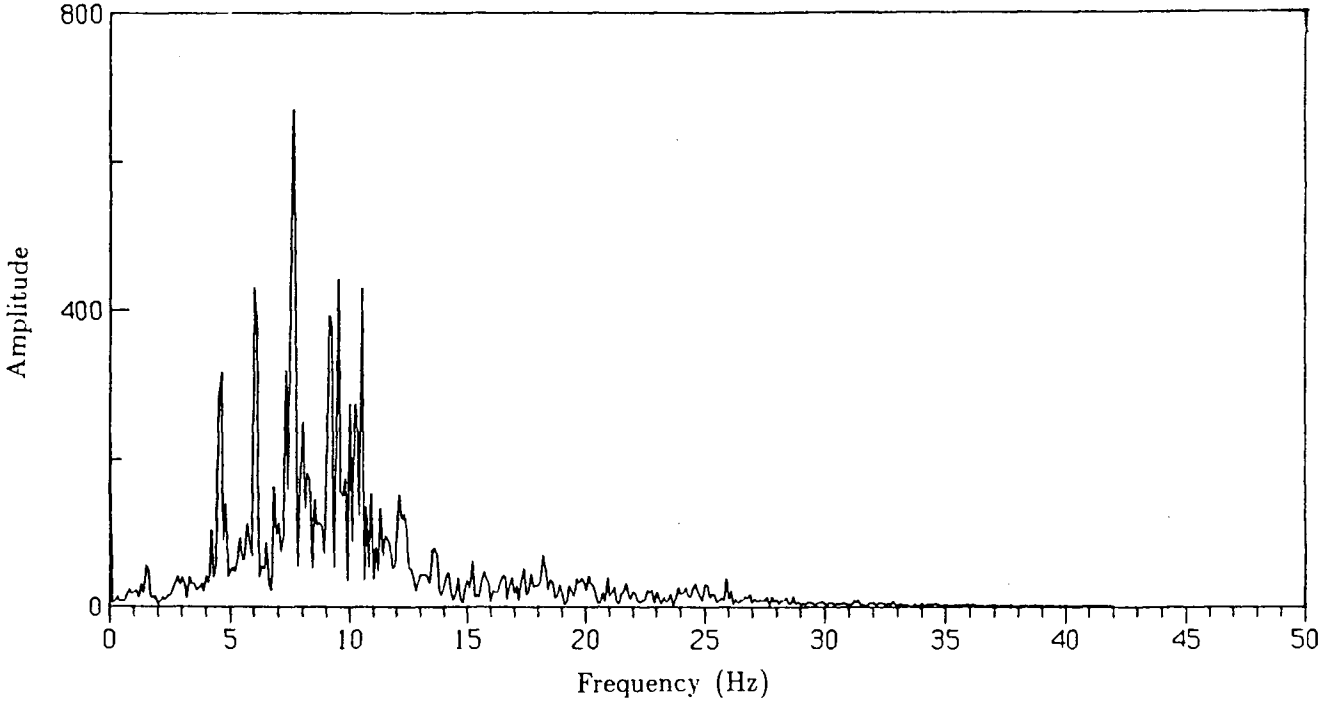

Fig. 7.34 Fourier Spectrum of ACC 1938 Record in Test LDO2/EQ4

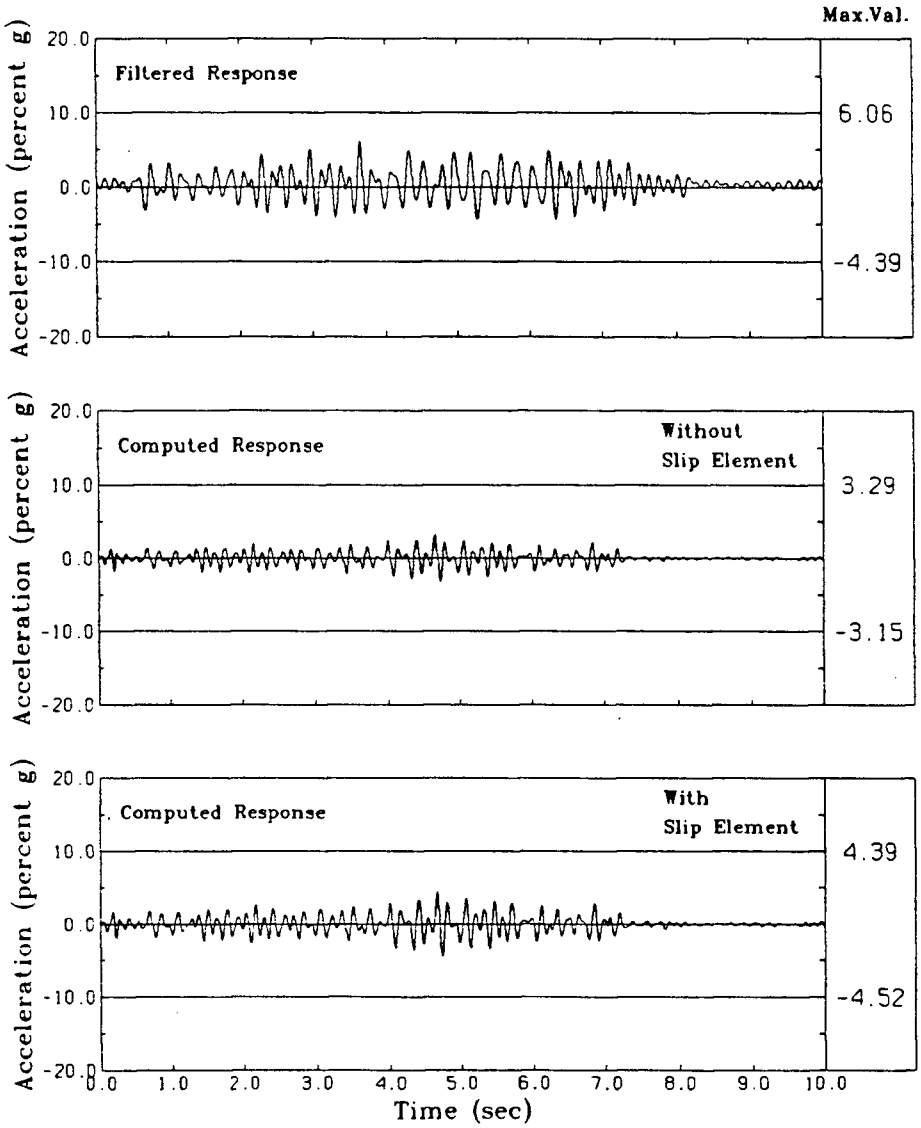

Fig. 7.35 Computed and Filtered Accelerations at the Location of ACC 1932 in Test LDO2/EQ4

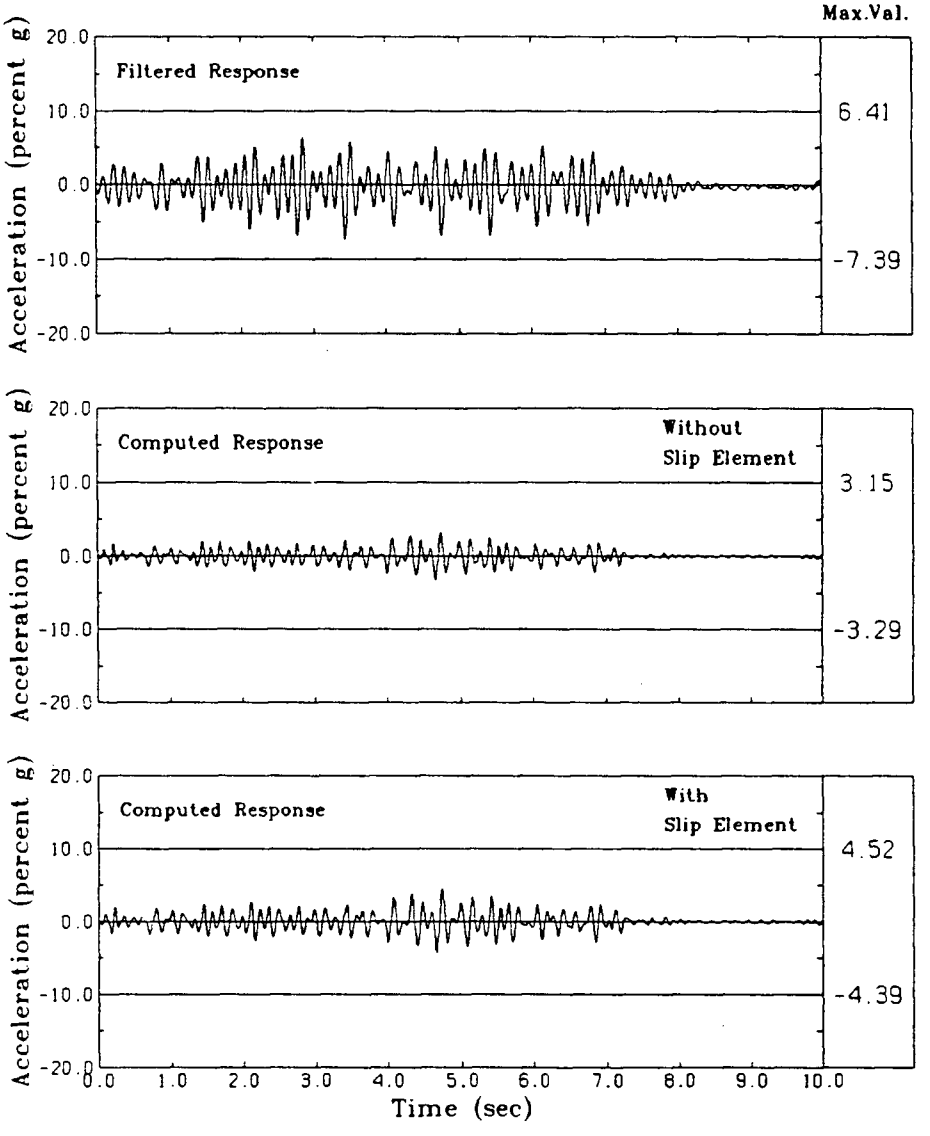

Fig. 7.36 Computed and Filtered Accelerations at the Location of ACC 1938 in Test LDO2/EQ4

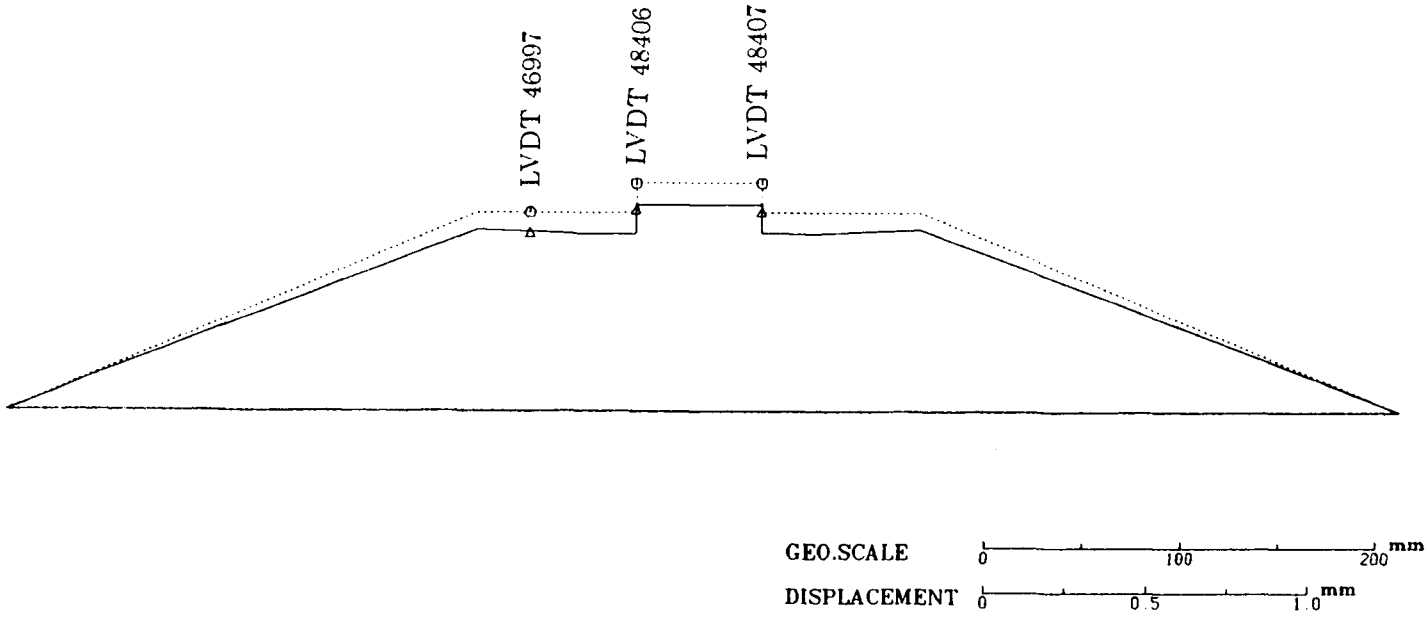

Fig. 7.37 Settlement Pattern in Test LDO2/EQ4

locations of the tips of the LVDTs and the triangular points show the final positions. It is clear that that the agreement between the computed and the measured vertical settlements is good.

Table 7.4 Comparison of Settlements in Test LDO2/EQ4

Transducer No.	Measured (mm)	Computed (mm)
46997	4.8	5.0
48407	5.3	6.9
48406	5.3	6.3

As noted earlier, the vertical settlements could not be measured satisfactorily on the slopes due to sliding of materials during shaking, the effects of wind erosion and the difficulties in setting up the LVDT properly on the slopes.

7.3 Verification Study Based on Test Series RSS110

7.3.1 Centrifuge Model in Test Series RSS110

A schematic view of a 2-D plane strain model in which the structure is embedded in the soil is shown in Fig. 7.38. The embankment was constructed by dry method described in section 5.5.1 using Leighton Buzzard B.S.S 52/100 sand. The estimated relative density of the sand is 64%. The sand foundation is 110mm high and has a base 900mm wide. The side slopes are at 2.2:1. The length of sand foundation perpendicular to the direction of shaking is 480mm.

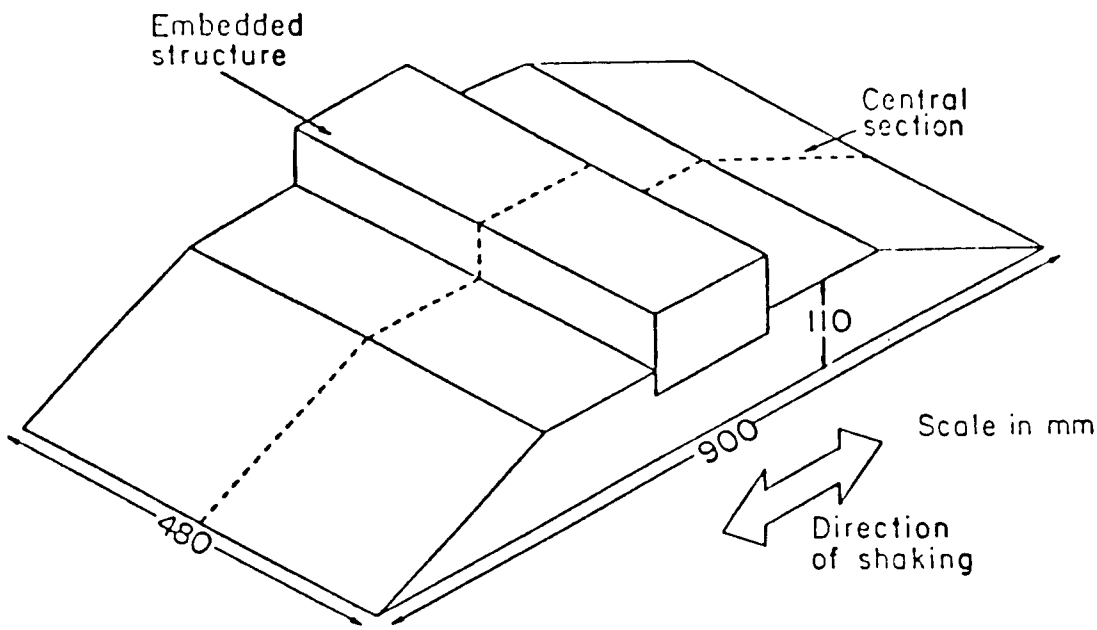

Fig. 7.38 Schematic of a Model Embankment With Embedded Structure

The heavy structure is made from a solid piece of aluminum alloy and has dimensions 105mm wide by 108mm high in the plane of shaking. The length perpendicular to the plane of shaking is 470mm. The structure is embedded to a depth of 25mm in the sand foundation. Coarse sand was glued to the base of the structure to prevent slip between structure and sand.

During the test the model experienced a nominal centrifugal acceleration of 80g. The model, therefore, simulated a structure approximately 8.64m in height, 12m in width and embedded to a depth 2m in sand foundation. The average contact pressure between the structure and sand foundation was approximately 240 kPa.

The complete instrumentation of the model is shown in Fig. 7.39. The input motion was measured by ACC 3441 mounted to the concrete base. Accelerometers ACC 1925, ACC 1552 and ACC 1572 measured vertical accelerations while the other accelerometers measured horizontal accelerations.

7.3.2 Model Response in Test RSS110

The model response to a simulated earthquake EQ1 is shown in Fig. 7.40. ACC 1925 and ACC 1552, which were located in the sand foundation, show large baseline shifts and they were not used in the study. These shifts may be due to drifts caused by poor earth connection (Steedman 1985). It is also probable that the gauges rotated so that they measure a mixture of vertical and horizontal accelerations. ACC 1572 is also very highly suspect because of the large baseline shift and the very noisy response. All accelerometer responses contain high frequecy noises and therefore they were filtered using a 10 Hz low pass filter.

The input motion measured by ACC 3441 is shown in Fig. 7.41 along with the baseline corrected motion at prototype scale. The baseline corrected motion was used as the input

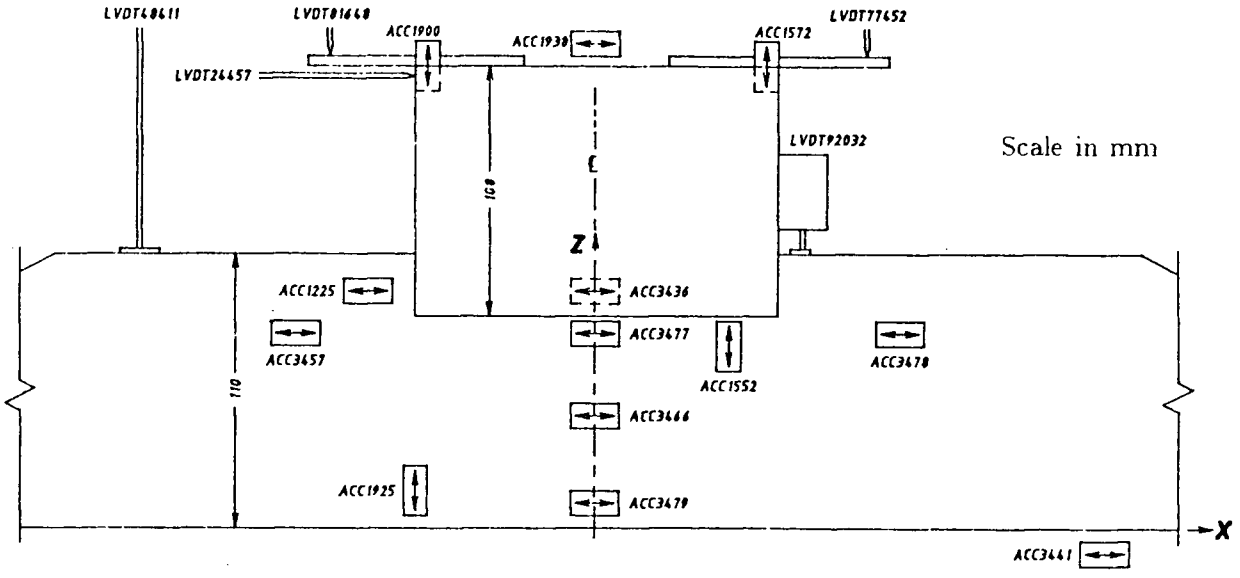

Fig. 7.39 Instrumented Model in Test Series RSS110

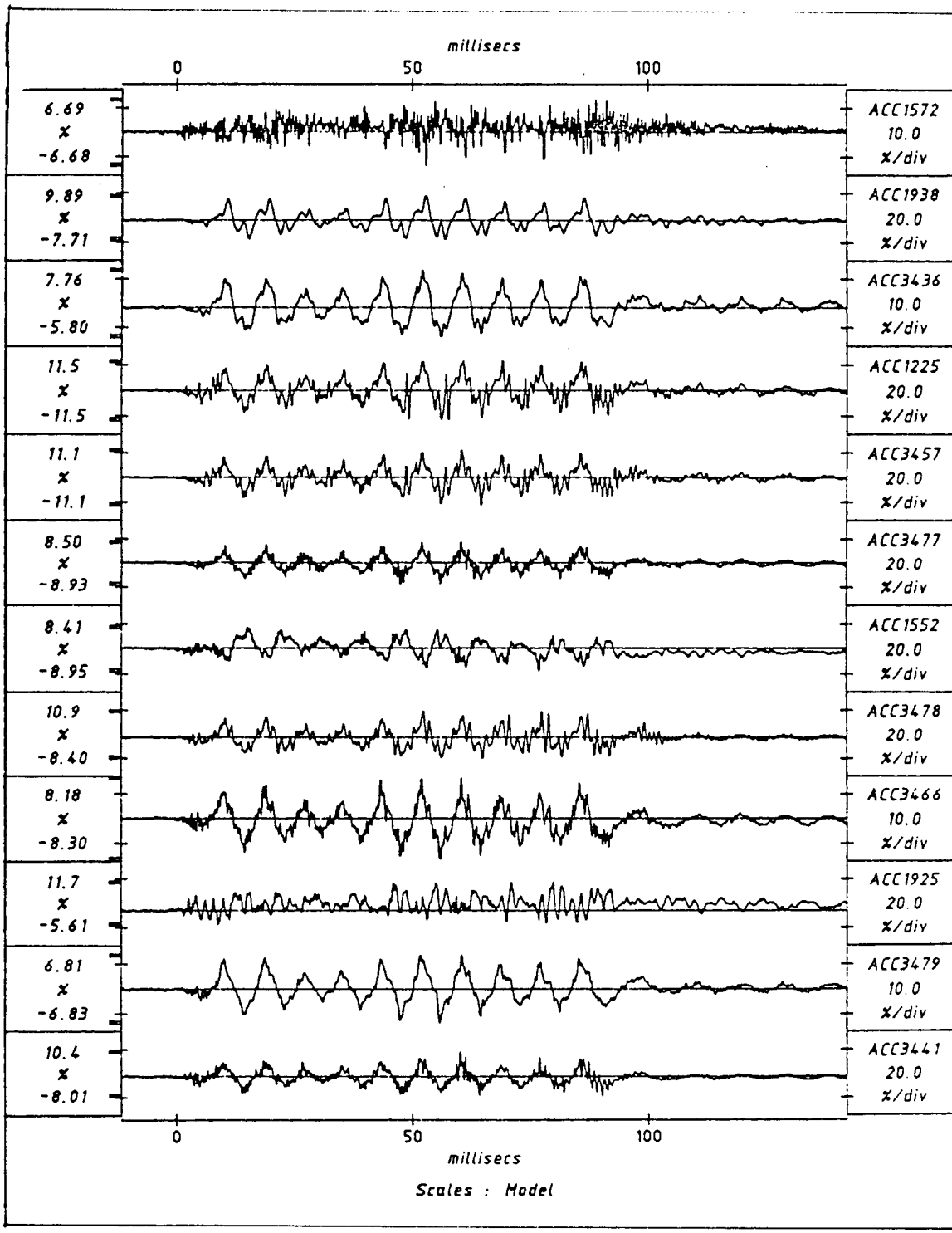

Fig. 7.40 Model Response in Test RSS110/EQ1

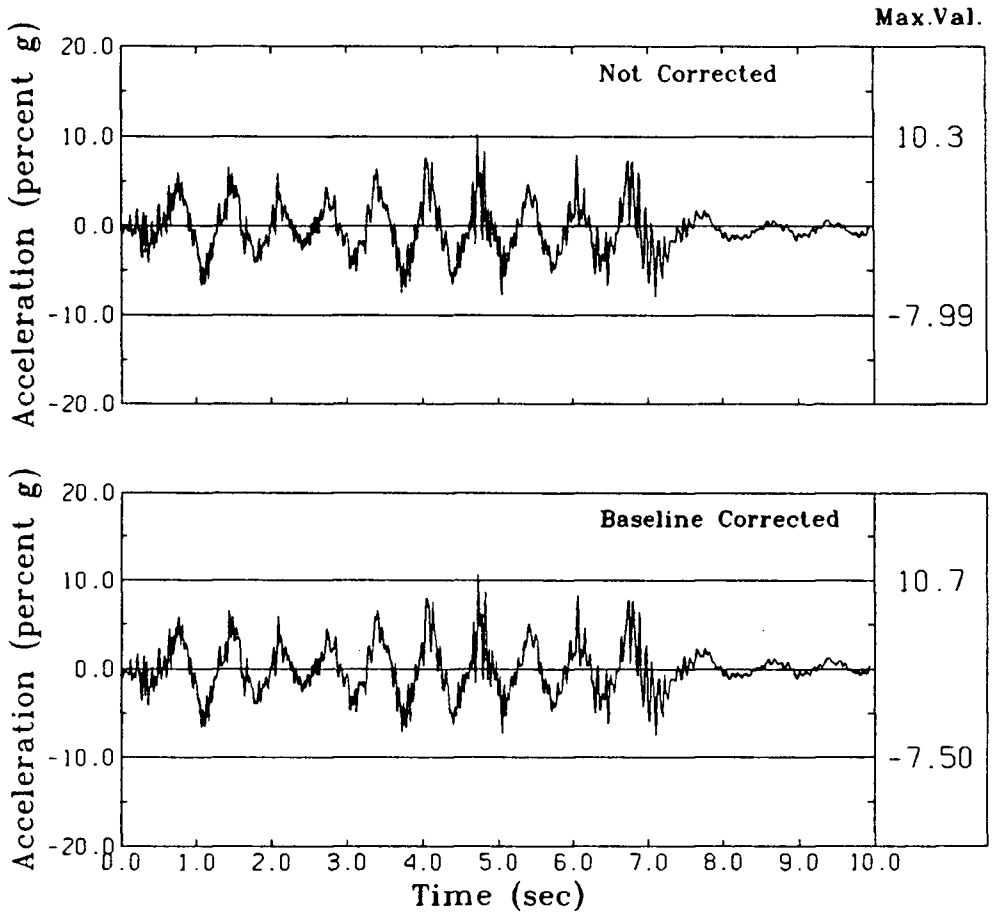

Fig. 7.41 Input Motion for Test RSS110/EQ1

for the TARA-3 analysis.

7.3.3 Comparison of Acceleration Responses of Test RSS110/EQ1

Figs. 7.42 to 7.44 compare the measured and computed acceleration responses at locations ACC 3479, ACC 3466 and ACC 3477 respectively. The comparison in terms frequency content and variation of amplitudes with time is good. The comparison of peak accelerations as shown in Table 7.5 is good at these locations.

Table 7.5 Comparison of Peak Accelerations in Test RSS110/EQ1

Transducer No.	Measured (%g)	Computed (%g)
ACC 3479	6.41	6.21
ACC 3466	7.10	6.50
ACC 3477	7.06	6.50
ACC 3478	10.6	7.42
ACC 3457	10.5	6.95
ACC 1225	11.6	6.88
ACC 1938	10.1	8.89
ACC 1572	3.79	3.76

ACC 3478 and ACC 3457 were located outside the edge of the structure and were placed symmetrically opposite about the centerline of the model. The comparison at these locations is shown in Fig. 7.45 and Fig. 7.46 respectively. Except for minor differences, the measured responses at these locations are similar. The measured responses contain higher

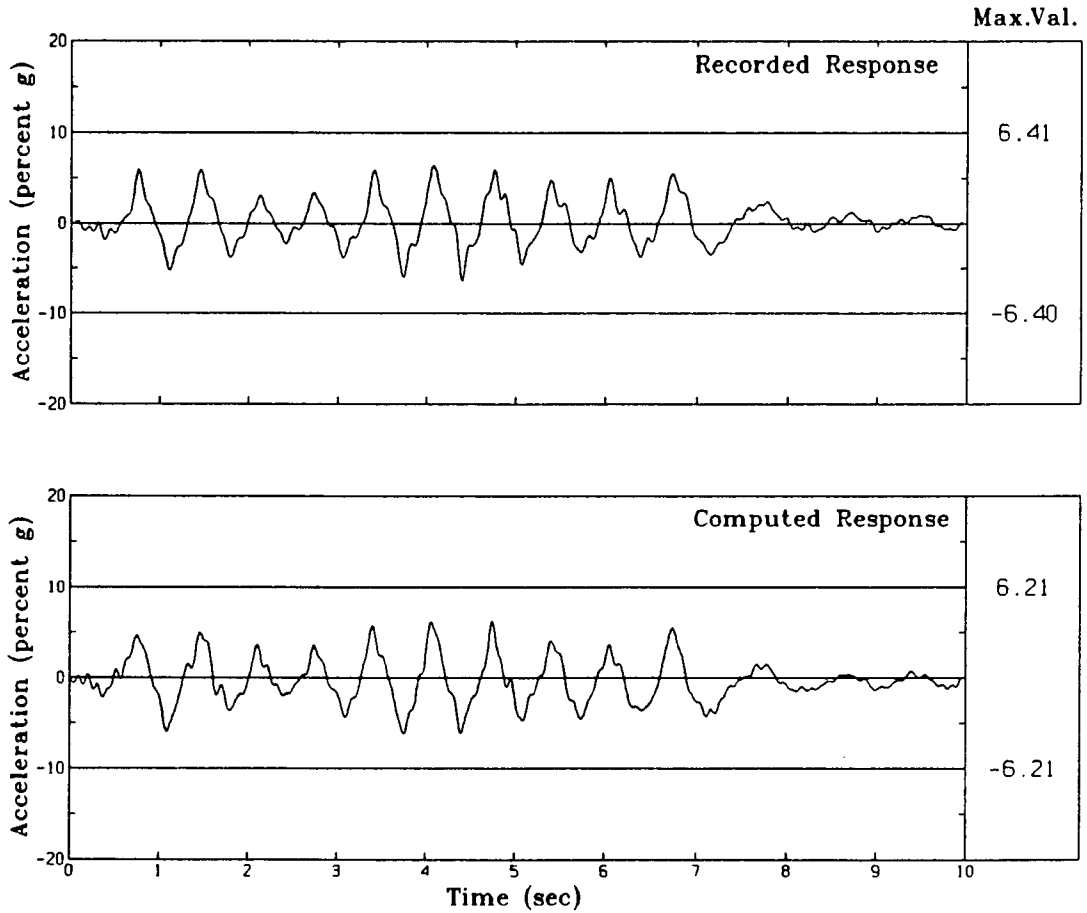

Fig. 7.42 Computed and Measured Accelerations at the Location of ACC 3479 in Test RSS110/EQ1

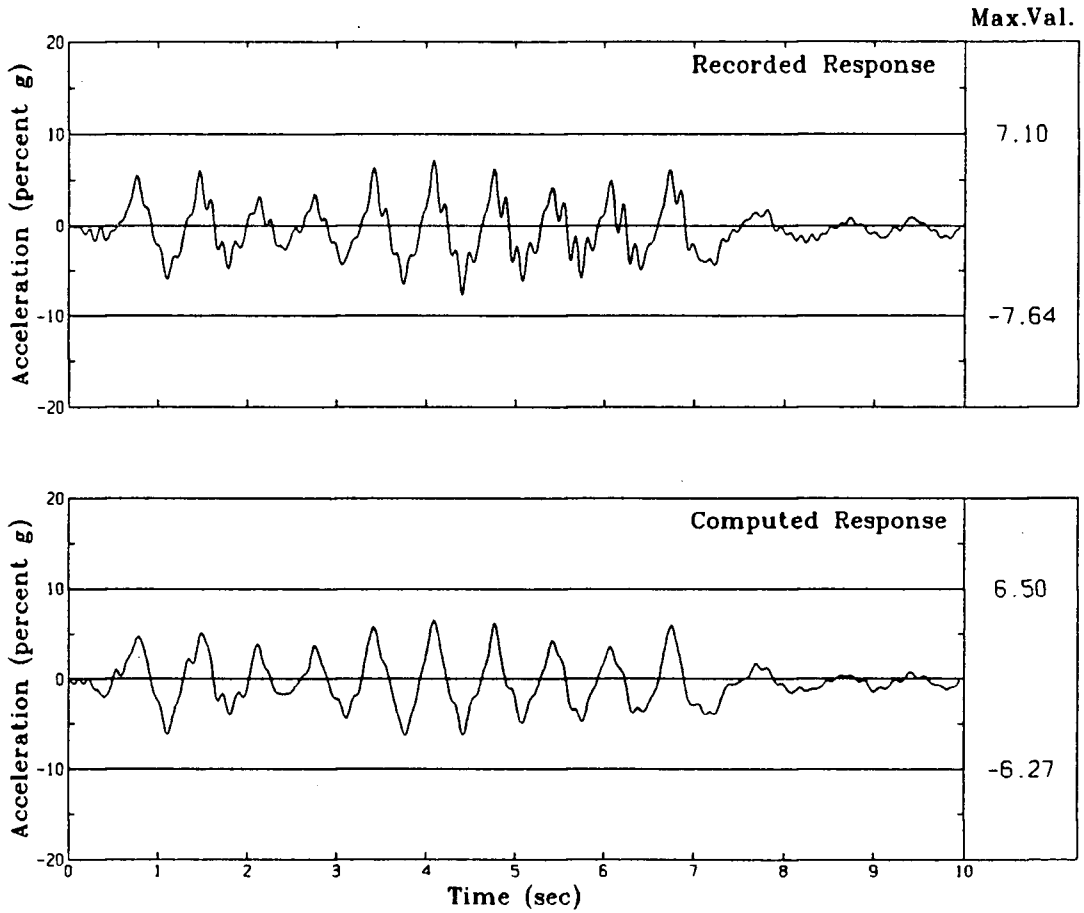

Fig. 7.43 Computed and Measured Accelerations at the Location of ACC 3466 in Test RSS110/EQ1

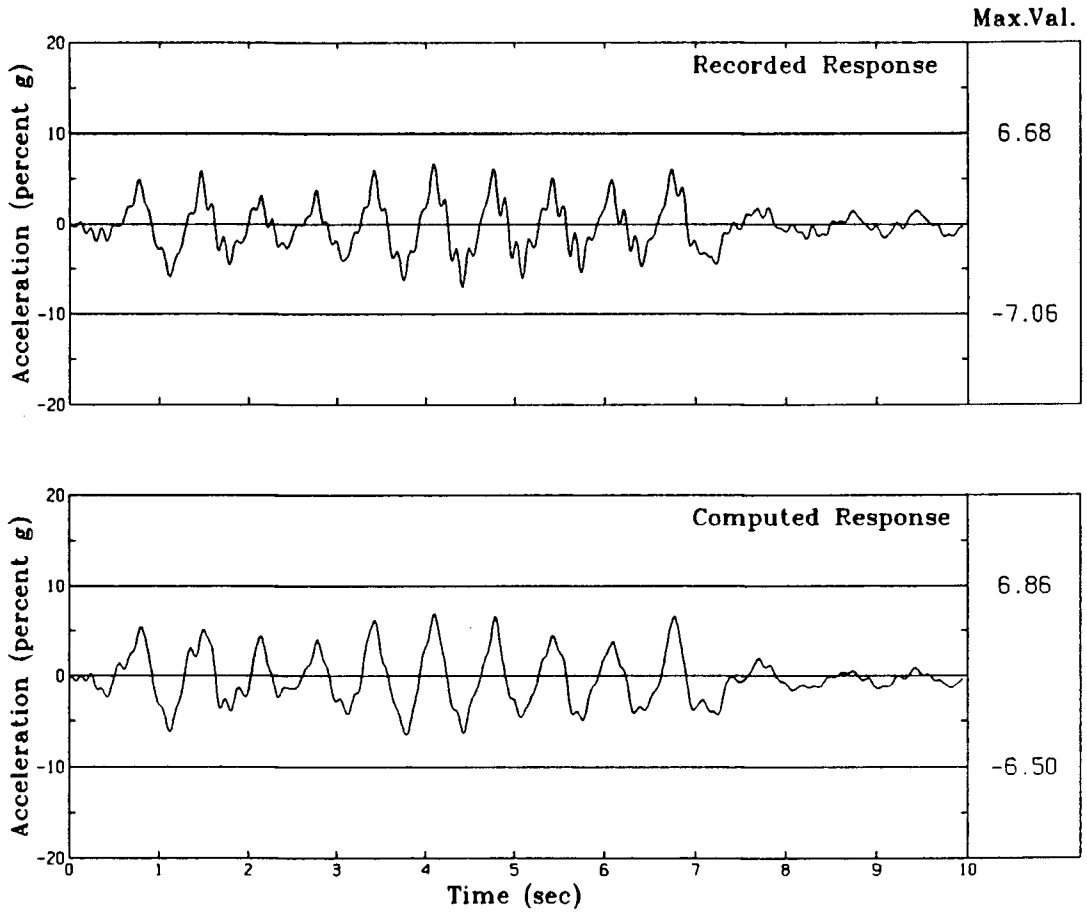

Fig. 7.44 Computed and Measured Accelerations at the Location of ACC 3477 in Test RSS110/EQ1

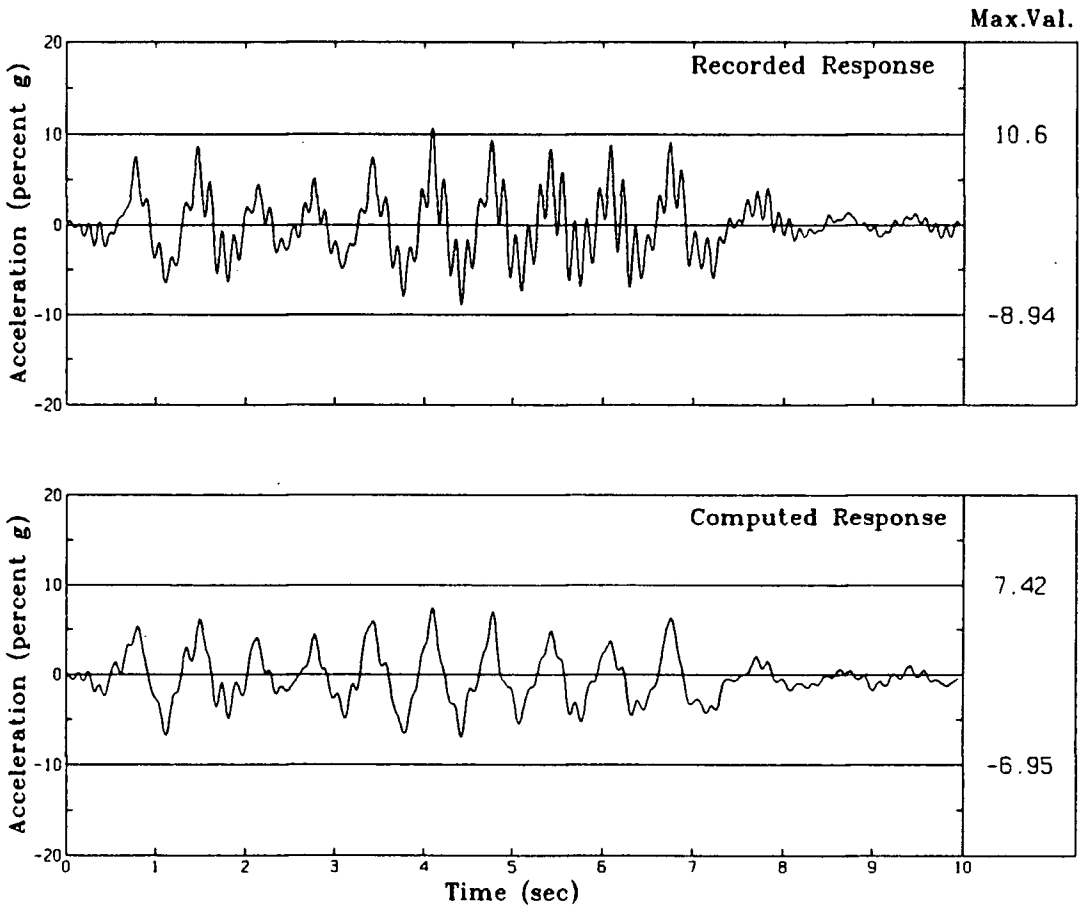

Fig. 7.45 Computed and Measured Accelerations at the Location of ACC 3478 in Test RSS110/EQ1

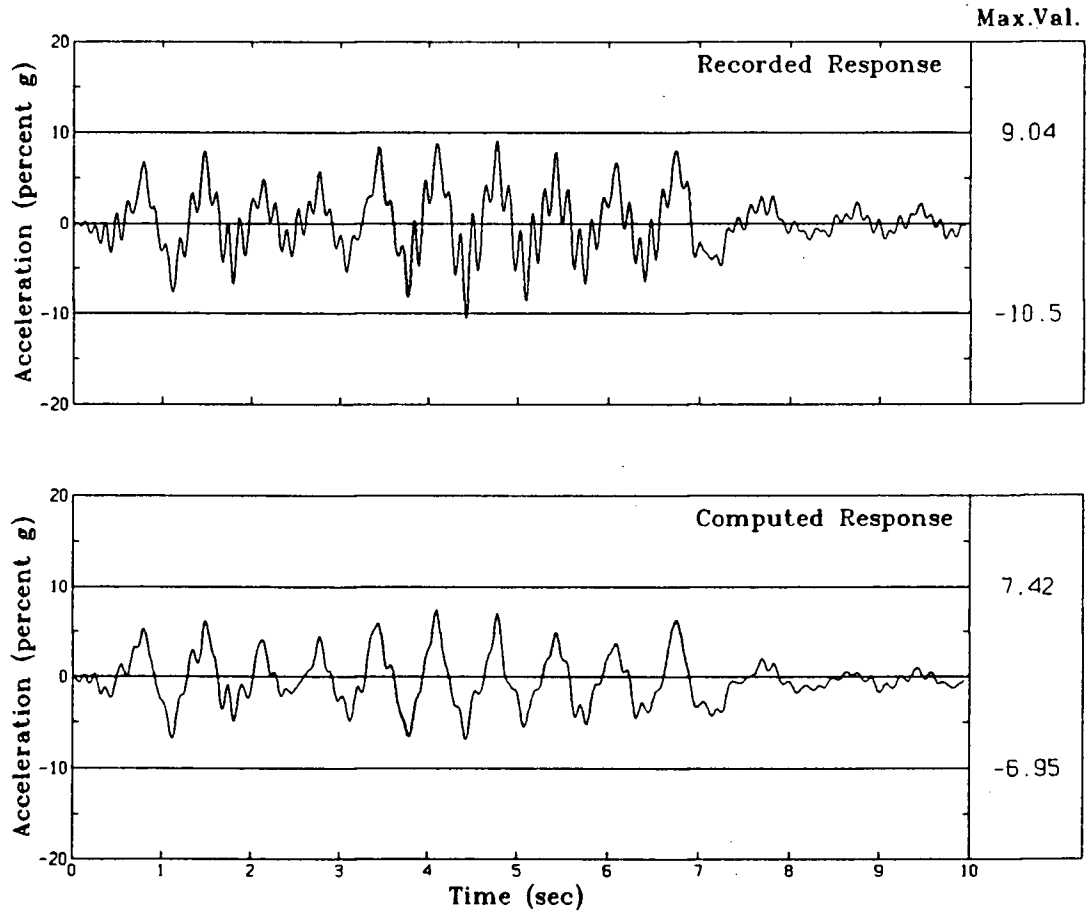

Fig. 7.46 Computed and Measured Accelerations at the Location of ACC 3457 in Test RSS110/EQ1

frequency contents than the computed responses and the measured peak amplitudes are consistently higher than the computed values. A similar order of difference is also observed at location ACC 1225 as shown in Fig. 7.47 and Table 7.5.

ACC 1938 was mounted on top of the structure to measure horizontal accelerations and ACC 1572 near the right hand edge to measure vertical accelerations. The measured and computed accelerations at location ACC 1938 are compared in Fig. 7.48. They are very similar in frequency content. The peak accelerations tabulated in Table 7.5 agree fairly closely.

The vertical acceleration due to rocking as recorded by ACC 1572 and those computed are shown in Fig. 7.49. Again, the computed accelerations closely match the recorded acceleration in both frequency contents and peak values.

7.3.4 Comparison of Settlement in Test RSS110/EQ1

The computed and measured settlements are tabulated in Table 7.6 at prototype scale. The comparison at locations on top of the structure (LVDT 81648 and LVDT 77452) is excellent with very little difference between the measured and computed values. However, at locations on the crest of the sand foundation (LVDT 48411 and LVDT 92032), the computed values are consistently higher than the measured value.

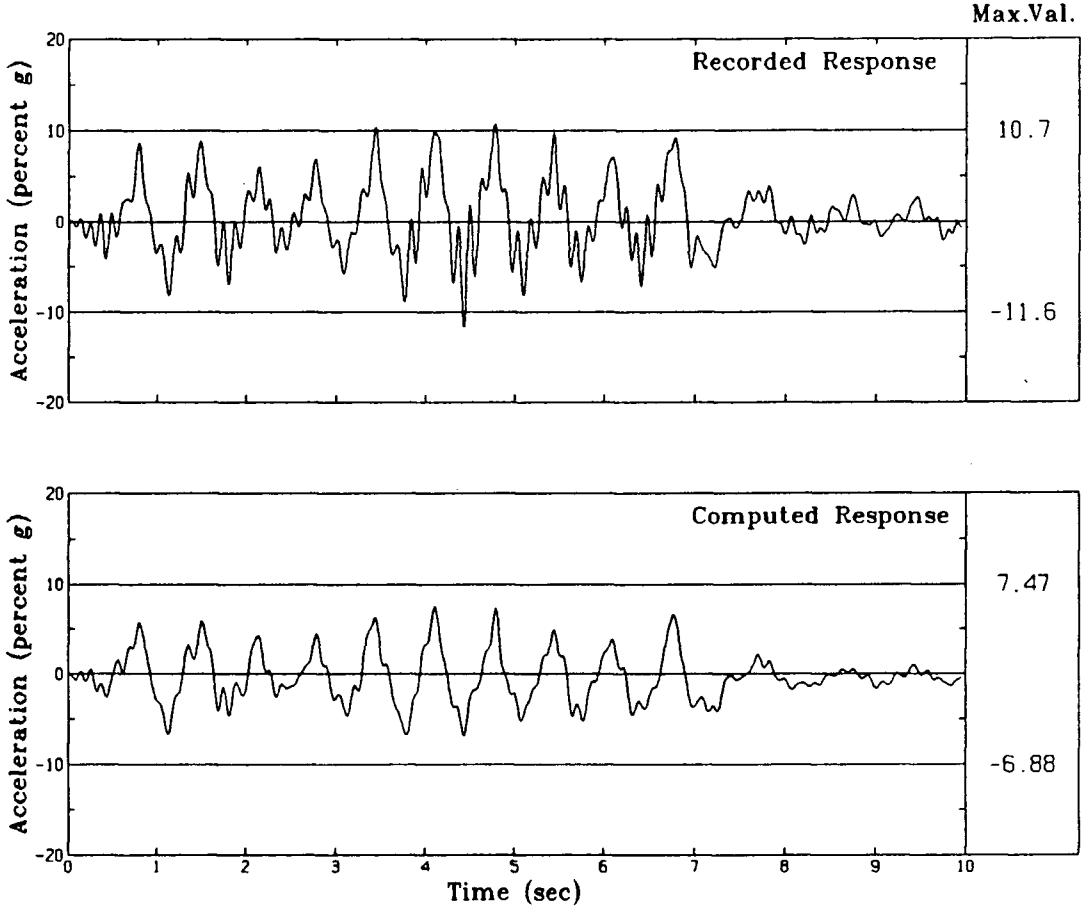

Fig. 7.47 Computed and Measured Accelerations at the Location of ACC 1225 in Test RSS110/EQ1

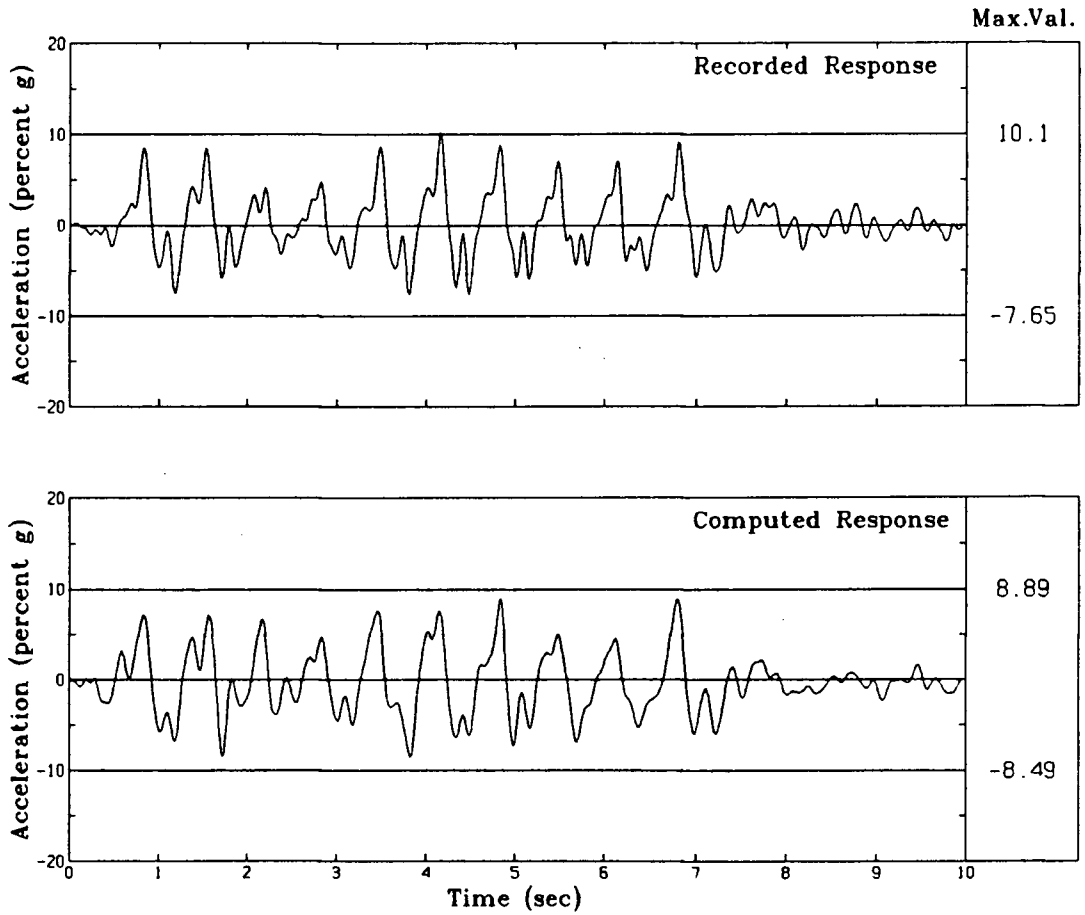

Fig. 7.48 Computed and Measured Accelerations at the Location of ACC 1938 in Test RSS110/EQ1

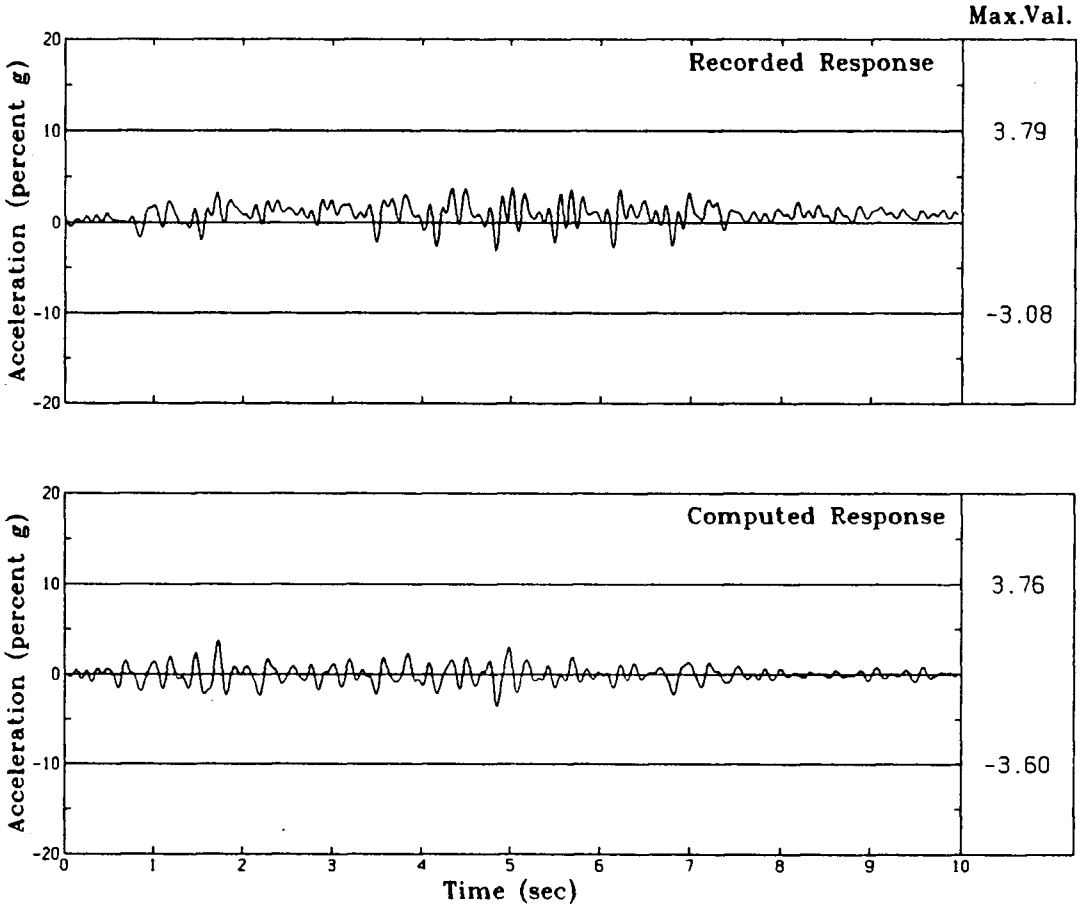

Fig. 7.49 Computed and Measured Accelerations at the Location of ACC 1572 in Test RSS110/EQ1

Table 7.6 Comparison of Settlements in Test RSS110/EQ1

Transducer No.	Measured (mm)	Computed (mm)
48411	2.4	3.6
81648	3.2	3.1
77452	3.2	3.5
92032	2.4	4.4

Part of this is due to the difficulty of making accurate measurements with the LVDTs in sand, especially when the dry sand is subject to mobilization by wind during flight.

The complete computed settlement pattern is shown in Fig. 7.50 along with the measured values. It should be noted that the settlements are plotted with a magnification of 300. The notations are same to those used in sections 7.1.4 and 7.2.4. It is clear that the measured and computed settlements lie closely at the locations on the top of the structure.

7.4 Verification Study Based on Test Series RSS90

7.4.1 Centrifuge Model in Test Series RSS90

A schematic view of a 3-D soil-structure model is shown in Fig. 7.51. The model was constructed by dry method as described in section 5.5.1 using Leighton Buzzard B.S.S 120/200 sand. The estimated relative density of the sand is 64%. The sand foundation was 110mm high, 900mm wide at the base and has side slopes of 2.2:1. The length of the sand foundation in the direction perpendicular to the plane of shaking is 480mm.

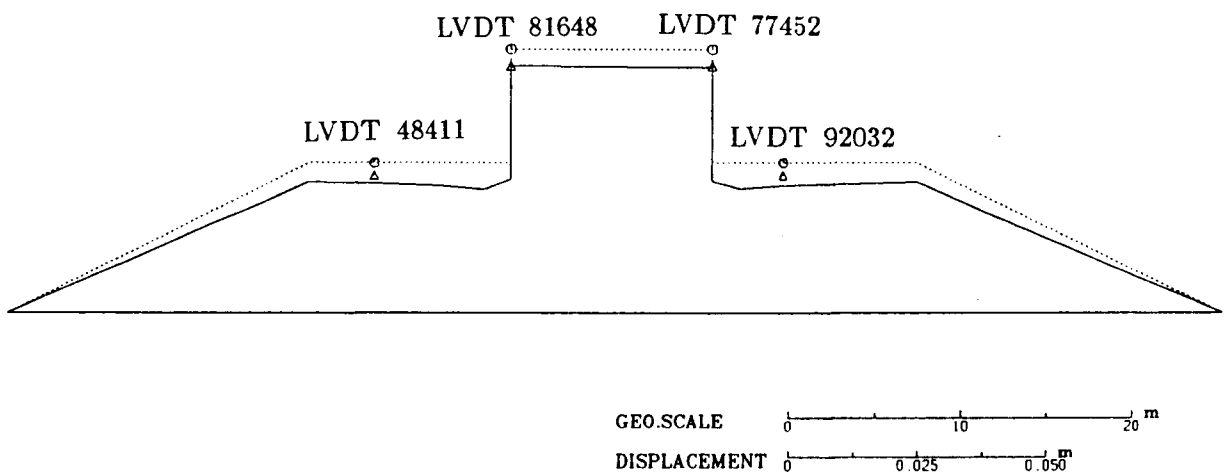

Fig. 7.50 Settlement Pattern in Test RSS110 EQ1

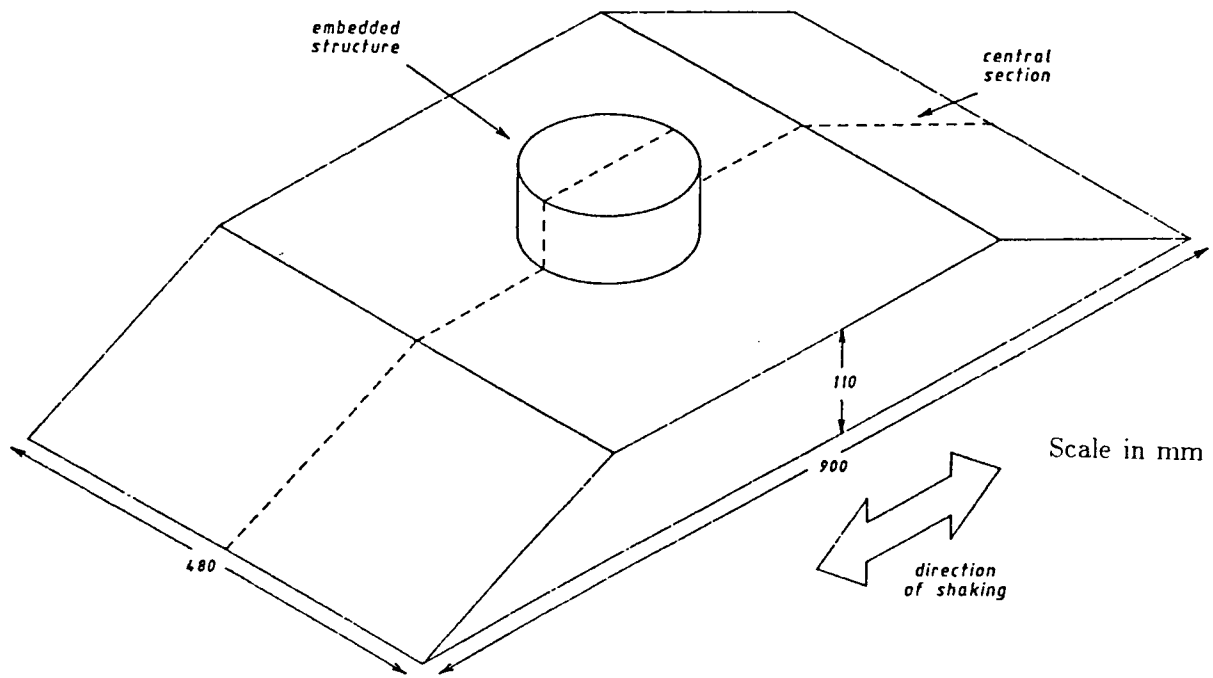

Fig. 7.51 Schematic of a 3-D Model Embankment With Embedded Structure

The embedded structure is a solid cylindrical block of aluminum alloy (Dural) 150mm in diameter and 100mm high. The block was embedded to a depth of 30 mm in the foundation soil.

During the test the model experienced a nominal centrifugal acceleration of 80g. Therefore, the model simulated a structure approximately 8m in height and 12m in diameter embedded to a depth 2.4m. The average contact pressure of the structure on the soil was 220 kPa.

The complete instrumentation of the model is shown in Fig. 7.52. Accelerometers ACC 728 and ACC 734 measured vertical accelerations while the others measured horizontal accelerations. ACC 2036 mounted on the concrete base measured the input motion to the model.

7.4.2 Model Response in Test RSS90

The first earthquake of this test series has a peak amplitude of the order of 5%g. The response to this earthquake was not analysed. Only the response to the second earthquake (EQ2) which has a peak amplitude of 21.0%g was analysed.

The model response to the second earthquake (EQ2) is shown in Fig. 7.53. ACC 1244 and ACC 1258 records show a large bias in one direction and they were not used in the study. As mentioned earlier, the shifts may have been caused by poor earth connection which make the signals float above the baseline. Except for the vertical records (ACC 734 and ACC 728), all other records show frequency characteristics similar to that of the input motion. ACC 734 and ACC 728 both show frequency characteristics typical of a vertical acceleration record. There is very little rocking evident in the early stages of shaking, i.e., up to the time around 50 milliseconds. Sharp increases in rocking are evident after time 50 milliseconds. This is due to the fact that there is an increase in input to the base of the

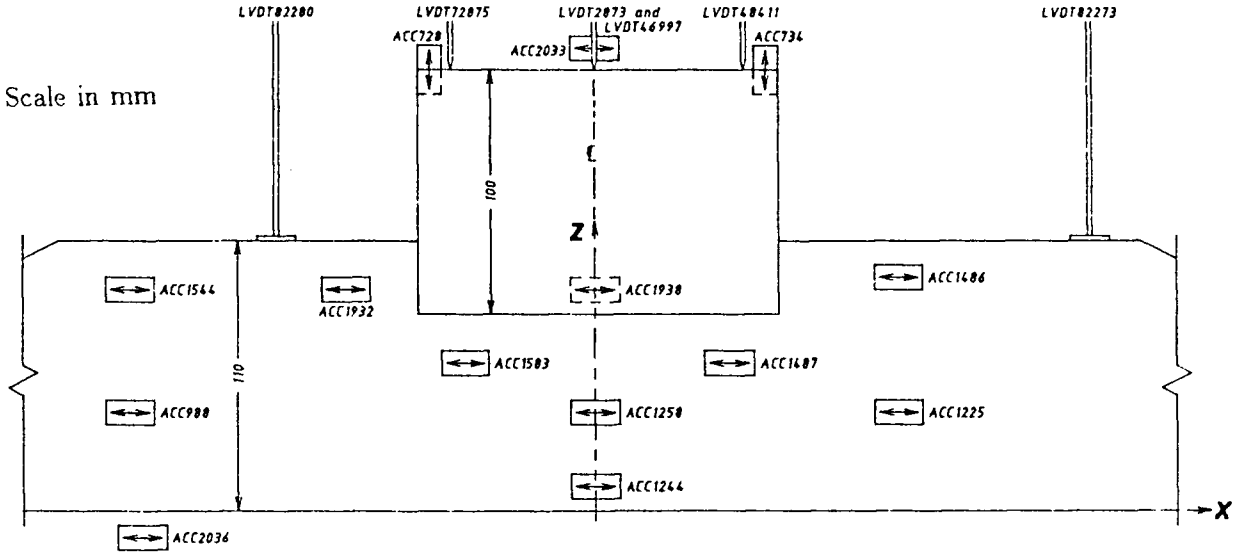

Fig. 7.52 Instrumented Model in Test Series RSS90

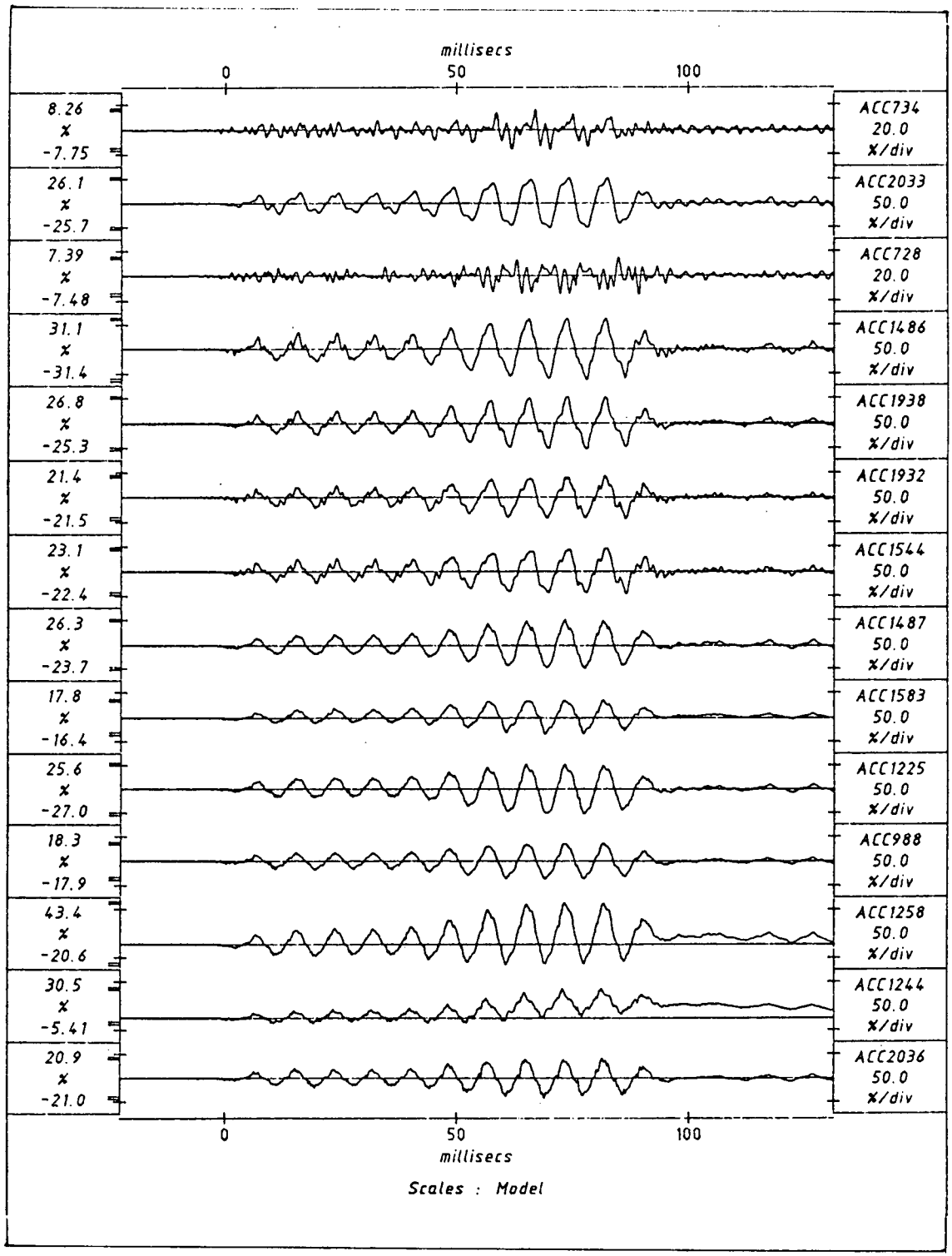

Fig. 7.53 Model Response in Test RSS90/EQ2

structure as shown in ACC 1583 and ACC 1487 records.

It is interesting to note that accelerometers in sand foundation on the right hand side of the centerline of the model measure peak values much higher than those of the counterparts on the left hand side. This suggests that the model may not be uniform and homogeneous in its properties about the centerline. For instance, ACC 1583 and ACC 1487, which were located under the structure and symmetrically opposite about the centerline, measure peak acceleration values which differ by 8.5%g. Further, ACC 1486 is located on the right hand side at a distance from the centerline approximately the same as the average distance of ACC 1932 and ACC 1544 which are located on the left hand side. Yet ACC 1486 measures peak acceleration value 9.9%g and 8.3%g higher than those of ACC 1932 and ACC 1544 respectively. The differences are too high and therefore there is certainly local inhomogeneity in the properties of the model.

The input motion is shown in Fig. 7.54 at prototype scale along with base corrected motion. It has a peak acceleration value of 21.0% g. It consists of 5 cycles of low level shaking followed by another $5\frac{1}{2}$ cycles of high level shaking. The total duration of input motion is around 10 seconds with the last 2.0 seconds of input representing wheel-off accelerations. The 3-D prototype was analysed as 2-D plane strain soil-structure system with the foundation soil assumed to be homogeneous with a relative density of 64%. Computed and corresponding measured responses are compared at prototype scale in the following sections.

7.4.3 Comparison of Acceleration Responses of Test RSS90/EQ2

Figs. 7.55 to 7.58 show comparison between the measured and computed responses at locations of ACC 988, ACC 1225, ACC 1583 and ACC 1487. These are located in foundation soil with ACC 988 and ACC 1225 in the free field away from the structure and

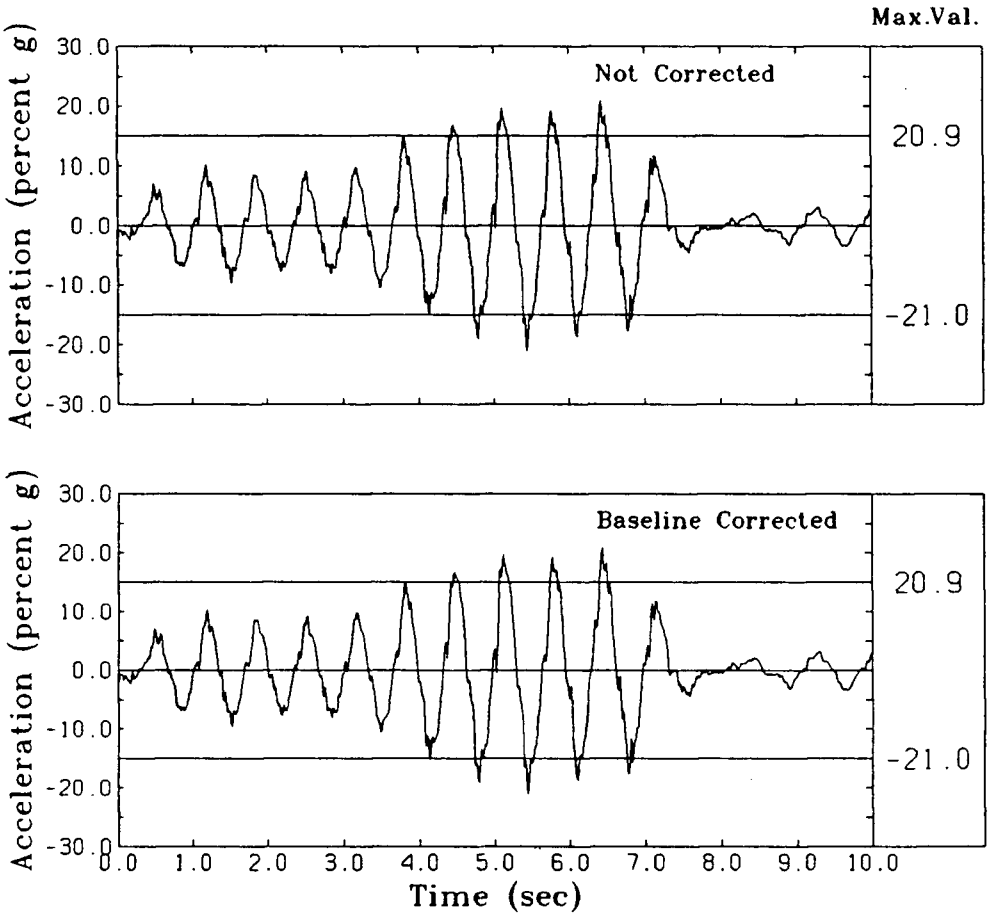

Fig. 7.54 Input Motion for Test RSS90/EQ2

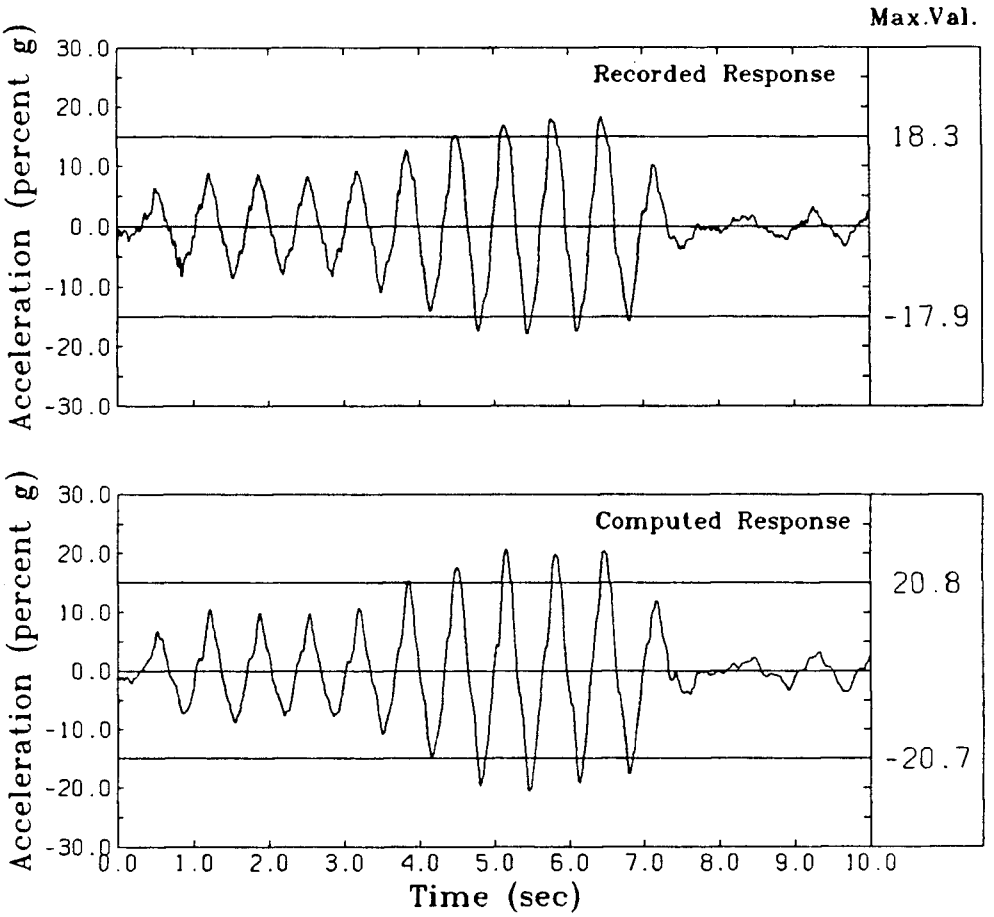

Fig. 7.55 Computed and Measured Accelerations at the Location of ACC 988 in Test RSS90/EQ2

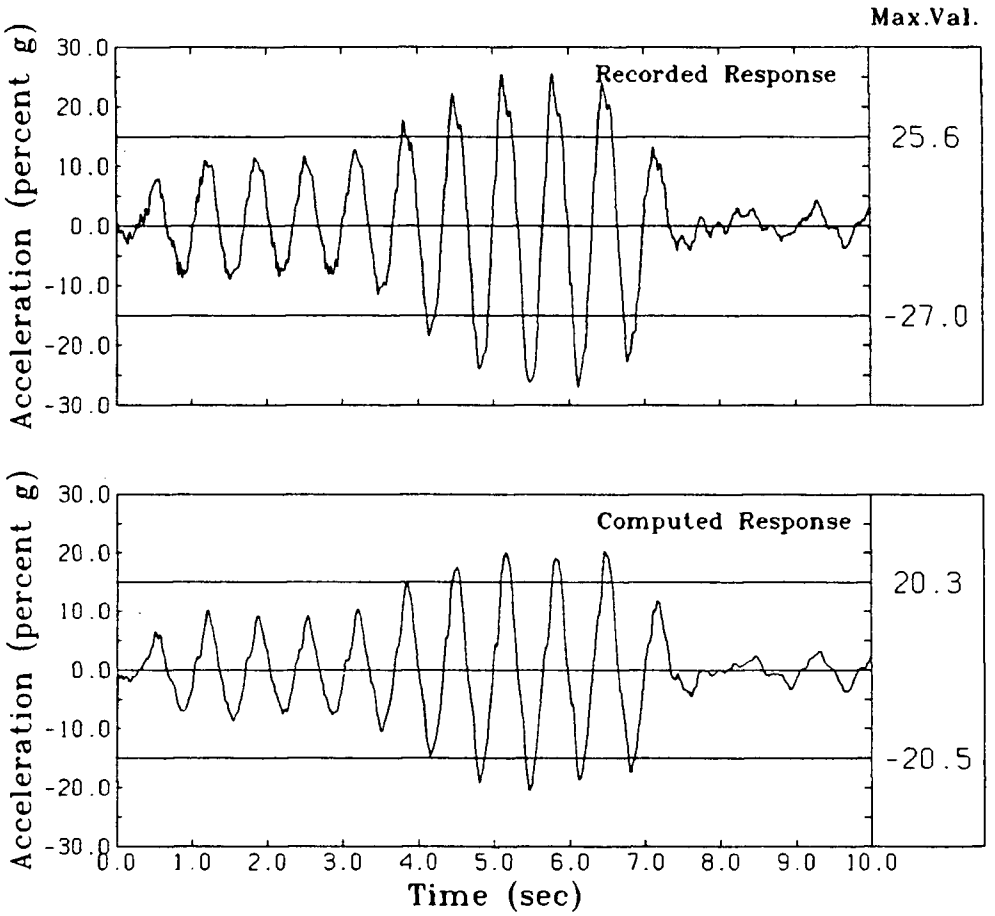

Fig. 7.56 Computed and Measured Accelerations at the Location of ACC 1225 in Test RSS90/EQ2

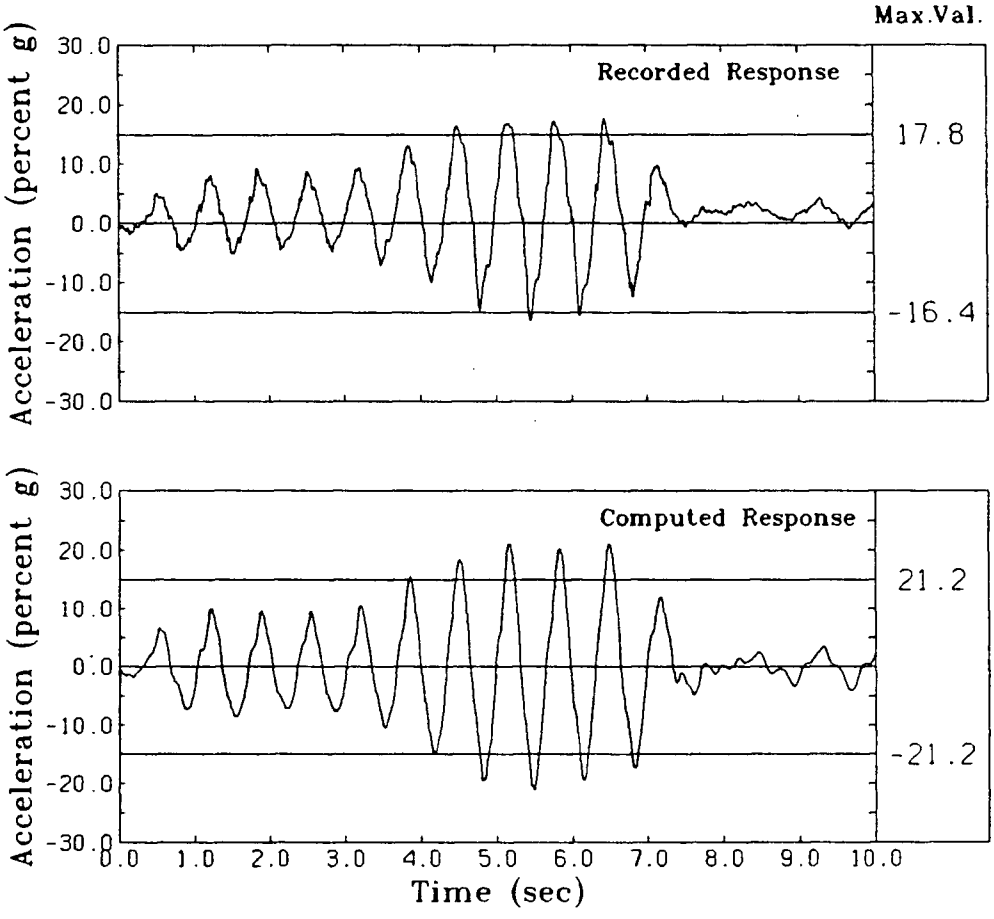

Fig. 7.57 Computed and Measured Accelerations at the Location of ACC 1583 in Test RSS90/EQ2

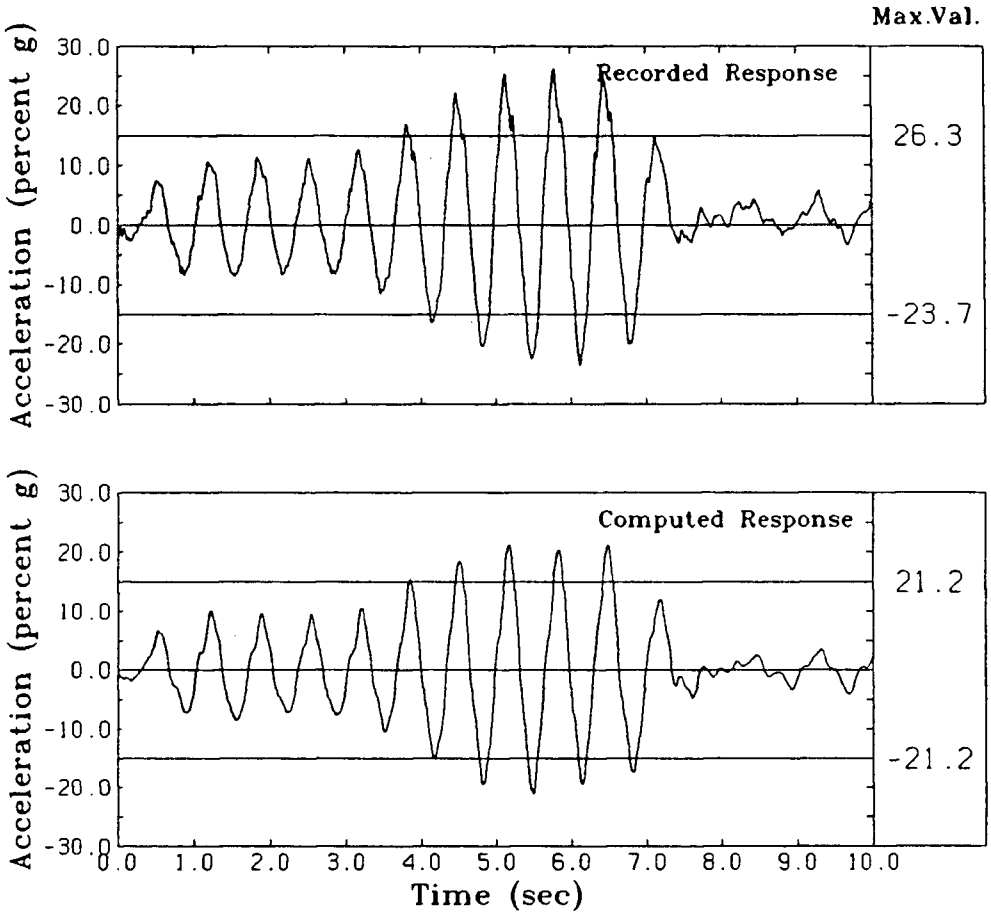

Fig. 7.58 Computed and Measured Accelerations at the Location of ACC 1487 in Test RSS90/EQ2

ACC 1583 and ACC 1487 under the structure. All responses show the same trend as the input motion; that is, they show a low amplitude response for the first 3.7 seconds followed by a high amplitude response for the next 4.0 seconds. Responses are very similar in frequency content, each corresponding to the frequency of the input motion. At locations of ACC 988 and ACC 1225 the agreement between the measured and computed peak accelerations is quite satisfactory. At locations of ACC 1583 and ACC 1487, measured peak acceleration values are 17.8%g and 26.3%g respectively, while computed values are both 21.2%g. For TARA-3 analysis, the model was assumed to be homogeneous and therefore it is not surprising to see the same computed peak values at these two locations.

Figs. 7.59 to 7.61 compare measured and computed responses at locations ACC 1544, ACC 1932 and ACC 1486 respectively. At locations of ACC 1544 and ACC 1932, comparison is good both in terms of magnitude and frequency contents. Measured and computed peak values at locations of ACC 1544 and ACC 1932 differ only slightly. Measured response at ACC 1486 has a peak value of 31.4%g, whereas computed has 23.7%g. Even though there is a large difference in peak values, frequency contents are very similar.

Comparison between measured and computed acceleration responses at locations on the structure are shown in Figs. 7.62 to 7.64. ACC 728, ACC 2033 and ACC 734 were mounted on top of the structure as shown in Fig. 7.52. ACC 728 and ACC 734 were placed to measure vertical accelerations due to rocking while ACC 2033 was placed in the middle of the structure to measure horizontal accelerations. At location ACC 2033, measured and computed accelerations closely match in both peak values and frequency content. Measured and computed peaks are 26.1%g and 26.6%g respectively. Both responses show characteristics very similar to that of the input motion. That is, they both show 5 cycles of low amplitude response followed by $5\frac{1}{2}$ cycles of high amplitude response. This observation is true for vertical acceleration responses, even though it is not as distinct as in the case

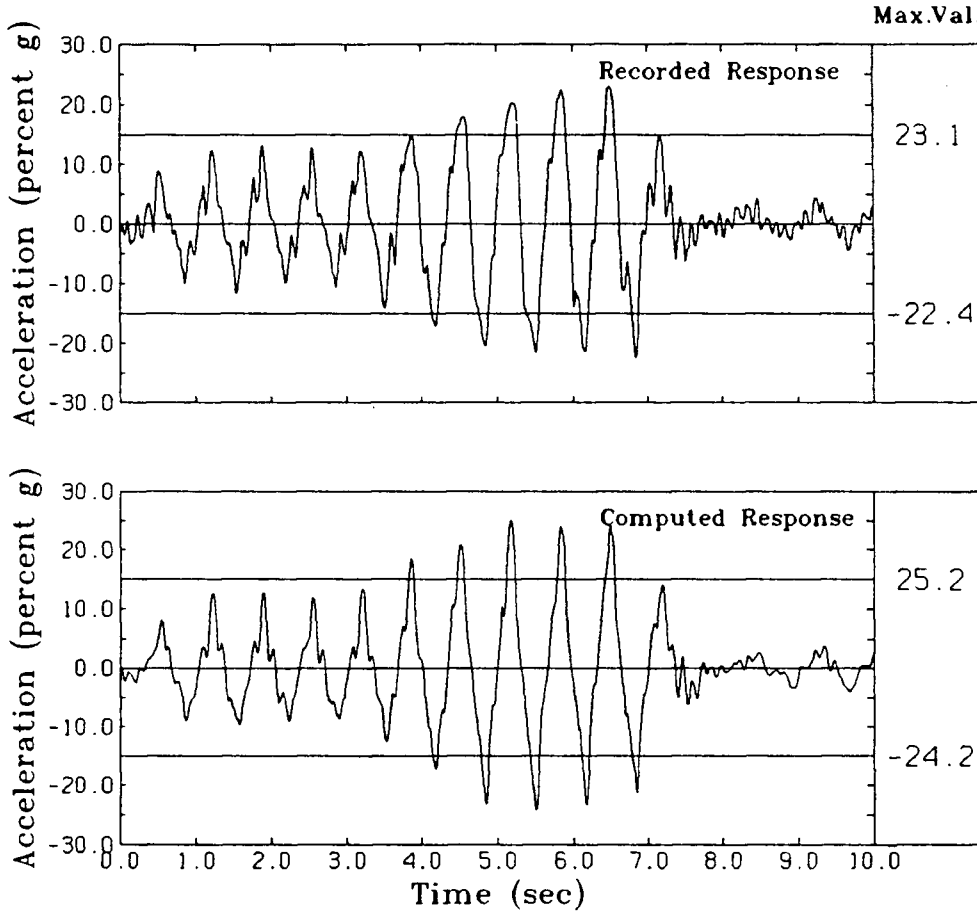

Fig. 7.59 Computed and Measured Accelerations at the Location of ACC 1544 in Test RSS90/EQ2

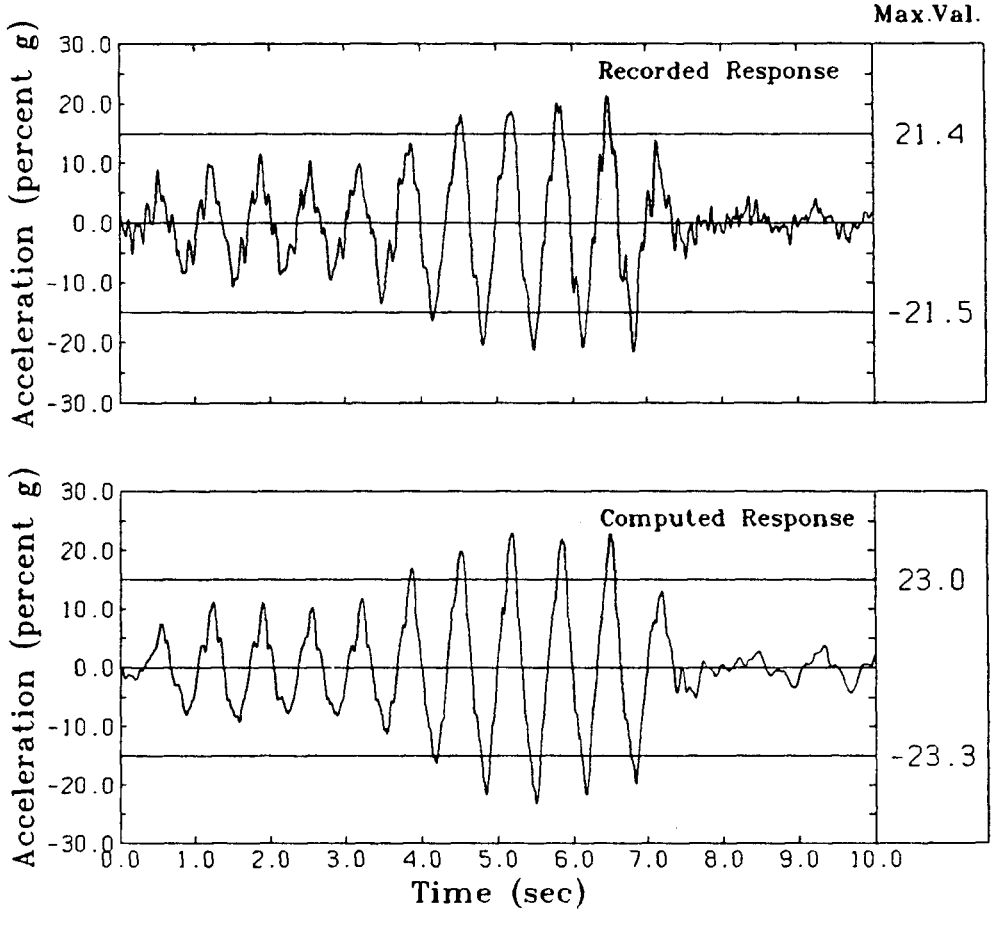

Fig. 7.60 Computed and Measured Accelerations at the Location of ACC 1932 in Test RSS90/EQ2

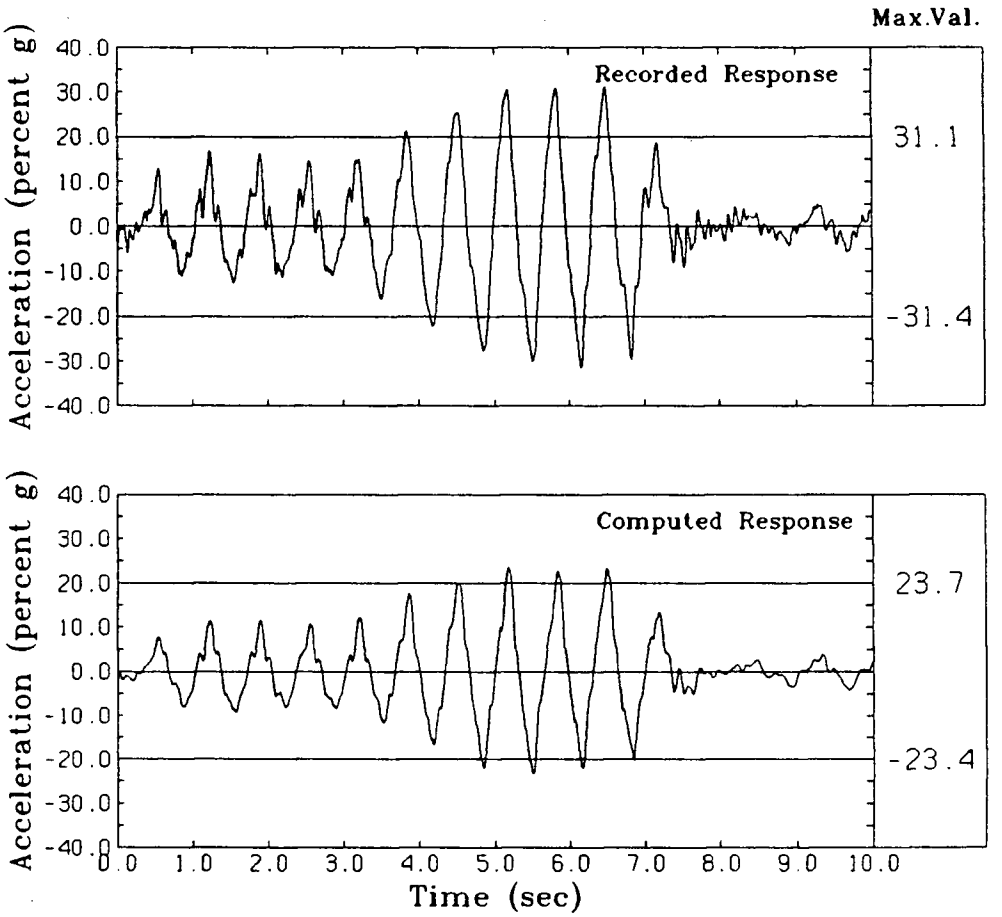

Fig. 7.61 Computed and Measured Accelerations at the Location of ACC 1486 in Test RSS90/EQ2

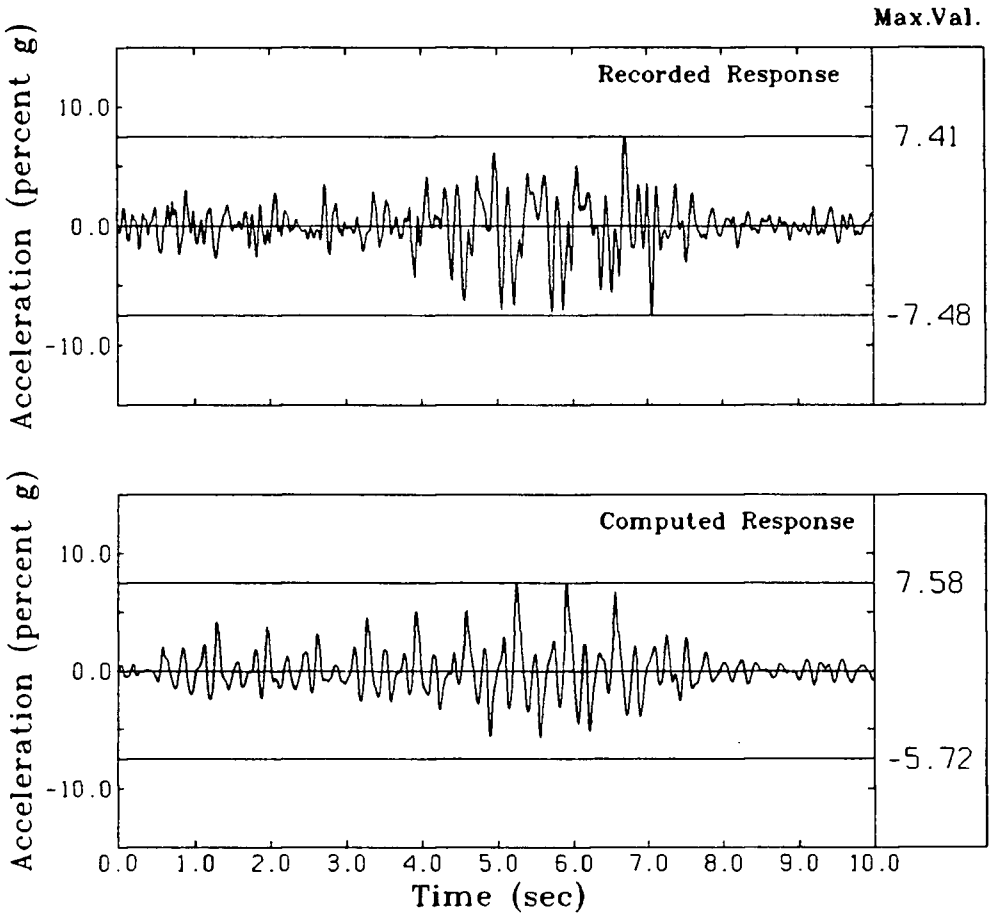

Fig. 7.62 Computed and Measured Accelerations at the Location of ACC 728 in Test RSS90/EQ2

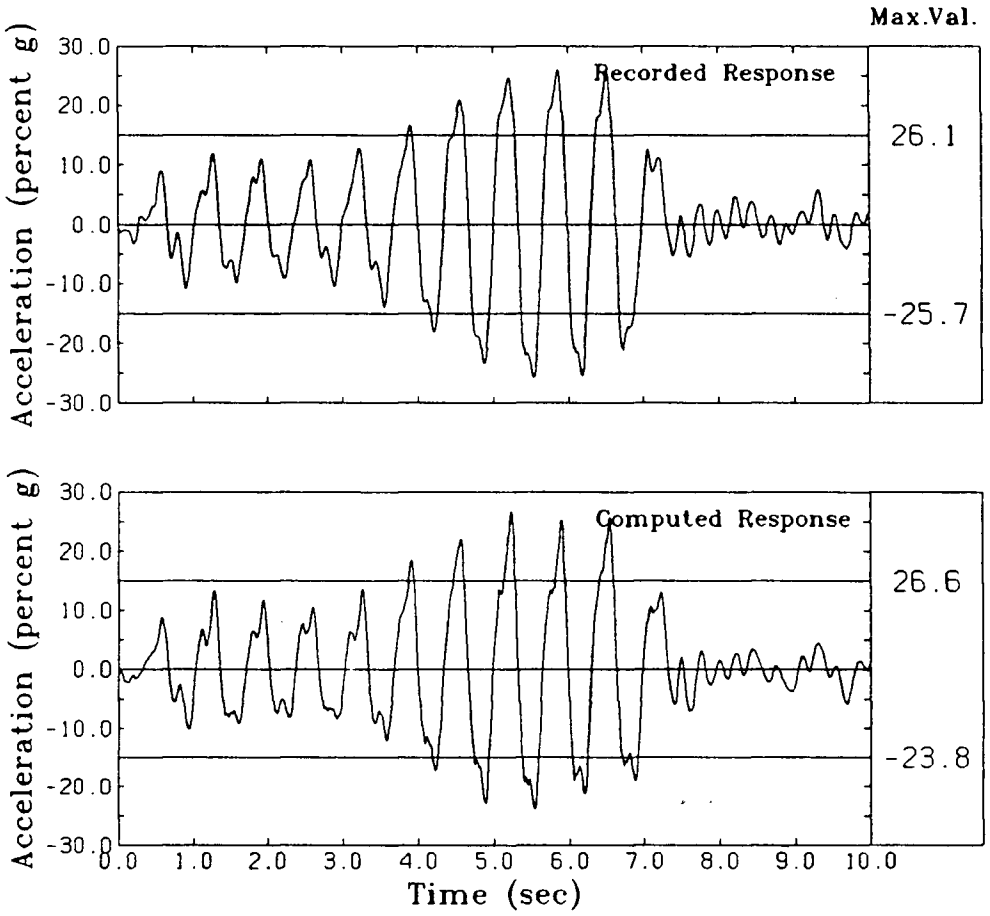

Fig. 7.63 Computed and Measured Accelerations at the Location of ACC 2033 in Test RSS90/EQ2

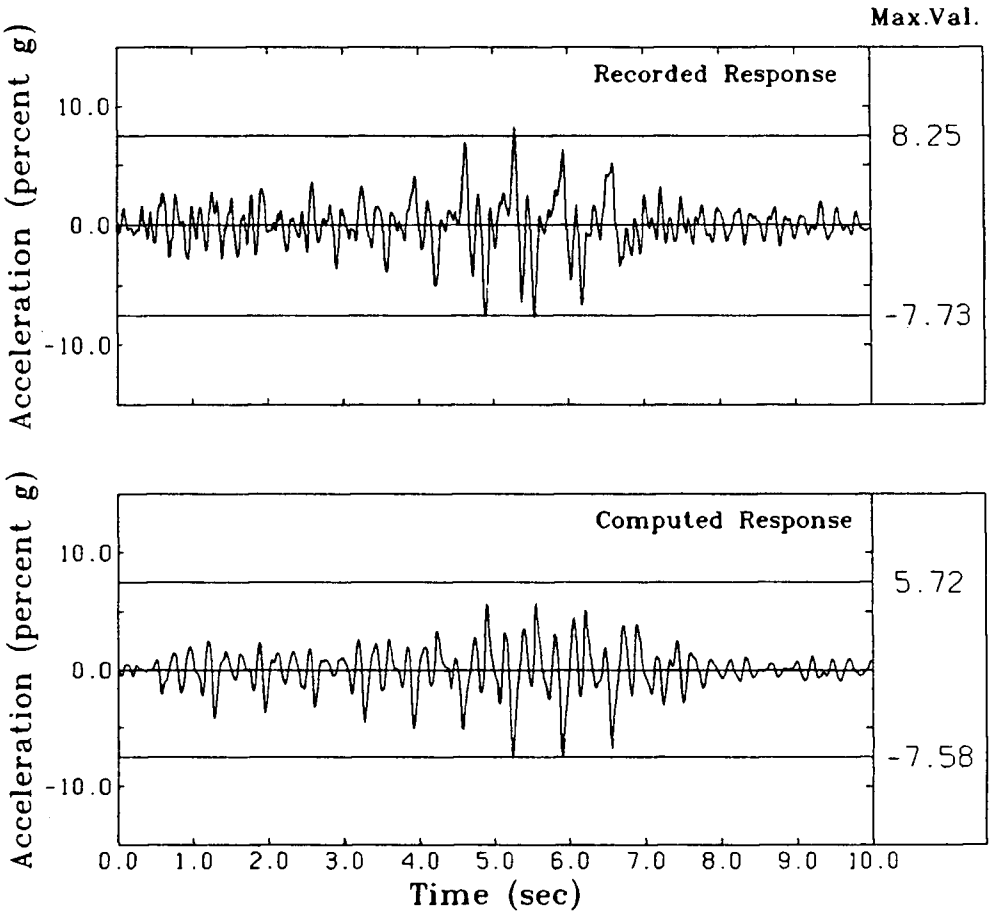

Fig. 7.64 Computed and Measured Accelerations at the Location of ACC 734 in Test RSS90/EQ2

of horizontal acceleration response. Both measured and computed responses at ACC 728 and ACC 734 have frequency content much higher than that of the horizontal acceleration response at the same level in the structure (ACC 2033) and that of the input motion ACC 2036. The reason for this has already been given in section 7.2.3.

Unlike symmetrical pairs of accelerometers in the foundation soil, the pair ACC 728 and ACC 734 measure peak acceleration values very close to each other. The measured peaks at ACC 728 and ACC 734 are 7.5%g and 8.3%g respectively. The computed peak for both case is 7.6%g. The differences are very small. The computed responses at locations ACC 728 and ACC 734 are such that they show a phase lag of 180 degrees. This indicates that rocking is accounted correctly in the computations.

There are two major factors contributing to discrepancies between measured and computed accelerations at some locations in this test. First, as observed earlier, the model is not homogeneous in its properties. Secondly, in TARA-3 analysis the responses were computed assuming plane strain behavior of the model. However, the model is a 3-D model. Hence it is not surprising that some discrepancies may exist between computed and measured accelerations.

7.4.4 Comparison of Settlement in Test RSS90/EQ2

The comparison between measured and computed vertical settlements at locations of LVDT 82280, LVDT 72875, LVDT 72873, LVDT 48411 and LVDT 82273 is given in Table 7.7. The values quoted in the table are at prototype scale. Settlements computed at LVDT 72875, LVDT 72873 and LVDT 48411, which were mounted on top of the structure, show remarkable agreement with measured values. LVDT 82280 was placed on top surface of the sand berm approximately half way between the shoulder of the berm and the edge of the structure. At this location, the comparison is very good with computed settlement 7.7%

higher than measured. LVDT 82273 is located close to right hand side shoulder of the berm. As seen from Table 7.7, measured value at location LVDT 82273 is very much higher than computed. Part of this is due to the effects of wind erosion during the centrifuge flight.

The vertical settlement is also compared in Fig. 7.65 where the recorded settlements are indicated by the triangles. It can be seen that the agreement between the computed and measured settlements is very good.

Table 7.7 Comparison of Settlements in Test RSS90/EQ2

LVDT No	Measured (mm)	Computed (mm)
82280	15.4	14.2
72875	12.7	12.6
72873	12.4	12.6
48411	12.0	12.6
82273	110.6	11.0

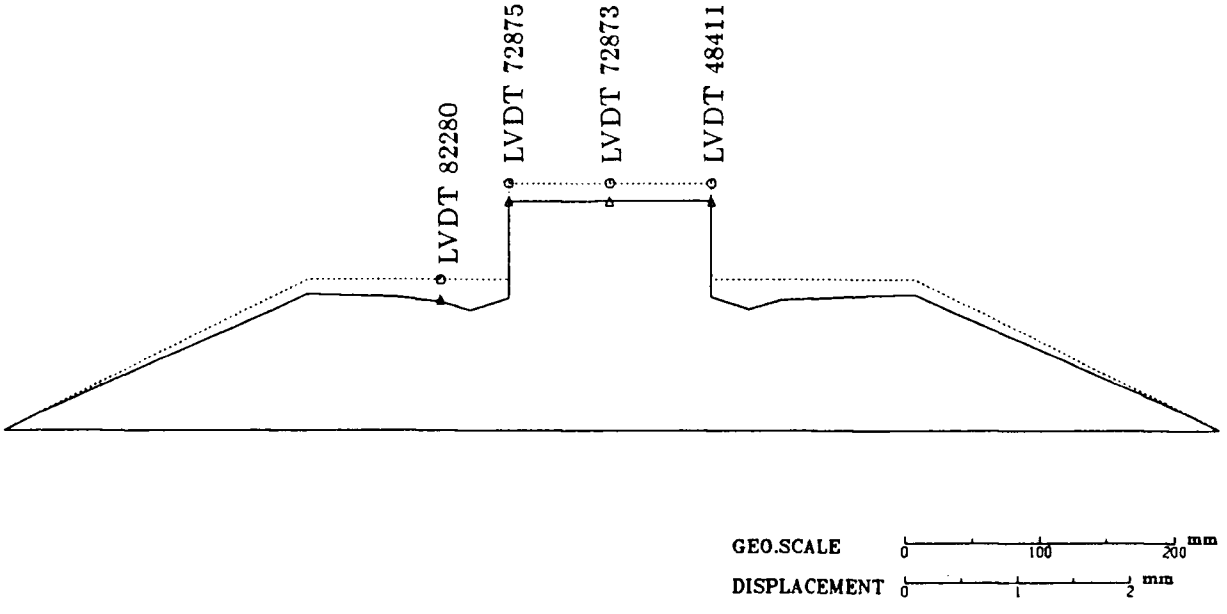

Fig. 7.65 Settlement Pattern in Test RSS90/EQ2

CHAPTER 8

VERIFICATION BASED ON SATURATED MODEL TESTS

8.1 Verification Study Based on Test Series LDO4

8.1.1 Centrifuge Model in Test Series LDO4

A schematic view of a 2-D plane strain saturated soil-structure model is shown in Fig. 7.18. The embankment was constructed by Method 1 described in section 5.5.2.1 using Leighton Buzzard B.S.S 120/200 sand. The estimated relative density of the sand is 91 ± 17%. The embankment is 110mm high and has a flat crest 230mm wide and a base 720mm wide. The length of the embankment perpendicular to the direction of shaking is 480mm.

The surface structure consisted of three mild steel plates, each of which is 15mm thick and 65mm wide. The steel plates were placed end to end along the centerline of the crest as depicted in Fig. 7.18. The two end pieces were each 40mm long and the central piece was 385mm long.

The model experienced a nominal centrifugal acceleration of 80g. The model, therefore, simulated a prototype embankment approximately 8.8m high with crest width and base width of 18.4m and 57.6m respectively and a structure approximately 1.2m high and 5.2m wide.

The instrumentation of the model is shown in Fig. 8.1. All accelerometers measured

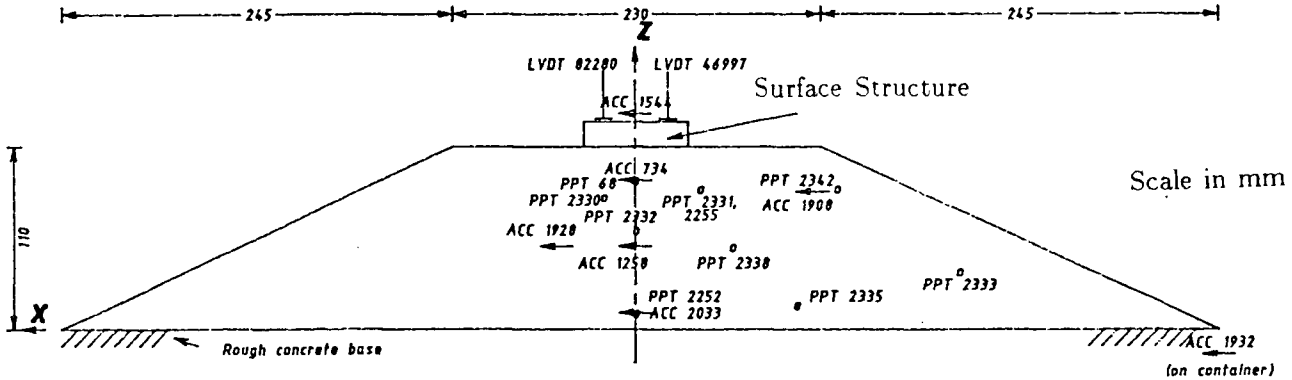

Fig. 8.1 Instrumented Model in Test Series LDO4

horizontal accelerations. ACC 1932 mounted on the base of the model container recorded the acceleration input to the model.

8.1.2 Model Response in Test LDO4

ACC 1932 was not working during the first earthquake of the test series. Only the response to the second earthquake, EQ2, was analysed using TARA-3. The smoothed data from all acceleration and porewater pressure transducers from the test LDO4/EQ2 are shown in Fig. 8.2 at model scale. The input motion measured by ACC 1932 has a peak amplitude of 16.4% of the centrifugal acceleration and has 10 complete cycles of significant shaking in the range 10 to 100 milliseconds. All acceleration records were filtered to remove frequencies above 10Hz at prototype scale. Also ACC 2033 located near the base shows baseline distortion in the form of a small drift in the negative direction and hence this record has to be baseline corrected.

Transducer PPT 2330 shows a record with negative porewater pressures in the entire time span. It is probable that the signs were switched around and hence it is assumed that the correct record is the exact opposite of that shown in Fig. 8.2. PPT 2332 record is anomalous as it does not show any accumulation of porewater pressures during shaking. This is not consistent with the input motion or with other tranducers located at similar location such as PPT 2331. Therefore, this record is ignored in the study. All other porewater pressure transducer records, except for PPT 2255 record, are very consistent with the input motion. They all show a rapid accumulation of porewater pressure during the first two cycles of strong shaking. During the next two cycles of weak shaking, the accumulation is shown to be very slow. However, during the subsequent two to three cycles of strongest shaking, rapid accumulation along with large swings of transient porewater pressures are shown in the records. Contrary to these observations, PPT 2255 record shows

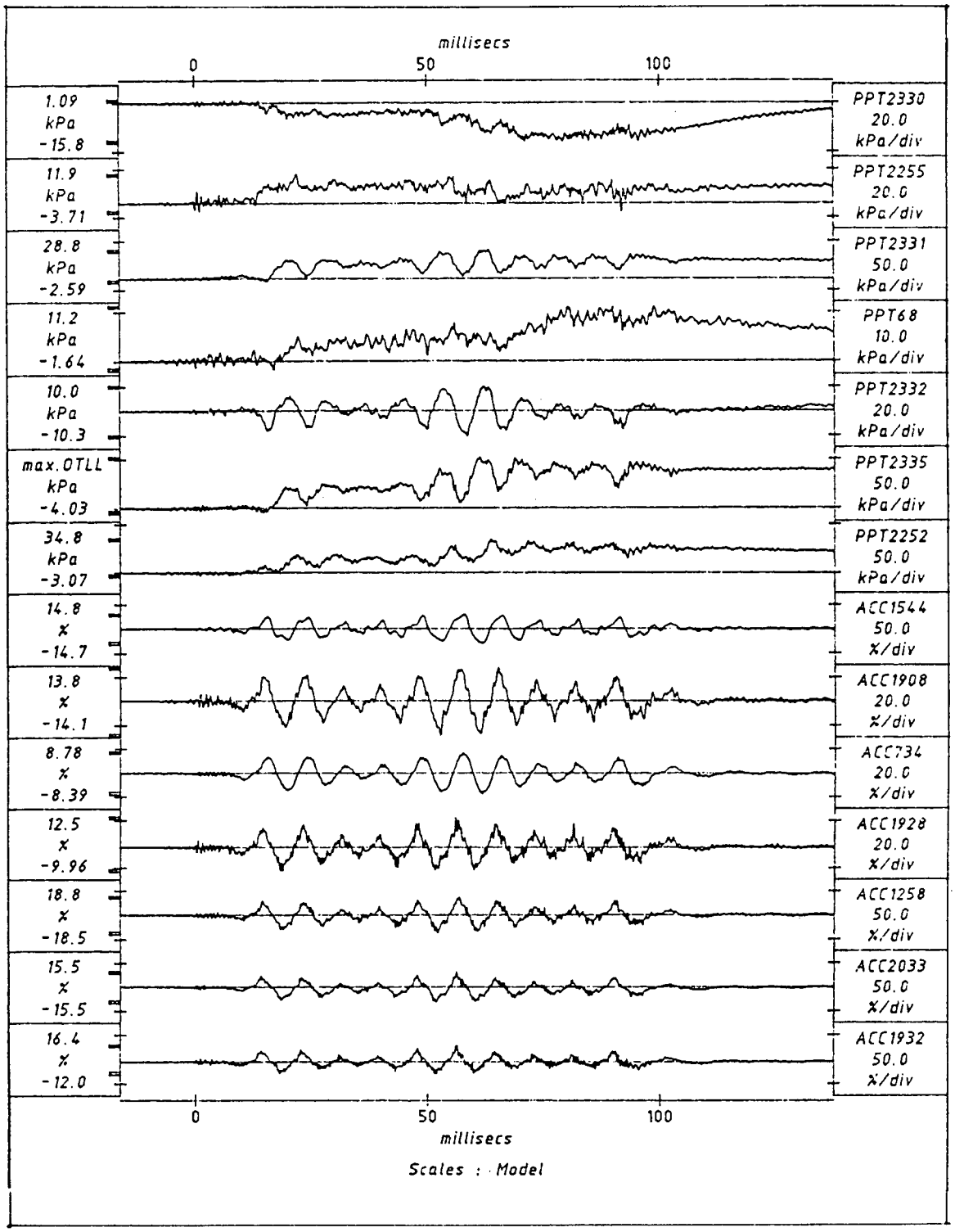

Fig. 8.2 Model Response in Test LDO4/EQ2

a large decrease in porewater pressure at the time of strongest shaking. This behavior at the location of PPT 2255 and also the behavior at the location of PPT 2332 may be due entirely to localised effects such as drainage along the cable leading to the transducers or tension on the transducer leads due to lateral displacements. Hence, data from these transducers have to be interpreted cautiously.

The effect of soil-structure interaction on porewater pressure responses can be clearly identified by comparing the records of PPT 2335 and PPT 2331 with those of PPT 2252 and PPT 68. PPT 2335 and PPT 2331 records show larger cycles of oscillations in pressures about the residual level than PPT 2252 and PPT 68 records. These oscilations are due to fluctuations in mean normal stresses caused by rocking of the structure. PPT 2252 and PPT 68 were located under the structure on the centerline of the model and hence they were not subject to large normal stress fluctuations. On the other hand, PPT 2331 and PPT 2335 were located close to edge of the structure and hence they were subject to larger normal stress fluctuations. Therefore, it is not surprising to see larger and more pronounced oscillations at locations PPT 2331 and PPT 2335 than at PPT 2252 and PPT 68.

The input motion of the earthquake EQ2 is shown in Fig. 8.3 along with the baseline corrected motion at prototype scale. The significant shaking starts around 1.0 seconds and ceases around 7.7 seconds. The peak acceleration of 16.3%g occurs at around 4.47 seconds. The predominant period of shaking is 0.67 seconds.

The prototype was analysed as a 2-D plane strain soil-structure system using TARA-3. The sand foundation was assumed to be homogeneous and uniform with a relative density of 75%. This value is within the range of values quoted for the model. The baseline corrected ACC 1932 record, shown in Fig. 8.3, was the input for the TARA-3 analysis. Slip elements were introduced at the interface between the structure and sand foundation to model slippage between them. The computed respones are compared with corresponding

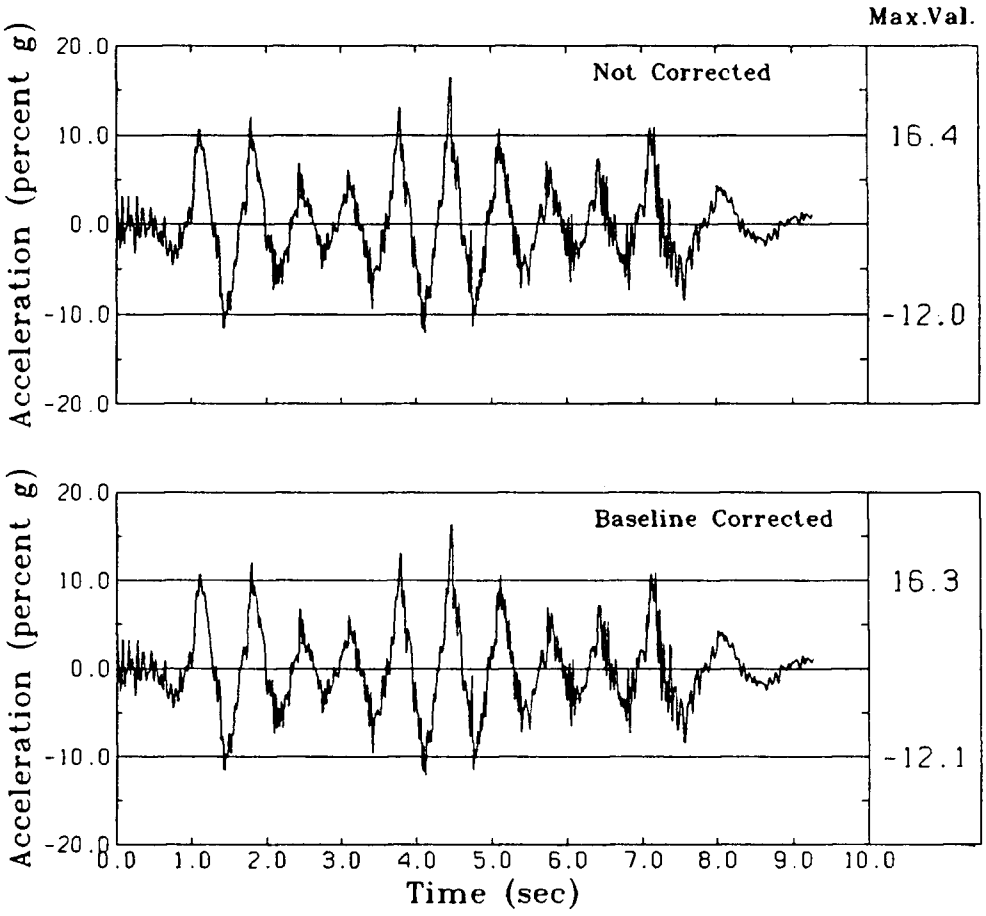

Fig. 8.3 Input Motion for Test LDO4/EQ2

measured responses at prototype scale in the next section.

8.1.3 Comparison of Acceleration Responses in Test LDO4/EQ2

The baseline distortion and the high frequency noises found in the measured ACC 2033 record is highlighted in Fig. 8.4. It also shows the comparison between the original and corrected records. As seen in the figure, the corrected record has no baseline distortion and/or high frequency noises. The corrected and computed responses are compared in Fig. 8.5. The comparison in terms of frequency content, peak amplitudes and variation of amplitude with time is excellent. Both responses show characteristics very similar to that of the input motion. The peak amplitudes both in the positive and negative directions are fairly close to the corresponding values of the input. This could be expected because ACC 2033 was located near the base. The measured and computed peak acceleration values are 15.8%g and 15.9%g respectively and the difference is very small.

ACC 1258 was located on the centerline of the model approximately half way between the base of the structure and the base of the model. The measured response is compared with the computed response in Fig. 8.6. The comparison in the time range 0.0 to 3.5 seconds is good. However, in the range 3.5 to 5.2 seconds, the computed accelerations are somewhat lower than the measured accelerations. But the overall agreement is good.

Fig. 8.7 compares the measured and computed accelerations at the location of ACC 1928. They are very similar except for one large peak in the computed response. ACC 1928 was located just outside the edge of the structure at the same elevation as ACC 1258. Yet the differences between measured accelerations at these two locations are very high, whereas the difference between computed accelerations are small, and for a uniform and homogeneous model as assumed in the analysis, this small difference seems to be reasonable. Therefore, the large difference between the measured and computed accelerations at these

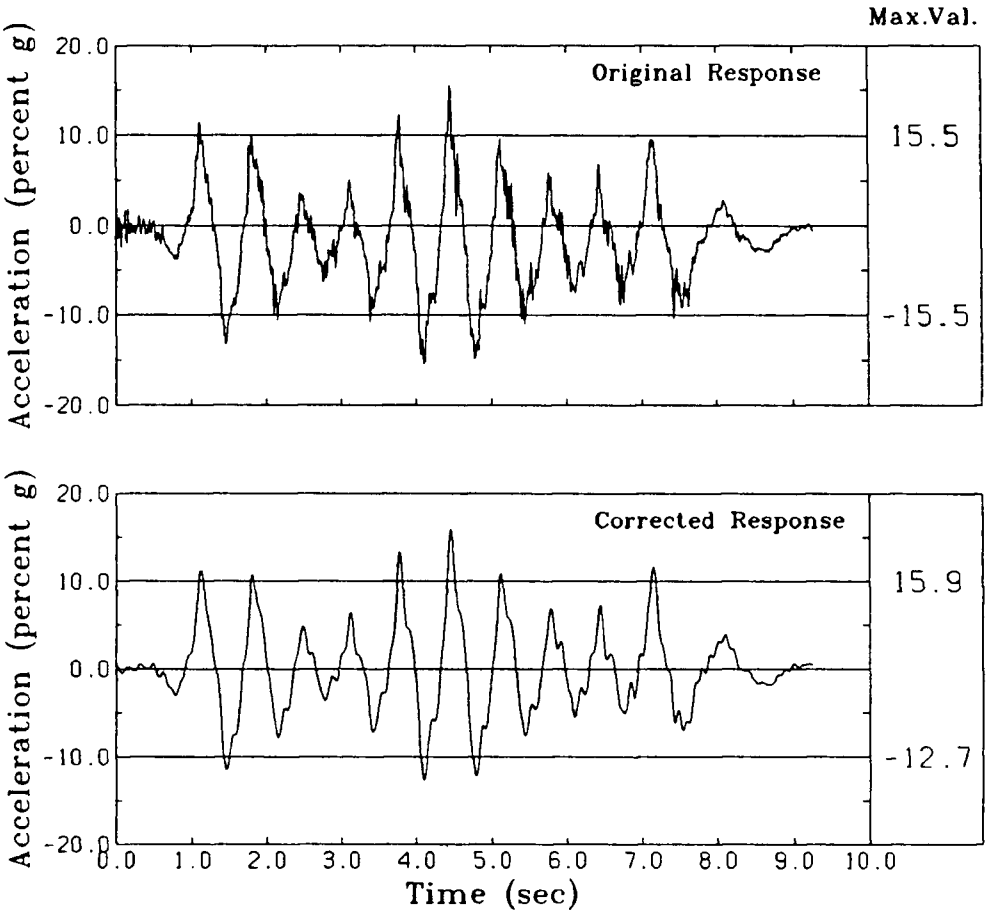

Fig. 8.4 Original and Corrected Accelerations at the Location of ACC 2033 in Test LDO4/EQ2

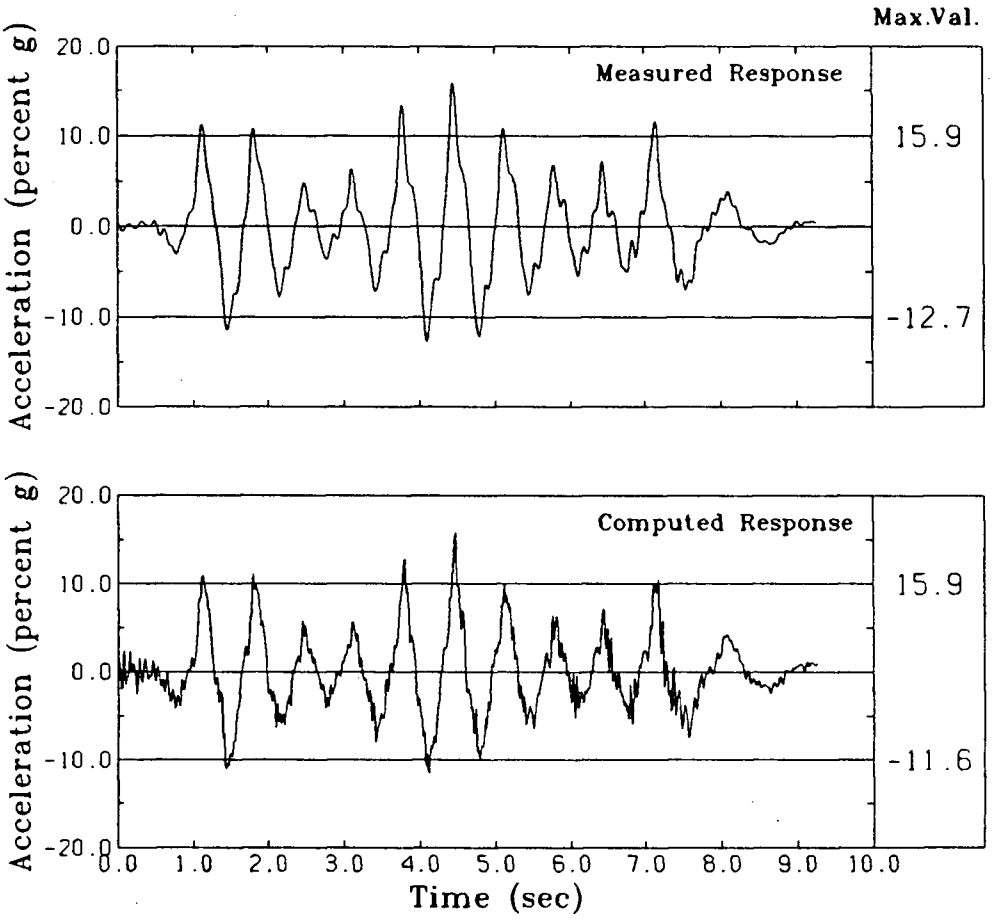

Fig. 8.5 Computed and Measured Accelerations at the Location of ACC 2033 in Test LDO4/EQ2

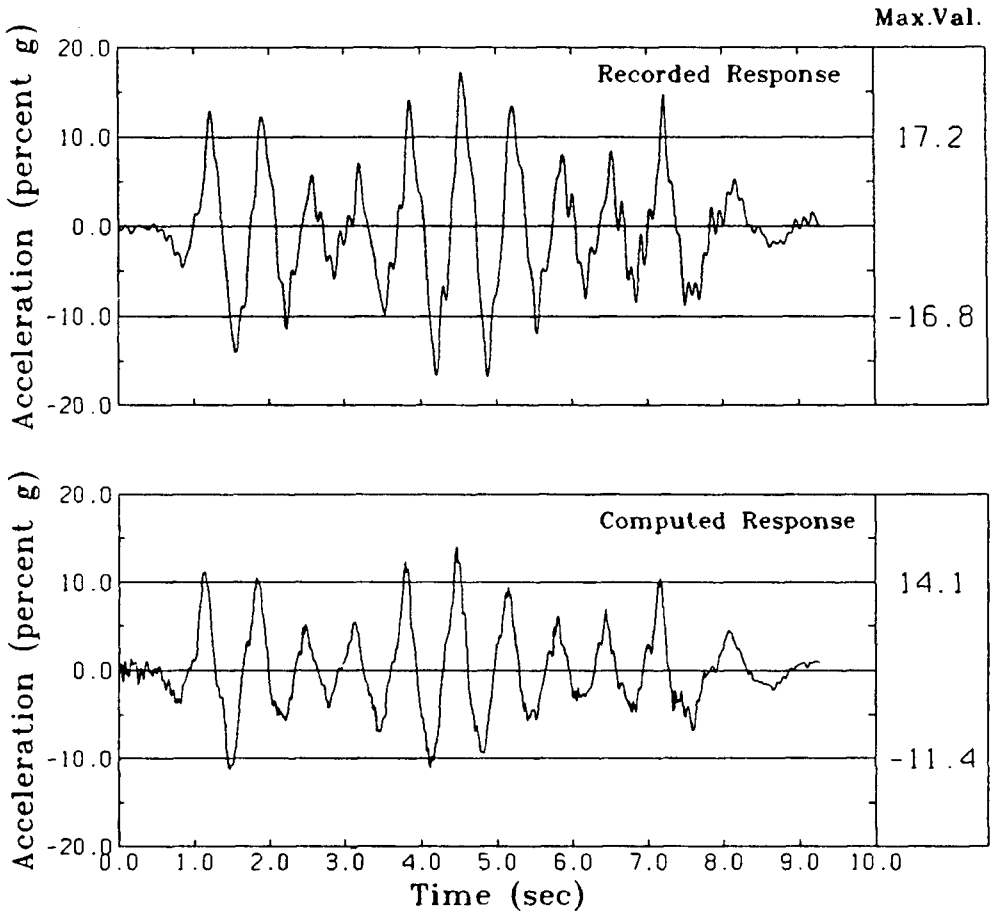

Fig. 8.6 Computed and Measured Accelerations at the Location of ACC 1258 in Test LDO4/EQ2

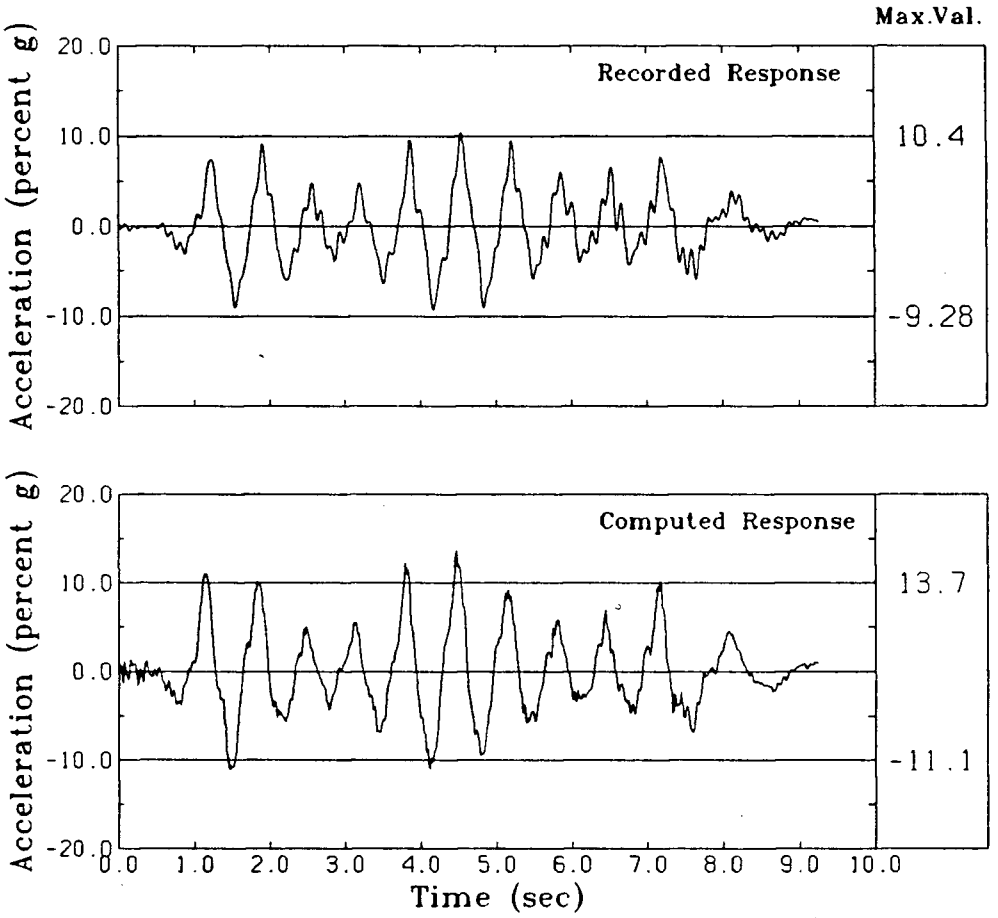

Fig. 8.7 Computed and Measured Accelerations at the Location of ACC 1928 in Test LDO4/EQ2

locations might primarily be due either to local inhomogeneity of the model in density or due to measurement error of the transducers.

The measured and computed accelerations at the location of ACC 1908 in the zone directly beneath the right hand shoulder of the model are shown in Fig. 8.8. The comparison in terms of frequency content, peak amplitude and distribution of amplitude with time is excellent. The measured peak value is 13.4%g and the computed peak value is 14.5%g.

ACC 1544 was mounted on the top of the structure, as shown in Fig. 8.1, to measure horizontal accelerations. The measured accelerations are compared with those computed by TARA-3 in Fig. 8.9. Except for the thin peak in the computed response, the peak values and frequency content agree very closely. The measured and computed peak accelerations are 14.7%g and 16.3%g respectively.

8.1.4 Comparison of Porewater Pressures in Test LDO4/EQ2

The measured porewater pressures near the base of the model at the location of PPT 2252 is shown in Fig. 8.10 along with those computed by TARA-3. Both the rate of development and peak residual porewater pressure are predicted very well. The measured and computed peak residual porewater pressure ratio, u/σ'_{yo}, are 23.0% and 22.0% respectively. The variation of amplitude in the input is clearly reflected in both measured and computed responses. For instance, during the strong shakings in the time ranges 1.0 to 2.2 seconds and 3.5 to 5.5 seconds, the accumulation of porewater pressures are rapid and during the weak shakings in the ranges 2.2 to 3.5 seconds and 5.5 to 9.8 seconds, the accumulation is very slow.

The comparison between the measured and computed porewater pressures at the location of PPT 2335 is shown in Fig. 8.11. The computed pressures are consistently lower than the measured pressures. The measured peak residual porewater pressure ratio is 46.0% and

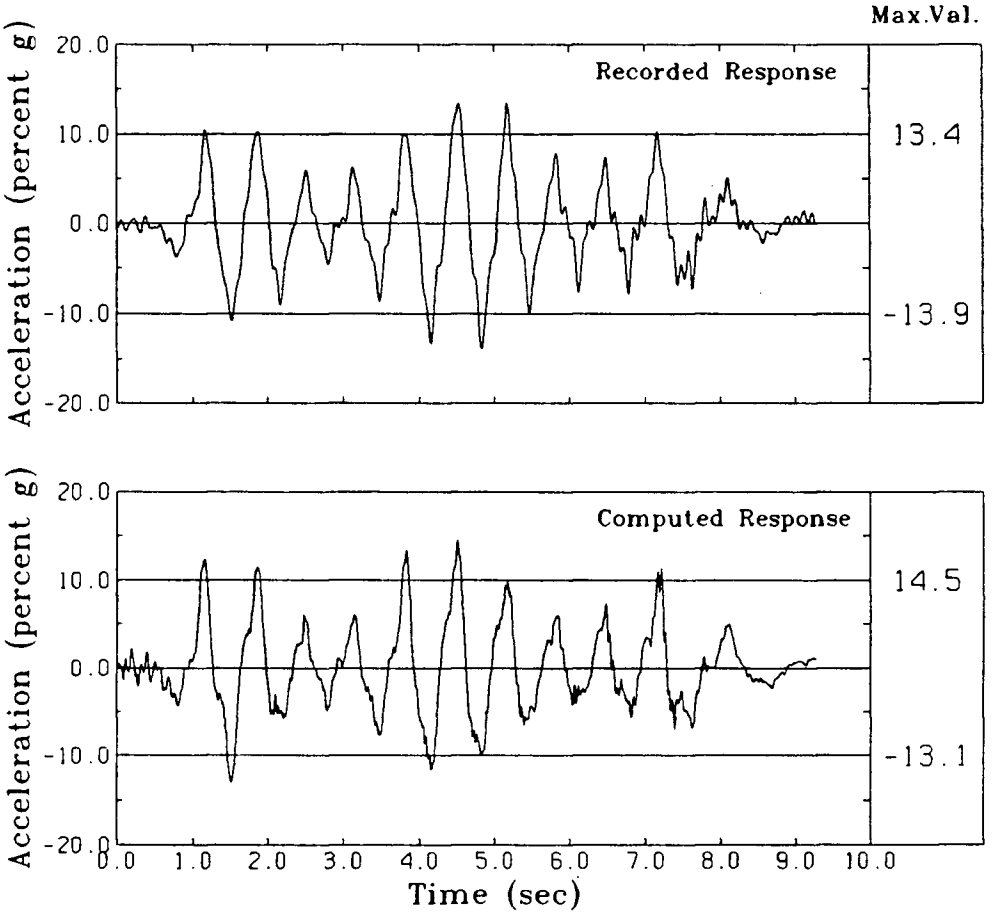

Fig. 8.8 Computed and Measured Accelerations at the Location of ACC 1908 in Test LDO4/EQ2

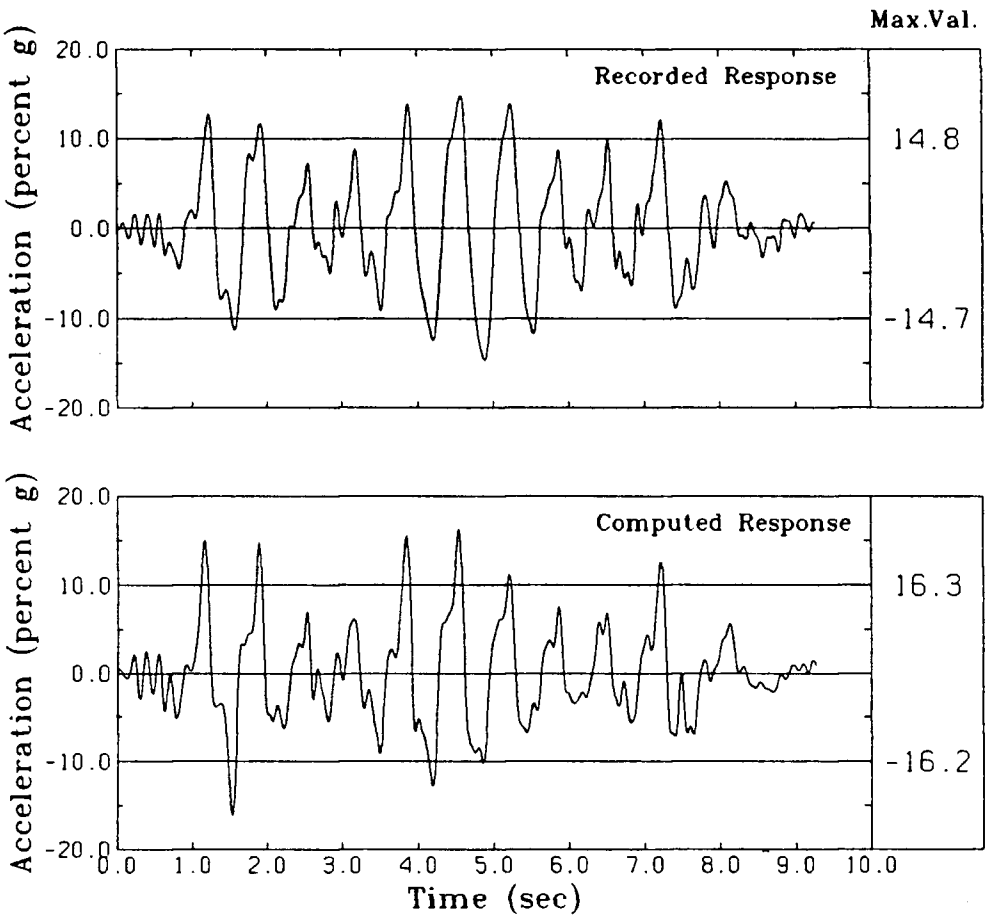

Fig. 8.9 Computed and Measured Accelerations at the Location of ACC 1544 in Test LDO4/EQ2

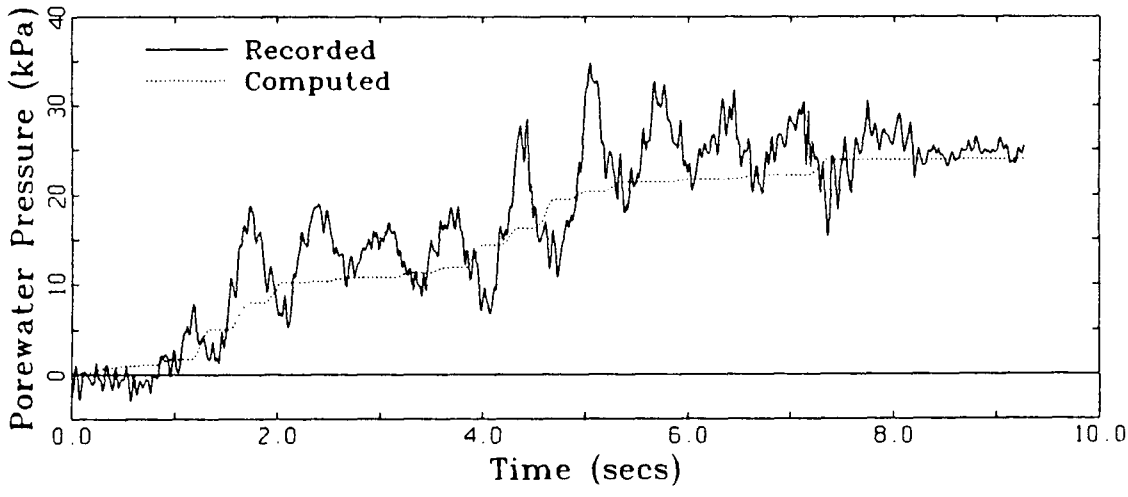

Fig. 8.10 Computed and Measured Porewater Pressures at the Location of PPT 2252 in Test LDO4/EQ2

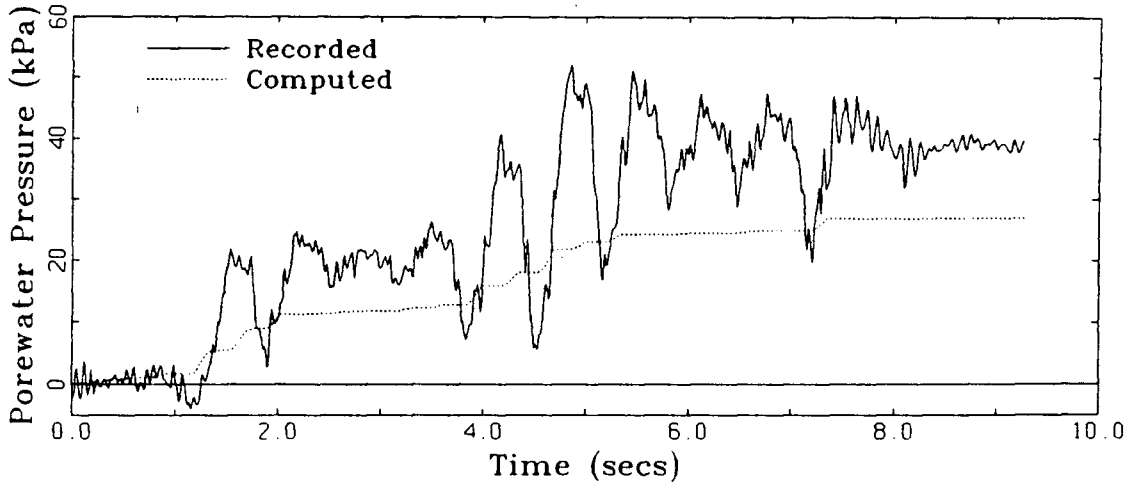

Fig. 8.11 Computed and Measured Porewater Pressures at the Location of PPT 2335 in Test LDO4/EQ2

the computed ratio is 31.0%. As indicated by the designation max.OTLL in Fig. 8.2, the maximum measured values of porewater pressures at this location are outside the guaranteed linear range of the tape recorder. Therefore, measured values have to be viewed with some skepticism.

Transducer PPT 2255 was located in the upper part of the sand foundation as shown in Fig. 8.1. The comparison of porewater pressures shown in Fig. 8.12 indicates that the computed and measured porewater pressures agree closely for the first 4.0 seconds of the record and then deviate sharply. As discussed in the previous section, the measured response is somewhat dubious. It shows a sudden decrease in porewater pressures at around 4.5 seconds when the strongest shaking occurs. In constrast to this, the computed response shows a steady build up of porewater pressure in response to the strong shaking. Hence it is postulated that during the strongest shaking either the transducer moved in relation to the surrounding soil and thereby caused an apparent decrease in the measurement or drainage occurred along the cable leading to the transducer.

Fig. 8.13 shows comparison of porewater pressure responses at the location of PPT 2331. The computed pressures are less than the measured pressures in the early stages of the shaking. However, after 4.0 seconds, the computed pressures build up rapidly and match the measured pressures in the later stages of shaking. The peak residual porewater pressure is predicted satisfactorily. The measured and computed peak porewater pressure ratios are 45.0% and 46.0% respectively.

Tranducer PPT 2330 was located under the structure as shown in Fig. 8.1. The porewater pressures at this location are compared in Fig. 8.14. The measured and computed pressures agree very closely for the first 5.5 seconds of the record. In subsequent stages, in constrast to the little development shown in the computed response, the measured response shows a steady increase upto 7.0 seconds and thereafter shows a steady decrease in pressures.

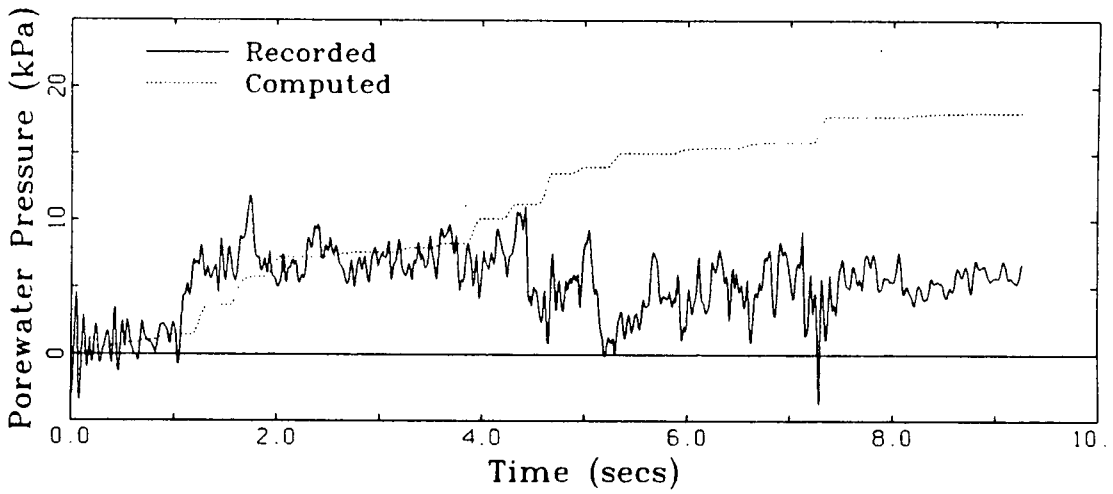

Fig. 8.12 Computed and Measured Porewater Pressures at the Location of PPT 2255 in Test LDO4/EQ2

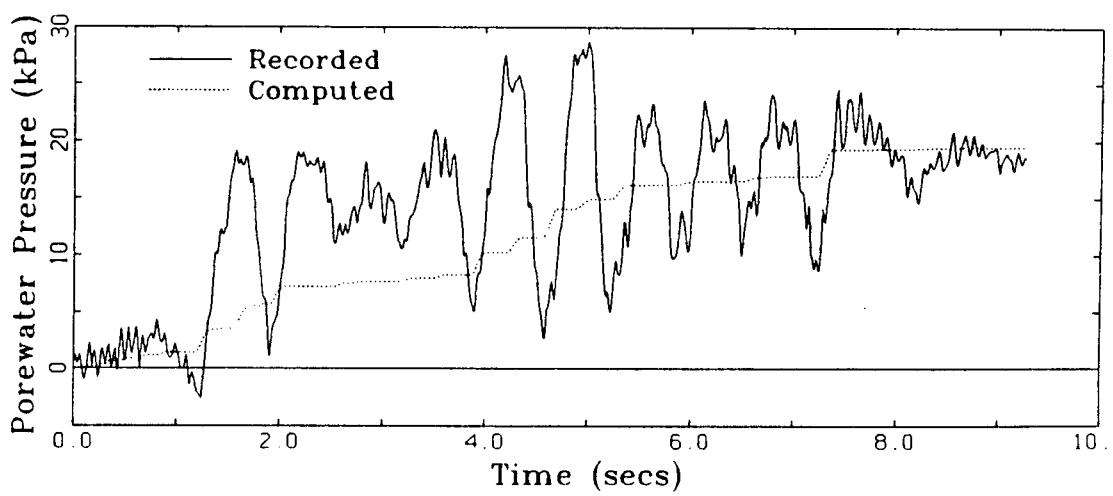

Fig. 8.13 Computed and Measured Porewater Pressures at the Location of PPT 2331 in Test LDO4/EQ2

The decrease in pressures is due to drainage after the quake ceased. A fairly reliable estimate of peak residual pressure is given by the record around 7.0 seconds. The peak residual porewater pressure ratio of the measured and computed responses are 18.0% and 14.8% respectively.

The measured porewater pressures at the location of PPT 68 are compared with the computed pressures in Fig. 8.15. As seen in Fig.8.1, PPT 68 was located directly beneath the structure on the centerline of the model. The measured porewater pressures are less than the computed pressures throughout the shaking. However, differences appear only in the range 3.5 to 6.0 seconds. The reason is that the rapid development exhibited in the computed pressures in response to the strongest shaking in the time range 3.5 to 5.5 seconds is absent in the measured response. Apart from this, the overall agreement is quite satisfactory. The measured and computed porewater pressure ratios at this location are 13.0% and 15.0% respectively.

8.1.5 Comparison of settlements in Test LDO4/EQ2

The measured vertical settlements at the locations of LVDT 82280 and LVDT 46997 are compared with corresponding computed values in Table 8.1. The values are reported at prototype scale. Both LVDTs were located symmetrically opposite about the centerline at top of the structure. The measured values are higher than the computed values.

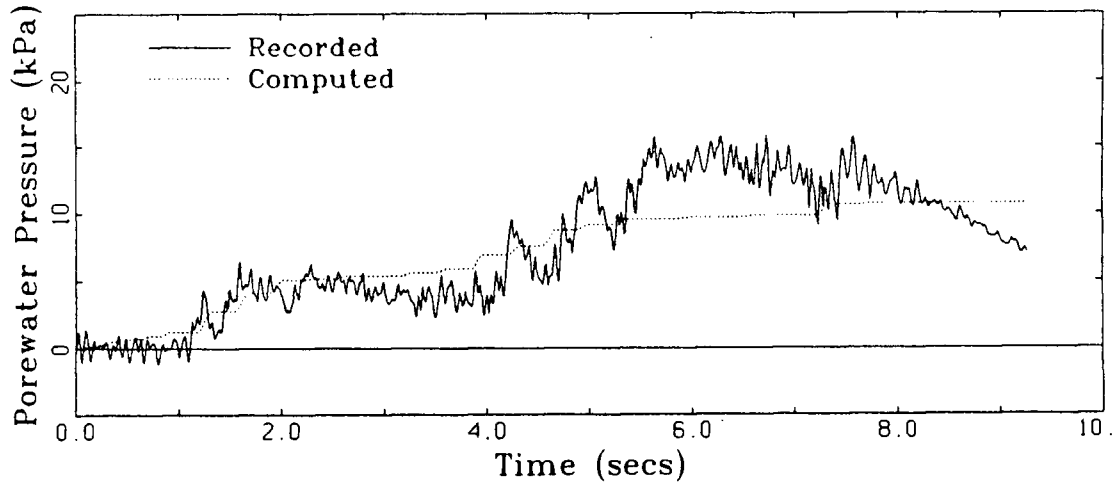

Fig. 8.14 Computed and Measured Porewater Pressures at the Location of PPT 2330 in Test LDO4/EQ2

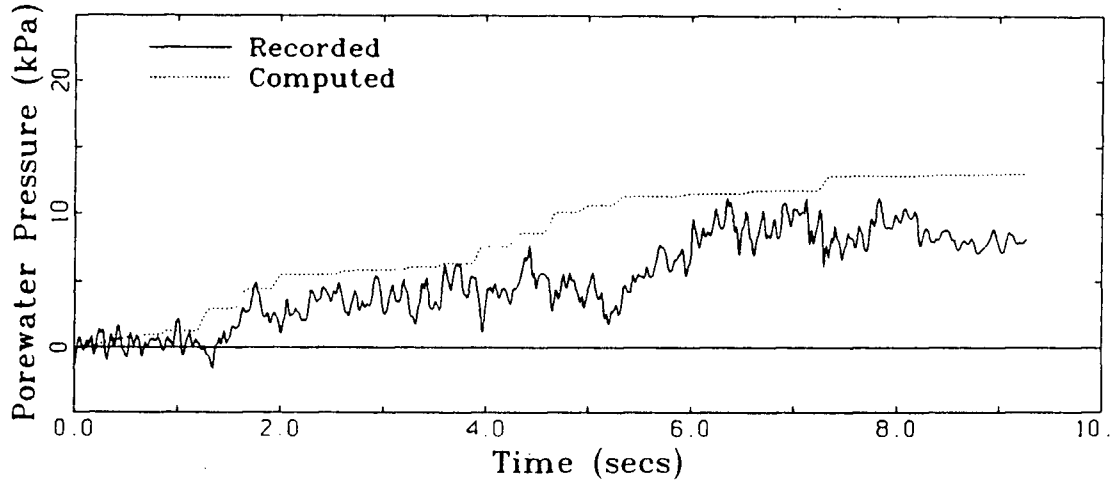

Fig. 8.15 Computed and Measured Porewater Pressures at the Location of PPT 68 in Test LDO4/EQ2

Table 8.1 Comparison of Settlements in Test LDO4/EQ2

Transducer No.	Measured (mm)	Computed (mm)
82280	16.1	8.5
46997	16.9	8.3

8.2 Verification Study Based on Test Series RSS111

8.2.1 Centrifuge Model in Test Series RSS111

A schematic view of a 2-D plane strain model structure embedded in a saturated foundation is shown in Fig. 7.38. The model was constructed by Method 2 described in section 5.5.2.2 using Leighton Buzzard B.S.S 52/100 sand. The sand was placed as uniformly as possible at a nominal relative density estimated to be about 52%. The sand foundation is 110mm high and has a base 900mm wide. The side slopes are at 2.2:1. The length of sand foundation perpendicular to the plane of shaking is 480mm.

The heavy structure is made from a solid piece of aluminum alloy and has dimensions 105mm wide by 108mm high in the plane of shaking. The length perpendicular to the plane of shaking is 470mm. The structure is embedded to a depth of 25mm in the sand foundation. Coarse sand was glued to the base of the structure to prevent slip between structure and sand.

During the test the model experienced a nominal centrifugal acceleration of 80g. The model, therefore, simulated a structure approximately 8.6m in height, 12m in width and embedded to a depth 2m in sand foundation. The average contact pressure between the

structure and sand foundation was approximately 240 kPa.

The locations of the accelerometers, porewater pressure transducers and LVDTs are shown in Fig. 8.16. ACC 3441 mounted on the base of the model container defined the acceleration input to the model.

In this test, as may be seen from Fig. 8.16, the porewater pressure transducers were duplicated at corresponding locations on both sides of the centerline of the model except for PPT 2255 and PPT 1111. The purpose of the duplication was to check the reliability of the recorded data. This was not done in earlier tests and in some cases it was difficult to decide whether differences between measured and computed responses were due to instrumentation problems, lack of homogeneity in the sand foundation or deficiencies in the method of analysis. If the model was homogeneous and the instrumentation was perfect, then theoretically responses measured at pairs of locations should yield very similar responses. The extent to which the records for corresponding locations agree with each other is an indication of reliability and homogeneity.

8.2.2 Model Response in Test RSS111

The smoothed data from all tranducers for the earthquake (EQ1) are shown in Fig. 8.17 and Fig. 8.18. The input motion measured by ACC 3441 has a peak amplitude of 14.3% of the centrifugal acceleration and has 10 complete cycles of significant shaking. Accelerometers ACC 1552, ACC 1925, ACC 1900 and ACC 1572 measured vertical accelerations and other accelerometers measured horizontal accelerations. ACC 3457 and ACC 1552 (Fig. 8.17) records have to be viewed with caution as they both show a large bias in one direction. Therefore, they have to be corrected for baseline distortion before making comparisons. Besides the drifts, ACC 1552 shows a response primarily at a frequency similar to that of the input motion right from the beginning of shaking. This is quite unusual

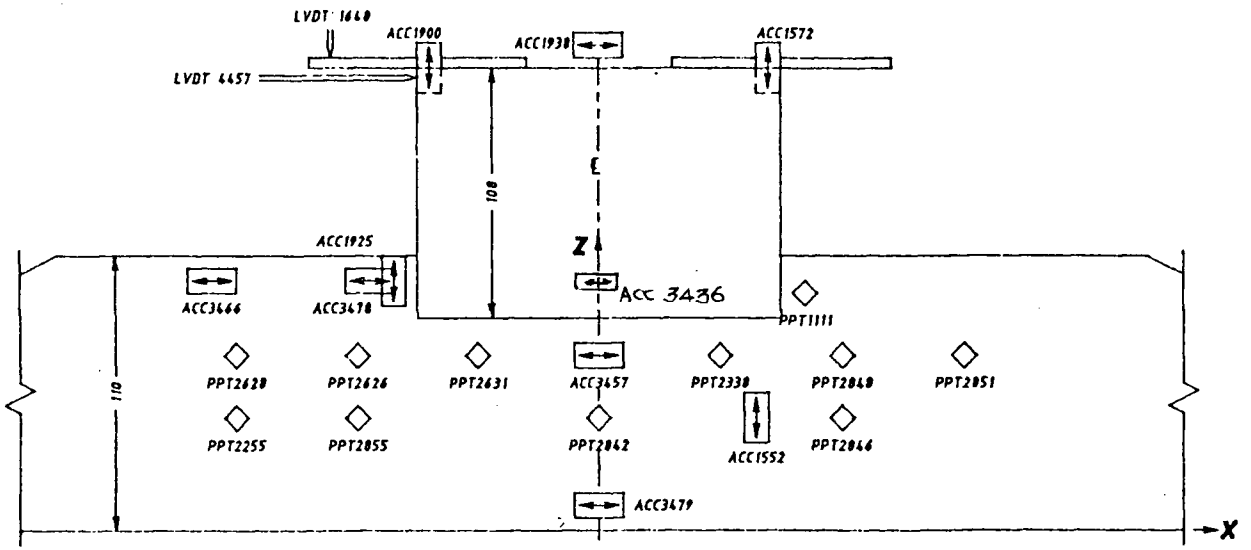

Fig. 8.16 Instrumented Model in Test Series RSS111

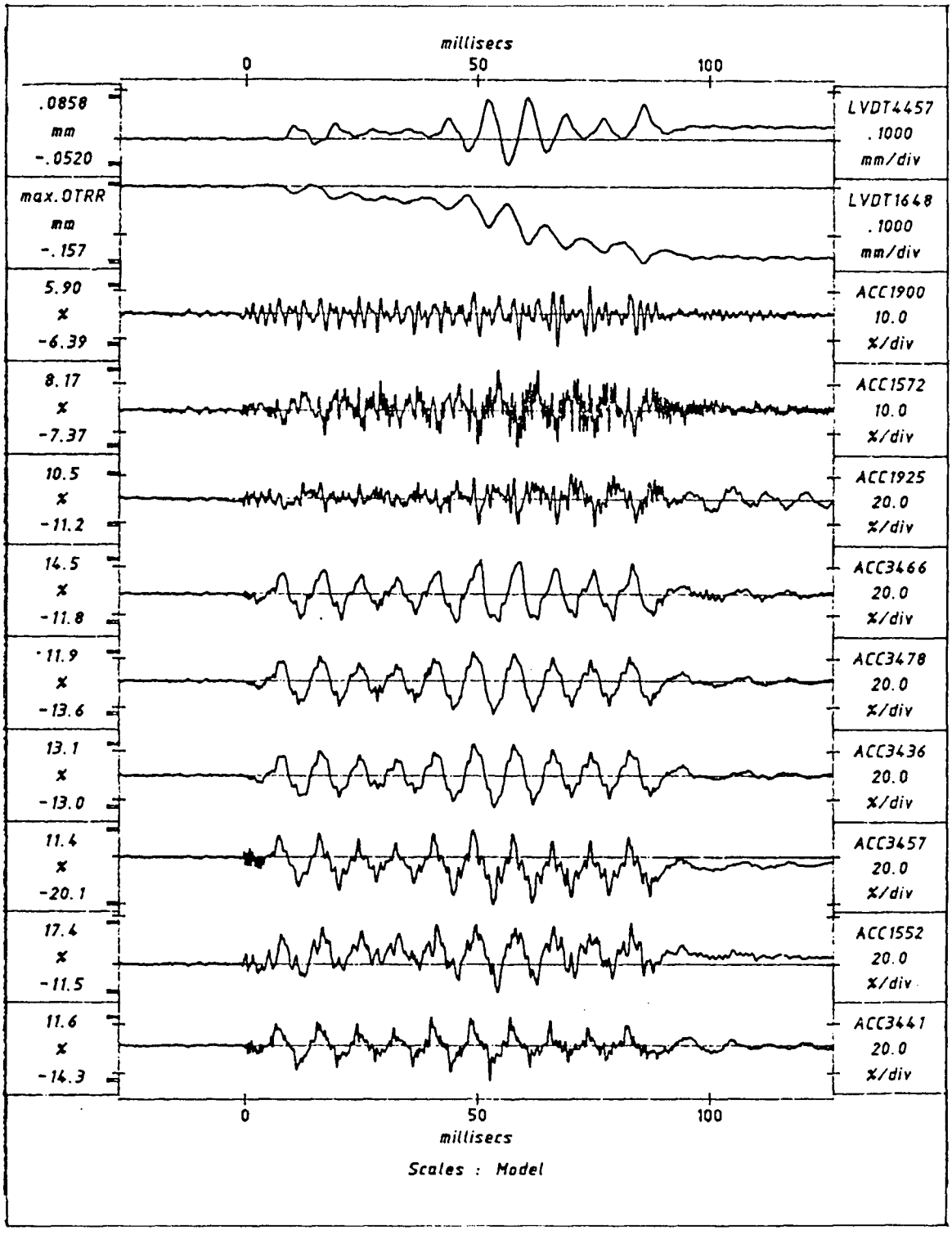

Fig. 8.17 Model Response in Test RSS111/EQ1

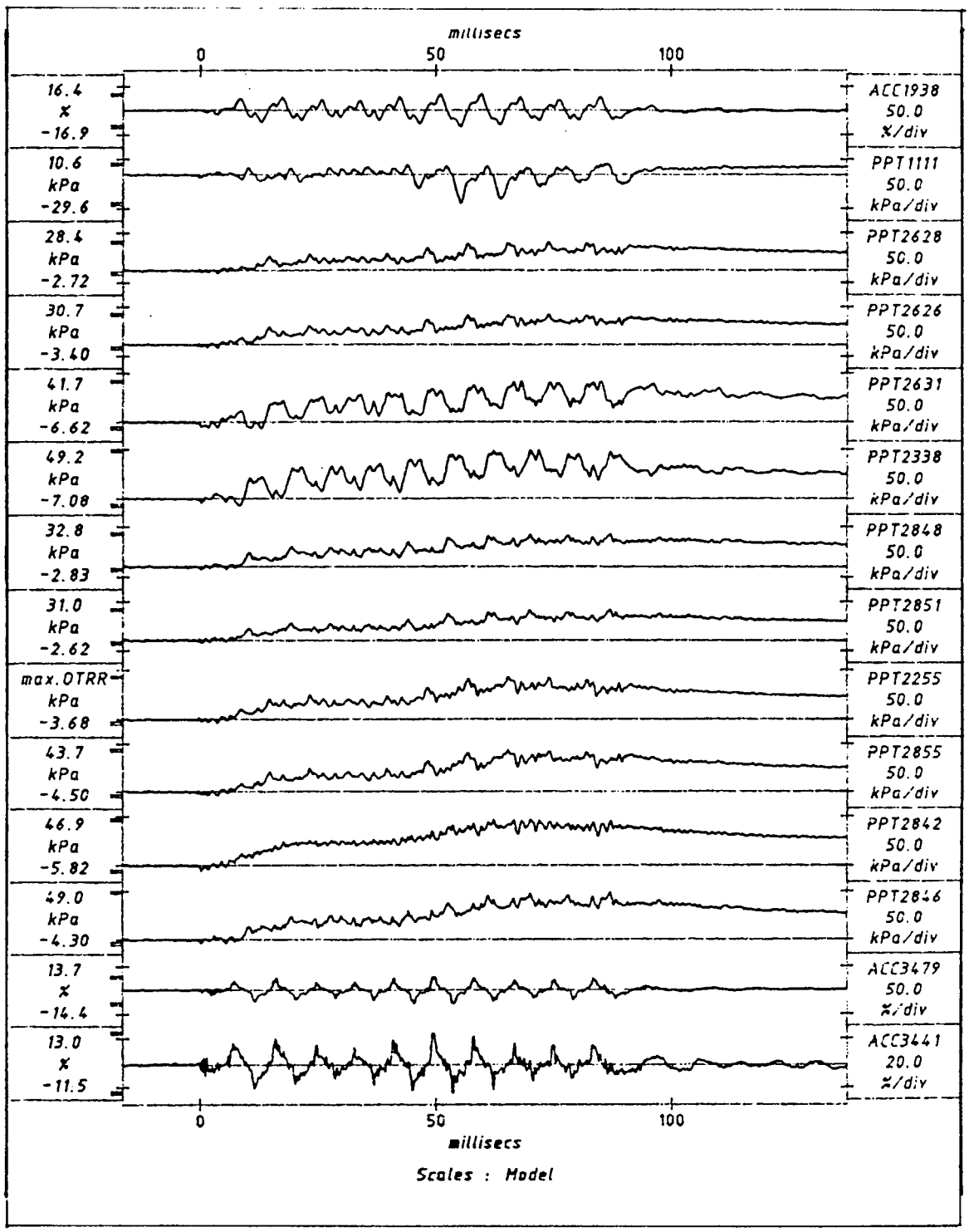

Fig. 8.18 Model Response in Test RSS111/EQ1

for a vertical acceleration record at a location in the middle of the sand foundation. It is probable that the transducer rotated so that it measures a mixture of vertical and horizontal accelerations. Because of the uncertainty, ACC 1552 was not used in the study. ACC 1925, located adjacent to the edge of the structure, shows significant response even after 95 milliseconds when the significant motion of earthquake had already ceased. This record may be suspect and therefore is not used in the study. ACC 1900 and ACC 1572 were placed at opposite edges of the structure symmetrically about the centerline of the model. Since the model embankment was constructed to be homogeneous, both these should record similar forms of response. Yet both records show quite different forms of responses. ACC 1572 has a lot noise compared to the much cleaner record of ACC 1900.

The porewater pressure data, shown in Fig. 8.18, show the sum of the transient and residual porewater pressures. The peak residual porewater pressures were attained when the earthquake excitations ceased at about 95 milliseconds. After this, most of the records show significant decreases in pressures due to drainage. The pressures recorded by the symmetric pairs PPT 2631 and PPT 2338, PPT 2626 and PPT 2848, PPT 2628 and PPT 2851, and PPT 2855 and PPT 2846 are quite similar although there are obviously minor differences in the levels of both transient and residual porewater pressures. Therefore it can be assumed that the sand foundation is remarkably symmetrical in its properties about the centerline of the model.

PPT 2631 and PPT 2338 records show large oscillations about the residual porewater pressure levels. These are due to soil-structure interaction. The transducers were located directly underneath the structure and therefore they were subjected to large cycles of normal stresses due to rocking of the structure. The fluctuations in stress resulted in similar fluctuations in mean normal stress and hence in porewater pressure. It is also apparent that the fluctuations in these records are almost 180 degrees out of phase. For instance,

at time 50 milliseconds, PPT 2338 records a pressure below the steady residual component while PPT 2631 records a pressure above it. The phase shift results from the fact that the cyclic normal stresses caused by rocking of the structure are 180 degrees out of the phase at these locations.

As free field is approached, it is evident that the influence of soil-structure interaction decreases. For instance, all other pairs show records that contain somewhat smaller oscillations than those contained in the pair PPT 2631 and PPT 2338. However, the pair PPT 2846 and PPT 2855 show somewhat larger oscillations than those recorded in the free field. The locations of PPT 2846 and PPT 2855 are close enough to the structure to be affected by the cyclic normal stresses caused by rocking and therefore it is not surprising to see small oscillations present in the records.

PPT 2842 is located on the centerline of the model approximately midway between the base of the model and the base of the structure. This location is not subjected to large normal stress fluctuations due to rocking and therefore the porewater pressure record does not oscillate much about the residual porewater pressure. However, PPT 2842 record is not consistent with other porewater pressure records or with the input motion. The strongest shaking occurs between time 50 and 75 milliseconds and strong shaking persists up to 90 milliseconds. Yet PPT 2842 shows significant drainage from time 60 milliseconds which is not evident in any other records. It is probable that drainage occurred along the lead of the transducer.

During strong shaking, PPT 1111 record show large fluctuations in pressures causing negative porewater pressures. PPT 1111 was located near the surface and adjacent to the structure. Hence, due to rocking of the structure, this was subjected to large shear strains. This, along with low confining pressure at this location led to the strong dilatant behavior.

The input motion measured by ACC 3441 is shown in Fig. 8.19 at prototype scale.

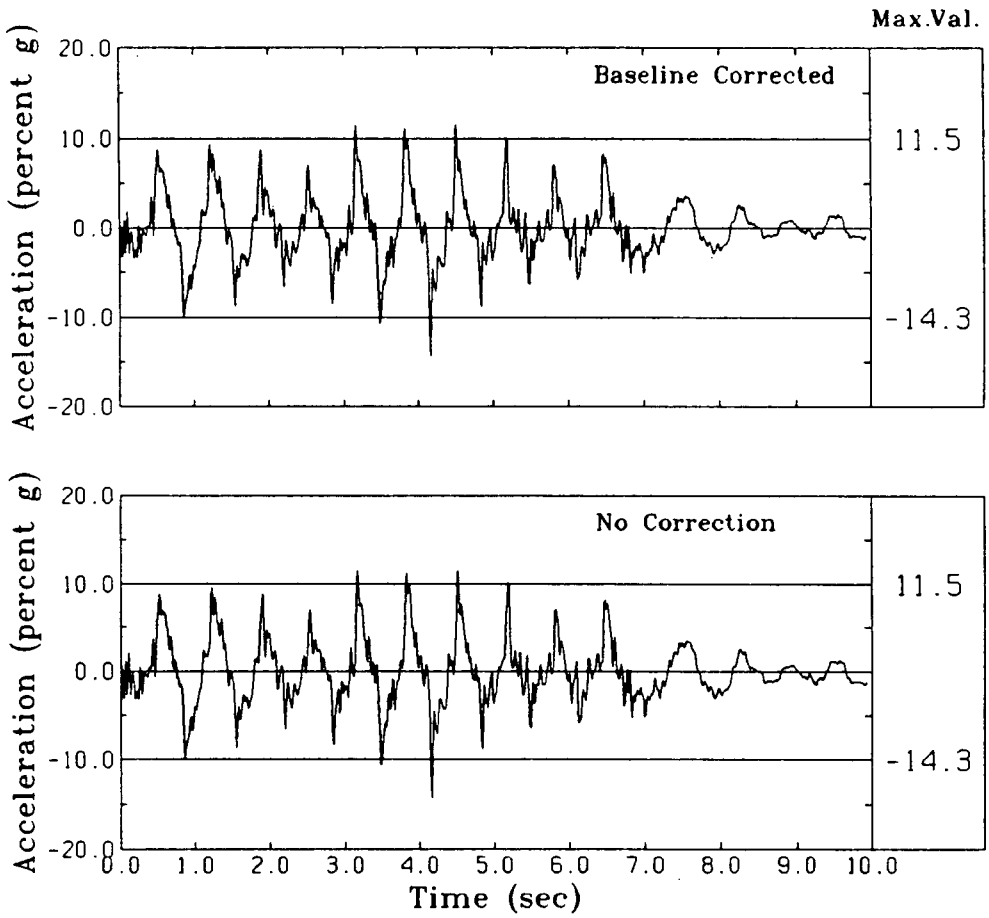

Fig. 8.19 Input Motion for Test RSS111/EQ1

It also include the baseline corrected motion. It can be seen that the uncorrected and corrected motions are identical. The total duration of the earthquake is around 10.0 seconds and significant shaking ceases around 7.5 seconds. The peak acceleration of 14.3%g occurs at 4.17 seconds.

The prototype was analysed as a 2-D plane strain problem using TARA-3. The foundation sand was assumed to be symmetrical in its properties about the centerline. In the centrifugal acceleration field of 80g, the heavy structure underwent consolidation settlement which led to an increase in density under the structure compared to that in the free field. For the analysis, the soil density under the structure was adjusted to be 64% based on the consolidation settlements.

8.2.3 Comparison of Acceleration Responses in Test RSS111/EQ1

Figs. 8.20 to 8.22 show comparison between measured and computed responses at locations of ACC 3479, ACC 3466 and ACC 3478 respectively. ACC 3479 was located near the base, ACC 3466 near the surface in the free field and ACC 3478 near the edge of the structure. Measured and computed responses at the location ACC 3479 (Fig. 8.20) are similar to that of the input motion. This is expected because ACC 3479 was located very close to the base. Computed peak amplitudes closely agree with those of measured ones. The measured and computed peaks are 14.4%g and 13.3%g respectively. Comparison in terms of frequency content is also good.

At location of ACC 3466, the comparison shown in Fig. 8.21 is generally good both in terms of peak values and frequency content. However, the computed peak ordinates between time 4.0 and 6.0 seconds are somewhat less than the measured values. The peak acceleration values for measured and computed responses are 14.4%g and 11.0%g respectively.

Comparison at the location of ACC 3478 in Fig. 8.22 is good with computed peak

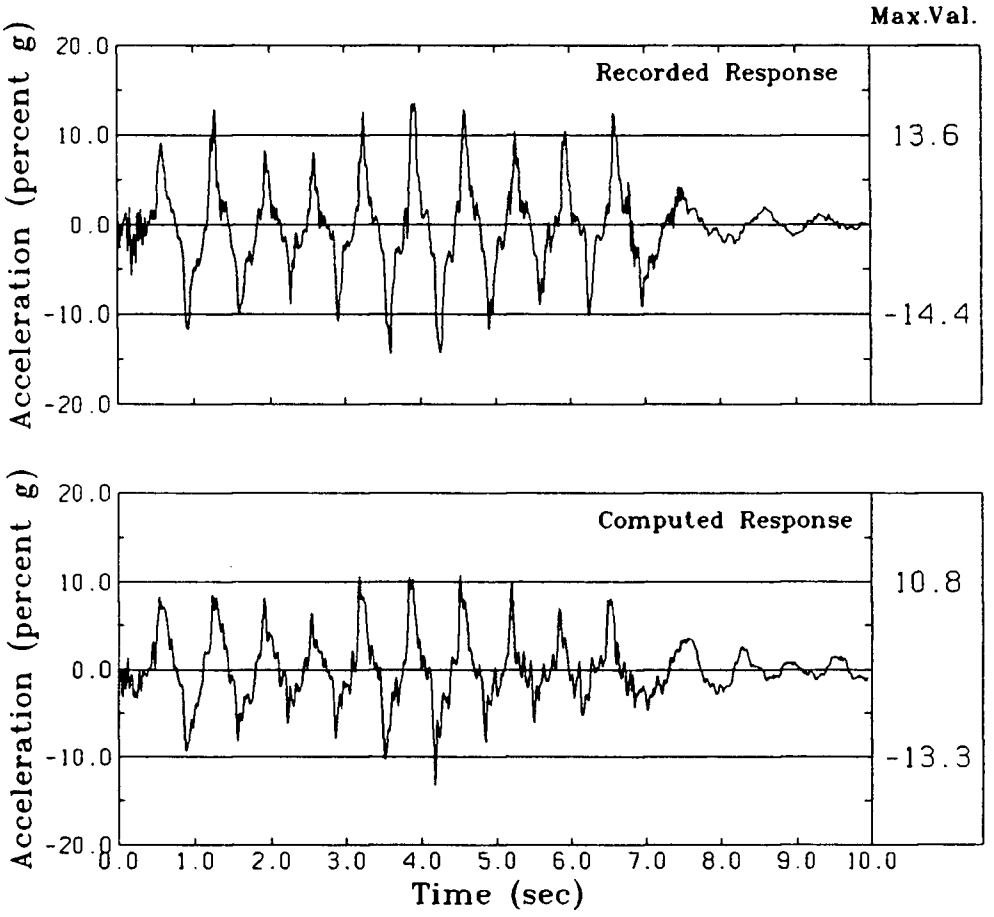

Fig. 8.20 Computed and Measured Accelerations at the Location of ACC 3479 in Test RSS111/EQ1

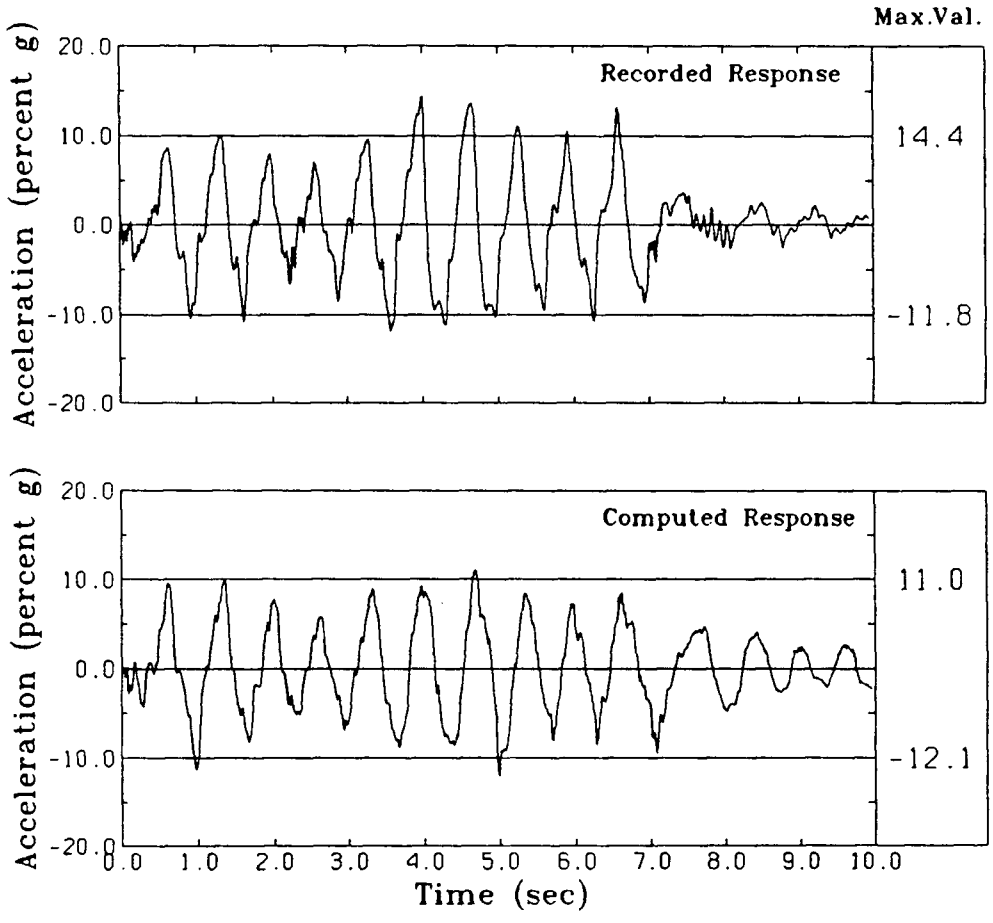

Fig. 8.21 Computed and Measured Accelerations at the Location of ACC 3466 in Test RSS111/EQ1

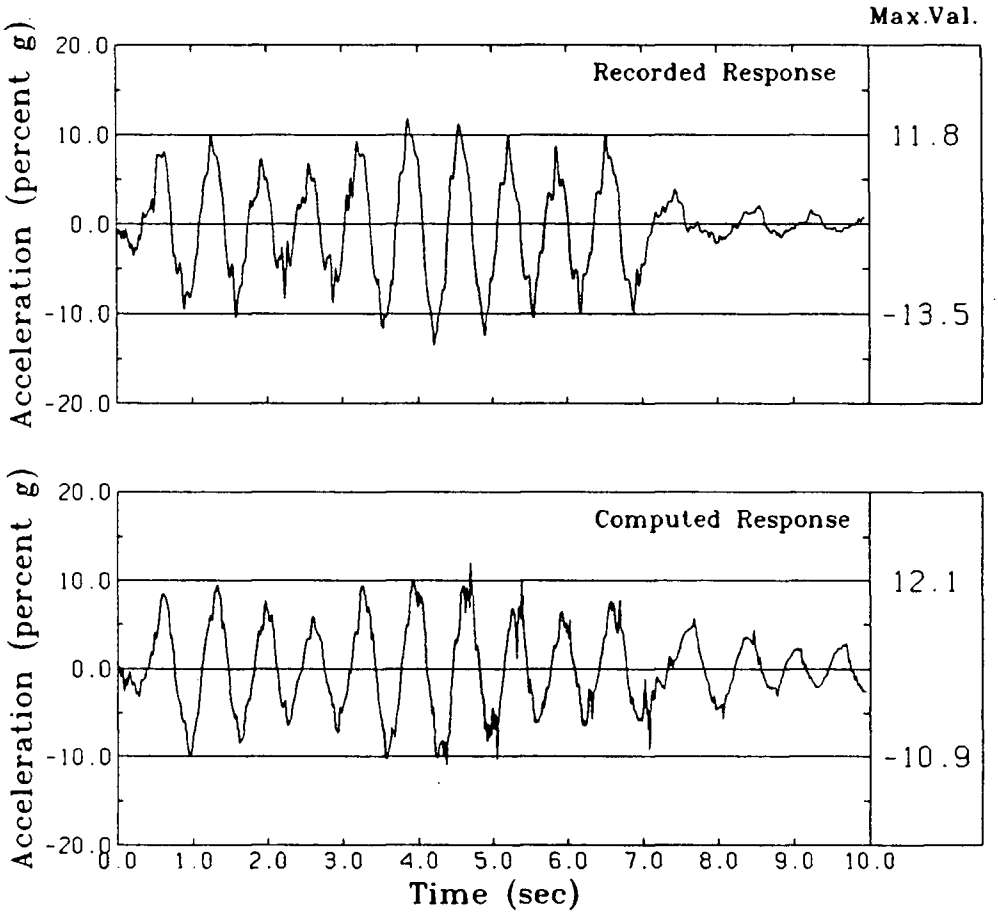

Fig. 8.22 Computed and Measured Accelerations at the Location of ACC 3478 in Test RSS111/EQ1

ordinates matching closely with those of the measured. The peak values in measured and computed responses are 13.5%g and 10.9%g respectively.

The measured and computed horizontal accelerations at the top of the structure at the location of ACC 1938 are shown in Fig. 8.23. They are very similar in frequency content, each corresponding to the frequency of the input motion given by ACC 3441 (Fig. 8.19). The peak accelerations agree fairly closely. The measured and computed peak values are 16.9%g and 16.3%g respectively.

The computed and measured vertical accelerations at the location of ACC 1900 are shown in Fig. 8.24. The computed response closely matches the recorded response in both peak values and frequency content. As seen in Fig. 8.17, high frequency noises are present in ACC 1572 record and therefore frequency components higher than 10.0 Hz were removed by a low pass filter. The original and filtered responses are shown in Fig. 8.25. The filtered response does not have the noises anymore and moreover it is now similar in frequency to ACC 1900 record. Fig. 8.26 shows the comparison of the filtered and computed responses. The agreement in both frequency content and peak values is excellent. The measured and computed peaks at location of ACC 1572 are 7.22%g and 6.86%g while at ACC 1900 they are 6.32%g and 6.86%g respectively. The measured and computed accelerations at the location of ACC 3436 are shown in Fig. 8.27. ACC 3436 was located on the vertical edge of the structure that lies parallel to the plane of shaking as shown in Fig. 8.16. The peak accelerations and frequency content agree fairly closely.

As may be seen from Fig. 8.17, ACC 3457 record shows a large shift in one direction. The original (uncorrected) and the baseline corrected records are compared in Fig. 8.28. The baseline distortion is not present in the corrected record. Fig. 8.29 shows that comparison between corrected and computed responses is good both in terms of frequency content and peak values. The measured and computed peaks are 12.7%g and 11.7%g respectively.

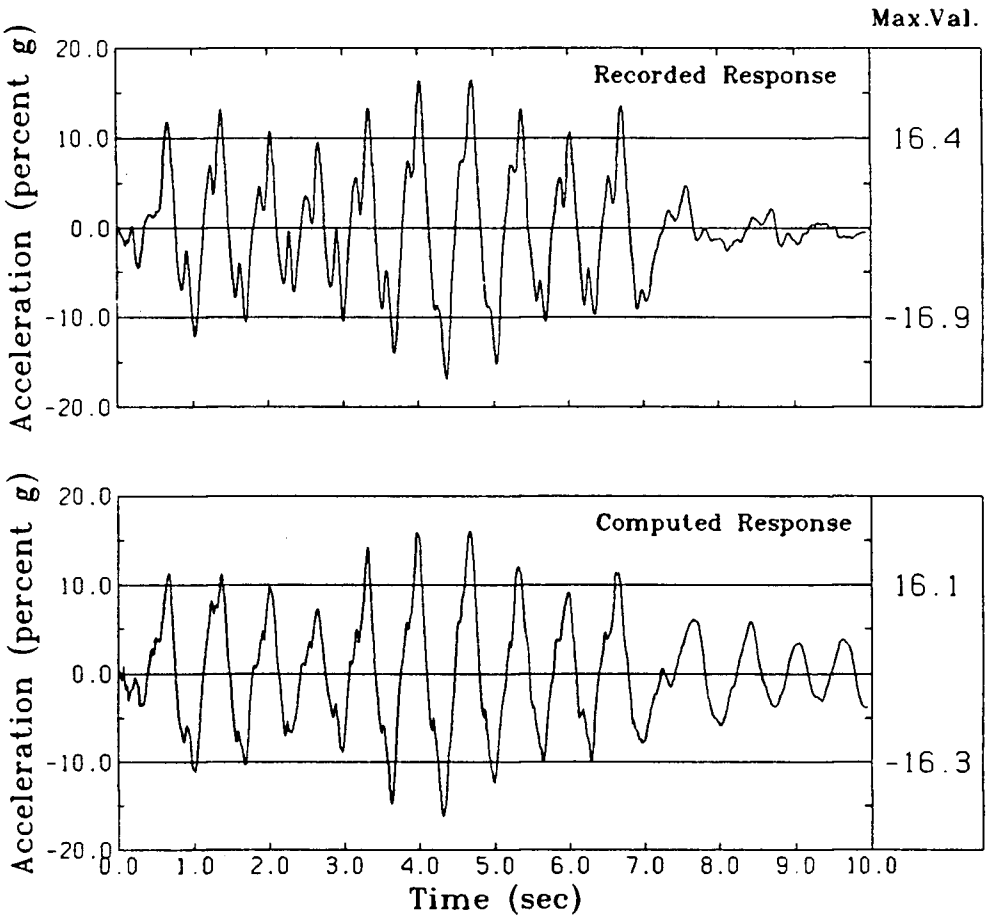

Fig. 8.23 Computed and Measured Accelerations at the Location of ACC 1938 in Test RSS111/EQ1

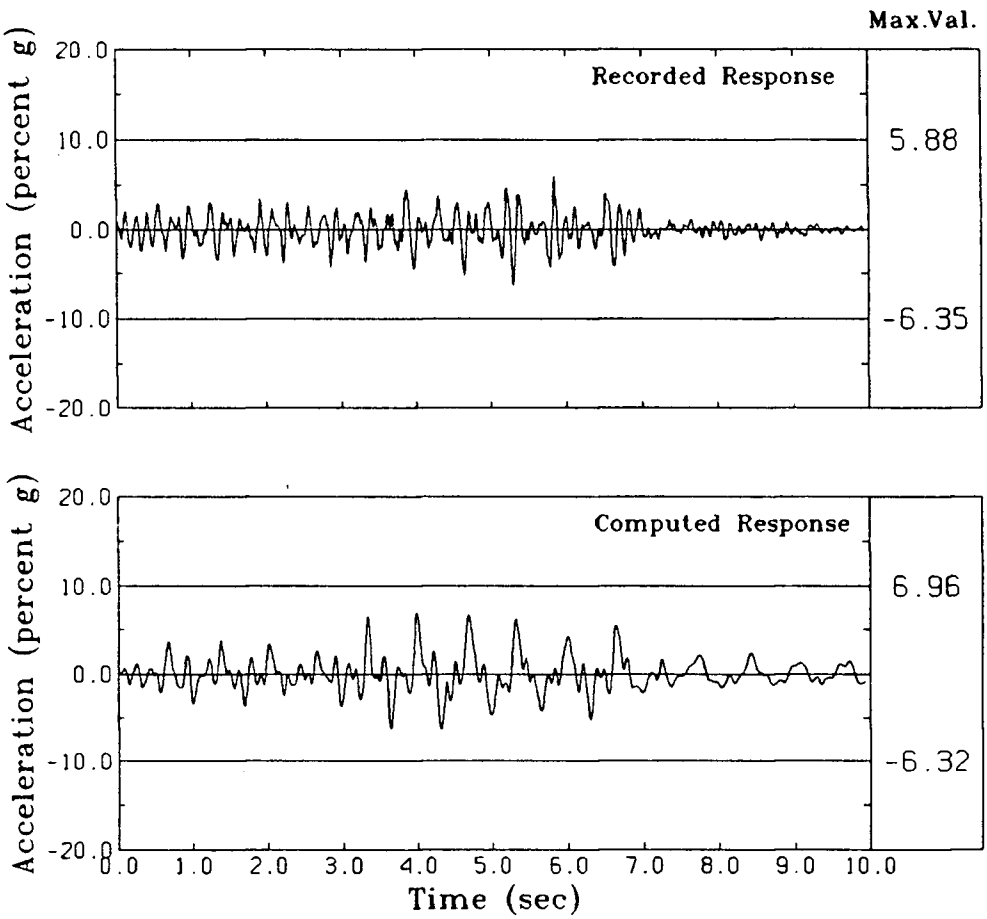

Fig. 8.24 Computed and Measured Accelerations at the Location of ACC 1900 in Test RSS111/EQ1

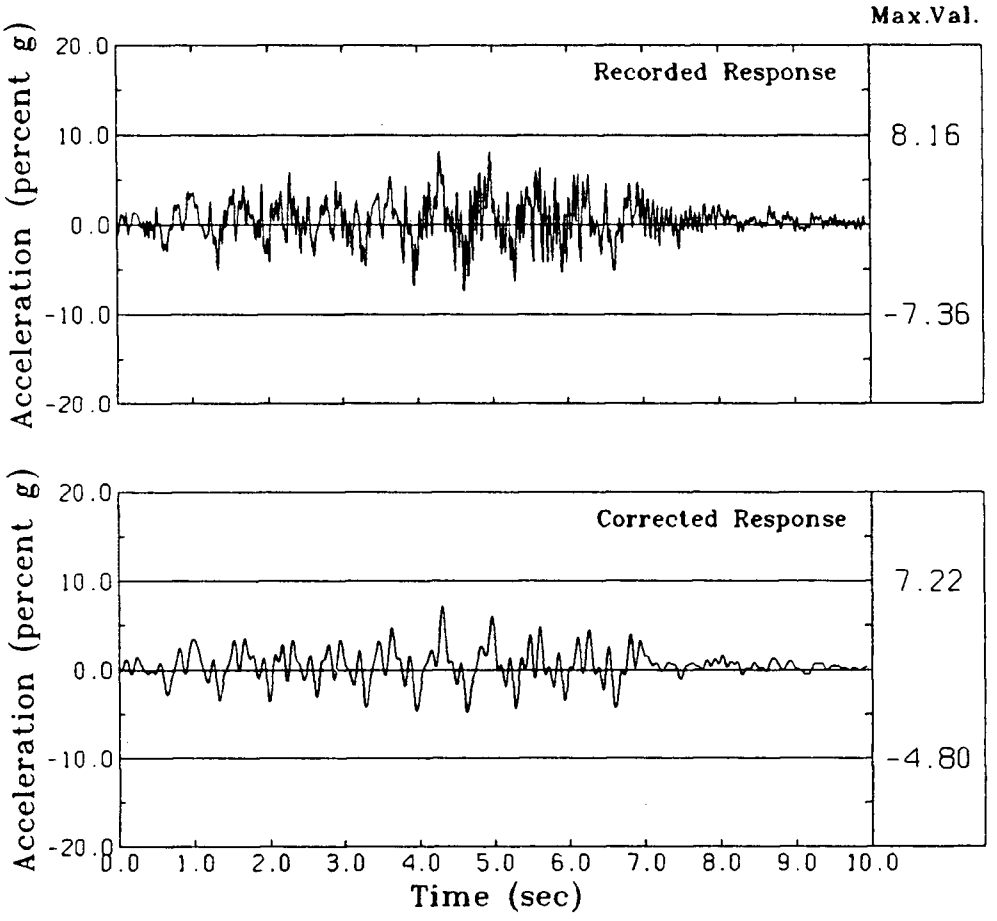

Fig. 8.25 Original and Corrected Accelerations at the Location of ACC 1572 in Test RSS111/EQ1

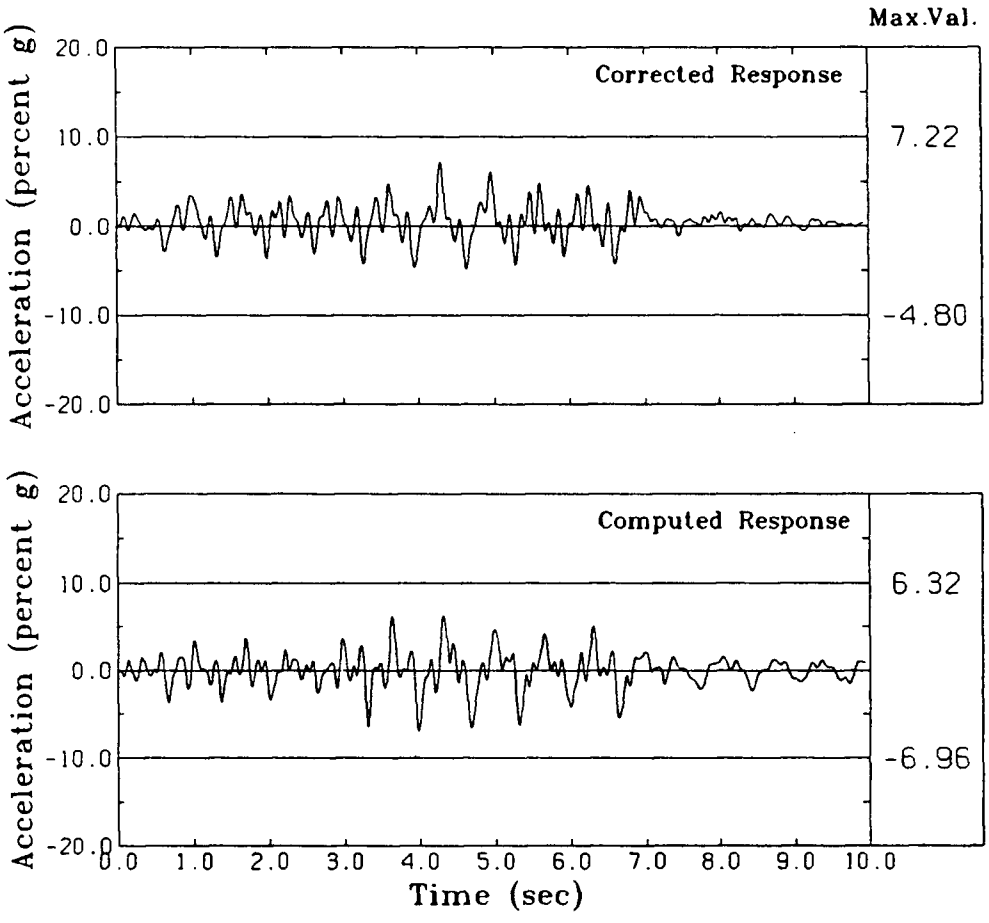

Fig. 8.26 Computed and Corrected Accelerations at the Location of ACC 1572 in Test RSS111/EQ1

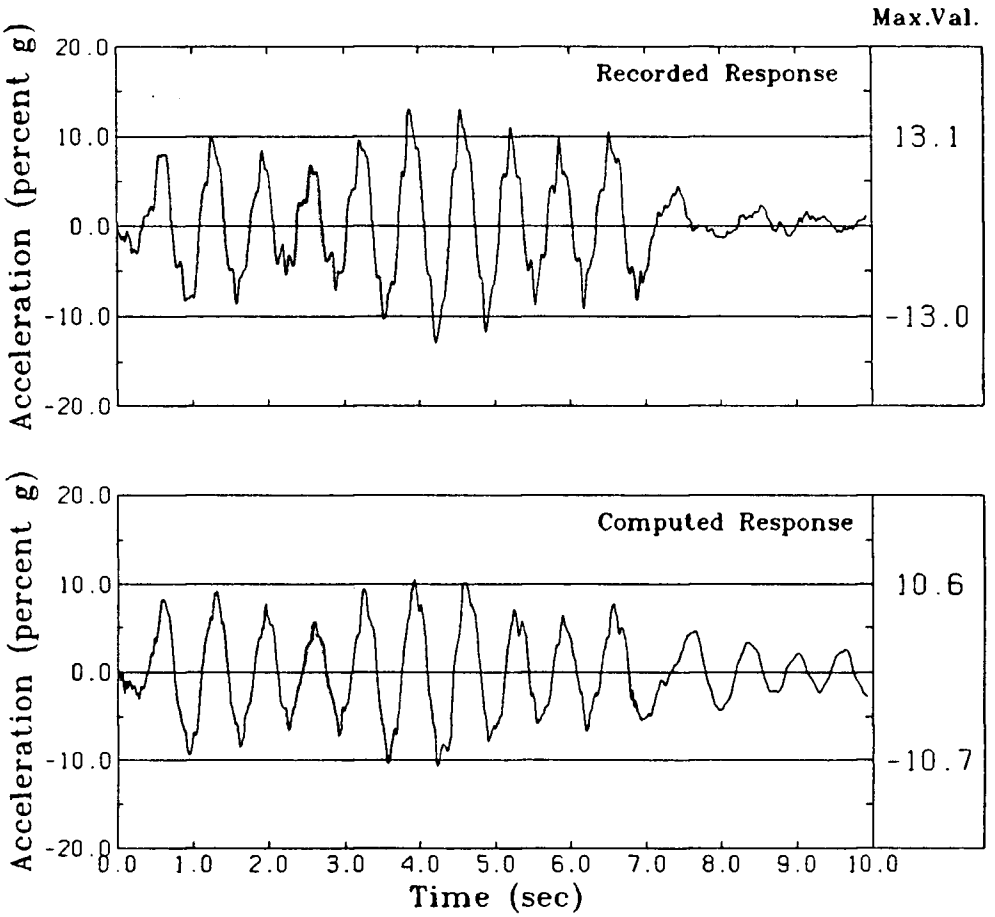

Fig. 8.27 Computed and Measured Accelerations at the Location of ACC 3436 in Test RSS111/EQ1

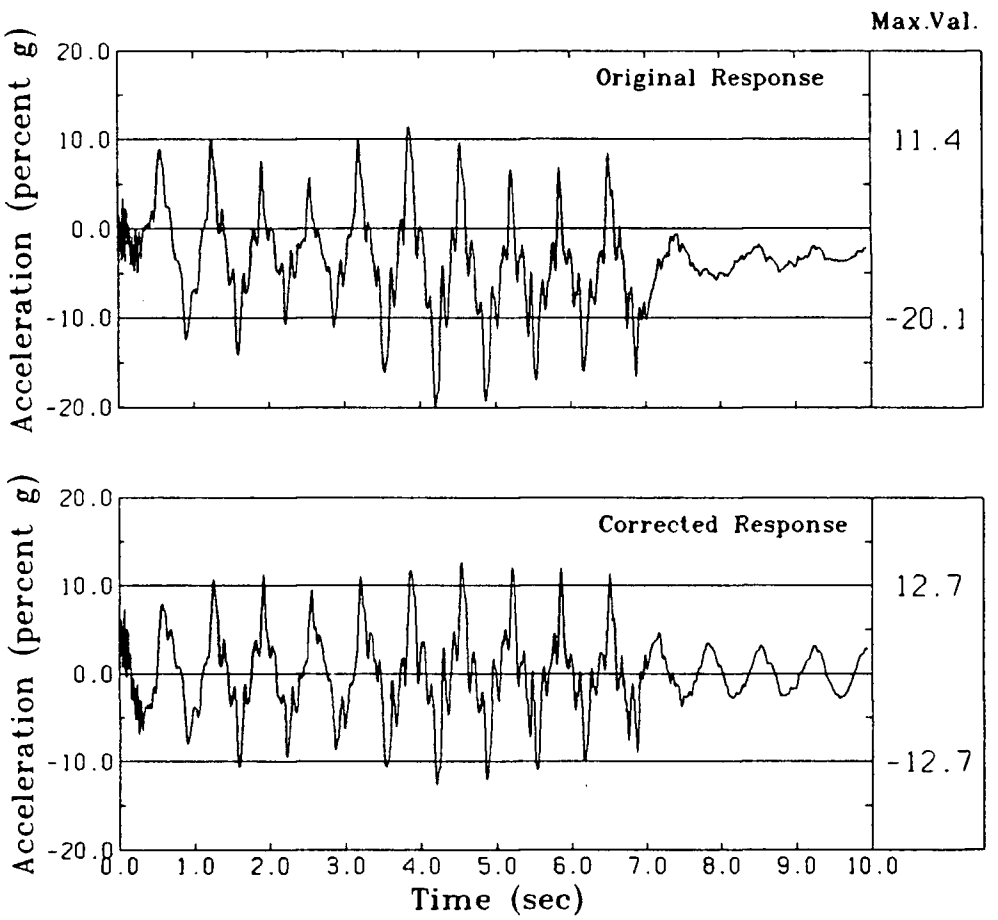

Fig. 8.28 Original and Corrected Accelerations at the Location of ACC 3457 in Test RSS111/EQ1

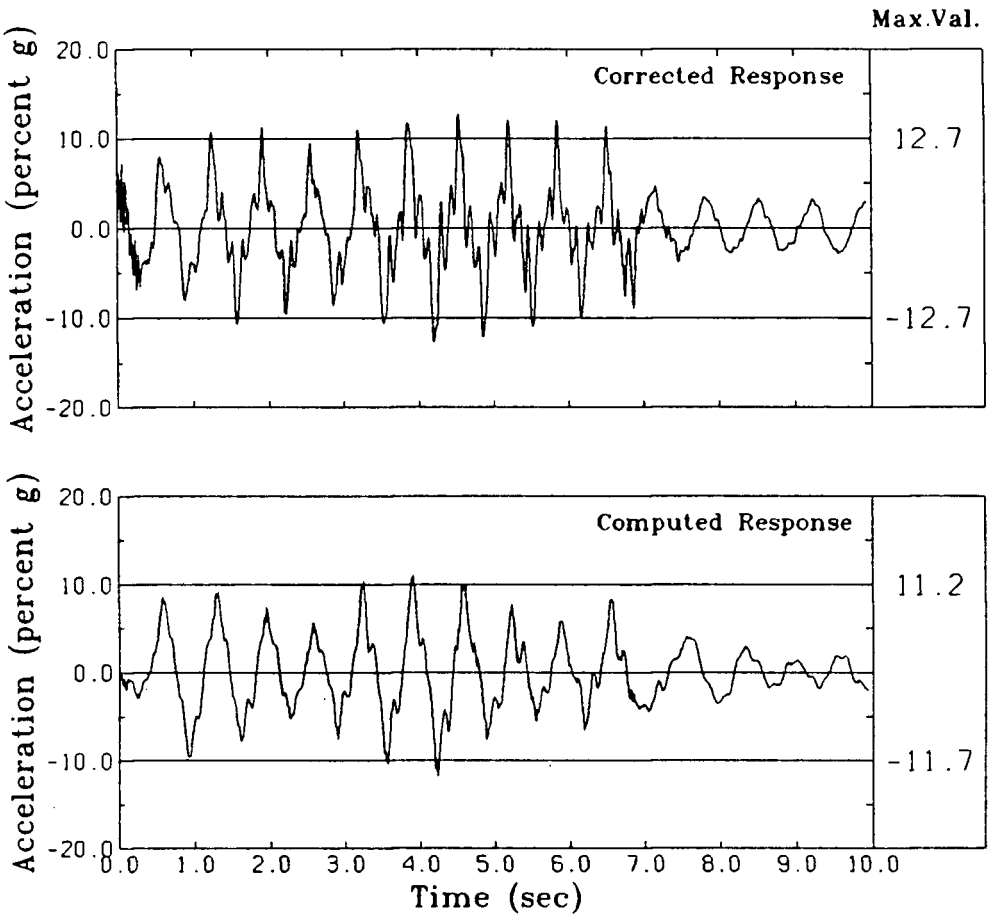

Fig. 8.29 Computed and Corrected Accelerations at the Location of ACC 3457 in Test RSS111/EQ1

8.2.4 Comparison of Porewater Pressure Response in Test RSS111/EQ1

The measured and computed porewater pressures at locations of PPT 2338 and PPT 2631 are shown in Fig. 8.30 and Fig. 8.31 respectively. These transducers were located directly beneath the structure and symmetric about the centerline. The measured responses have two types of oscillations superimposed on steady accumulating residual porewater pressures. The first type is the large oscillations with cycles of loading which are of low frequency and second type is the higher frequency peaks superimposed on the large oscillations. The low frequency oscillations are due to fluctuations in mean normal stresses caused by rocking of the structure and the higher frequency peaks are due to dilations caused by shear strains. However, the computed responses do not have any of these oscillations because only residual porewater pressures are computed by TARA-3. The computed rate of porewater pressure development at both locations matches fairly well with that of the measured response. The maximum residual porewater pressure is observed between 7.0 and 7.5 seconds just after the strong shaking has ceased and before significant drainage has time to occur. The measured and computed residual porewater pressure, as given in Table 8.2, agree very well at both locations. The computed maximum residual porewater pressure at both locations is 16.0% of the initial effective vertical stress. It is also clearly evident that both measured responses show significant drainage starting at time 7.5 seconds immediately after the strong shaking has ceased.

The pair PPT 2848 and PPT 2626 were located symmetrically about the centerline, outside the edge of the structure at the same elevation as the pair PPT 2338 and PPT 2631, and the comparisons are shown in Fig. 8.32 and Fig. 8.33 respectively. The pressures measured at these locations show somewhat smaller oscillations than those recorded under the structure. This is due to the fact that the effect of rocking on mean normal stresses at these locations is less than at locations under the structure. In these cases, the computed

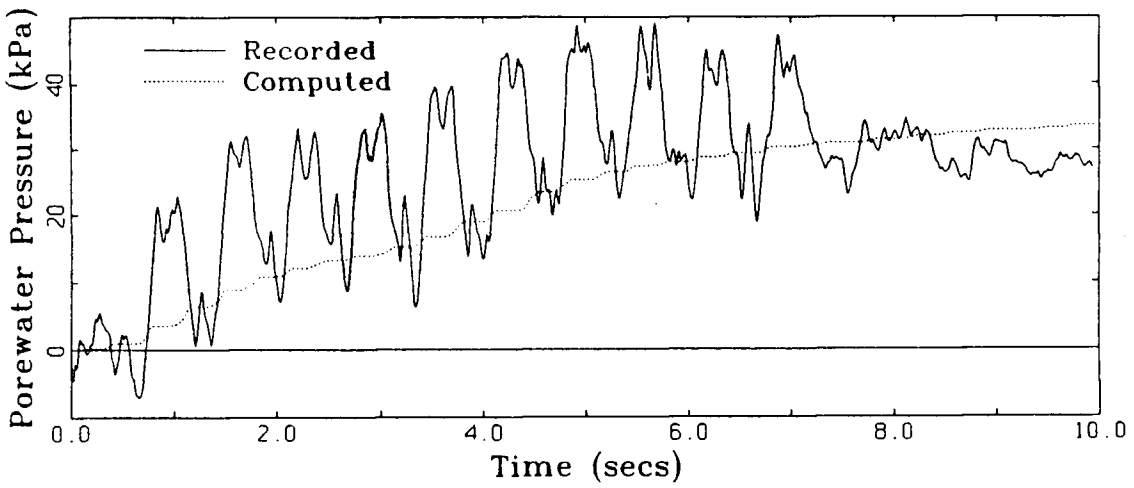

Fig. 8.30 Computed and Measured Porewater Pressures at the Location of PPT 2338 in Test RSS111/EQ1

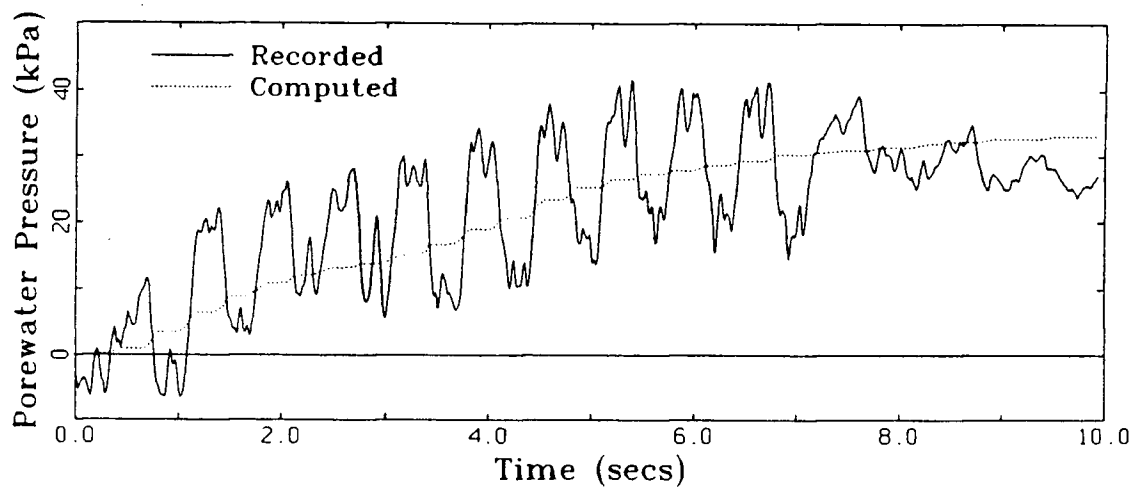

Fig. 8.31 Computed and Measured Porewater Pressures at the Location of PPT 2631 in Test RSS111/EQ1

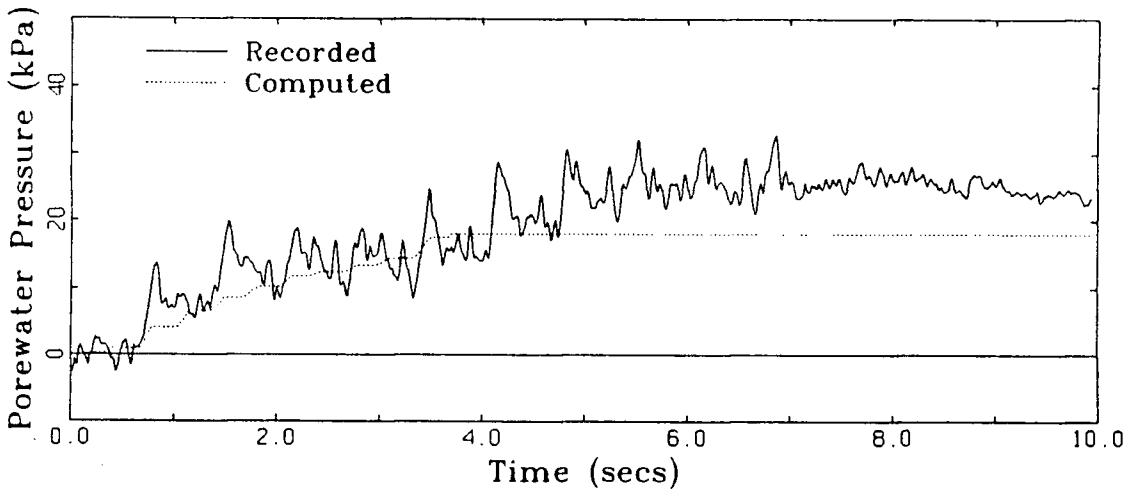

Fig. 8.32 Computed and Measured Porewater Pressures at the Location of PPT 2848 in Test RSS111/EQ1

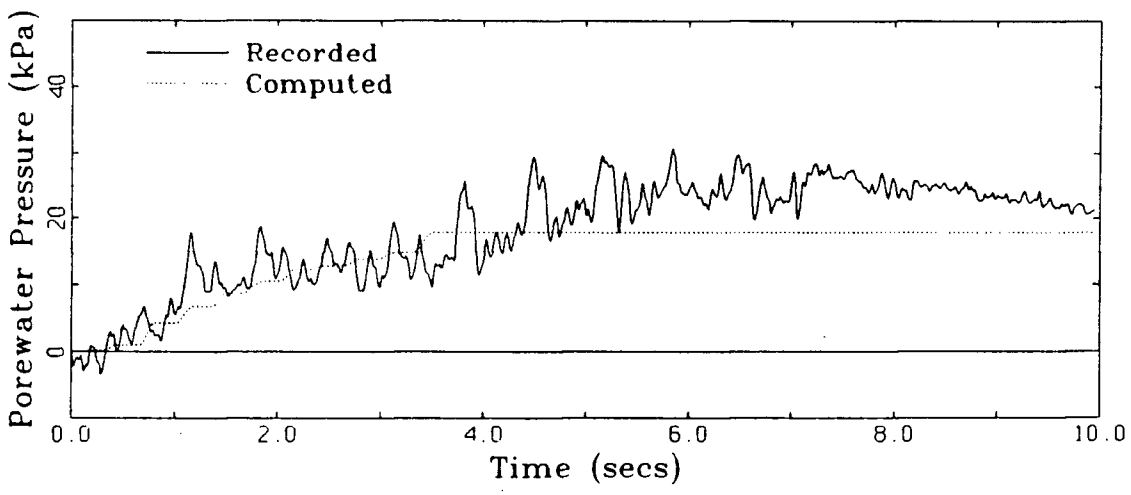

Fig. 8.33 Computed and Measured Porewater Pressures at the Location of PPT 2626 in Test RSS111/EQ1

residual porewater pressures are less than the measured ones (Table 8.2) but the overall agreement is quite satisfactory.

Table 8.2 Comparison of Peak Residual Porewater Pressures in Test RSS111/EQ1

Transducer No.	Measured (kPa)	Computed (kPa)
PPT 2338	33.5	33.5
PPT 2631	33.0	33.5
PPT 2848	24.5	18.0
PPT 2626	24.0	18.0
PPT 2851	24.3	26.6
PPT 2628	23.7	26.6
PPT 2846	38.1	38.0
PPT 2855	36.0	38.0
PPT 2342	-	72.0
PPT 2255	37.0	38.0
PPT 1111	4.0	2.9

It is interesting to note that measured PPT 2848 response shows a slight increase in pressures in the range 7.5 to 8.2 seconds before showing a decrease in pressures. This increase is thought to have occurred due to migration of porewater pressures from surrounding areas of high porewater pressure such as the location of PPT 2338. However, unlike PPT 2848, PPT 2626 record shows decrease in pressures after 7.5 seconds. Since the drainage and internal redistribution are not modeled in TARA-3 analysis during shaking, differences

between the measured and computed responses could occur especially after 7.5 seconds when drainage begins to dominate.

The pair PPT 2851 and PPT 2628 were located out in the free field at the same elevation as the pair PPT 2338 and PPT 2631 and the responses at these locations are compared in Fig. 8.34 and Fig. 8.35 respectively. The measured peak residual porewater pressure is slightly less than the computed one but the overall agreement is good. As seen from Table 8.2, the differences in measured and computed peak residual values are small. It is also interesting to note that at these locations little drainage takes place even though they are close to drainage boundaries. This is again due to migration of porewater pressures from areas of high porewater pressures.

Fig. 8.36 and Fig. 8.37 show comparison of porewater pressure responses at the locations of PPT 2846 and PPT 2855 respectively. In both cases, the comparison is excellent both in terms of the rate of development and peak residual value. The measured and computed peak residual porewater pressures, shown in Table 8.2, agree closely. As expected, significant differences appear only in the time range 7.5 to 10.0 seconds owing to drainage and diffusion. The large low frequency oscillations observed in the PPT 2338 and PPT 2631 responses are absent indicating that the influence of soil-structure interaction is not prominent at these locations.

PPT 2842 was located on the centerline midway between the base of the model and base of the structure. Computed and measured porewater pressures shown in Fig 8.38 agree closely for the first 5.0 seconds of the record and then deviate sharply. As discussed in section 8.2.2, the measured pressures are not compatible with all other records or the input motion. The record shows significant drainage from time 5.0 seconds. The only possible reason for such drainage is that during the strongest shaking in the range 4.0 to 6.0 seconds, a drainage path developed along the cable to the tranducer PPT 2842. The

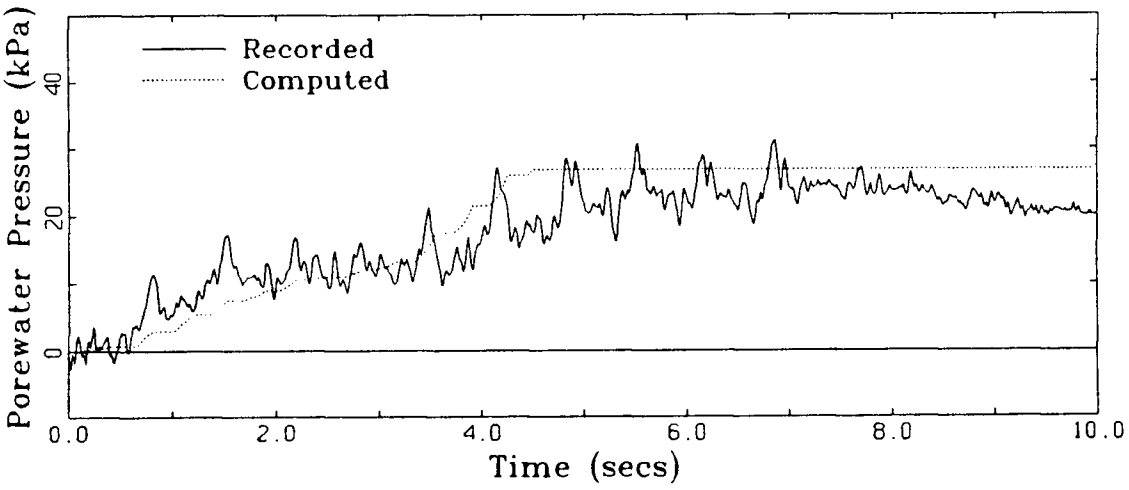

Fig. 8.34 Computed and Measured Porewater Pressures at the Location of PPT 2851 in Test RSS111/EQ1

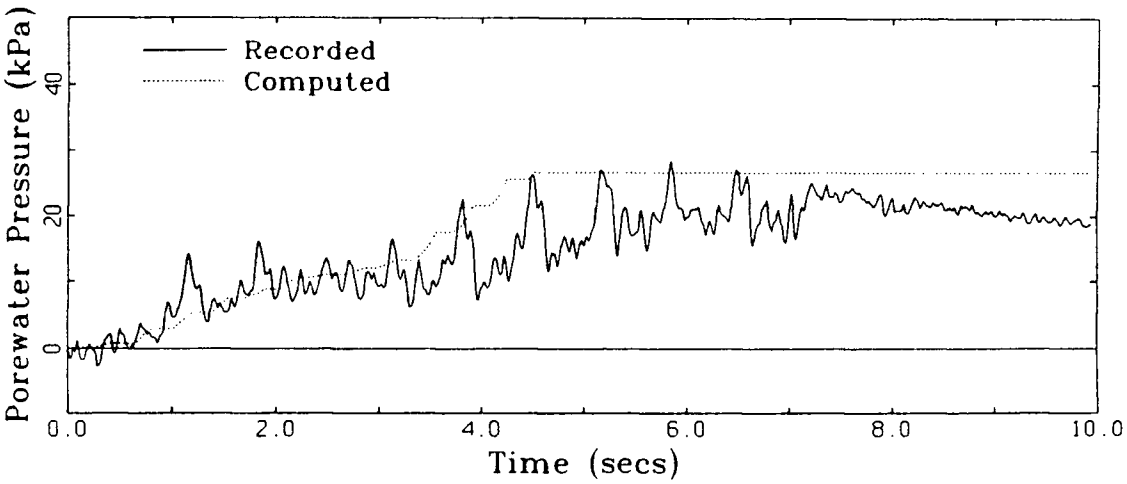

Fig. 8.35 Computed and Measured Porewater Pressures at the Location of PPT 2628 in Test RSS111/EQ1

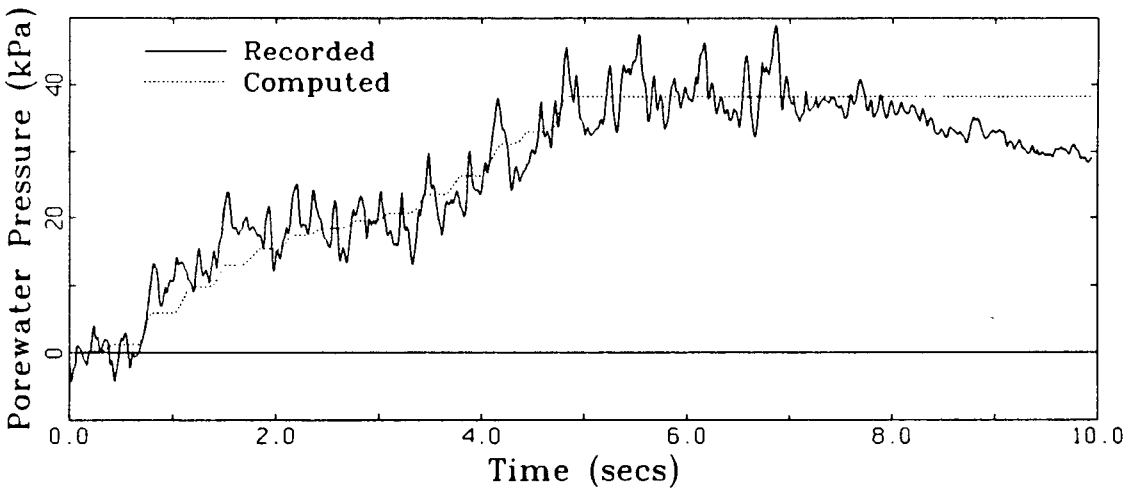

Fig. 8.36 Computed and Measured Porewater Pressures at the Location of PPT 2846 in Test RSS111/EQ1

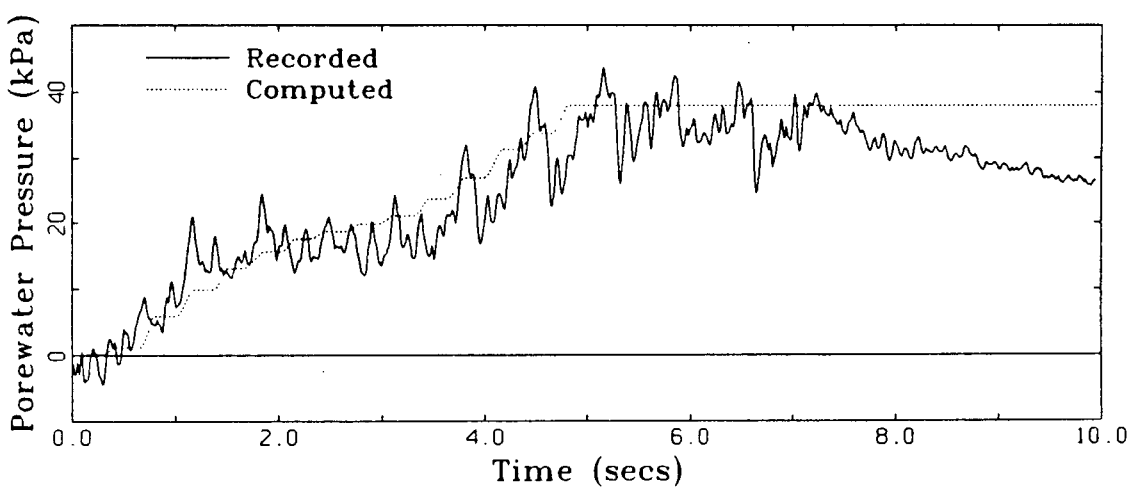

Fig. 8.37 Computed and Measured Porewater Pressures at the Location of PPT 2855 in Test RSS111/EQ1

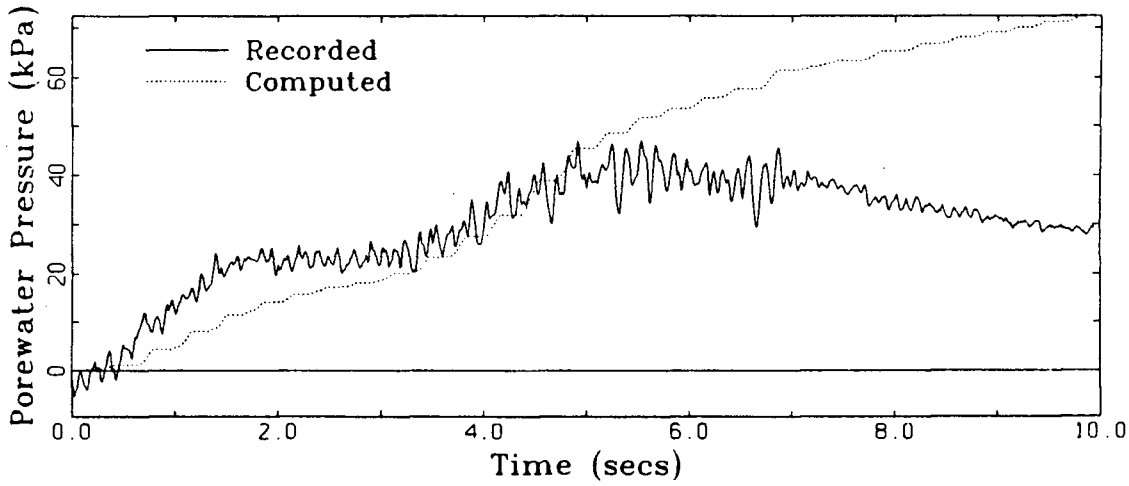

Fig. 8.38 Computed and Measured Porewater Pressures at the Location of PPT 2842 in Test RSS111/EQ1

computed pressures show a steady increase in the range 4.0 to 6.0 seconds consistent with the input. The demonstrated homogeneity of the model about the centerline and the close agreement between measured and computed porewater pressures for all other transducers support the notion that the behavior of PPT 2842 is anomalous.

Fig. 8.39 compares responses at the locations of PPT 2255 which was located out in the free field directly below PPT 2628. Computed and measured pressures at this location agree very well for the first 7.0 seconds and then show differences. The measured response shows significant drainage after time 7.0 seconds and therefore it is not strange to see discrepancies between them after 7.0 seconds. However, the measured and computed peak residual pressures differ only by a few percent.

The contours of peak residual porewater pressures computed by TARA-3 are shown in Fig. 8.40. The integers are the contour values in the unit kPa. The triangles show the locations where the porewater pressures were measured and the numbers with the decimal points indicate values of measured peak residual pressures. The figure demonstrates the overall agreement between the measured and computed values. It also illustrates the symmetric nature of the contours. The contours also support the notion that the movement of water during drainage and diffusion is from areas under the structure to outside towards the sloping and top horizontal boundaries of the sand foundation.

8.2.5 Stress-Strain Behavior

Computed shear stress-strain responses at selected locations are presented in this section to illustrate the effect of soil-structure interaction and porewater pressures on stress-strain responses. Fig. 8.41 and Fig. 8.42 show stress-strain responses at the locations of PPT 2338 and PPT 2842 respectively. At these locations, hysteretic behavior is evident but the response for the most part is only mildly nonlinear. This is not surprising as the initial

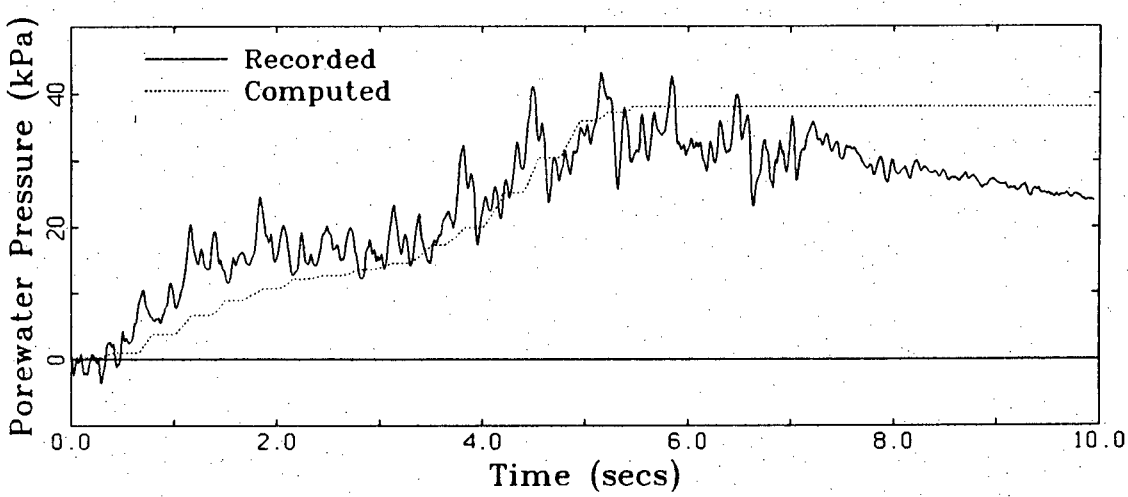

Fig. 8.39 Computed and Measured Porewater Pressures at the Location of PPT 2255 in Test RSS111/EQ1

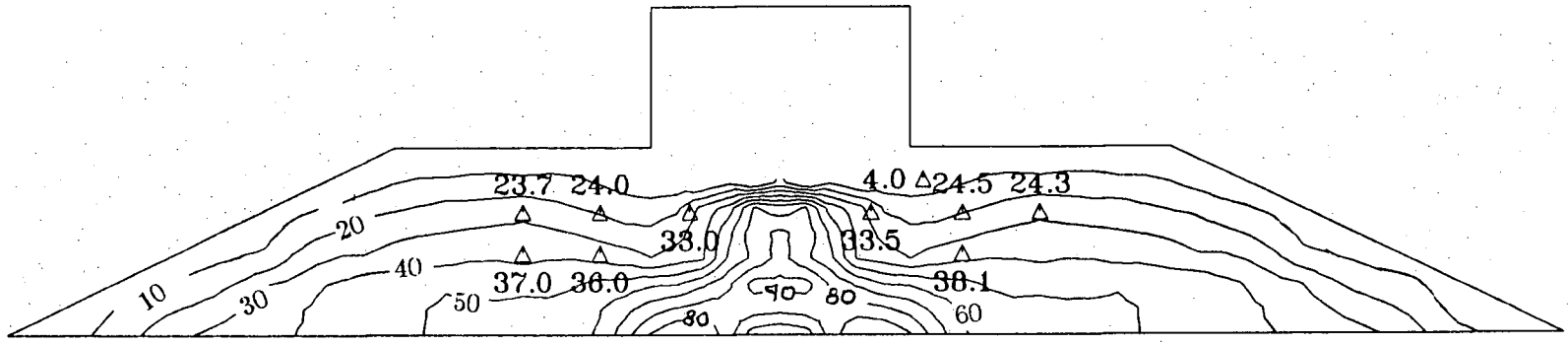

Fig. 8.40 Contours of Computed Peak Residual Porewater Pressures

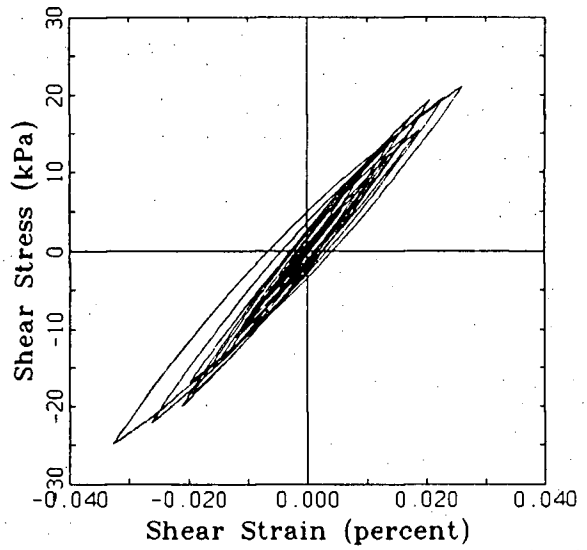

Fig. 8.41 Shear Stress-Strain Response at the Location of PPT 2338 in Test RSS111/EQ1

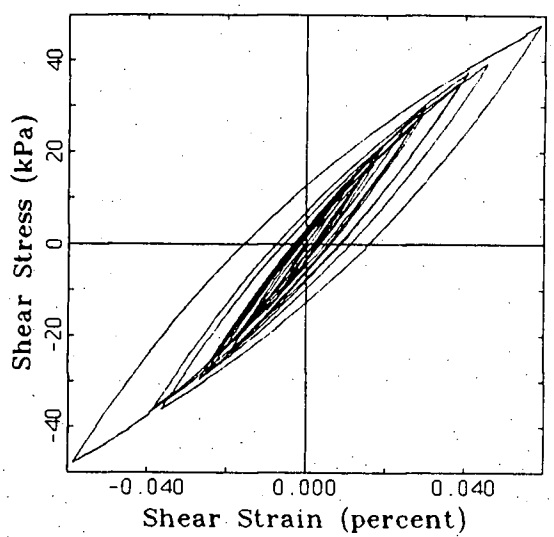

Fig. 8.42 Shear Stress-Strain Response at the Location of PPT 2842 in Test RSS111/EQ1

stresses under the structure are high and the porewater pressure ratio, u/σ'_{yo}, defined as the ratio between porewater pressure, u, and the initial effective vertical stress, σ'_{yo}, reached a level of only 16% and 24% at the locations of PPT 2338 and PPT 2842 respectively. Such low porewater pressure in relation to the initial effective vertical stress does not cause significant reduction in either shear modulus or shear strength; hence hysteretic loops remain narrow and stiff.

As the free field is approached, strong nonlinear behavior is evident. Particularly, the response in the free field at the location of PPT 2851 (Fig. 8.43) is strongly nonlinear with large hysteresis loops. This indicates considerable softening due to high porewater pressures and shear strains. At this location, the porewater pressure ratio reached about 80%. The stiffer loops found in the response are associated with the initial stages of the shaking where very low porewater pressure are generated. However, as the shaking continues, high porewater pressures are generated and as a result shear modulus and shear strength are reduced giving rise to the softer and flatter hysteretic loops.

At the location of PPT 2848, even though the response as shown in Fig. 8.44 is nonlinear, it is not as strongly nonlinear as at the location of PPT 2851. The porewater pressure ratio reached a level of about 66% at this location. At the location of PPT 2846, where the porewater pressure ratio reached a level of 65%, the stress-strain response shown in Fig. 8.45, has the same trend as at the location of PPT 2848.

8.2.6 Comparison of Displacements in Test RSS111/EQ1

The displacement time histories shown in Fig. 8.16 were not considered for comparison as LVDTs used in this test series have poor dynamic response characteristics (Steedman, 1986). That is, the response of the LVDT is frequency dependent. Therefore, unless the measured cyclic displacements are corrected appropriately for the frequency dependency

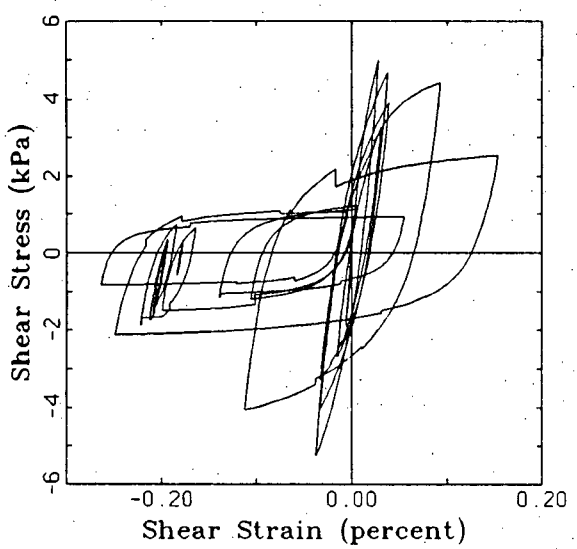

Fig. 8.43 Shear Stress-Strain Response at the Location of PPT 2851 in Test RSS111/EQ1

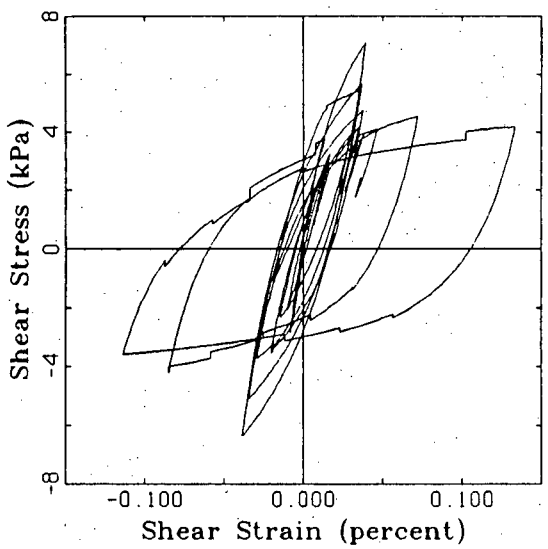

Fig. 8.44 Shear Stress-Strain Response at the Location of PPT 2848 in Test RSS111/EQ1

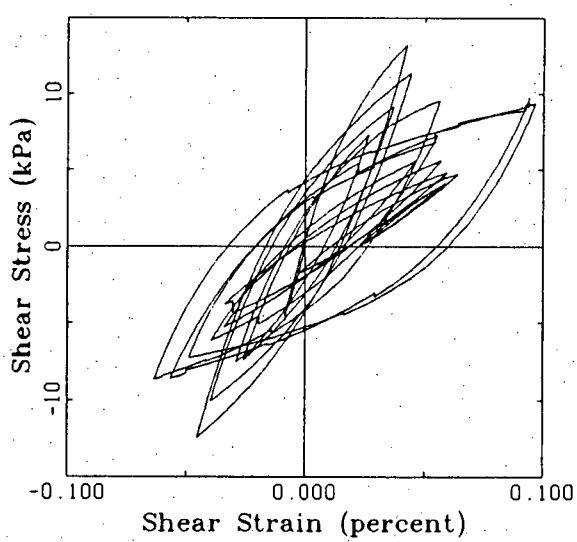

Fig. 8.45 Shear Stress-Strain Response at the Location of PPT 2846 in Test RSS111/EQ1

of the LVDTs, they cannot be used for comparison.

In order to illustrate the influence of frequency dependence of LVDT on cyclic displacements, the measured ACC 1938 acceleration record and the LVDT 4457 record are plotted together at prototype scale in Fig. 8.46. ACC 1938 was mounted on top of the structure and LVDT 4457 on the top left hand edge of the structure to measure horizontal displacements. Therefore, one should expect the horizontal acceleration response of ACC 1938 to be almost in phase with the horizontal displacement record of LVDT 4457. But it is evident as indicated in the figure that the displacement cycle lags behind the acceleration cycle by almost 50 degrees. This phase lag cannot be entirely due to dynamic response but primarily due to LVDT response. Problems of this nature have already been reported in the literature. Lambe and Whitman (1985) reported a similar phase lag between acceleration and displacement cycles in their centrifuge tests. They have also conducted calibration tests to study the frequency dependence of LVDTs used to measure transient displacements in their centrifuge tests. Fig. 8.47 shows a typical result obtained in their study. The circles and crosses show the results measured for two different LVDTs. The figure clearly shows that the amplitude ratio is a function of the cyclic frequency and it depends on the particular LVDT used. Therefore, improvements must be made in methods employed for measuring transient displacements. Ideally, one should use transducers that have flat frequency characteristics in the range of frequencies contributing to the transient displacement time history.

However, for static readings, LVDTs used in this test series are often adequate. The final displacements produced by the earthquake are compared at the locations of LVDT 1648 and LVDT 4457 in Table 8.3. The values quoted are at prototype scale. LVDT 1648 was mounted at the left hand top edge of the structure so as to measure vertical settlement while LVDT 4457 was located around the same place to measure horizontal displacement.

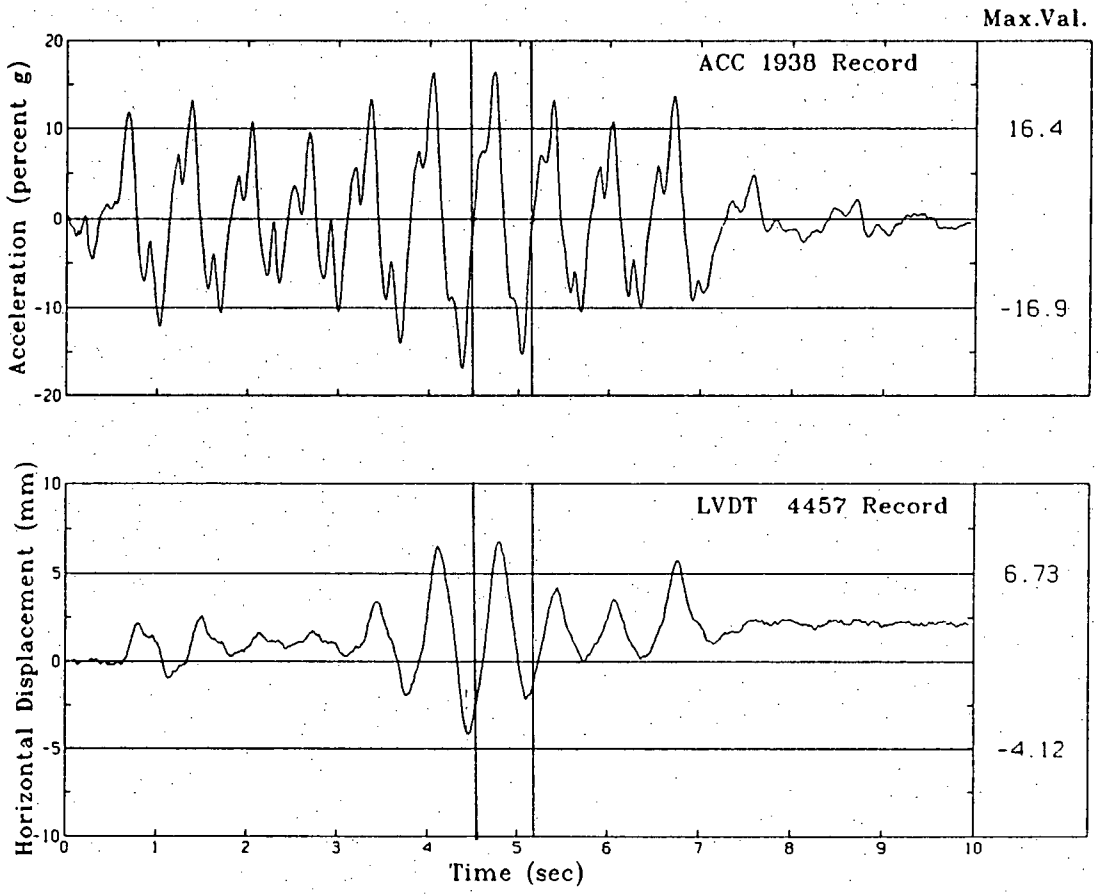

Fig. 8.46 Measured cyclic displacement and accelerations at the Locations of LVDT 4457 and ACC 1938 in Test RSS111/EQ1

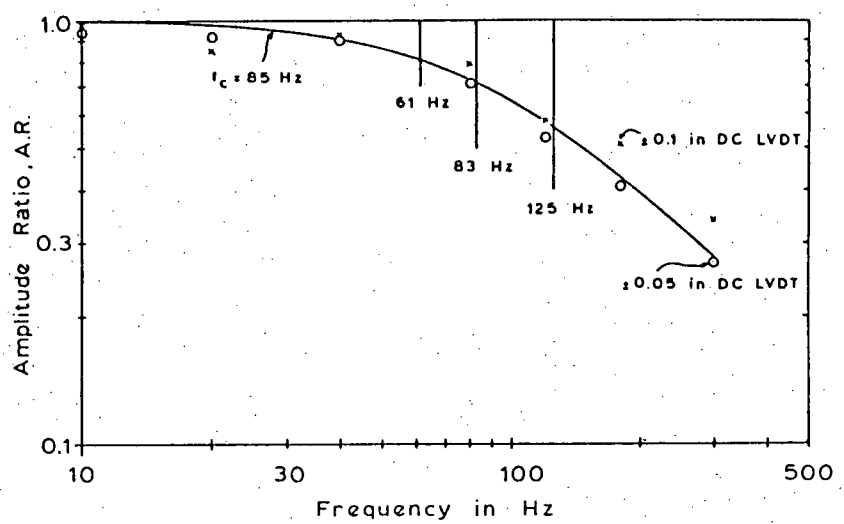

Fig. 8.47 Frequency Dependent Characteristics of LVDTs

It can be seen that the computed vertical settlement is 66% more than measured settlement. The computed horizontal displacement is very much higher than the measured value.

The final deformation pattern as computed by TARA-3 is shown in Fig. 8.48. The discontinuous line shows the undeformed shape and the solid line shows the deformed shape. It should be noted that for the purpose of clear illustration the deformations are magnified about 10 times. The top surface of the sand foundation settles more than the structure. Also, at the lower end of the sloping faces, the sand bulges out on both sides. This is close to a constant volume type of deformation as often found in fully saturated cases.

Table 8.3 Comparison of Displacements in Test RSS111/EQ1

Transducer No.	Measured (m)	Computed (m)	Direction
LVDT 1648	0.012	0.020	Vertical
LVDT 4457	0.0016	0.006	Horizontal

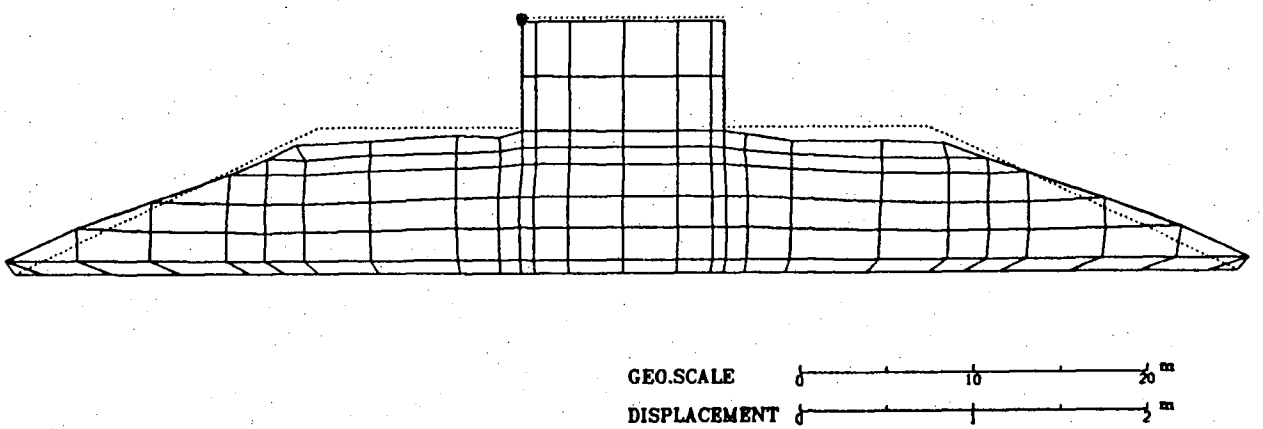

Fig. 8.48 Computed Deformation Pattern in Test RSS111/EQ1

CHAPTER 9

SUMMARY AND CONCLUSIONS

9.1 Summary

A nonlinear effective stress method of analysis for determining the static and dynamic response of 2-D embankments and soil-structure interaction systems is presented. The method of analysis has been incorporated into the computer program TARA-3. It is a revised and extensively modified version of an earlier program TARA-2 and has more efficient algorithms and additional features including energy transmitting boundaries.

An extensive verification of the capability of TARA-3 to model the dynamic response of structures using comprehensive data from a series of simulated earthquake tests on centrifuged model is presented. The models simulated a variety of structures ranging from simple embankments to soil-structure interaction systems which included surface and embedded structures on both dry and saturated sand foundation.

The centrifuge model tests used in the verification of TARA-3 were conducted over a three year period from 1983 to 1986. In the earlier period, the technology of model construction and as well as the technology for conducting seismic tests on large scale models was in its infancy. Consequently, the earlier model construction techniques led to rather inhomogeneous models with wide variations in density as evident from data in tests such

as the LDO4 series. At some locations in these models, it was difficult to decide whether differences between the computed and measured responses were due to instrumentation problems, lack of homogeneity in the sand foundation or deficiencies in the method of analysis.

As the test series progressed, model construction improved with experience and a new technique that produced homogeneous models was developed. Further, in order to obtain an unambiguous data base, the instruments were duplicated at corresponding locations on both sides of the centerline of the model. The extent to which the records at corresponding locations agree is an indication of the reliability and homogeneity. The model in test series RSS111 was constructed in this new approach and the data indicated that the model was very homogeneous. The differences between the computed and measured responses in this model were found to be very small and within the acceptable accuracy for engineering purposes. This indicates that TARA-3 is capable of conducting dynamic response analysis of soil structure systems with acceptable accuracy for engineering purposes.

9.2 Conclusions

The study described in this thesis led to the following conclusions:

1) This study clearly demonstrated the utility of centrifuge modeling in providing a comprehensive data base for validating methods of seismic response analyses. In no other way can such complete data coverage be obtained when required and at such a low cost.

2) The centrifuge tests clearly demonstrated key aspects of soil-structure interaction, namely, the high frequency rocking response, the effects of rocking on porewater pressure patterns and the distortion of free-field motions and porewater pressures by the presence of a structure.

3) The comparison between measured and computed responses for the various centrifuged models demonstrated the wide ranging capability of TARA-3 for performing complex effective stress soil-structure interaction analysis with acceptable accuracy for engineering purposes. Seismically induced residual porewater pressures are satisfactorily predicted even when there are significant effects of soil-structure interaction. Computed accelerations agree in magnitude, frequency content and distribution of peaks with those recorded. In particular, the program was able to model the high frequency rocking vibrations of the model structures. This is an especially difficult test of the ability of the program to model soil-structure interaction effects. Computed settlements also agree reasonably well with those measured.

4) It is necessary to incorporate an energy transmitting base to account properly for the energy transmitted into the underlying medium. The usual rigid base assumption may result in overestimation of the the dynamic response of the soil deposit.

5) Appropriate lateral boundaries for the model are also necessary to avoid feedback to the structure from the sides. Satisfactory results can be obtained when lateral boundaries are located at an appropriate distance from the edge of the structure. For both linear and nonlinear problems, the simple roller boundary proved as efficient and more economical than the other types of lateral boundaries.

9.3 Recommendations For Further Study

1) The capability of the method of analysis may be extended for the analysis 3-D problems.

2) Additional validation studies may be carried out to verify the predictive capability of TARA-3 to model the dynamic response of other geotechnical soil structures such as retaining walls and anchored bulkheads.

3) The program has been validated for models with homogeneous sand foundations. However, the method is also applicable to more heterogeneous conditions of real sites. It is obviously highly desirable when field become available to test the capability of TARA-3 under these variable conditions. Such a study is planned for later in 1988 when seismic data from the Lo Tung Reactor in Taiwan becomes available.

REFERENCES

Abghari, A., (1983), "Centrifuge Modeling of Soil Liquefaction", M.Sc Thesis, University of California, Davis,

Arulanandan, K., Anandarajah, K. and Abghari, A., (1983), "Centrifugal Modeling of Soil Liquefaction Susceptibility", Journal of the Geotechnical Engineering Division, ASCE, Vol. 109, No. 3, March, pp. 281-300.

Barton, Y.O., (1982), "Laterally Loaded Model Piles in Sand; Centrifuge Tests and Finite Element Analyses", Ph.D Thesis, Engineering Department, Cambridge University, June.

Bhatia, S.K., (1982), "The Verification of Relationships for Effective Stress Method to Evaluate Liquefaction Potential of Saturated Sands", Ph.D Thesis, Department of Civil Engineering, University of British Columbia, Vancouver, Canada.

Biot, M.A., (1941), "General Theory for Three Dimensional Consolidation", Journal of Applied Physics, Vol. 12, pp. 155-164.

Byrne, P.M., (1981), Class Notes: Numerical Methods in Soil Mechanics (CE573), University of British Columbia, Vancouver, B.C., Canada.

Byrne, P.M., and Cheung, H., (1984), "Soil Parameters for Deformation Analysis of Sand Masses", Soil Mechanics Series No. 81, Department of Civil Engineering, University of British Columbia, Vancouver, B.C., Canada.

Byrne, P.M., and Duncan, J.M., (1979), "NLSSIP: A Computer Program for Nonlinear Analysis of Soil-Structure Interaction Problems", Soil Mechanics Series No. 41, Department of Civil Engineering, University of British Columbia, Vancouver, Canada.

Byrne, P.M., and Eldridge, T.L., (1982), "A Three Parameter Dilatant Elastic Stress-Strain Models for Sand", International Symposium on Numerical Model in Geomechanics, Zurich, Sept., pp. 73-79.

Byrne, P.M., and Janzen, W., (1984), "INCOIL: A Computer Program for Nonlinear Analysis of Stress and Deformations in Oil Sand Masses", Soil Mechanics Series No. 80, Department of Civil Engineering, University of British Columbia, Vancouver, Canada.

Chang, C.S., (1982), "Residual Undrained Deformation from Cyclic Loading", Journal of the Geotechnical Engineering Division, ASCE, Vol. 108, GT4, April, pp. 637-646.

Chern, J.C., (1981), "Effect of Static Shear on Resistance to Liquefaction", M.A.Sc. Thesis, The University of British Columbia, Vancouver, May.

Clough, R.W. and Penzien, J. (1975), "Dynamics of Structures", McGraw Hill Book Co., New York, U.S.A.

Dean, E,T.R., (1973), "FLY-14 Program Suite: in Flight Data Handling and Analysis Manual", Report, Engineering Department, Cambridge University, Cambridge, U.K.

Dean, E.T.R., and Lee, F.H., (1984), "Seismically Induced Settlements in Soils: Data Report of Centrifuge Model Tests, LDO1-7", Engineering Department, Cambridge University, Cambridge, England.

Desai, C.S., and Abel, J.F., (1972), "Introduction to the Finite Element Method - A Numerical Method for Engineering Analysis", Van Nostrand Reinhold Company, New York, U.S.A.

Desai, C.S., and Christian, J.T., (1977), "Numerical Methods in Geotechnical Engineering", McGraw Hill Book Co., New York, U.S.A.

Duncan, J.M., Byrne, P.M., Wong, K.S., and Mabry, P., (1978), "Strength, Stress-Strain and Bulk Modulus Parameters for Finite Element Analyses of Stresses and Movements in Soil Masses", Report No. UCB/GT/78-02, April.

Duncan, J.M., and Chang, C.Y., (1970), "Non-linear Analysis of Stress and Strain in Soils", Proceedings, ASCE, Vol. 96, No. SM5, pp. 1629-1653.

Eyton, D.G.P., (1982), "Triaxial Tests on Sand With Viscous Pore Fluid", Part 2, Project Report, Engineering Department, Cambridge University, Cambridge, England.

Felio, G.Y., and Briaud, J.L., (1986), "Procedure for a Rod Shear Test", Geotechnical Testing Journal, ASTM, GTJODJ, Vol. 9, No. 3, pp. 133 - 139, September.

Finn, W.D. Liam., (1981), "Liquefaction Potential Development Since 1976", Proceedings, International Conference on Recent Advances in Geotechnical Earthquake Engineering and Soil Dynamics, St. Louis, Missouri, April 26-May 2, pp. 655-681.

Finn, W.D. Liam., (1987), "Dynamic Effective Stress Analysis of Embankments", Proceedings, International Symposium on Earthquakes and Dams, Vol. II, Beijing, China, May 27.

Finn, W.D. Liam., and Byrne, P.M., (1976), "Estimating Settlements in Dry Sands During Earthquakes", Canadian Geotechnical Journal, Vol. 13, No. 4, pp. 355-363.

Finn, W.D. Liam., and Gohl, W.B., (1987), "Centrifuge Model Studies of Piles under Sim-

ulated Earthquake Lateral Loading", Proceedings, Dynamic Response of Pile Foundations– Experiment, Analysis and Observation, Geotechnical Special Publication 11, ASCE Convention, Atlantic City, New Jersey, April 27.

Finn, W.D. Liam, Lee, K.W. and Martin, G.R. (1977), "An Effective Stress Model for Liquefaction", Journal of the Geotechnical Engineering Division, ASCE, June, pp. 517-533.

Finn, W.D. Liam., Martin, G.R., and Lee, K.W., (1978), "Comparison of Dynamic Analysis of Saturated Sands", Proc. ASCE Geotechnical Engineering Division, Specialty Conference on Earthquake Engineering and Soil Dynamics, Pasadena, California, June 19-21, pp. 472-491.

Finn, W.D.Liam., Yogendrakumar, M., Yoshida, N., and Yoshida, H., (1986), "TARA-3: A Program to Compute the Response of 2-D Embankments and Soil-Structure Interaction Systems to Seismic Loadings", Department of Civil Engineering, University of British Columbia, Vancouver, Canada.

Goodman, R.E., and Seed, H.B., (1966), "Earthquake Induced Displacements in Sand Embankments", Journal of the Soil Mechanics and Foundations Division, ASCE, Vol. 92, SM2, March, pp. 125-146.

Goodman, R.E., Taylor, R.L. and Brekke, T.L. (1968), "A Model for the Mechanics of Jointed Rock", Journal of the Soil Mechanics and Foundation Division, ASCE, May, pp. 637-659.

Hardin, B.O., and Drenevich, V.P., (1972), "Shear Modulus and Damping in Soils, Design Equations and Curves", Journal of the Soil Mechanics and Foundation Division, ASCE, Vol. 98, SM7, Proc. Paper 9006, July, pp. 667-692.

Iai, S., Tsuchida, H. and Finn, W.D.Liam., (1985), "An Effective Stress Analysis of Liquefaction at Ishinomaki Port During the 1978 Miyaki-Ken-Oki Earthquake", Report of the Port and Harbour Research Institute, Vol. 2, No. 2, June.

Joyner, W.B. (1975), "A Method for Calculating Nonlinear Seismic Response in Two Dimensions", Bulletin of the Seismological Society of America, Vol. 65, No. 5 pp. 1337-1357.

Joyner, W.B., and Chen, A.T.F., (1975), "Calculation of Nonlinear Ground Response in Earthquakes", Bulletin of the Seismological Society of America, Vol. 65, No. 5, pp. 1315 - 1336, October.

Kondner, R.L., and Zelasko, J.S., (1963), "A Hyperbolic Stress-Strain Formulations of Sands", Proceedings of 2nd Pan American Conference on Soil Mechanics and Foundation Engineering, Vol. 1, Brazil.

Kulhawy, F.H., Duncan, J.M., and Seed, H.B., (1969), "Finite Element Analysis of Stresses and Movements in Embankments During Construction", Geotechnical Engineering Reasearch Report No. TE-69-4, Department of Civil Engineering, University of California, Berkeley, Nov.

Kunar, R.R., and Marti, J., (1981), "A Non-Reflecting Boundary for Explicit Calculations", Winter Annual Meeting, ASME: Computational Methods for Infinite Media-Structure Interaction, AMD 46, Washington, D.C., pp 182-204, November.

Lambe, P.C., and Whitman, R.V., (1985), "Dynamic Centrifugal Modeling of Horizontal Dry Sand Layer", Journal of the Geotchnical Engineering Division, ASCE, Vol. 111, No. 3, March, pp. 265-287.

Lee, K.W., (1965), "Triaxial Compressive Strength of Saturated Sands Under Seismic Loading Conditions", Ph.D Thesis, University of California, Berkeley.

Lee, K.L., (1974), "Seismic Permanent Deformations in Earth Dams", Report to the National Science Foundation, School of Engineering and Applied Science, University of California, Los Angeles, December.

Lee, M.K.W., (1975), "Mechanical Model for the Analysis of Liquefaction of Horizontal Soil Deposits", Ph.D. Thesis, Department of Civil Engineering, University of British Columbia, Vancouver, B.C., Canada, Sept.

Lee, M.K.W., and Finn, W.D Liam., (1975), "DESRA-1: Program for Dynamic Effective Stress Response Analysis of Soil Deposits including Liquefaction Evaluation , Soil Mechanics Series, No.36, Dept. of Civil Engineering, University of British Columbia, Vancouver, B.C., Canada.

Lee, M.K.W. and Finn, W.D. Liam (1978) "DESRA-2: Dynamic Effective Stress Response Analysis of Soil Deposits with Energy Transmitting Boundary Including Assessment of Liquefaction Potential" Soil Mechanics Series Report No. 38, Dept of Civil Engineering, University of British Columbia, Vancouver, Canada.

Lysmer, J., and Kuhlemeyer, R.L., (1969), "Finite Dynamic Model for Infinite Media", Journal of the Engineering Mechanics Division, ASCE, Vol. 95, EM4, Sept. pp. 859-877

Lysmer, J., Udaka, T., Tsai, C.F., and Seed, H.B., (1975), "FLUSH: A Computer Program for Approximate 3-D Analysis of Soil-Structure Interaction Problems", Report No. EERC 75-30, Earthquake Engineering Research Center, University of California, Berkeley, California.

Lysmer, J., and Wass, G., (1972), "Shear Waves in Plane Infinite Structures", Journal of Engineering Mechanics Division, ASCE, Vol. 98, EM1, Feb., pp. 85-105.

Martin, G.R., Finn, W.D. Liam., and Seed, H.B., (1975), "Fundementals of Liquefaction Under Cyclic Loading", Journal of the Geotechnical Engineering Division, ASCE, Vol. 101, GT5, May, pp 423-438.

Masing, G., (1926) "Eigenspannungen and Verfestigung Beim Messing", Proceedings, 2nd International Congress of Applied Mechanics, Zurich, Switzerland.

National Research Council of the United States (1982), "Earthquake Engineering -1982", Report by Committee on Earthquake Engineering Research, National Academy Press, Washington, D.C.

National Research Council of the United States (1985), "Liquefaction of Soils During Earthquakes", Report by Committee on Earthquake Engineering, National Academy Press, Washington, D.C.

Naylor, D.J., and Pande, G.N., (1981), "Finite Elements in Geotechnical Engineering", Rainbow - Bridga Book Co. Ltd.

Newmark, N.M., (1959), "A Method of Computation for Structural Dynamics", Journal of the Engineering Mechanics Division, ASCE, Vol. 85, EM3, July.

Newmark, N.M., (1965), "Effects of Earthquake on Dams and Embankments", 5th Rankine Lecture, Geotechnique 15, No.2, pp. 139-160.

Newmark, N.M., and Rosenblueth, E., (1971), "Fundermentals of Earthquake Engineering", Prentice-Hall Inc., Englewood, Cliff, N.J., pp. 162-163.

Ozawa, Y., and Duncan, J.M., (1973), "ISBILD: A Computer Program for Analysis of Static Stresses and Movements in Embankments", Geotechnical Engineering Research Report No. TE-73-4, Department of Civil Engineering, University of California, Berkeley, Dec.

Prevost, J.H., (1981), "DYNAFLOW: A Nonlinear Transient Finite Element Analysis Program", Department of Civil Engineering, Princeton University, Princeton, New Jersey, U.S.A.

Roesset, J.M., and Ettouney, M.M., (1977), "Transmitting Boundaries: A Comparison", International Journal for Numerical and Analytical Methods in Geomechanics, Vol. 1, pp. 151 - 176.

Robertson, P.K., (1982), "In-situ Testing of Soils with Emphasis on Its Application to Liquefaction Assessment", Ph.D Thesis, Department of Civil Engineering, University of British Columbia, Vancouver, Canada.

Roscoe, K.H, (1968), "Soils and Model Tests", Journal of Strain Analysis, No. 3, pp. 57-64.

Schnabel, P.B., Lysmer, J., and Seed, H.B., (1972), "SHAKE: A Computer Program for Earthquake Response Analysis of Horizontally Layered Sites", Report No. EERC 72-12, Earthquake Engineering Research Center, University of California Berkeley, Dec.

Schofield, A.N., (1981), "Dynamic and Earthquake Geotechnical Centrifuge Modelling", International Conference on Recent Development in Earthquake Engineering and Soil Dynamics, Missouri, U.S.A., April 28-May2.

Scott, R.F, (1978), "Summary Specialty Session 7 - Modeling" Proceedings, Specialty Conference on Earthquake Engineering and Soil Dynamics, ASCE, Vol. III, Pasadena, CA, June 19-22,

Seed, H.B., (1979a), "Considerations in the Earthquake-Resistant Design of Earth and Rockfill Dams", 19th Rankine Lecture, Geotechnique 29, No. 3, pp. 215-263.

Seed, H.B., (1979b), "Soil Liquefaction and Cyclic Mobility Evaluation for Level Ground During Earthquakes", Journal of Geotechnical Engineering Division, ASCE, Vol. 105, No. GT2, pp. 201-255.

Seed, H.B., and Idriss, I.M., (1970), "Soil Moduli and Damping Factors for Dynamic Response Analysis", Report No. EERC 70-10, Earthquake Engineering Research Center, Univ. of California, Berkeley, December.

Seed, H.B., and Lee, K.L., (1966), "Liquefaction of Saturated Sands During Cyclic Loading", Journal of the Soil Mechanics and Foundation Engineering Division, ASCE, Vol. 92, No, SM6, November.

Serff, N., Seed, H.B., Makdisi, F.I., and Chang, C.Y., (1976), "Earthquake Induced Deformations of Earth Dams", Report No. EERC 76-4, Earthquake Engineering Research Center, University California, Berkeley, Sept.

Siddharthan, R., (1984), "A Two-Dimensional Nonlinear Static and Dynamic Response Analysis of Structures", Ph.D Thesis, Department of Civil Engineering, University of British Columbia, Vancouver, Canada.

Siddharthan, R., and Finn, W.D. Liam., (1982), "TARA-2: Two Dimensional Nonlinear Static and Dynamic Response Analysis", Department of Civil Engineering, University of

British Columbia, Vancouver, Canada.

Simons, H.A., and Randolph, M.F., (1986), "Short Communication: Comparison of Transmitting Boundaries in Dynamic Finite Element Analyses using Explicit Time Integration", International Journal for Numerical and Analytical Methods in Geomechanics, Vol. 10, pp. 329-342.

Steedman, R.S., (1985), "Seismically Induced Settlements in Soils: Data Report of Centrifuge Model Tests, RSS90 and RSS91", Engineering Department, Cambridge University, Cambridge, England.

Steedman, R.S., (1986), "Embedded Structure on Sand Foundation: Data Report of Centrifuge Model Tests, RSS110 and RSS111", Engineering Department, Cambridge University, Cambridge, England.

Tatsuoka, F., and Haibara, O., (1985), "Shear Resistance Between Sand and Smooth or Lubricated Surfaces", Soils and Foundations, Vol. 25, No. 1, pp. 89-98.

Uesugi, M., and Kishida, H., (1986), "Influential Factors of Friction Between Steel and Dry Sands", Soils and Foundations, Vol. 26, No. 2, pp. 33-46.

Vaid, Y.P., and Chern, J.C., (1981), "Effect of Static Shear on resistance to Liquefaction", Soil Mechanics Series No. 51, Department of Civil Engineering, University of British Columbia, Vancouver, Canada.

Vaid, Y.P., and Finn, W.D. Liam., (1979), "Effect of Static Shear on Liquefaction Potential", Journal of the Geotechnical Engineering Division, ASCE, Vol. 105, GT10, OCT., pp. 1233-1246.

Vaziri-Zanjani, H.H., (1986), "Nonlinear Temperature and Consolidation Analysis of Gassy Soils", Ph.D Thesis, Department of Civil Engineering, University of British Columbia, Vancouver, Canada.

Wedge, N.E., (1977), "Problems in Nonlinear Analysis of Movements in Soils", M.A.Sc Thesis, Department of Civil Engineering, University of British Columbia, Vancouver, Canada.

Wilson, E.L., Farhomand, I., and Bathe, K.J., (1973), "Non-Linear Dynamic Analysis of Complex Structures", International Journal of Earthquake Engineering and Structural Dynamics, Vol. 1, pp 241-252.

Yogendrakumar, M. and Finn, W.D. Liam., (1984), "SIMCYC: Simulation of the Cyclic Simple Shear Tests on Dry and Saturated Sands" Soil Dynamics Group, University of British Columbia, Canada.

Yogendrakumar, M., and Finn, W.D. Liam., (1986), "C-PRO: A Program for Evaluating the Constants in the Martin-Finn-Seed Porewater Pressure Model" Soil Dynamics Group, Department of Civil Engineering, University of British Columbia, Vancouver, Canada, November.

Yoshimi, Y., and Kishida, T., (1981), "A Ring Torsion Apparatus for Evaluating Friction Between Soil and Metal Surfaces", Geotechnical Testing Journal, GTJODJ, Vol. 4, No. 4, pp. 145-152.

Zienkiewicz, O.C., and Cheung, Y.K., (1967), "Finite Element Method in Structural and Continuum Mechanics", McGraw Hill Book Company.

APPENDIX I

STIFFNESS MATRIX IN TERMS OF EFFECTIVE STRESSES

The strain vector, $\{\epsilon\}$, is related to the nodal displacement vector, $\{\delta\}$, as follows:

$$\{\epsilon\} = [B]\{\delta\} \tag{A1.1}$$

in which,

$[B]$ = strain displacement matrix which depends on the element geometry.

The effective stress vector, $\{\sigma'\}$, is related to the strain vector by

$$\{\sigma'\} = [D]\{\epsilon\} \tag{A1.2}$$

where,

$[D]$ = elasticity matrix.

$\{\sigma'\}$ and $[D]$ for 2-D plane strain problems are given by

$$\{\sigma'\} = \begin{Bmatrix} \sigma'_x \\ \sigma'_y \\ \tau_{xy} \end{Bmatrix} \tag{A1.3}$$

and

$$[D] = \begin{bmatrix} B + 4/3\,G & B - 2/3\,G & 0 \\ B - 2/3\,G & B + 4/3\,G & 0 \\ 0 & 0 & G \end{bmatrix} \tag{A1.4}$$

where,

B = bulk modulus and

G = shear modulus.

For equilibrium, the principle of virtual work requires that the work done by the virtual displacement, $\{\bar{\delta}\}$, must equal the work done by the internal stresses.

Supposing virtual strains due to the virtual displacement, $\{\bar{\delta}\}$, be $\{\bar{\epsilon}\}$, then the internal work done, W_{in}, is given by

$$W_{in} = \iiint_V \{\bar{\epsilon}\}^T \{\sigma\}\, dV \qquad (A1.5)$$

where,

$\{\sigma\}$ = total stress vector.

Now by effective stress principles,

$$\{\sigma\} = \{\sigma'\} + \{u\} \qquad (A1.6)$$

where,

$\{u\}$ = porewater pressure vector which is defined as,

$$\{u\} = \begin{Bmatrix} u_o \\ u_o \\ 0 \end{Bmatrix} \qquad (A1.7)$$

in which,

u_o = porewater pressure in the element.

Substituting equation $(A1.6)$ into equation $(A1.5)$ yields,

$$W_{in} = \iiint_V \{\bar{\epsilon}\}^T \left[\{\sigma'\} + \{u\} \right] dV \qquad (A1.8)$$

Further from relationship in equation $(A1.2)$,

$$W_{in} = \iiint_V \{\bar{\epsilon}\}^T \left[[D] \{\epsilon\} + \{u\} \right] dV \qquad (A1.9)$$

Using equation (A1.1), the above expression can be rewritten as,

$$W_{in} = \iiint_V \{\bar{\delta}\}^T \left[[B]^T [D] [B] \{\delta\} + [B]^T \{u\} \right] dV \qquad (A1.10)$$

Supposing the external load vector is $\{p\}$, then the external work done, W_{ex}, is

$$W_{ex} = \{\bar{\delta}\}^T \{p\} \tag{A1.11}$$

Now by principle of virtual work,

$$W_{ex} = W_{in} \tag{A1.12}$$

or

$$\{\bar{\delta}\}^T \{p\} = \iiint_V \{\bar{\delta}\}^T \left[[B]^T [D] [B] \{\delta\} + [B]^T \{u\} \right] dV \tag{A1.13}$$

or

$$\{p\} = \iiint_V [B]^T [D] [B] \, dV \, \{\delta\} + \iiint_V [B]^T \, dV \, \{u\} \tag{A1.14}$$

or

$$\{p\} = [k] \{\delta\} + [k^*] \{u\} \tag{A1.15}$$

in which,

$[k]$ = element stiffness matrix,

$[k^*]$ = element porewater pressure matrix.

They are defined as,

$$[k] = \iiint_V [B]^T [D] [B] \, dV \tag{A1.16}$$

$$[k^*] = \iiint_V [B]^T \, dV \tag{A1.17}$$

Nonlinear problems are solved using incremental elastic approach. Therefore, the displacements, stresses, strains and moduli values are replaced by incremental displacements, incremental stresses, incremental strains and tangent moduli respectively.

The global incremental equation can then be written as,

$$\{\Delta P\} = [K_t] \{\Delta\} + [K^*] \{\Delta U\} \tag{A1.18}$$

where,

$\{\Delta P\}$ = incremental global load vector,

$[K_t]$ = global tangent stiffness matrix,

$[K^*]$ = global porewater pressure matrix,

$\{\Delta\}$ = incremental global displacement vector,

$\{\Delta U\}$ = incremental global porewater pressure vector.

It is often required to express nodal forces in an element in terms of stresses and strains. The following expressions give nodal forces in terms of stresses and strains respectively.

$$\{p\} = \iiint_V [B]^T \{\sigma'\}\, dV \qquad (A1.20)$$

and

$$\{p\} = \iiint_V [B]^T [D] \{\epsilon\}\, dV \qquad (A1.19)$$

APPENDIX II

STIFFNESS MATRIX FOR SLIP ELEMENT

The force displacement relationship at any point within the slip element shown in Fig. A2.1 is given by

$$\begin{Bmatrix} f_s \\ f_n \end{Bmatrix} = \begin{bmatrix} K_s & 0 \\ 0 & K_n \end{bmatrix} \begin{Bmatrix} w_s \\ w_n \end{Bmatrix} \qquad (A2.1)$$

or,

$$\{f\} = [k]\{w\} \qquad (A2.2)$$

in which,

f_s = shear force per unit area of the element,

f_n = normal force per unit area of the element,

K_s = unit shear stiffness in the direction of the element,

K_n = unit normal stiffness in the direction normal to the element,

w_s = shear displacement at the point of interest and,

w_n = normal displacement at the point of interest.

Let u_P, u_Q, u_R and u_S be the nodal displacements in the direction of the slip element of nodes P, Q, R and S respectively. Since the variation in displacement is assumed to be linear, then the displacement, u_{top}, in the direction of the slip element at any point on segment RS at a distance l from S, is given as

$$u_{top} = \frac{l}{L} u_R + \left(1 - \frac{l}{L}\right) u_S \qquad (A2.3)$$

or

$$u_{top} = N_1 u_R + N_2 u_S \qquad (A2.4)$$

in which,

$$N_1 = \frac{l}{L} \tag{A2.5}$$

$$N_2 = (1 - \frac{l}{L}) \tag{A2.6}$$

Similarly, the displacement in the direction normal to the slip element, u_{bot}, at any point on segment PQ at a distance l from P, is given by

$$u_{bot} = N_1 \; u_Q + N_2 \; u_P \tag{A2.7}$$

Now, the shear displacement, w_s at that point is given by,

$$w_s = u_{top} - u_{bot} \tag{A2.8}$$

or

$$w_s = [\, -N_2 \quad -N_1 \quad N_1 \quad N_2 \,] \begin{Bmatrix} u_P \\ u_Q \\ u_R \\ u_S \end{Bmatrix} \tag{A2.9}$$

Similarly, the normal displacement, w_n, can be shown as,

$$w_n = [\, -N_2 \quad -N_1 \quad N_1 \quad N_2 \,] \begin{Bmatrix} v_P \\ v_Q \\ v_R \\ v_S \end{Bmatrix} \tag{A2.10}$$

Combining equations (A2.9) and (A2.10) will yield,

$$\{w\} = \begin{bmatrix} -N_2 & 0 & -N_1 & 0 & N_1 & 0 & N_2 & 0 \\ 0 & -N_2 & 0 & -N_1 & 0 & N_1 & 0 & N_2 \end{bmatrix} \begin{Bmatrix} u_P \\ v_P \\ u_Q \\ v_Q \\ u_R \\ v_R \\ u_S \\ v_S \end{Bmatrix} \tag{A2.11}$$

This takes the form,

$$\{w\} = [B_s]\ \{\delta\} \tag{2.12}$$

Now, the elastic energy stored in the slip element due to the applied forces, $\{f\}$, is given by

$$\phi_E = \frac{1}{2}\ \int_0^L \{w\}^T\ \{f\}\ dl \tag{A2.13}$$

Using the relationships in equations $(A2.12)$ and $(A2.2)$, ϕ_E can be expressed as,

$$\phi_E = \frac{1}{2}\ \int_0^L \{\delta\}^T\ [B_s]^T\ [k]\ [B_s]\ \{\delta\}\ dl \tag{A2.14}$$

This can be arranged as,

$$\phi_E = \frac{1}{2}\ \{\delta\}^T\ \left[\int_0^L [B_s]^T\ [k]\ [B_s]\ dl\right]\ \{\delta\} \tag{A2.15}$$

Therefore, the stiffness matrix, $[K_{sn}]$, of the slip element can be deduced as,

$$[K_{sn}]\ =\ \int_0^L [B_s]^T\ [k]\ [B_s]\ dl \tag{A2.16}$$

That is,

$$[K_{sn}]\ =\ \int_0^L [K]\ dl \tag{A2.17}$$

where,

$$[K] = \begin{bmatrix} -N_2 & 0 \\ 0 & -N_2 \\ -N_1 & 0 \\ 0 & -N_1 \\ N_1 & 0 \\ 0 & N_1 \\ N_2 & 0 \\ 0 & N_2 \end{bmatrix} \begin{bmatrix} K_s & 0 \\ 0 & K_n \end{bmatrix} \begin{bmatrix} -N_2 & 0 & -N_1 & 0 & N_1 & 0 & N_2 & 0 \\ 0 & -N_2 & 0 & -N_1 & 0 & N_1 & 0 & N_2 \end{bmatrix} \tag{A2.18}$$

Equations $(A2.17)$ and $(A2.18)$ indicate that the following integrals have to be evaluated in order to define terms in $[K_{sn}]$,

$\int_0^L N_1^2\,dl$, $\int_0^L N_1 N_2\,dl$ and $\int_0^L N_2^2\,dl$.

Now,

$$\int_0^L N_1^2\,dl \;=\; \int_0^L (\frac{l}{L})^2\,dl$$

$$\int_0^L N_1^2\,dl \;= \frac{L}{3} \tag{A2.19}$$

$$\int_0^L N_1 N_2\,dl \;=\; \int_0^L (\frac{l}{L})\;(1-\frac{l}{L})\,dl$$

$$\int_0^L N_1 N_2\,dl \;= \frac{L}{6} \tag{A2.20}$$

$$\int_0^L N_2^2\,dl \;=\; \int_0^L (1-\frac{l}{L})^2\,dl$$

$$\int_0^L N_2^2\,dl \;= \frac{L}{3} \tag{A2.21}$$

Using equations $(A2.17)$ through $(A2.21)$, $[K_{sn}]$ can be shown as,

$$[K_{sn}] = \frac{L}{6}\begin{bmatrix} 2K_s & 0 & K_s & 0 & -K_s & 0 & -2K_s & 0 \\ 0 & 2K_n & 0 & K_n & 0 & -K_n & 0 & -2K_n \\ K_s & 0 & 2K_s & 0 & -2K_s & 0 & -K_s & 0 \\ 0 & K_n & 0 & 2K_n & 0 & -2K_n & 0 & -K_n \\ -K_s & 0 & -2K_s & 0 & 2K_s & 0 & K_s & 0 \\ 0 & -K_n & 0 & -2K_n & 0 & 2K_n & 0 & K_n \\ -2K_s & 0 & -K_s & 0 & K_s & 0 & 2K_s & 0 \\ 0 & -2K_n & 0 & -K_n & 0 & K_n & 0 & 2K_n \end{bmatrix} \tag{A2.22}$$

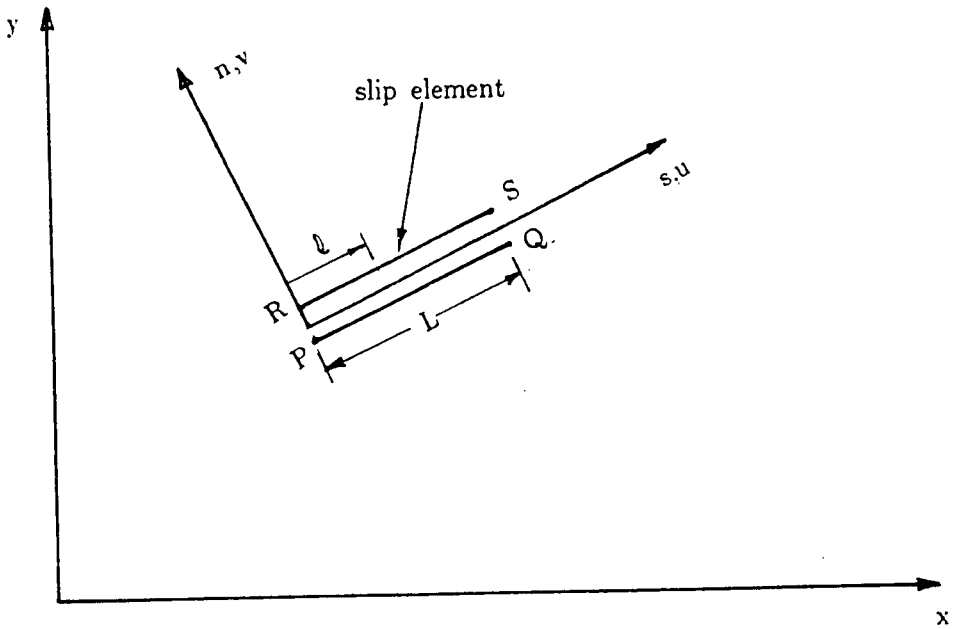

Fig. A2·1 Definition of Slip Element

Publications

1. Finn, W.D. Liam, Yogendrakumar, M. and Yoshida, N., "Dynamic Nonlinear Hysteretic Effective Stress Analysis in Geotechnical Engineering", Invited State-of-the-Art Address, Sixth International Conference on Numerical Methods in Geomechanics to be held in Innsbruck, Austria, April 1988.

2. Finn, W.D. Liam and Yogendrakumar, M., "Seismic Soil-Structure Interaction", Proceedings of the Pacific Conference on Earthquake Engineering, Auckland, New Zealand, August 1987.

3. Finn, W.D. Liam and Yogendrakumar, M., "Centrifugal Modelling and Analysis of Soil-Structure Interaction", Proceedings of the Fifth Canadian Conference on Earthquake Engineering, Ottawa, Canada, July 6-8, 1987.

4. Finn, W.D. Liam, Yogendrakumar, M., Yoshida, N. and Yoshida, H., "Analysis of Pore Pressures in Seismic Centrifuge Tests", Proceedings of the Third International Conference on Soil Dynamics and Earthquake Engineering, Princeton, N.J., U.S.A., June 22-24, 1987.

5. Finn, W.D. Liam, Yogendrakumar, M. and Nichols, A., "Seismic Response Analysis: Prediction and Performance", Invited State-of-the-Art Address, Proceedings of the International Symposium on Prediction and Performance in Geotechnical Engineering, Calgary, Canada, 1987, Editors: R.C. Joshi and F.J. Griffiths.

6. Finn, W.D. Liam, Yogendrakumar, M., Yoshida, N. and Yoshida, H., "Verification of Dynamic Soil-Structure Interaction Analysis", Proceedings of the Seventh Japan Earthquake Engineering Symposium, Tokyo, Japan, December 1986.

7. Finn, W.D. Liam, Steedman, R.S., Yogendrakumar, M. and Ledbetter, R.H., "Seismic Response of Gravity Structures in a Centrifuge", Proceedings of the Seventeenth Offshore Tech. Conference, OTC paper #4885, Houston, Texas, U.S.A., May 1985.

8. Finn, W.D. Liam, Siddharthan, R. and Yogendrakumar, M., "Response of Caisson Retained and Tanker Islands to Waves and Earthquakes", Proceedings of the 36th Canadian Geotechnical Conference, Vancouver, Canada, June 22, 1983.